THE UNIVERSITY *of* EDINBURGH

HOSSAIN ZADHOUSH

NUMERICAL MODELLING OF GROUND PENETRATING RADAR FOR OPTIMISATION OF THE TIME-ZERO ADJUSTMENT AND COMPLEX REFRACTIVE INDEX MODEL

NUMERICAL MODELLING OF GROUND PENETRATING RADAR FOR OPTIMISATION OF THE TIME-ZERO ADJUSTMENT AND COMPLEX REFRACTIVE INDEX MODEL

HOSSAIN ZADHOUSH

THE UNIVERSITY
of EDINBURGH

Doctor of Philosophy

2020

I dedicate my thesis to my family for
their love, prayers and support.

DECLARATION

I hereby declare that this thesis and the work reported herein was composed and originated entirely by myself, under the supervision of Dr. Antonios Giannopoulos in the School of Engineering at The University of Edinburgh.

The following journal publications are as a result of the research conducted for this thesis, which has not been submitted for any other degree or professional qualification.

- Zadhoush, H., Giannopoulos, A. and Giannakis, I., (2021), "Optimising the Complex Refractive Index Model for estimating the permittivity of heterogeneous concrete models," *Remote Sensing*, 13(4), 723.
- Zadhoush, H., Giannopoulos, A. and Giannakis, I., (2021), "A Revised Complex Refractive Index Model for Inferring the Permittivity of Heterogeneous Concrete Models," *European Geosciences Union (EGU)*.
- Zadhoush, H. and Giannopoulos, A., (2021), "Optimising GPR time-zero adjustment and two-way travel time wavelet measurement using a realistic 3D numerical model," *Near Surface Geophysics*. (Submitted for publication).

Edinburgh, 2020

Hossain Zadhoush

ABSTRACT

Time-zero adjustment or the true ground surface for Ground Penetrating Radar (GPR) applications is a very important aspect and an essential factor in order to carry out accurate shallow depth measurements. As the transmitted and received signals from GPR antennas are affected by the presence of different materials with various dielectric constants and electromagnetic properties adjusting the time-zero appropriately is important. This study uses a realistic Three Dimensional (3D) numerical model of a GPR transducer in order to examine where is the best location for time-zero on a GPR trace. It is shown that in order to establish a robust and consistent time-zero position careful consideration is needed also of the way the two-way travel time of the reflected GPR wavelet is estimated as well. Starting with a simple homogeneous model with a set of different targets a better process of time-zero adjustment and time picking of the GPR wavelets is put forward that is verified using further more complex and realistic heterogeneous models. Further verification is obtained by using experimental data.

Estimating the permittivity of heterogeneous mixtures based on the permittivity of their individual components is of high importance with many applications in GPR and in electrodynamics-based sensing in general. The Complex Refractive Index Model (CRIM) is the most mainstream approach for estimating the bulk permittivity of heterogeneous materials and has widely been applied for GPR applications. The popularity of CRIM is primarily based on its simplicity while its accuracy has never been rigorously tested. In the current study, an optimized shape factor is derived that is fine-tuned for modelling the dielectric properties of concrete. The bulk permittivity of concrete is expressed with respect to its components i.e, aggregate particles, cement particles, air-void and volumetric water fraction. Different combinations of the above materials are accurately modelled using the Finite-Difference Time-Domain (FDTD) method. The numerically estimated bulk permittivity is then used to fine-tune the shape factor of the CRIM model. Then, using laboratory measurements it is shown that the revised CRIM model over-performs the default shape factor and provides with more accurate estimations of the bulk permittivity of concrete.

Numerical modelling of a heterogeneous concrete model and a bowtie antenna with a separate transmitter and receiver that are able to move independently are also presented in this study. Both models are used for the optimisation of the time-zero position and the CRIM model shape factor.

ACKNOWLEDGEMENTS

I would like to express my sincere gratitude to my supervisor Dr. Antonios Giannopoulos for his continuous support and guidance throughout my PhD studies. His passion and knowledge on the subject were invaluable. Thank you for being my supervisor and helping me become a better researcher.

I would also like to acknowledge Dr. Iraklis Giannakis for his help and support along with the useful advice's he gave me. Also would like to thank Dr. Craig Warren for his support during the first stages on my PhD.

Finally, and most importantly, I would like to say an exclusive thank you to my mother and father for their endless support, prayers and motivation throughout my university career. Also would like to say thanks to my sisters for caring about my success in my university studies. I would like to give a special thank you my beautiful wife and gorgeous daughter for their huge support, love and encouragement during my PhD. Your encouragement when times got tough are much appreciated and hope to make up for all your hard work.

CONTENTS

ACRONYMS

ABC	Absorbing Boundary Condition
CEM	Computational Electromagnetics
CFS-PML	Complex Frequency Shifted Perfectly Matched Layer
CFS	Complex Frequency Shifted Courant-Friedrichs-Lewy
CFL	Courant-Friedrichs-Lewy
CO	Common Offset
CMP	Common Mid-Point Reflection
CPML	Convolutional Perfectly Matched Layer
CRIM	Complex Refractive Index Model
CPU	Central Processing Unit
DMI	Distance Measurement Instrument
EMF	Electro-Motive Force
EM	Electromagnetic
FD	Finite-Differences
FDTD	Finite-Difference Time-Domain
FEM	Finite Element Method
FETD	Finite Element Time-Domain
GPR	Ground Penetrating Radar
GSSI	Geophysical Survey Systems Inc
GPU	Graphics Processing Unit
HPC	High-Performance Computing
MoM	Method of Moments
1D	One Dimensional
PCB	Printed Circuit Board
PEC	Perfect Electric Conductor
PML	Perfectly Matched Layer
PSO	Particle Swarm Optimisation
RADAR	Radio Detection And Ranging
RIPML	Recursive Integration Perfectly Matched Layer
Rx	Receiver
SC-PML	Stretched Coordinates Perfectly Matched Layer

3D	Three Dimensional
TLM	Transmission Line Matrix
2D	Two Dimensional
TWTT	Two Way Travel Time
Tx	Transmitter
UPML	Uniaxial Perfectly Matched Layer
UWB	Ultra Wide Band
VPA	Variable Precision Arithmetic
WARR	Wide-Angle Reflection-Refraction

1 INTRODUCTION

1.1 MOTIVATION AND AIMS OF THE RESEARCH

Ground Penetrating Radar (GPR) is a non-destructive geophysical technique which is used in a variety of geophysical and engineering applications (Daniels, 2004; Annan, 2005; Jol, 2008) especially civil engineering where it is extensively used and it has been shown to be an effective tool providing high resolution data.

GPR uses electromagnetic radar pulses to investigate below the ground's surface or within non-transparent objects. It is an established tool in engineering applications such as calculating the thickness of pavements (Shangguan & Al-Qadi, 2014), concrete moisture content (Klysz & Balayssac, 2007; Mai et al., 2015), detecting different types of targets and estimating their depth (Lauro et al., 2013).

It is also used for surveying buried utilities (El-Mahallawy & Hashim, 2013), roads (Saarenketo & Scullion, 2000a; Diamanti & Redman, 2012; Annan et al., 2016), tunnels (Cardarelli, Marrone, & Orlando, 2003), bridges (Hugenschmidt, 2002; Hugenschmidt & Mastrangelo, 2006; Diamanti, Annan, & Redman, 2017) and concrete (Maierhofer, 2003). It is also used for detecting landmines (Giannakis, Giannopoulos, & Davidson, 2014), concrete steel bars (Chang, Lin, & Lien, 2009), moisture clusters (Mai et al., 2015) and air-voids in asphalt (Shang, 2002; Hoegh et al., 2015). GPR is an electromagnetic investigative tool which it has been around for many years but GPR modelling is rapidly becoming increasingly useful and the quality of GPR models is becoming more realistic (Daniels, 2004).

1.1.1 *Introduction to time-zero*

In order to obtain accurate depth measurements, a good estimation of both the wave propagation velocity, which relates to the host material properties, and of the time it takes for the GPR wave to travel from the transmitter to the target and back to the receiver are needed. In this work, we are not concerned directly with the estimation of the material properties and hence with the GPR propagation velocity, which we will mostly assume known, but we will focus on understanding how accurately we measure the time it takes from transmission to reception of the wave. However, the accuracy of travel time measurement impacts often the velocity calculation as in most practical GPR surveys is obtained directly from the GPR data and not using other independent methods. Therefore, the more accurately we measure travel time the

more accurate our interpretations will be. In order to measure travel time, there are a number of practical issues. As most GPR systems are employing separate antennas for transmitting and receiving, there is a time delay between the start of transmission to the first signal reception at the receiver. This delay in general depends on the separation distance between the antennas and on the variation of the material properties that surround them (Al-Qadi, Xie, et al., 2010). These effects must be taken into consideration when working with GPR signals.

In theory, the absolute time-zero of the GPR system can be possibly used to accurately time the arrivals of events, but in this case, there is ambiguity on when a signal has been received because it will correspond to a very small variation of the background field and in the presence of noise and clutter this would be very difficult to determine. So, a more robust indication of where measurement should start in time should be made and this is achieved by what is normally termed as the time-zero adjustment. This often brings the time reference position to the first received pulse which is usually the wave that has propagated directly from the transmitter to the receiver (i.e. direct coupling) and does not coincide with the time of initiation of the radiating field from the transmitting antenna. This, therefore, is an artificially set time-zero and how and where is set on the GPR received signal affects the accuracy of the measurements in estimating the GPR two-way travel time and hence, the depth determination.

Time-zero adjustment is mostly seen as a GPR system issue that has been known in the industry for a while and indeed most GPR manufacturers have their own recommendations of time-zero settings for their systems. There is surprisingly not much published work that explicitly investigates the time-zero adjustment. A number of years ago Yelf (2004) presented the results of a survey of GPR users and manufacturers and of his own experimental investigations on determining the position of the time-zero. In that paper, the author also considered the different possible positions that the time-zero can be placed. The results indicated that for most GPR systems time-zero should be adjusted according to the antenna used and the surrounding materials. The author also mentioned that using the positive peaks presented the best result as it is easy to detect and therefore used by most GPR users (Yelf, 2004). However, depending on the environment and the type of antenna, different error corrections will result from this position which are altered subsequently after the completion of the data collection. More specifically in Yelf's study (2004), for a specific antenna, the Geophysical Survey Systems Inc (GSSI) with a centre frequency of 1.5 GHz, the time-zero was best found to be located at 0.61ns before the first positive peak of the first wavelet. The measurements where made using air as the host material and the ground reflection as the target response, something however that does not reflect the real use of GPR in normal practice.

A more recent study (Mezgeen, Vega, & Assunção, 2018) mentions that the time-zero position is crucial in order to obtain accurate depth measurements in which they use three different antennas located in air given a certain height to predict the Two Way Travel Time (TWTT) and subsequently determine the time-zero. As the method is based, similarly to (Yelf, 2004), on using primarily propagation in air, the suitability for generic use when the antennas are close to the material interfaces is not as evident. Additionally, it appears that there is a need for a better procedure to set the time-zero as this study investigates. Previous work investigated the physical properties of concrete and the effect it has on time-zero (Viriyametanont et al., 2008). Measurements such as the Wide-Angle Reflection-Refraction (WARR) method used to predict the ground wave velocity in order to find the correct time-zero and the correct time shift for each receiver (Diamanti et al., 2018; Kaufmann et al., 2018; Angelis, Warren, & Diamanti, 2019). Using velocity analysis to determine the change in moisture levels of concrete is time-zero dependant which for this particular case, time-zero is set to be the maximum energy of the direct wave (Philipp et al., 2018). As shown, many researchers have problems with the time-zero position and numerous experiments are performed to find a good prediction for time-zero. These predictions are different from each other and the problem of which position predicts the true ground surface remains mainly unsolved especially if robust error control and accuracy is required. Overall, individual researchers set the time-zero in line with the research being carried out but a process in determining a position that predicts the most accurate depth and also shows consistency throughout is still largely unspecified.

So far, there is no apparent universal agreement between GPR users for time-zero positioning. However, it is clear that methods for time-zero positions are very important as shallow reflections or near field data can be removed from the radargram if time-zeros are not positioned correctly as stated in (Ernenwein, 2006). For example in (Ernenwein, 2006), the "first break" position (when the signal starts to bend from the zero crossing) of the direct wave is used as the time-zero. Researchers set a specific time-zero for a particular case which may differ in comparison with other published research. The most common procedure used for adjusting time-zero is to adopt to a position as indicated in previous published literature (Yelf, 2004) and make adjustments accordingly (Benedetto et al., 2017; Dinh, Gucunski, & Duong, 2018a, 2018b; Dinh, Gucunski, & Zayed, 2019). Finally, in another study, the time-zero was defined at the zero amplitude point (zero crossing) between the positive and negative peaks of the direct wave (De Pue, Van Meirvenne, & Cornelis, 2016).

Setting the time-zero, as we have seen is important but not a task that has a clearly well defined process, as the signals are affected by different materials and antenna types. Also the hardware components

timing instabilities might cause problems in defining a "correct" time-zero. The aim of this study is to investigate the time-zero adjustment problem using realistic 3D numerical modelling aiming to examine these issues and develop a more generic and also robust approach to the time-zero adjustment that is not necessarily error free but is as consistent as possible. In doing so, we investigate the most suitable time-zero position in conjunction with considering at the same time the most suitable point of time reference on the actual reflected GPR wavelet. Separating these two timing processes will be shown that creates ambiguity on the accuracy of the time measurement and hence time-zero adjustment without establishing a wavelet time-picking process is problematic if robustness is to be achieved in error control. It is that by investigating the variation of timing errors a more robust process can be proposed in order to make the best accurate time measurements possible. As the approach is based on a realistic model of the actual transducer used in the field, the unknown factor that actual material properties play in an experiment can be eliminated to allow examining the time-zero and general timing of GPR wavelets appropriately. As the model of a specific GPR transducer is used the results are strictly applicable to this transducer however it is reasonable to expect that the proposed process is transferable to other similar transducers and also the working framework and hypothesis can be easily extended if models of other GPR transducers are made available.

1.1.2 *Introduction to CRIM model*

One of the most important applications of GPR is monitoring and condition assessment of concrete structures. Investigations that usually take place for GPR applications involve shallow-depth buried targets or ones that are located close to the surface. For instance, such applications are detecting the location of rebars, air-voids, moisture content and cracks (Pérez-Gracia, Garcia, & Abad, 2008). For concrete construction, many mixtures exist with a variety of content combinations dependant on the application. These mixtures have various material percentages for aggregate, cement and sand which can result in different dielectric constants of the resulting concrete product. Concrete is a heterogeneous material and the calculation of the dielectric constant has been the interest of many researchers (Tsui & Matthews, 1997; Bourdi et al., 2008; Klysz, Balayssac, & Ferrières, 2008). When analysing GPR data, having the wrong estimation of the dielectric properties will result in an incorrect interpretation of key parameters that will be extracted from them. For example, these parameters can be the reflector's depth measurement, Electromagnetic (EM) wave velocity and the targets position. So, if the dielectric constant is not estimated correctly, the GPR analysis of the data will be wrong and problematic. Therefore, in order to investigate the electrical properties of concrete, the dielectric

constant should be calculated accurately (Bourdi et al., 2012). There are many methodologies that have been used in the past for this purpose which raise an issue concerning which method is the most effective for estimating the bulk permittivity of concrete mixtures.

Over the years many methods have been developed to estimate the bulk permittivity of heterogeneous materials (Böttcher, 1952; Sihvola, 1999). Most common methods (Al-Qadi, Leng, et al., 2010) are based on the Complex Refractive Index Model (CRIM) model (Birchak et al., 1974), the Rayleigh model (Rayleigh, 1892), the Böttcher model (Böttcher & Bordewijk, 1978), the Brown model (Brown, Franz, & Forsbergh, 1956), the Wagner model (Wagner, 1914) the Bruggeman model (Bruggeman, 1935) and Topp model (Topp, Davis, & Annan, 1980). These models calculate the dielectric constant of the mixture with respect to the dielectric properties and the volumetric fractions of its components. From the mentioned models, CRIM has been established as the mainstream methodology in the GPR community mainly due to its simplicity and its straightforward implementation.

In this study, the focus is on the CRIM mixing model and a key geometric parameter of the model is investigated in detail. A methodology is presented in order to investigate the shape factor further and evaluate different estimates of it. This allows to determine the best shape factor and present a fine-tuned value for concrete structures. Our approach is based on numerical-synthetic experiments executed using gprMax (Giannopoulos, 2005; Warren, Giannopoulos, & Giannakis, 2016) an open source electromagnetic solver using Finite-Difference Time-Domain (FDTD) method (Yee, 1966; Chen & Huang, 1998; Taflove & Hagness, 2005). FDTD is robust, accurate, flexible, computationally efficient and uses time domain discretization which is ideal for GPR scenarios (Sadiku, 2000; Cassidy, 2007; Cassidy & Millington, 2009). As computational resources have improved and become more accessible, an increase in the knowledge and effectiveness of GPR modelling has been observed (Giannakis, Giannopoulos, & Warren, 2016). One of the advantages of GPR numerical modelling is that it is able to produce models that are close to reality and support research effort when restrictions exist to execute it physically. Numerical modelling has been widely used for designing various models and optimising complex antennas (Lee et al., 2004; Uduwawala, 2006; Giannakis, Giannopoulos, & Warren, 2019). FDTD has been widely used to simulate different antenna models such as bowties (Bourgeois & Smith, 1996; Klysz et al., 2004; Caratelli, Yarovoy, & Ligthart, 2009), dipoles (Bourgeois & Smith, 1997; Radzevicius et al., 2003; Lampe & Holliger, 2005; Diamanti & Annan, 2013) and horn antennas (Venkatarayalu et al., 2004; Turk et al., 2007). In this study, the antenna used for the simulations is a model-equivalent of a GSSI antenna with centre frequency of 1.5GHz available for experimentation (Warren & Giannopoulos, 2011; Giannakis, Giannopoulos, & Warren, 2019).

Numerous realistic concrete models are simulated using an automatic framework that generates different distribution of aggregate particles, cement, air-voids and moisture content. The chloride content within the concrete is negligible thus the effects are not noticeable and were not considered in the numerical experiments (Robert, 1998; Al-Saleh, 2015). The moisture content is a very important aspect and has been shown that greatly affects the overall dielectric properties of the concrete mixture (Laurens et al., 2005; Wu, Wong, & Buenfeld, 2017). It has been reported that moisture content greater than 5% has an important influence on the transmitted signal travelling through the concrete (Shaw, 1998). Therefore, in the current study, different mixtures with various degrees of moisture content have been numerically simulated and tested. In another framework, different mixtures with constituent variations have been tested and have shown minor effects on the permittivity in comparison with the moisture content, air-voids, cement and aggregate particles (Soutsos et al., 2001).

Using the mentioned numerical framework, a coherent set of synthetic examples is generated. The synthetic set is subsequently used to fine-tune and optimise the shape factor such as the CRIM-based bulk permittivity to match the actual one. Using numerical experiments allowed to have full control on the volumetric fractions of the concrete's components. Thus, every term in the CRIM formula can be accurately implemented. The resulting optimised shape factor using the suggested scheme is evaluated in both synthetic and a real-laboratory experiments indicating the validity and robustness of the revised CRIM model.

1.1.3 *Objectives*

The key objectives of the present thesis are summarised as follows:

- Using numerical modelling, develop more advanced concrete models to be as close as possible to reality.
- Develop a numerical model of an antenna with separated transmitter and receiver antennas for employing it to specific measurements using methods such as the WARR and Common Mid-Point Reflection (CMP) methods. The final antenna model an extension of an existing GSSI antenna design developed by Warren and Giannopoulos (2011).
- Investigate the time-zero position in great amount of detail to present a method that is robust and works for most cases without the need of adjustment.
- Using the new time-zero method along with a realistic heterogeneous model to investigate a new shape factor for the CRIM model.

- Use the proposed time-zero method in the laboratory using a real GPR antenna and compare the results with the outputs of the numerical simulations.
- Validate CRIM model's proposed shape factor through experimental work.

1.2 THESIS OVERVIEW

Here the structure of each chapter is presented to give an overall view of the thesis.

CHAPTER 2: The introduction and history of GPR is presented. The main focus is on GPR principles and how it operates. Electromagnetic waves propagating through different media, types of antenna used and cross-sectional results are discussed.

CHAPTER 3: This Chapter begins with introducing Maxwell's equations and the FDTD method used for GPR simulations. The advantages and disadvantages are discussed. This is followed by Yee's algorithm and how it is used in numerical modelling.

CHAPTER 4: The advanced concrete modelling is discussed in this chapter. Starting from a homogeneous model and moving towards a more complex heterogeneous model is presented. The pros and cons of converting a Two Dimensional (2D) model to a 3D model are reported. The effect of real shape aggregates on the propagated wavelet in comparison with sphere aggregates is also discussed.

CHAPTER 5: In this chapter the time-zero topic, one the most important and challenging aspects of GPR is presented. Many techniques are simulated and compared. Finally, one method that has shown to be robust and works for the majority of cases is presented.

CHAPTER 6: A 3D numerical model of a bowtie antenna structure is designed with a separate Transmitter (Tx) and Receiver (Rx) geometry in order for the Tx and Rx to have the ability to move away or towards each other.

CHAPTER 7: A new geometric parameter investigation is presented in this chapter. The shape factor is optimised to give the permittivity measurements a better accuracy. The new time-zero method is also been implemented in this framework.

CHAPTER 8: The numerical work has been validated in this chapter through Laboratory Experiments.

CHAPTER 9: The conclusions and recommendations for future research work is discussed in this chapter.

2

THE PRINCIPLES OF GROUND PENETRATING RADAR

In this chapter, the principles of GPR are briefly explained. A short history of GPR is also presented to show its evolution over the past decades. The purpose of GPR usage and its capabilities are discussed. Data collection methods are shown and explained with wave propagation snap-shots to show how the wave is transmitted and received. Different cross sections (B-scans) and how they are processed further e.g., migration, time-zero correction, is presented.

2.1 INTRODUCTION AND HISTORY

During the early 20^{th} century, many researchers started to conduct research on radio wave propagation. The first use of electromagnetic signals is credited to Hülsmeyer in 1904 and six years later in 1910 this was mentioned in a German patent by Leimbach and Löwy (Daniels, 2004). In the 1950's, the development of GPR became increasingly more and an attempt on subsurface measurement was reported by El-Said (1956). It used radio waves to find the depth of the subsurface water content. The research continued to the 1970's which coal mines (Cook, 1973) and ground salt (Holser et al., 1972) were detected using GPR. GPR grew significantly in the 1980's as it started to be used for many more subsurface applications (Owen, 1981; Olsson et al., 1987). As the advantages and disadvantages of GPR were better understood, GPR researchers became more interested in this technology. In the last decade of the 20^{th} century and early 21^{st} century, the evolution in technology and computers made GPR highly advanced which meant large volume of data could be processed in a small amount of time (Maijala et al., 1992; Goodman, 1994; Jol, Smith, & Meyers, 1996; Lampe & Holliger, 2000). As a result two dimensional (2D) (Oristaglio & Hohmann, 1984; Zeng et al., 1995) and three dimensional (3D) (Moghaddam et al., 1991; Bourgeois & Smith, 1996; Roberts & Daniels, 1997; Giannopoulos, 1998; Bergmann et al., 1999) numerical modelling became possible in which Moghaddam et al. (1991) was one of the first to move on to 3D modelling uning the FDTD method. This was an evolution for complex GPR problems which could not be solved the traditional way. More history of GPR can be found in (Annan, 2002).

Since ground penetrating radar (GPR) was invented, it has been used in many applications. The usage has become broader over the last few years and continues to grow as the technology becomes more advanced. One of the fields that it is well known for is the geological or geophysical

engineering applications. There are many geophysical techniques that are used to image the sub-surface structures and gather information like the physical properties. In other words, dielectric properties are identified by GPR in order to carry out further measurements. Then GPR uses the gathered information to map the dielectric properties distribution. The dielectric properties are the permittivity, conductivity and permeability. As these parameters are identified, a better understanding of the target's shape, material composition, size and depth are achieved. Target detection and depth estimation of the target are two major reasons GPR is used for geophysical engineering. For example, information that can be retrieved from the sub-surface, are utility identification, landmine detection, forensic evidence and fossil discoveries.

2.2 GPR SYSTEM

GPR systems contain a control and display platforms which allows the user to set and adjust specific settings. Depending on the survey, GPR systems are mounted on various units such as vehicles and carts. The key component is that the transmitting and receiving GPR antennas are used to send electromagnetic pulses below the subsurface and receive the pulse back due the reflection of a target. GPR antennas can be monostatic or multi-static. In other words, the transmitter and receiver can be part of one unit or be separate depending on the surveying method. On the other hand, the transmitter and receiver can be separated and function individually (e.g. designed bowtie antenna model in chapter 6). The polarisation of the transmitter can be horizontal (co-polarised) or vertical (cross-polarised) to the polarisation of the receiver. In addition, GPR antennas can be air-coupled or ground-coupled. For example, for road surveys usually air-coupled transducers are used and for concrete inspection ground-coupled transducers are employed.

The frequency range which normally GPR applications mainly involve is from 10MHz to 3 GHz. However, the frequency range of GPR in theory can vary from 1MHz to 10 GHz. Below 1MHz the electromagnetic waves may not act as waves and higher than 10 GHz creates great amount of losses making GPR unreliable (Giannakis, 2016). Furthermore, GPR antenna units can be divided into the time-domain and the frequency-domain. Due to the large frequency bandwidth of transmitted pulses, the time-domain GPR is also known as Ultra Wide Band (UWB).

2.2.1 *GPR principle of operation*

Radio Detection And Ranging (RADAR) is an electromagnetic system that sends a pulse through the air at the speed of light to detect a target and measures the distance. GPR is a RADAR system that transmits electromagnetic waves in a specific direction and receives a response

back from a target. Additionally, GPR is a type of RADAR system that detects the electrical property discontinuities of the subsurface. Although the purpose of RADAR is to detect targets above the ground, GPR uses the same principle to detect targets below the surface.

2.2.2 *GPR wave propagation*

Understanding the wave propagation and what affects it along its path help us analyse the output better. As a transmitting antenna radiates, a pulse travels through the air and subsurface. Once it reaches a target (a material with different dielectric properties), the radiated pulse is reflected back and received by the receiver. The first response recorded is known as the direct waves. The direct wave is a combination of the direct air and direct ground wave. These waves travel from the transmitter straight to the receiver. The second response which comes at a later time is the reflection from the target. Due to the low attenuation of the direct transmitter-receiver path, the amplitude of the direct wave is greater than the target reflection amplitude (Figure 2.1). The reason the reflection is smaller in amplitude in comparison with the amplitude of the direct wave is that when the wave propagates through the medium, energy is lost due to the losses in the subsurface. Such losses are transmission and reflection losses, losses from other materials (clutter, rubble, etc), spreading and distance travelled losses, etc.

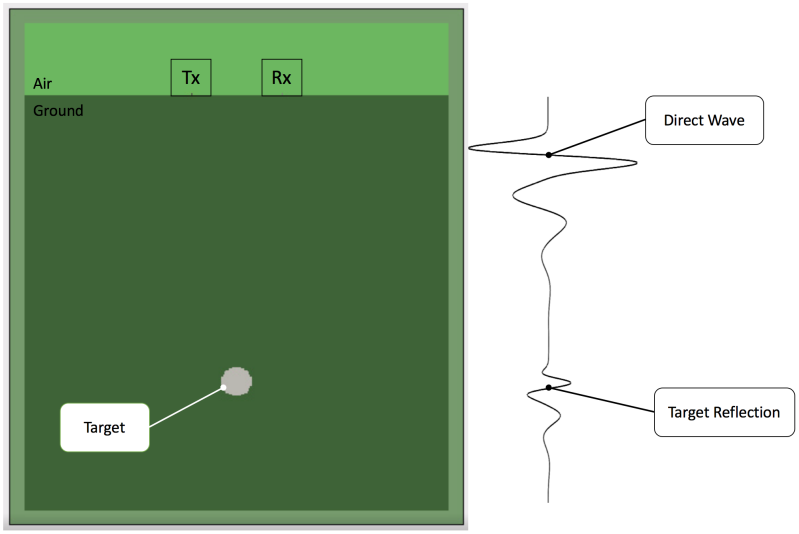

Figure 2.1: Simulation setup showing the wave propagation towards the target (left) and the received response (right).

Figure 2.2 illustrates a GPR electromagnetic wave behaviour through a medium. It shown how the wave propagates from the transmitter to the target and how the wave is reflected back to the receiver.

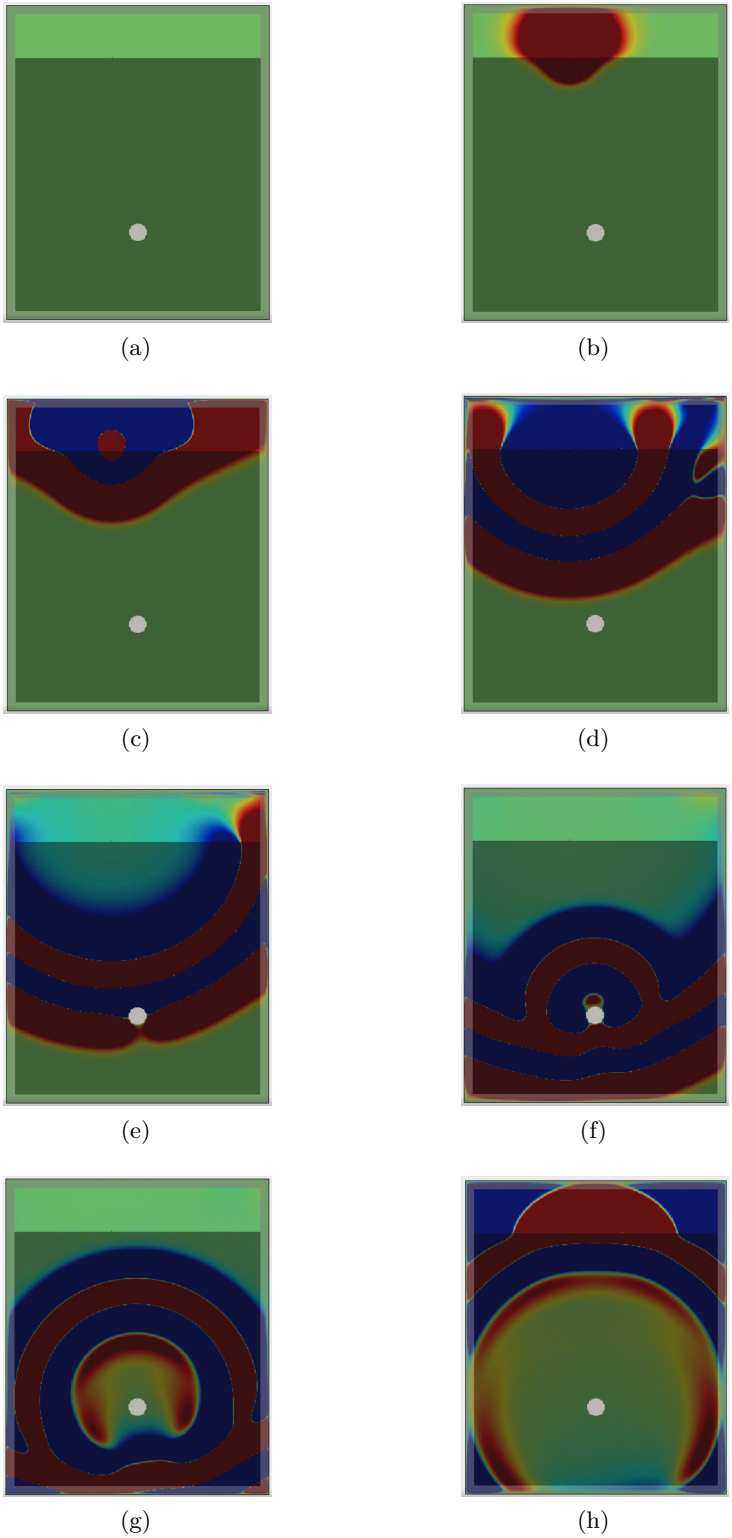

(a) (b) (c) (d) (e) (f) (g) (h)

Figure 2.2: (a) to (h) illustrate different snapshots for increasing time steps. The target is a cylinder and it is positioned at 20cm below the ground surface. The radius of the cylinder is 1cm. The positions of the transmitter and receiver are shown in Figure 2.1.

2.3 DIELECTRIC PROPERTIES

The sub-surface materials are often known as dielectrics and the permittivity and conductivity parameters that affect the electric and magnetic fields are described as the dielectric properties. For GPR applications, these properties are very important as they help identify the material, shape and depth of buried obstacles.

Relative electric permittivity (ε_r) and relative magnetic permeability (μ_r) are calculated with respect to dielectric properties of free-space as shown in equation (2.1). The relative dielectric properties have no physical dimensions. For non-magnetic materials the relative permeability is equal to 1 (Everett, 2013).

$$\varepsilon_r = \frac{\varepsilon_s}{\varepsilon_0} \qquad \mu_r = \frac{\mu_s}{\mu_0} \tag{2.1}$$

where:

ε_r = relative static permittivity

ε_s = static permittivity (F/m)

ε_0 = permittivity of free-space $(8.854 \times 10^{-12}\ F/m)$

μ_r = relative static permeability

μ_s = static permeability (H/m)

μ_0 = permeability of free-space $(4\pi \times 10^{-7}\ H/m)$

2.3.1 *Reflection coefficient*

When an electric current reaches the antenna terminals, they radiate the received current as an electromagnetic waves. This wave propagates through the ground to various distances depending on the antenna centre frequency. The change in material or permittivity variation causes the wave to be reflected. The reflected wave contains energy which the amount is dependant on the reflection coefficient. A simple estimate considering a plane wave hitting an interface at normal incident is given by (2.2) (Balanis, 1989).

$$Z = \sqrt{\frac{\mu}{\varepsilon}}, \quad R = \frac{Z_2 - Z_1}{Z_2 + Z_1} \tag{2.2}$$

where:

Z = intrinsic impedance (Ω)

R = reflection coefficient

Z_1 = intrinsic impedance of material 1 (Ω)

Z_2 = intrinsic impedance of material 2 (Ω)

For non-magnetic materials the permeability is equal to the permeability of free-space hence we have $\mu_0 = \mu_1 = \mu_2$ (Everett, 2013). By rearranging the formula we reach the final equation shown in equation (2.3).

$$R = \frac{\sqrt{\frac{\mu_2}{\varepsilon_2}} - \sqrt{\frac{\mu_1}{\varepsilon_1}}}{\sqrt{\frac{\mu_2}{\varepsilon_2}} + \sqrt{\frac{\mu_1}{\varepsilon_1}}} \rightarrow R = \frac{\sqrt{\frac{\mu_0}{\varepsilon_2}} - \sqrt{\frac{\mu_0}{\varepsilon_1}}}{\sqrt{\frac{\mu_0}{\varepsilon_2}} + \sqrt{\frac{\mu_0}{\varepsilon_1}}} \rightarrow R = \frac{\sqrt{\varepsilon_1} - \sqrt{\varepsilon_2}}{\sqrt{\varepsilon_1} + \sqrt{\varepsilon_2}} \quad (2.3)$$

where:

ε_1, μ_1 = permittivity and permeability of material 1

ε_2, μ_2 = permittivity and permeability of material 2

If the permittivity of the first layer is higher than the second layer ($\varepsilon_1 > \varepsilon_2$), the sign of the reflection coefficient is positive. In a different case, if the permittivity of the first layer is lower than the second layer ($\varepsilon_1 < \varepsilon_2$), the sign of the reflection coefficient is negative. In this case, there is a phase inversion of the pulse.

2.3.2 *Dielectric constant - electric permittivity*

A capacitor contains two metal plates with each plate having an amount of charge equal and opposite to each other. If one plate loses some electrons, the other plate gains the same amount of electrons. The stored charge in the capacitor can be altered by changing the area of the plates (A), changing the plate voltage (V) or by changing the distance between the two plates (d). Decreasing the distance of the two plates, increases the charge stored. Another way to increase the stored charge is to insert a dielectric between the plates. Dielectric materials are insulators which help the capacitor to store more charge. Ceramic, glass and plastic are some examples of a dielectric. When a dielectric is inserted in a capacitor, polarisation occurs meaning that the electron distribution can shift with the positive charges in the electric field direction pulled towards the negative plate and the negative charges opposite to the electric field pulled towards the positive plate. So, the positive charge of the dielectric facing the negative plate attracts more electrons and the negative dielectric charge facing the positive plate

pushes electrons off the plate. This makes the positive charge of the positive plate to increase and negative charge for the negative plate to become higher resulting in the capacitor to store more charge. The permittivity relates the electric flux density to the electric field and it is calculated in Farads per meter. The relationship between the electric field, permittivity and the electric flux density is shown in equation (2.4).

$$\vec{D} = \varepsilon_0 \vec{E} \tag{2.4}$$

where:

$\vec{D}$ = electric flux density $(F.V/m^2,\ C = F.V \rightarrow C/m^2)$

ε_0 = permittivity of free-space $(8.854 \times 10^{-12}\ F/m)$

$\vec{E}$ = electric field intensity (V/m)

Equation (2.5) represents the force equation.

$$F = \frac{q_1 q_2}{4\pi\varepsilon_0 r^2} \tag{2.5}$$

The electric field is equal to the electric force (N) per unit charge (C).

$$E = \frac{F}{q} \tag{2.6}$$

Substituting (2.5) into (2.6) will result in (2.7) where k is Coulomb's constant (Nm^2/C^2).

$$E = \frac{q}{4\pi\varepsilon_0 r^2} = \frac{kq}{r^2} \tag{2.7}$$

Replacing (2.7) in (2.4) we get

$$D = \frac{q}{4\pi r^2} \tag{2.8}$$

2.3.3 *Magnetic permeability*

In most GPR applications, the magnetic permeability is often close to free-space $(1.26 \times 10^{-6}\ H/m)$ as the magnetic effect of materials has small effect on the wave propagation (Olhoeft, 1998; Cassidy &

Jol, 2009). Permeability is divided into diamagnetic ($\mu_r < 1$ such as gold and water), paramagnetic ($\mu_r > 1$ such as air and aluminum) and ferromagnetic (high $\mu_r >> 1$ such as steel and iron). Similarly to the electric permittivity, the relationship between the permeability with the magnetic flux density and the magnetic field is given by (2.9).

$$\vec{B} = \mu_0 \vec{H} \tag{2.9}$$

where:

$\vec{B}$ = magnetic flux density
$A.H/m^2,\ Wb = A.H \rightarrow Wb/m^2 \rightarrow T\ (Tesla = \frac{Weber}{(meter)^2})$

μ_0 = permeability of free-space $(4\pi \times 10^{-7}\ H/m)$

$\vec{H}$ = magnetic field intensity (A/m)

2.3.4 *Electrical conductivity*

Conductive materials are divided into lossless, low-loss and lossy sections. lossless ($\sigma = 0$) materials have no electric or magnetic loss such as air or vacuum. Low-loss ($\sigma > 0$) materials such as salty water have some amount of loss. Finally, lossy ($\sigma >> 0$) materials have high number of free electrons and most of the electromagnetic energy is lost (as heat for example) hence, the effectiveness of GPR applications in these environments is very low. The electric conductivity relationship between the electric field and the current density is shown in equation (2.10) which is also known as Ohm's law.

$$\vec{J_c} = \sigma \vec{E} \tag{2.10}$$

where:

$\vec{J_c}$ = conduction current density (A/m^2)

σ = electric conductivity $(A/Vm \rightarrow S = A/V \rightarrow (S/m))$ $(\frac{Siemens}{meter})$

$\vec{E}$ = electric field intensity (V/m)

2.4 ANTENNA ORIENTATION

The transmitting and receiving GPR antennas can be placed in different arrangements as shown in Figure 2.3. The orientation of the antennas affects the received reflection in terms of visibility of the

target, for example. The broadside (PR-BD) and end-fire (PL-EF) arrangements are perpendicular and parallel to the survey direction respectively.

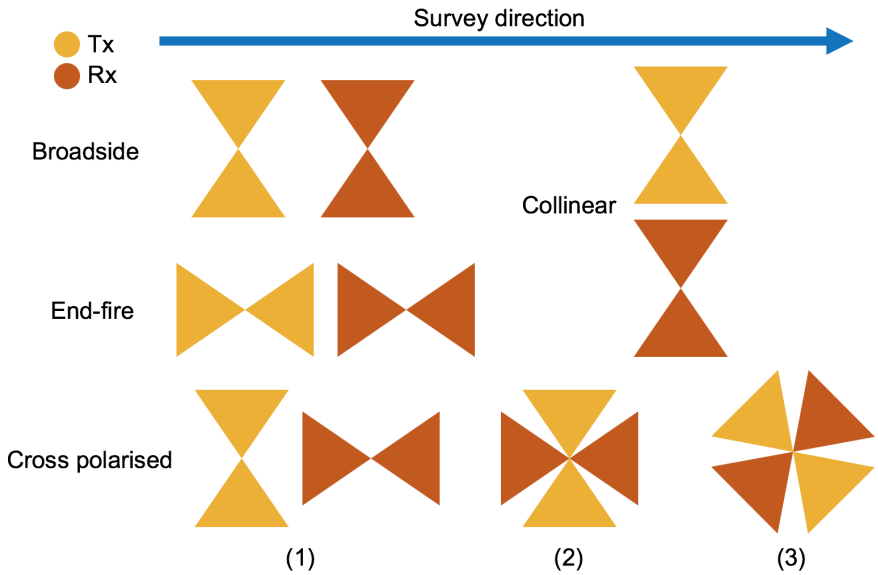

Figure 2.3: Transmitter and receiver arrangement for a GPR bowtie antenna.

2.5 DATA COLLECTION AND PROCESSING

To carry out a GPR survey, the data can be collected in three different common methods. The Common Mid-Point (CMP) method, Wide Angel Refraction Reflection (WARR) method and Common Offset (CO) method. These methods are shown in Figure 2.4. For the CMP method (Figure 2.4a), the transmitter and receiver are separate and can be moved independently away from a common centre. It is typically used to produce a velocity depth profile (Warren, 2009). The WARR method (Figure 2.4b) is similar to the CMP (transmitter and receiver are separate) but here, the transmitter is fixed and the receiver is moved away from the transmitter along a survey line. For the CO method (Figure 2.4c), the transmitter and receiver could be separate having a fixed distance between them or be placed in the same enclosure. This method is the most commonly used method for commercial GPR systems. In Chapter 5, this method is used for the data collection and depth estimation. This method has also been used for the bulk permittivity calculation in chapter 7.

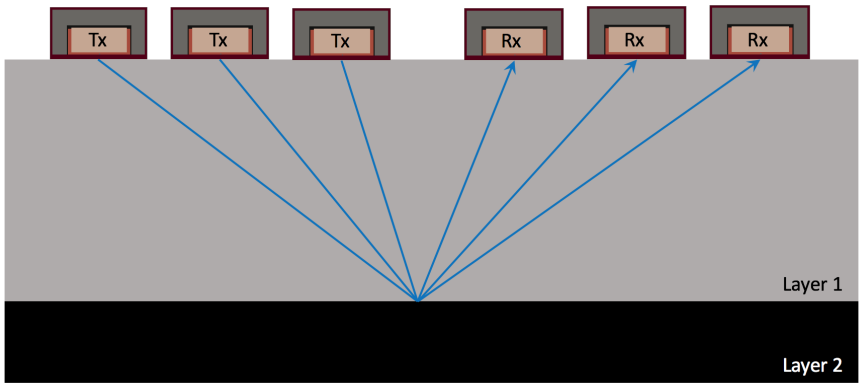

(a) CMP

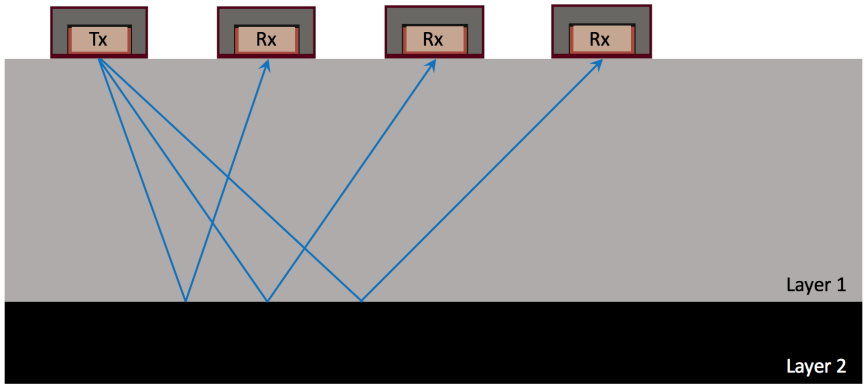

(b) WARR

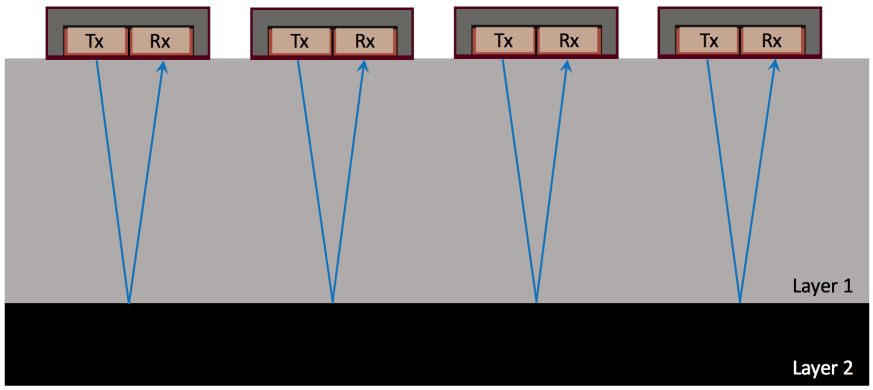

(c) CO

Figure 2.4: 2.4a is the Common Mid-Point method (CMP), 2.4b is the Wide Angel Refraction Reflection (WARR) and 2.4c Common Offset (CO) method.

2.5.1 *GPR two-way travel time to depth calculation*

In theory, the same antenna can be used as the transmitter and receiver (mono-static radar). In this case, the antenna transmits a pulse and switches off in order for the receiver to receive the signal back. In this case, the wave propagation will be a straight line to the target and back to the same spot where the wave was transmitted. This type of mechanism is not used in GPR as the switching process needs to be done very fast hence separated antennas are used. For separated antennas, the ray path forms a triangular shape below the Tx-Rx pair and from this the depth to a target can be calculated using equation (2.11). Not taking antenna separation into consideration results in a two-way travel time or depth estimation error. The most sensitive case for this type of calculation is when a large antenna separation cases and shallow depth targets occur as the wave propagates with a wider angle hence a greater time in comparison with a wave that is transmitted and received at the same spot or close to each other. For small antenna separation and targets located far away from the antenna, the depth calculation result is not affected as much. For higher accuracy though, the antenna separation is better to be considered.

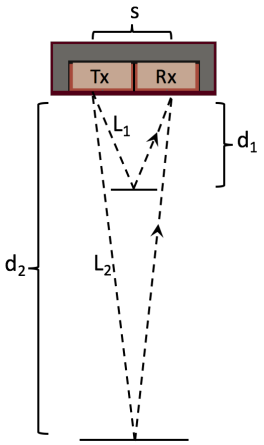

Figure 2.5: This Figure shows the wave propagation from a transmitter to a target and back to a receiver and how the depths d_1 and d_2 should be related to travel paths L_1 and L_2.

$$d_1 = \sqrt{L_1^2 - \frac{s^2}{4}} \qquad d_2 = \sqrt{L_2^2 - \frac{s^2}{4}} \tag{2.11}$$

where, L is the wave propagation path, s is the separation between transmitter and receiver and d is the target depth.

2.5.2 *Cross section (B-scan) demonstration*

To scan an area with GPR, a GPR transducer pair is moved along the ground surface in order to build a radar image and display the subsurface structure. During the survey, a One Dimensional (1D) trace (A-scan) is collected for each spatial step. By grouping all traces together a GPR cross-section image (B-scan) is formed.

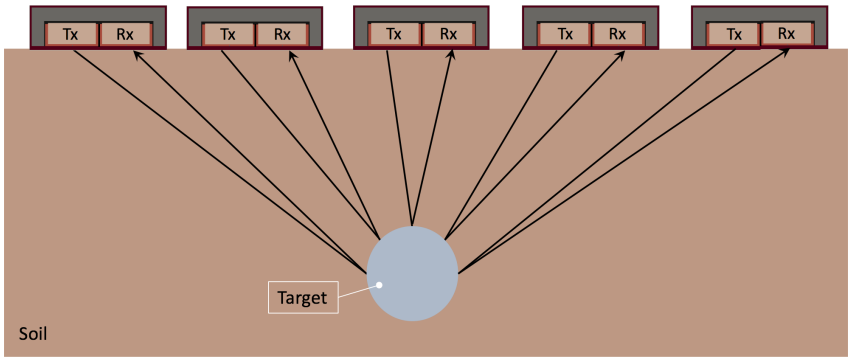

Figure 2.6: A GPR antenna is moved from one side to the other in regular steps and each trace is recorded to form a cross section

As shown in Figure 2.7, by adding the trace together, a hyperbola formation can be observed when the subsurface target is of spherical or cylindrical shape. Each trace is dependent on the position of the antenna with respect to the targets depth. Therefore, the various reflections of each trace vary in time as the signal propagation path is different when the antenna is moved along the ground surface. For example, when the antenna pair distance in respect to the target increases, the two way travel time increases hence, the reflection appears at a later time.

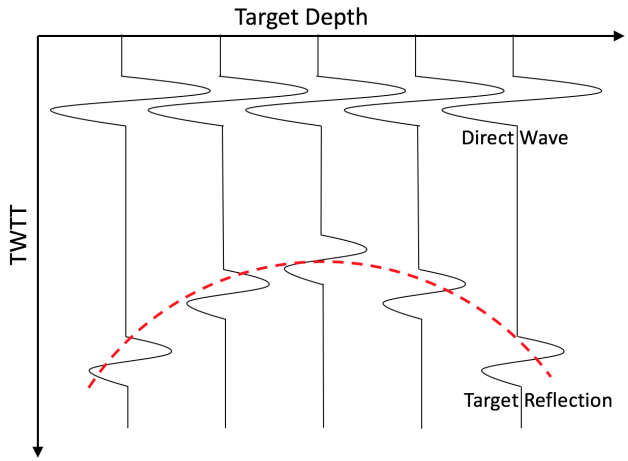

Figure 2.7: Cross section and the formation of a hyperbola

2.5.3 *Two cross section responses*

Reflections originating target comprised by different materials can vary in amplitude as they propagate through different materials. The higher the material contrast the stronger the reflection. A Perfect Electric Conductor (PEC) produces a strong reflection as it reflects all of the electromagnetic wave back (Figure 2.8a). However, an air-void target having a low permittivity, it produces a low amplitude reflection hence a faint response (Figure 2.8b). To enhance the response time-varying gain is applied so the late time arrivals or smaller responses can be easier visualised.

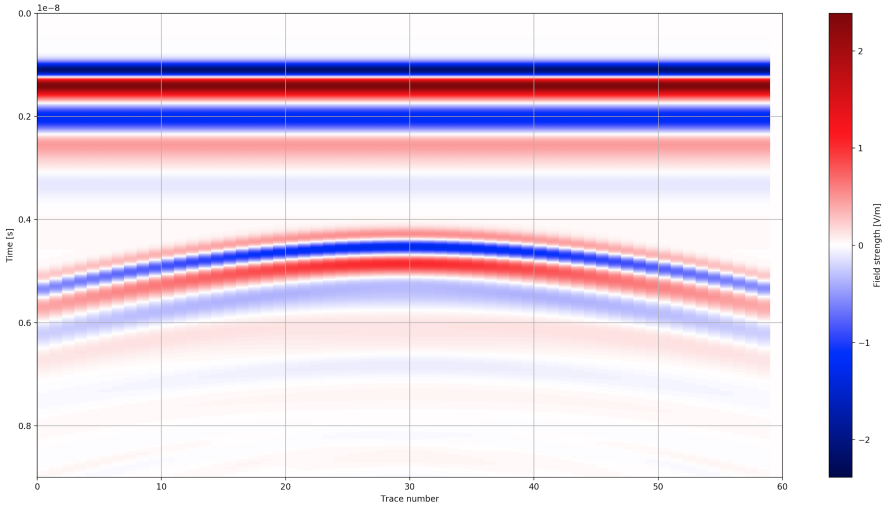

(a) PEC Target

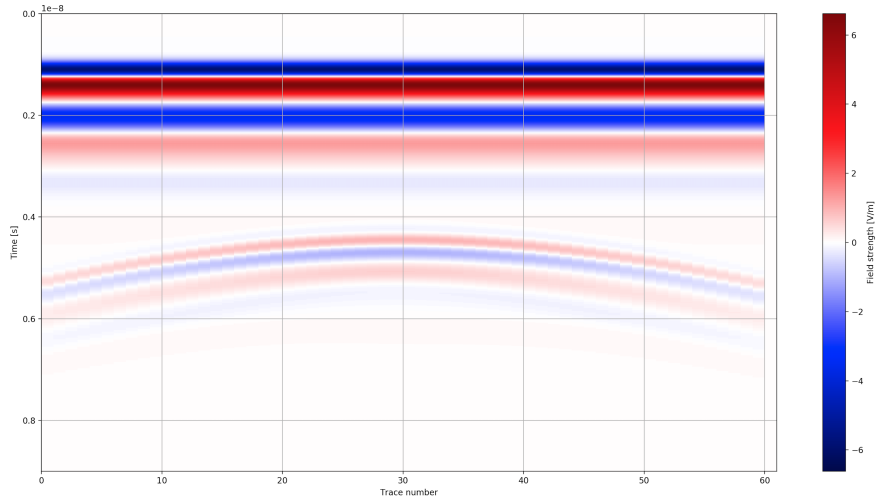

(b) Air-void Target

Figure 2.8: Numerical modelling results of a PEC target and an air-void target. PEC target (2.8a) shows a stronger response in regards to the air-void target (2.8b).

2.5.4 *Target in heterogeneous environments*

To visualise and compare the same target but placed in heterogeneous environments, two complex cases, a concrete model (see Chapter 4) and Peplinski soil model (Peplinski, Ulaby, & Dobson, 1995b) were selected as shown in Figures 2.9a and 2.9b. Both models have noise and clutter that produce variation in the target response. Also the differences of the material contrasts in the medium cause further reflections. Heterogeneous models are much more realistic as it is very rare to encounter purely homogeneous blocks.

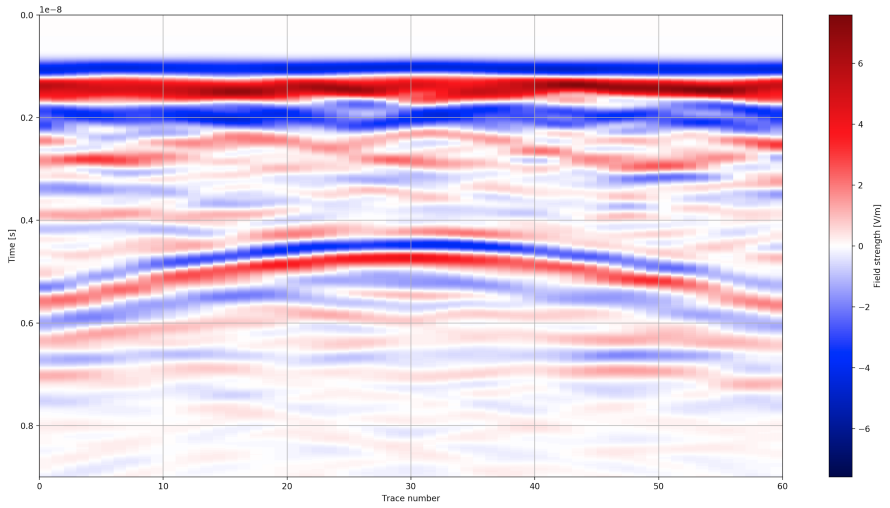

(a) Heterogeneous concrete model

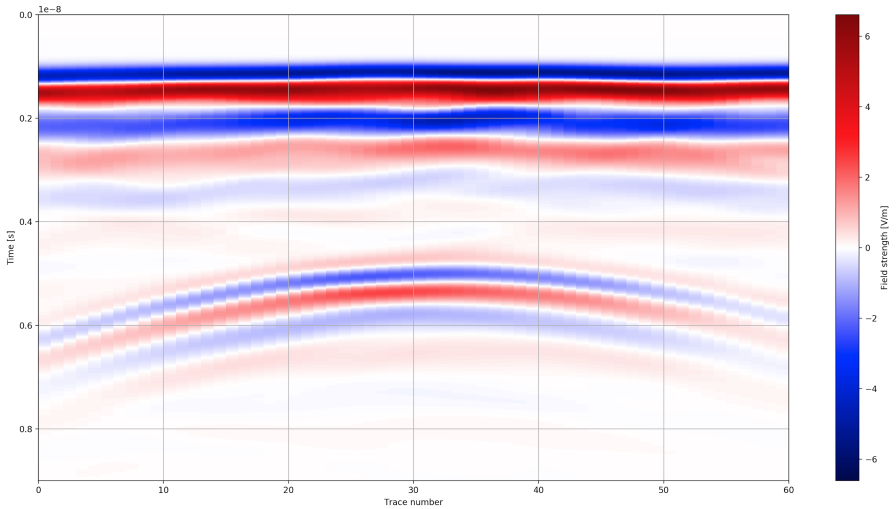

(b) Peplinski model

Figure 2.9: Heterogeneous concrete model vs Peplinski model. A PEC cylinder in buried in these two environments and the antenna used was the GSSI 1.5 GHz.

2.5.5 *Time-zero or true ground surface correction*

Time-zero adjustment is one of the least researched topics yet one of the most important processes for GPR applications. Time-zero correction is crucial in obtaining accurate shallow depth estimations and one of the key aspects in determining the thickness of a layer or target. Chapter 5, extensively presents the time-zero adjustment and the best picking position was researched substantially. Figure 2.10 presents two cross section in which the before and after time-zero correction result can be seen.

2.5.6 *Migration*

By moving GPR over the ground surface, a cross section showing a hyperbola (target reflection) can be produced as shown in Figure 2.11c. Migration algorithms are an imaging technique which reduce the subsurface reflections by gathering the energy transmitted back from the target. In other words, the process of migration is a process trying to focus the energy back from the hyperbola to the scatterer of origin. If the scatterer is from a spherical or cylindrical target, the energy will be focused to that point or the hyperbola is squeezed together to form a dot. Additionally, the migration process improves the target detection rate (Schofield, Daniels, & Hammerton, 2014). This technique requires an input of the waves velocity of propagation through the medium.

There are many migration techniques such as frequency-wavenumber migration (F-K migration) (Stolt, 1978; Gazdag and Sguazzero, 1984; González-Huici, Catapano, and Soldovieri, 2014; Smitha et al., 2016) and Kirchhoff migration (Schneider, 1978; Devaux, Gardner, & Rampersad, 1996; Yilmaz, 2001).

2.5.6.1 *F-K Migration*

In this research, F-K migration is used (Garcia et al., 2013). The F-K migration is based on the Fourier transform technique which is also known as the phase-shift migration (Gazdag, 1978). The migration process reduces the reflection curve to a dot to increase the target detection rate. A cross section before and after migration is shown in Figure 2.11 from numerical modelling data. It shows the same process but with time-zero correction applied. Without the time-zero correction applied the migrated graph (Figure 2.11b) illustrates a wrong depth of 0.2 m. Therefore time-zero correction is essential for finding the correct target depth. Figure 2.11d shows the correct depth of 0.18 m. Here the new time-zero method discussed in chapter 5 has been implemented.

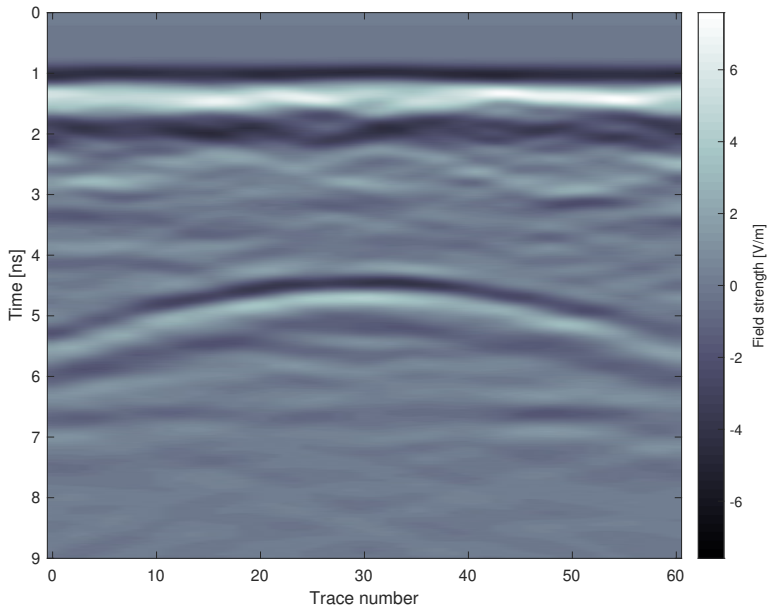

(a) Without time-zero correction

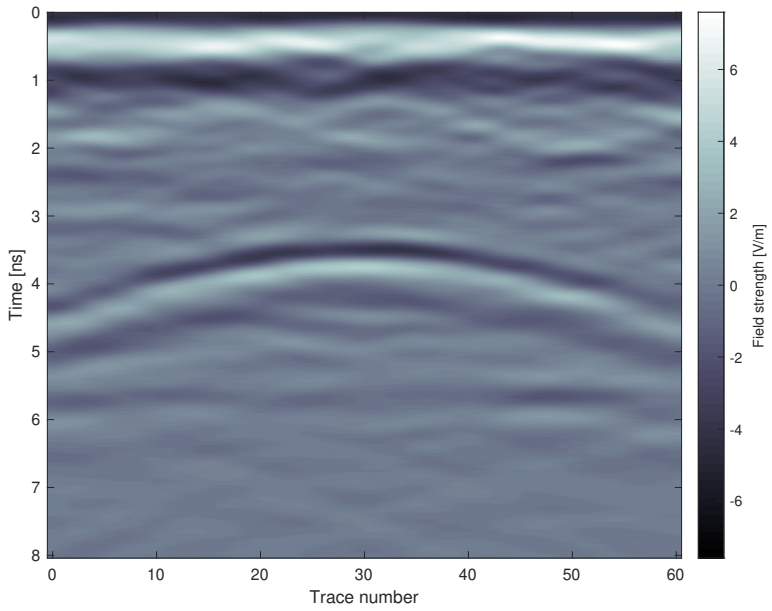

(b) With time-zero correction

Figure 2.10: After time-zero correction has been implemented, the image is shifted upwards so that the first received response starts at zero time.

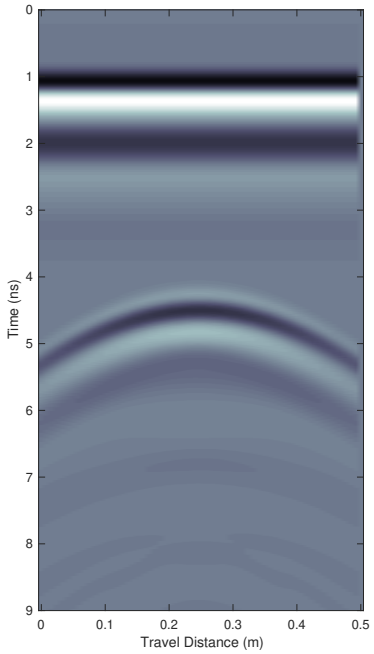

(a) Before migration

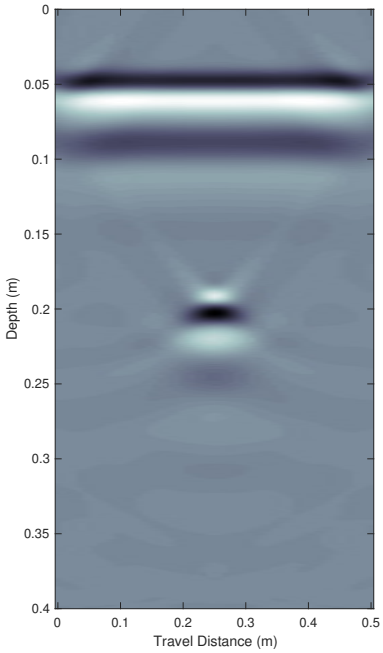

(b) After migration

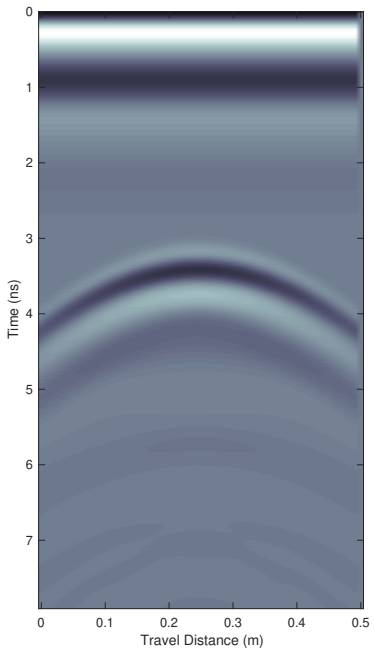

(c) Before migration with time-zero

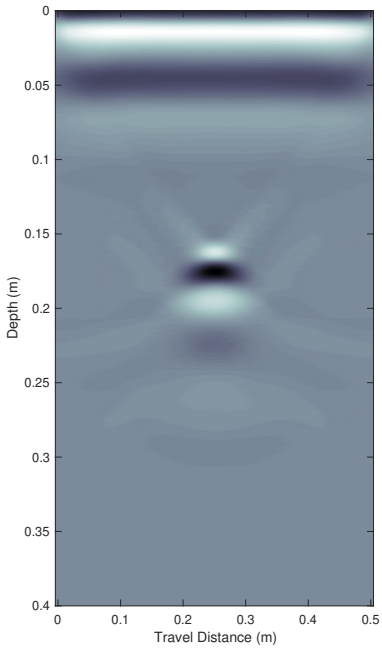

(d) After migration with time-zero

Figure 2.11: 2.11a shows the raw data. 2.11b is the raw data migrated. 2.11c is the raw data with time-zero correction. 2.11d is the raw data reflection after migration and time-zero correction.

2.5.7 *Velocity of propagation*

The two-way travel time of an electromagnetic wave propagating to a target and back to the receiver is given by the travelled distance over the velocity of the propagating wave. Here, the travelled distance is twice the targets depth as the wave travels from the antenna to the target back to the receiver.

$$t = \frac{2d}{v} \tag{2.12}$$

where:

t = two-way travel time (s)

d = depth of target (m)

v = velocity of wave propagation (m/s)

Considering a monochromatic wave in the frequency domain, the propagation constant is given by (2.13) where α is defined as the real part and β is defined as the imaginary part (Balanis, 1989).

$$\gamma = \alpha + j\beta \tag{2.13}$$

where:

γ = propagation constant (Np/m)

α = attenuation constant (Np/m)

β = phase constant (rad/m)

j = imaginary unit $\sqrt{-1}$

The real part is known as the attenuation constant which is given by (2.14).

$$\alpha = \omega \sqrt{\frac{\mu\varepsilon}{2}\left(\sqrt{1+\left(\frac{\sigma}{\omega\varepsilon}\right)^2}-1\right)} \tag{2.14}$$

The imaginary part is known as the phase constant which is given by (2.15).

$$\beta = \omega \sqrt{\frac{\mu\varepsilon}{2}\left(\sqrt{1+\left(\frac{\sigma}{\omega\varepsilon}\right)^2}+1\right)} \tag{2.15}$$

The velocity of electromagnetic waves is affected by the dielectric properties of that material. Therefore, the velocity of the wave that propagates through a material is given by (2.16) (Balanis, 1989).

$$v = \frac{\omega}{\beta} \tag{2.16}$$

where ω is the angular frequency (rad/s). By replacing β with (2.15) leads to the following:

$$v = \frac{\omega}{\omega\sqrt{\frac{\mu_r\mu_0\varepsilon_r\varepsilon_0}{2}\left(\sqrt{1+(\frac{\sigma}{\omega\varepsilon})^2}+1\right)}} \tag{2.17}$$

This can be expressed mathematically as:

$$v = \left(\frac{\mu_r\varepsilon_r}{2c^2}\left(\sqrt{1+\left(\frac{\sigma}{\omega\varepsilon}\right)^2}+1\right)\right)^{-1/2} \tag{2.18}$$

The velocity of an electromagnetic wave propagating through a good conductor $(\frac{\sigma}{\omega\varepsilon})^2 >> 1$ (lossy) material, is expressed as:

$$v = c\left(\frac{\mu_r\varepsilon_r}{2}\left(\sqrt{1+\left(\frac{\sigma}{\omega\varepsilon}\right)^2}+1\right)\right)^{-1/2} \tag{2.19}$$

The velocity of an electromagnetic wave propagating through a good dielectric $(\frac{\sigma}{\omega\varepsilon})^2 << 1$ (low-loss) material, is expressed as:

$$v = \frac{1}{\sqrt{\mu\varepsilon}} = \frac{c}{n} \tag{2.20}$$

As the velocity of free-space (2.21) and the refractive index (2.22) is given by

$$c = \frac{1}{\sqrt{\mu_0\varepsilon_0}} \qquad \frac{1}{\sqrt{\frac{N}{C^2/s^2}\frac{C^2}{Nm^2}}} \rightarrow m/s \tag{2.21}$$

$$n = \frac{c}{v} \rightarrow n = \frac{1/\sqrt{\mu_0\varepsilon_0}}{1/\sqrt{\mu\varepsilon}} \rightarrow n = \sqrt{\frac{\mu\varepsilon}{\mu_0\varepsilon_0}} = \sqrt{\mu_r\varepsilon_r} \tag{2.22}$$

the velocity can be derived as

$$\mu_r = 1 \rightarrow v = \frac{c}{\sqrt{\varepsilon_r}} \tag{2.23}$$

where:

c = velocity of free-space $(299,792,458\ m/s,\ \approx 3 \times 10^8\ m/s)$

v = velocity through material (m/s)

ε_r = relative permittivity

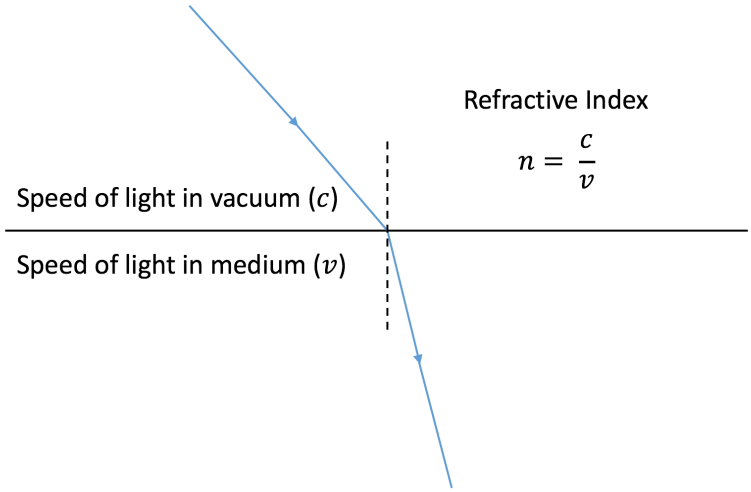

Figure 2.12: The refractive index is equal to the speed of the signal traveling through vacuum over the speed of the signal propagating inside a medium.

2.6 SUMMARY

The aim of this chapter was to give an overview of the principles of ground penetrating radar, a non-destructive geophysical method which is used to detect subsurface objects. The history of GPR, the dielectric properties, how the GPR system works and how the data from a survey is collected and processed have been described.

3

MAXWELL'S EQUATIONS AND THE FDTD METHOD

In this chapter, an overview of the electromagnetic field theory is presented. A short history about Maxwell's equations is discussed. The FDTD method and Yee's algorithm are explained along with the advantages and disadvantages they have.

3.1 MAXWELL'S EQUATIONS

In the 19^{th} century (1862), a Scottish physicist and mathematician called James Clerk Maxwell published a set of equations that included Lorentz force law. These equations are the basic laws of electromagnetic field theory. Maxwell's equations can be expressed in integral and differential forms and they are known as Gauss's law for both magnetic and electric fields, Faraday's law and Ampere's law. These laws are commonly referred to as Maxwell's equations. These equations show the propagation of the electric and magnetic fields and how they are affected by different environments and materials.

3.1.1 *Gauss's Law for electric fields*

Gauss's law was discovered by a German mathematician and physicist called Carl Friedrich Gauss in 1813. Gauss's electric field law describes how the electric field behaves around electric charges. This law is a mathematical statement that can be written in the form of divergence of the electric flux density equal to the electric charge density at a point, as shown in (3.1).

$$\nabla \cdot \vec{D} = \rho \tag{3.1}$$

where:

$\nabla\cdot$ = the divergence operator

$\vec{D}$ = electric flux density (C/m^2)

ρ = volume charge density (C/m^3)

Additionally, Gauss's law states that the integral of a closed surface of an electric flux is proportional to the total charge surrounded by

the surface. Assuming a volume (V) with a boundary or surface (S), Gauss's law can be written in integral form as shown in (3.2).

$$\iiint_V \nabla \cdot \vec{D}\, dv = \iint_S \vec{D} \cdot ds = \iiint_V \rho\, dv = Q_{enc} \tag{3.2}$$

where:

ds	=	area of an infinitesimal piece of the surface S (m^2)
dv	=	volume of an infinitesimal piece of the volume V (m^3)
Q_{enc}	=	enclosed charge (C)

The divergence of the flux density is equal to zero unless there is an existing electric charge. If an electric charge is present, we can determine the amount of electric flux exiting the arbitrary volume. D can be divided into normal (D_n) and tangential (D_t) components. The electric flux inside a volume is affected by the normal component and the tangential component only circles around the volume without any effect. In other words, D_n contributes to the electric flux entering or exiting a volume. Therefore, writing $D \cdot ds$ means the D that affects the electric flux of the volume is of interest. The sum of all the electric flux density of interest along a surface, is $\iint_S D \cdot ds$.

3.1.2 *Gauss's Law for magnetic fields*

Similarly to Gauss's law for electric field, the divergence of the magnetic flux density is equal to the volume magnetic charge density. However, magnetic charge has never been proven to exist or has not been established yet. Therefore, the divergence of the magnetic flux density is equal to zero as stated in (3.3).

$$\nabla \cdot \vec{B} = 0 \tag{3.3}$$

As the magnetic field (H) and the magnetic flux density are related by the magnetic permeability (μ), according to (3.3), one can state that the divergence of the magnetic field is also zero. The integral form of Gauss's magnetic field law can be written as (3.4).

$$\iint_S \vec{B} \cdot \vec{ds} = 0 \tag{3.4}$$

where:

$\vec{B}$ = magnetic flux density (Wb/m^2)

$\vec{ds}$ = area of an infinitesimal piece of the surface S (m^2)

S = enclosed surface such as sphere or torus

$\nabla\cdot$ = the divergence operator

3.1.3 *Ampere's Law*

Ampere's law was created by a French physicist called Andre Marie Ampere in 1823. He stated that the enclosed electric current flowing through a surrounding surface is equal to the line integral of the magnetic field around a closed loop.

$$I = \oint \vec{H} \cdot d\vec{L} \tag{3.5}$$

where:

I = electric current intensity (A)

$\vec{H}$ = magnetic field intensity (A/m)

$d\vec{L}$ = infinitesimal vector element of a closed loop

The integral form of Maxwell's equation for the Ampere's law section (the final Maxwell's equation) is shown in (3.6). It presents that the line integral of the magnetic field around a closed loop is equal to the surface integral of the current density.

$$\oint \vec{H} \cdot d\vec{L} = \iint_S \vec{J} \cdot \vec{ds} \tag{3.6}$$

The current density can be split into different parts which are presented in (3.7) and (3.8).

$$\vec{J_d} = \frac{\partial \vec{D}}{\partial t} \tag{3.7}$$

$$\vec{J_c} = \sigma \vec{E} \tag{3.8}$$

In more in depth presentation of how these equations are derived into the following are given in Appendix B.2.

$$\oint \vec{H} \cdot d\vec{L} = \iint_S \left(\vec{J}_s + \sigma \vec{E} + \frac{\partial \vec{D}}{\partial t} \right) \cdot \vec{ds} \tag{3.9}$$

Using Stoke's theorem we can derive Maxwell's Ampere's law in differential form as shown in (3.10).

$$\nabla \times \vec{H} = \vec{J}_s + \sigma \vec{E} + \frac{\partial \vec{D}}{\partial t} \tag{3.10}$$

A more formal way of writing it is

$$\nabla \times \vec{H} = \vec{J} + \frac{\partial \vec{D}}{\partial t} \tag{3.11}$$

where:

$\vec{J}_d$ = electric displacement current density (A/m^2)

$\vec{J}_c$ = electric conductivity current density (A/m^2)

$\vec{J}_s$ = impressed source current density (A/m^2)

σ = electrical conductivity (S/m^2)

$\vec{E}$ = electric field (V/m)

3.1.4 *Faraday's Law*

Faraday's law was discovered by an English scientist called Michael Faraday in 1831. He stated that the electric voltage is equal to changes of the magnetic flux over time as presented in (3.12).

$$V = -\frac{d}{dt} \iint_S \vec{B} \cdot ds \tag{3.12}$$

The integral form of Maxwell's equation for the Faraday's law is shown in (3.13). It presents that the Electro-Motive Force (EMF) around a circuit or loop is equal to the rate of change of the magnetic flux through a closed loop.

$$\oint \vec{E} \cdot d\vec{L} = - \iint_S \left(\frac{\partial \vec{B}}{\partial t} \right) \cdot \vec{ds} \tag{3.13}$$

where $d\vec{L}$ is the infinitesimal vector element of a closed contour, $\vec{E}$ is the electric field and $\vec{B}$ is the magnetic flux density.

Using Stoke's theorem we can derive Maxwell's Faraday's law in differential form as shown in (3.14). It states that the curl of the electric field is equal to the rate of change of the magnetic flux. A more in depth presentation can be found in Appendix B.1.

$$\nabla \times \vec{E} = -\frac{\partial \vec{B}}{\partial t} \tag{3.14}$$

where:

$\nabla\times$ = the curl operator

$\vec{E}$ = electric field (V/m)

$\frac{\partial \vec{B}}{\partial t}$ = magnetic displacement current density (A/m^2)

EMF is not a force but an energy per unit charge which produces a current flow through a circuit from the positive to the negative terminals. Faraday's law of induction defines that, the energy in a wire loop that is responsible for the movement of the charge around the loop is the EMF. It is defined as the rate of change of the magnetic flux in a circuit as shown in (3.15).

$$EMF = -\frac{d\Phi_B}{dt} \tag{3.15}$$

where, EMF is the electromotive force (V) and Φ is the magnetic flux (T). In 1834 a Russian physicist called Heinrich Friedrich Emil Lenz stated that the induced EMF causing a current to flow in a coil or loop producing a magnetic field is opposite to the change in magnetic flux. In other words, when a magnet is positioned next to a coil an EMF is created (Faraday's law) which repels the magnet that created the EMF (Lenz's law). Therefore the minus sign is (3.15) is implemented by Lenz which shows the direction of the force. Not having Lenz's law would cause the magnet to attract the coil creating an increase in EMF. It is not possible to create energy from nothing hence the magnetic field and the magnet must repel one another as stated by Lenz.

3.2 MAXWELL'S CURL EQUATIONS

By substituting the constitutive parameters as discussed in Chapter 2 and rearranging Maxwell's Faraday and Ampere's laws we get Maxwell's curl equations as shown in (3.16) and (3.17).

$$\frac{\partial \vec{E}}{\partial t} = \frac{1}{\varepsilon}\left(\nabla \times \vec{H} - \vec{J_s} - \sigma \vec{E}\right) \tag{3.16}$$

$$\frac{\partial \vec{H}}{\partial t} = \frac{1}{\mu}\left(-\nabla \times \vec{E} - \vec{M_s} - \sigma^* \vec{H}\right) \tag{3.17}$$

where:

σ = electric conductivity (S/m)

σ^* = equivalent magnetic loss (Ω/m)

M_s = magnetic current density impressed source A/m^2

J_s = electric current density impressed source A/m^2

The electric and magnetic fields are a three dimensional vectors with x, y, z components as defined in (3.18) and (3.19).

$$E = E_x\hat{x} + E_y\hat{y} + E_z\hat{z} = \begin{bmatrix} E_x \\ E_y \\ E_z \end{bmatrix} \tag{3.18}$$

$$H = H_x\hat{x} + H_y\hat{y} + H_z\hat{z} = \begin{bmatrix} H_x \\ H_y \\ H_z \end{bmatrix} \tag{3.19}$$

where $\hat{x}$ is a unit vector in the x-direction, $\hat{y}$ is a unit vector in the y-direction and $\hat{z}$ is a unit vector is the z-direction. The curl of the electric and magnetic vector fields are expressed in (3.20) and (3.21).

$$\nabla \times \vec{E} = \left(\frac{\partial \vec{E_z}}{\partial y} - \frac{\partial \vec{E_y}}{\partial z}\right)\hat{x} + \left(\frac{\partial \vec{E_x}}{\partial z} - \frac{\partial \vec{E_z}}{\partial x}\right)\hat{y} + \left(\frac{\partial \vec{E_y}}{\partial x} - \frac{\partial \vec{E_x}}{\partial y}\right)\hat{z} \tag{3.20}$$

$$\nabla \times \vec{H} = \left(\frac{\partial \vec{H}_z}{\partial y} - \frac{\partial \vec{H}_y}{\partial z}\right)\hat{x} + \left(\frac{\partial \vec{H}_x}{\partial z} - \frac{\partial \vec{H}_z}{\partial x}\right)\hat{y} + \left(\frac{\partial \vec{H}_y}{\partial x} - \frac{\partial \vec{H}_x}{\partial y}\right)\hat{z} \tag{3.21}$$

where the partial derivatives such as $\frac{\partial \vec{E_z}}{\partial y}$ are the rate of change of E_z in the y-direction, $\frac{\partial \vec{E_y}}{\partial z}$ are the rate of change of E_y in the z-direction and so on. $\frac{\partial \vec{E_z}}{\partial y} - \frac{\partial \vec{E_y}}{\partial z}$ calculates the field rotation in the $y-z$ plane. Finally, the curl measures the rotation of a field.

Substituting (3.20) and (3.21) in Maxwell's curl equations ((3.16),(3.17)), six partial differential equations are derived ((3.22) and (3.23)) which are the base of the FDTD method and will be used to derive the finite difference expressions later.

$$\frac{\partial \vec{E_x}}{\partial t} = \frac{1}{\varepsilon}\left[\frac{\partial \vec{H_z}}{\partial y} - \frac{\partial \vec{H_y}}{\partial z} - \vec{J}_{s_x} - \sigma \vec{E_x}\right] \tag{3.22a}$$

$$\frac{\partial \vec{E_y}}{\partial t} = \frac{1}{\varepsilon}\left(\frac{\partial \vec{H_x}}{\partial z} - \frac{\partial \vec{H_z}}{\partial x} - \vec{J}_{s_y} - \sigma \vec{E_y}\right) \tag{3.22b}$$

$$\frac{\partial \vec{E_z}}{\partial t} = \frac{1}{\varepsilon}\left(\frac{\partial \vec{H_y}}{\partial x} - \frac{\partial \vec{H_x}}{\partial y} - \vec{J}_{s_z} - \sigma \vec{E_z}\right) \tag{3.22c}$$

$$\frac{\partial \vec{H_x}}{\partial t} = \frac{1}{\mu}\left(\frac{\partial \vec{E_y}}{\partial z} - \frac{\partial \vec{E_z}}{\partial y} - \vec{M}_{s_x} - \sigma^* \vec{H_x}\right) \tag{3.23a}$$

$$\frac{\partial \vec{H_y}}{\partial t} = \frac{1}{\mu}\left(\frac{\partial \vec{E_z}}{\partial x} - \frac{\partial \vec{E_x}}{\partial z} - \vec{M}_{s_y} - \sigma^* \vec{H_y}\right) \tag{3.23b}$$

$$\frac{\partial \vec{H_z}}{\partial t} = \frac{1}{\mu}\left(\frac{\partial \vec{E_x}}{\partial y} - \frac{\partial \vec{E_y}}{\partial x} - \vec{M}_{s_z} - \sigma^* \vec{H_z}\right) \tag{3.23c}$$

3.3 THE FINITE-DIFFERENCE TIME-DOMAIN (FDTD) METHOD

3.3.1 *Yee's Algorithm*

The FDTD method was created by Kane S. Yee in 1966. This method is characterised by the solution of Maxwell's equations using the central Finite-Differences (FD) based on the partial derivatives of space and time. The FDTD method is one of the most popular techniques in Computational Electromagnetics (CEM) to solve Maxwell's equations. Over the past decade, it has been widely used by electromagnetic simulation tools. A number of other methods that can be addressed are the Method of Moments (MoM) (Peterson, Ray, & Mittra, 1998), Finite Element Method (FEM) (Jin, 2002), Finite Element Time-Domain (FETD) (Lee, Lee, & Cangellaris, 1997), Finite-Differences FD (Crank & Nicolson, 1947) and Transmission Line Matrix (TLM) and FDTD method (Giannopoulos, 1998). These methods are common in their ability to model complex geometries and use different approximations in order to analyse Maxwell's equations. In this research, the FDTD method was used as it has many advantages such as simplicity, robustness, it is relatively fast and well-established technique plus capable of solving very complex problems. Additionally, the gprMax software (Giannopoulos, 2005; Warren, Giannopoulos, & Giannakis, 2016; Warren et al., 2019) used in this research uses the FDTD method. Despite its popularity, the FDTD method comes with some disadvantages. For instance, it requires a complete discretisation of the electric and magnetic fields throughout the whole volume domain. For example, a heterogeneous concrete model that contains sphere shape aggregates can be problematic as the FDTD method is forced to model a large amount of white-space (an area that a sphere can not be placed) when packing the spheres together (Gedney, 2011). The white-space would be the volume of each sphere, plus the area between each sphere separating it from the neighbouring ones. Therefore, the larger the FDTD grid is the more white-space there will be between the spheres resulting in the spheres being less compact in the model. A sub-gridding method which has been critical in increasing the efficiency and accuracy of the FDTD method needs to be used. With this method, a much smaller grid can be used within the normal grid which can help more realistic and accurate modelling to be achieved for complex models in a timely manner (Diamanti & Giannopoulos, 2011; Wei et al., 2017; Hartley, Giannopoulos, & Warren, 2018). Hence, with the sub-gridding technique the white-spaces between the spheres are reduced resulting in a more compact model.

3.3.2 *FDTD Grid*

As shown in Figure 3.1, Yee's cell is a 3D cube that to create a 3D geometry model, many such cubes are used. that buildup on each other

to create a specific model. Yee's grid of cells also known as the FDTD grid is made from electric and magnetic components. Each electric field component is surrounded by magnetic field components and vice versa. The E-field and H-field components update one another in every time step meaning that the E-field component is updated by the previous in time H-field component and similarly the H-field is updated by the previous E-field and finally the process is repeated again. This type of updating is called the leapfrog approach which Maxwell used to update the electric and magnetic fields.

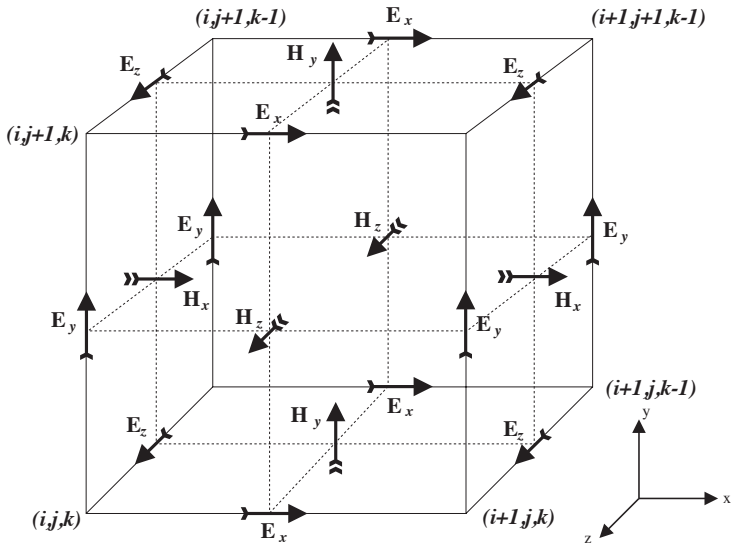

Figure 3.1: The three dimensional cube known as Yee's cell showing the location of the electric and magnetic field components (Giannopoulos, 1998).

3.3.3 *FD Notation*

A lattice space point is defined in (3.24) and a notation u is defined in (3.25).

$$(i, j, k) = (i\Delta x, j\Delta y, k\Delta z) \tag{3.24}$$

$$u(i\Delta x, j\Delta y, k\Delta z, n\Delta t) = u|^{n}_{i,j,k} \tag{3.25}$$

where i, j, k, n are integers, Δt is the time increment and $\Delta x, \Delta y, \Delta z$ are the lattice grid space increments, also known as spatial steps.

3.3.4 *FD Expressions*

By using the u notation and the central difference (finite difference) approximation of the partial derivative of "u" with respect to time we get

$$\begin{aligned}\frac{E_x\Big|_{i,j+\frac{1}{2},k+\frac{1}{2}}^{n+\frac{1}{2}} - E_x\Big|_{i,j+\frac{1}{2},k+\frac{1}{2}}^{n-\frac{1}{2}}}{\Delta t} = &-\left(\frac{1}{\epsilon_{i,j+\frac{1}{2},k+\frac{1}{2}}}\right)\sigma_{i,j+\frac{1}{2},k+\frac{1}{2}} E_x\Big|_{i,j+\frac{1}{2},k+\frac{1}{2}}^{n-\frac{1}{2}} \\ &+\left(\frac{1}{\epsilon_{i,j+\frac{1}{2},k+\frac{1}{2}}}\right)\frac{H_x\Big|_{i,j+1,k+\frac{1}{2}}^{n} - H_z\Big|_{i,j,k+\frac{1}{2}}^{n}}{\Delta y} \\ &-\left(\frac{1}{\epsilon_{i,j+\frac{1}{2},k+\frac{1}{2}}}\right)\frac{H_y\Big|_{i,j+\frac{1}{2},k+1}^{n} - H_y\Big|_{i,j+\frac{1}{2},k}^{n}}{\Delta z} \\ &-\left(\frac{1}{\epsilon_{i,j+\frac{1}{2},k+\frac{1}{2}}}\right) J_{S_x}\Big|_{i,j+\frac{1}{2},k+\frac{1}{2}}^{n}\end{aligned} \tag{3.26}$$

The right hand side of the expression contains E_x at time space $n-\frac{1}{2}$. As this is not compatible with the memory of a computer, we use the semi-implicit approximation to over come this problem.

$$E_x\Big|_{i,j+\frac{1}{2},k+\frac{1}{2}}^{n} = \frac{E_x\Big|_{i,j+\frac{1}{2},k+\frac{1}{2}}^{n+\frac{1}{2}} + E_x\Big|_{i,j+\frac{1}{2},k+\frac{1}{2}}^{n-\frac{1}{2}}}{2} \tag{3.27}$$

By implementing (3.27) and rearranging (3.26) will result in an update equation for E_x as shown in (3.28). The remaining of the update

equations are given in Appendix A.

$$
\begin{aligned}
E_x\Big|_{i,j+\frac{1}{2},k+\frac{1}{2}}^{n+\frac{1}{2}} &= \left(\frac{1-\frac{\sigma_{i,j+\frac{1}{2},k+\frac{1}{2}}\Delta t}{2\epsilon_{i,j+\frac{1}{2},k+\frac{1}{2}}}}{1+\frac{\sigma_{i,j+\frac{1}{2},k+\frac{1}{2}}\Delta t}{2\epsilon_{i,j+\frac{1}{2},k+\frac{1}{2}}}}\right) E_x\Big|_{i,j+\frac{1}{2},k+\frac{1}{2}}^{n-\frac{1}{2}} \\
&+ \left(\frac{\frac{\Delta t}{\epsilon_{i,j+\frac{1}{2},k+\frac{1}{2}}}}{1+\frac{\sigma_{i,j+\frac{1}{2},k+\frac{1}{2}}\Delta t}{2\epsilon_{i,j+\frac{1}{2},k+\frac{1}{2}}}}\right) \frac{H_x\Big|_{i,j+1,k+\frac{1}{2}}^{n} - H_z\Big|_{i,j,k+\frac{1}{2}}^{n}}{\Delta y} \\
&- \left(\frac{\frac{\Delta t}{\epsilon_{i,j+\frac{1}{2},k+\frac{1}{2}}}}{1+\frac{\sigma_{i,j+\frac{1}{2},k+\frac{1}{2}}\Delta t}{2\epsilon_{i,j+\frac{1}{2},k+\frac{1}{2}}}}\right) \frac{H_y\Big|_{i,j+\frac{1}{2},k+1}^{n} - H_y\Big|_{i,j+\frac{1}{2},k}^{n}}{\Delta z} \\
&- \left(\frac{\frac{\Delta t}{\epsilon_{i,j+\frac{1}{2},k+\frac{1}{2}}}}{1+\frac{\sigma_{i,j+\frac{1}{2},k+\frac{1}{2}}\Delta t}{2\epsilon_{i,j+\frac{1}{2},k+\frac{1}{2}}}}\right) J_{S_x}\Big|_{i,j+\frac{1}{2},k+\frac{1}{2}}^{n}
\end{aligned}
\tag{3.28}
$$

As shown in Figure 3.1, the electric field components are surrounded by magnetic field components and the H-field components are surrounded by the E-field components. Additionally, the E-field and H-field are half a cell apart in space meaning that the E-field component is calculated using the previous H-field then the H-field components is calculated using the previous E-field. Figure 3.2 illustrates this process. For time incrementation, the H-field components at time $n+\frac{1}{2}$ is calculated using the previously updated E-field components. Similarly, the E-field components at time $n+1$ gets updated using the previously updated H-field components. This process continues until the required time is reached.

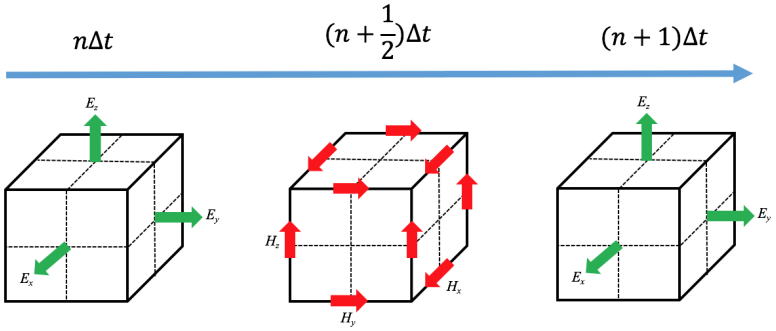

Figure 3.2: 3D FDTD grid for the electric and magnetic fields updating each other every half a time step.

3.3.5 *Stability, numerical dispersion, and errors*

One important aspect of the FDTD method is that it is a conditional stable method, where the stability is given by the Courant-Friedrichs-Lewy (CFL) condition. As shown in equation (3.29), the stability condition also known as the Courant limit, relates the time step and the spatial steps (Gedney, 2011). For a smaller spatial step, the time step becomes smaller therefore, the computational run-time increases.

$$\Delta t \leq \frac{1}{c\sqrt{\frac{1}{(\Delta x)^2}+\frac{1}{(\Delta y)^2}+\frac{1}{(\Delta z)^2}}} \tag{3.29}$$

where:

Δt	=	time step
$\Delta x, \Delta y, \Delta z$	=	spatial step
c	=	speed of light

For a 1D model we have $\Delta l = \Delta x = \Delta y = \Delta z$, the stability condition (Courant limit) becomes $\frac{c\Delta t}{\Delta l} \leq 1$. For 2D it becomes $\frac{c\Delta t}{\Delta l} \leq \frac{1}{\sqrt{2}}$ and for 3D it becomes $\frac{c\Delta t}{\Delta l} \leq \frac{1}{\sqrt{3}}$ (Taflove & Hagness, 2005). Although the dispersion of 3D is more complex but if using $\Delta l = \Delta x = \Delta y = \Delta z$, the time step is decreased by a factor of $\sqrt{3}$.

Another limitation of the FDTD method is the staircasing error. As shown in Figure 3.3, depending on the spatial step the circle in FDTD will look like a circle with rough edges. The lower the spatial step the lower the error as the staircasing will be reduced. However, the error reduction comes with a increase in computational run-time by decreasing the spatial steps. Numerical dispersion is another limitation of the FDTD method meaning that the phase velocity of the numerical wave can be different from the speed of light. This can cause the propagating wave to have some delay or phase errors that can lead to ringing of the pulse (Taflove & Hagness, 2005).

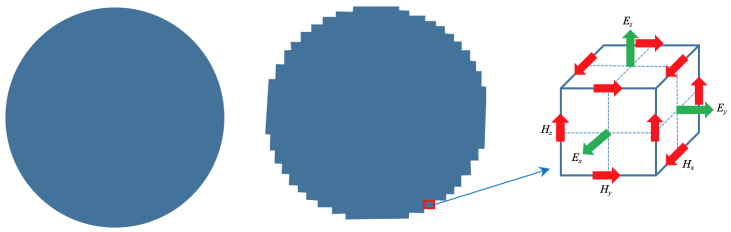

Figure 3.3: This Figure represents how a circle or sphere is designed with the FDTD method. As shown, the middle circle has rigid edges as the cells are built on one another to form a circle. This is known as the stair-case error.

3.4 ABSORBING BOUNDARY CONDITION

When using the FDTD method for electromagnetic wave simulations, in order to be as close as possible to reality, the model domain needs to represent an infinite space or a large area. This is impossible due to the computational requirements hence the computational domain needs to be truncated by introducing an artificial boundary. An Absorbing Boundary Condition (ABC) represents a boundary that absorbs transmitted or reflected electromagnetic waves that propagate towards the boundary. This region prevents any energy from being reflected back into the model domain by absorbing all or most of it. With an ABC placed at the boundaries of the FDTD grid, an unbound region is achieved. There are a number of different ABC that have been developed for this purpose.

The first ABC to truncate the area of computation was developed by Engquist and Majda (1977). They developed a systematic method (boundary condition) to minimize artificial reflections. The first attempt to solve the boundary condition for the FDTD method was by Mur (1981). In the following years, many more attempts were made to truncate the FDTD absorbing boundaries and therefore make the FDTD method a high standard computational tool for electromagnetic modelling (Liao et al., 1984; Higdon, 1986, 1987; Betz & Mittra, 1992).

The most successful and well known ABC for the FDTD method is the Perfectly Matched Layer (PML) which was introduced by Berenger et al. (1994). This is an absorbing layer used to decrease the computational region to a finite domain and is very commonly used in the FDTD modelling. The accuracy (Taflove & Hagness, 2005) and stability (Bérenger, 2007) of the PML is much higher in comparison with other ABC. The PML can be used in anisotropic (Sacks et al., 1995; Gedney, 1996a), dispersive, heterogeneous, non-linear and lossy media (Gedney, 1996b, 2011). An advantage of the absorbing boundary is that it only requires knowledge of the truncation boundary or the surroundings in the domain. Also the PML reflection errors are much smaller than other ABC methods.

A number of different perfectly matched layers have been designed in which some of these approaches are: Convolutional Perfectly Matched Layer (CPML) (Roden & Gedney, 2000), Complex Frequency Shifted Perfectly Matched Layer (CFS-PML) (Roden & Gedney, 2000), Uniaxial Perfectly Matched Layer (UPML) (Gedney, 1996b) and Stretched Coordinates Perfectly Matched Layer (SC-PML) (Chew & Weedon, 1994). The CPML combined with the Complex Frequency Shifted (CFS) parameters applied to the FDTD method is the most robust and efficient method for truncating FDTD grid (Gedney, 2011).

The PML that is embedded in gprMax is the Recursive Integration Perfectly Matched Layer (RIPML) and it is used for this study (Drossaert

& Giannopoulos, 2007; Giannopoulos, 2008, 2011, 2018).

Figure 3.4 presents the original problem or an open boundary electromagnetic problem (Figure 3.4a). This means that there is no fixed boundary or an infinite amount of space. In other words, for an open boundary condition the radiating fields decay while propagating. To carry out such a condition, an infinite computational domain is needed which is not practical. Therefore the computer has to have a boundary condition and be finite to be computationally possible. As a result the domain is constrained by the lack of computational resources. Figure 3.4b shows an artificial boundary (PML) that absorbs the propagating waves and minimises the reflection of the transmitted wave hence, creating an impression of an open space (no boundary).

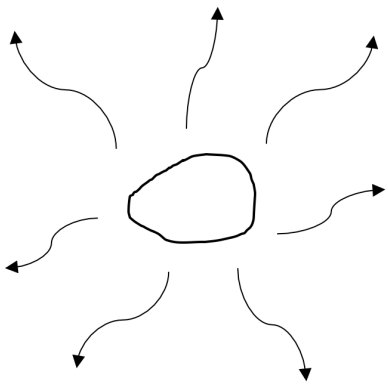

(a) Original problem (no ABC)

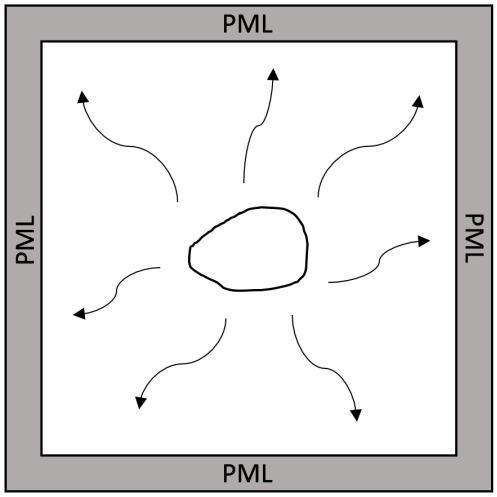

(b) Artificial boundary (ABC)

Figure 3.4: 3.4a presents a open boundary problem with no fixed boundary (infinite space) and 3.4b shows an artificial boundary simulating an open space.

3.5 SUMMARY

The aim of this chapter was to present Maxwell's equations and the base of the FDTD method and how they relate to each other. Maxwell's four equations (Gauss's Law for electric and magnetic fields, Faraday's and Ampere's Law) have been explained. Maxwell's curl equations are introduced along with the derivation from the differential form of Faraday's and Ampere's law to the curl equations. These equations are used to update the electric and magnetic fields forming the FDTD grid. A general overview of Yee's algorithm and its relation to the FDTD method is presented. Yee's cells are the building blocks of an FDTD grid in time and space. The update equations are explained and shown how they are derived. The error and limitations of the FDTD method were discussed. Finally, a brief overview of the ABC's is presented which truncate the computational domain. The PML method is shown to be the most efficient method for truncating an FDTD grid. Finally, in this chapter the most robust methods for GPR modelling have been overviewed.

4

ADVANCED HALF-SPACE MODELLING

This chapter presents the development of a concrete model from a simple 2D homogeneous model to a 3D more advanced heterogeneous model by adding randomly distributed aggregates, moisture content and air-voids. An overview of a aggregate shape design and the way they are distributed without collision or overlapping is also presented. The model is used further to investigate the time-zero position and the CRIM model shape factor.

4.1 INITIAL DEVELOPMENT OF THE CONCRETE MODEL

To keep the framework simple, the design of the initial concrete model was introduced as a 2D homogeneous model. As the research work progressed, the model was redesigned to a more advanced model which mimics a real concrete slab.

4.1.1 *Homogeneous two dimensional model*

A good starting point was to develop a simple homogeneous model with minimum reflections from inhomogeneities as it was easier to understand the output response and distinguish the received wavelet. Here, a half-space that has relative permittivity of 3 is defined and also a PEC plate as shown in Figure 4.1. The simulation employs a simple theoretical source such as a line source. The domain size is $0.3\ m \times 0.36\ m$ with a spatial discretisation of $\Delta x = \Delta z = 1\ mm$.

4.2 OPTIMISATION OF THE CONCRETE MODEL

Simple homogeneous concrete models are commonly used to describe concrete in GPR modelling. However, concrete is a mixture of aggregate, cement, air-void and moisture and the size of aggregate can play an important role for GPR reflections, especially at high frequencies. Therefore, a more complex model was developed. The outcome of this model will be used for the analysis of the time-zero adjustment in the following chapters. The goal was to design a model that replicates a real concrete slab by inserting aggregates to make the model as close as possible to reality. For the early stages of this research, aggregates were inserted as spheres in the model for easy volume measurement purposes.

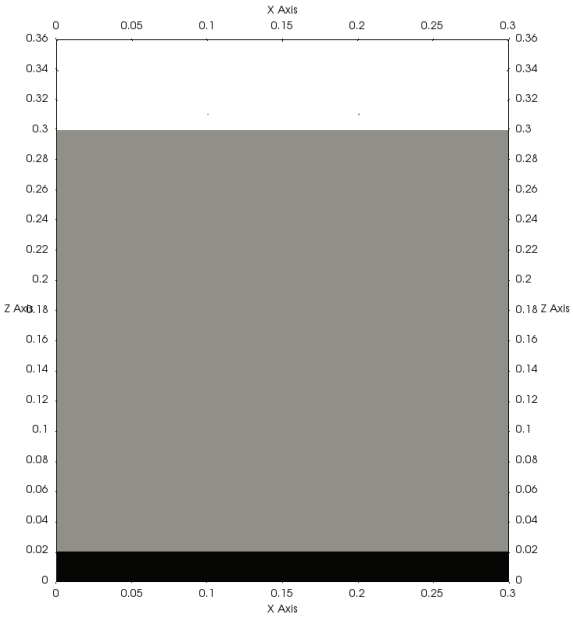

Figure 4.1: Homogeneous two dimension model with line source (two dots) on top of a constant half-space and a PEC target at the bottom.

4.2.1 *Generating non-overlapping circles/spheres*

In reality, aggregates do not overlap or collide with each other therefore the aggregates are modelled in a non-overlapping environment. Before doing so, non-overlapping circles, random distribution and circle packing were researched. The non-overlapping concept is shown in Figure 4.2.

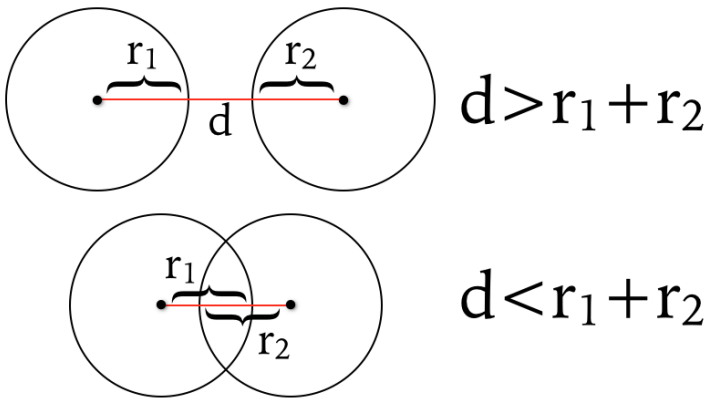

Figure 4.2: The concept behind the design of non-overlapping circles. If the distance (d) measurement of the two points is less than the combination of the two radius's ($r_1 + r_2$) then the circles are overlapping. If the distance is greater than the radius's added together, the circles are not overlapping.

This was programmed in Python to generate non-overlapping circles with the addition of random radius's packed in a single window frame as shown in Figure 4.3. Each circle has a random (x, y) position and radius (r). Initially, a point was chosen randomly and it was checked if it intersects with an other circle. If it does then the circle would not be created and another point will be chosen. If the collision check for the new point is negative, the circle would be drawn at that position. Obviously, the search for a free, non-overlapping space is infinite so a maximum attempt to find such spaces was set which in this case was 10000 times. All successful circles were added to an array or list of circles in which every new found circle was checked against the existing circles in the list. If they do not overlap with one another, the circle would be added to the list showing that a new space has been found to draw a circle.

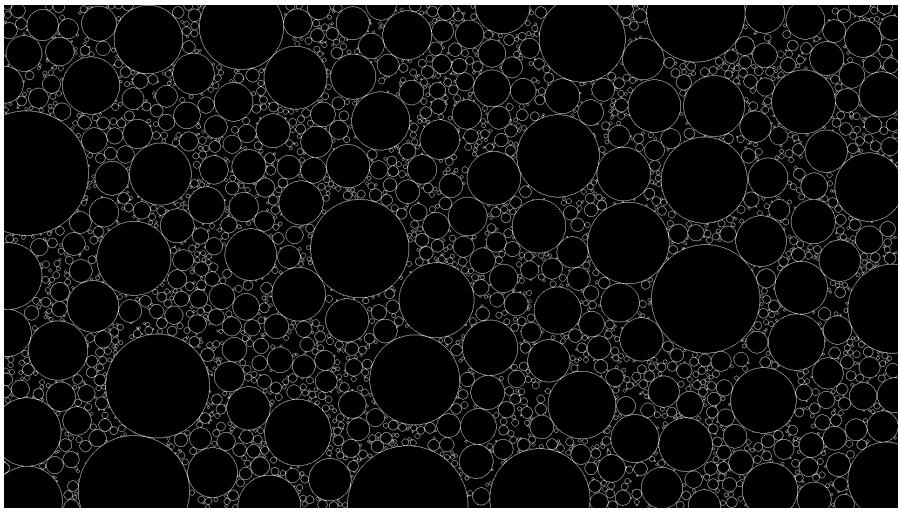

Figure 4.3: Randomly packed circles without overlapping (Anthony, 2017).

4.2.2 *Heterogeneous two dimension model*

Once this concept was successfully generated, it was used as an input in gprMax (Appendix D.1). Here, the larger or coarse aggregates (usually 4 to 8 *mm* radius) are created first. As the model runs out of free space to draw a circle with a large radius, the radius was reduced to fit more circles producing fine aggregates. The result of this process is shown in Figure 4.4. The aggregates with random positions and radius's were created in a background medium (cement). A theoretical line source was positioned 1 *cm* above the surface and the transmitter and receiver were 10 *cm* apart. A PEC target was positioned at the bottom of the model. The disadvantage of this type of packing is that it is very time-consuming as it requires a long Central Processing Unit (CPU) run-time. This is because the aggregates need to find a position that doesn't collide or overlap with another aggregate. Simulating such models can

take days or even weeks of run-time depending on the volume of spheres and the degree of compactness.

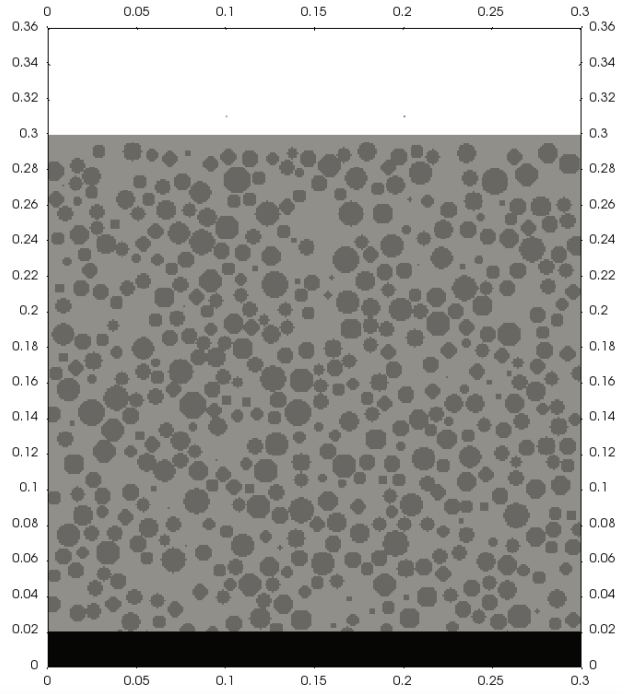

Figure 4.4: Heterogeneous two dimensional model with non-overlapping aggregates.

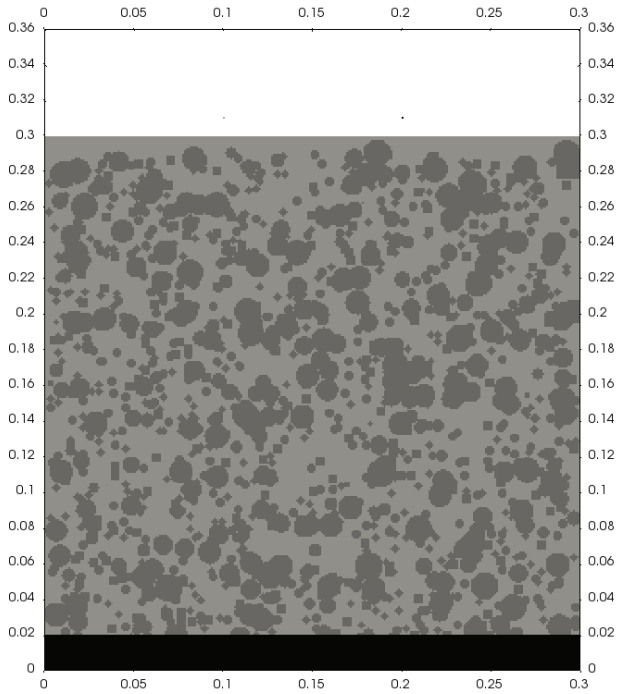

Figure 4.5: Heterogeneous two dimensional model with overlapping aggregates.

Eliminating the process that searches for a non-collision space results in the aggregates to overlap as presented in Figure 4.5. Both 2D models were simulated and the results are compared in the following section.

4.2.3 *Overlapping spheres vs non-overlapping spheres*

The simulation results for both overlapping and non-overlapping aggregates were obtained. As the model becomes more complex, a higher volume of clutter responses and ringing was detected. As shown in Figure 4.6, the main response for the overlapping aggregates is similar to the non-overlapping version but with variable clutter as expected. In other words, in regards to the two-way travel time of the target and the time-zero position, both cases do not affect the two-way travel time as the target reflections occur at the same time hence, the velocity which was used to estimate the permittivity of the mixture. Overlapping affects the overall amplitude but the choice of using either model was irrelevant as they have minimal effect on the outcome of the research topic.

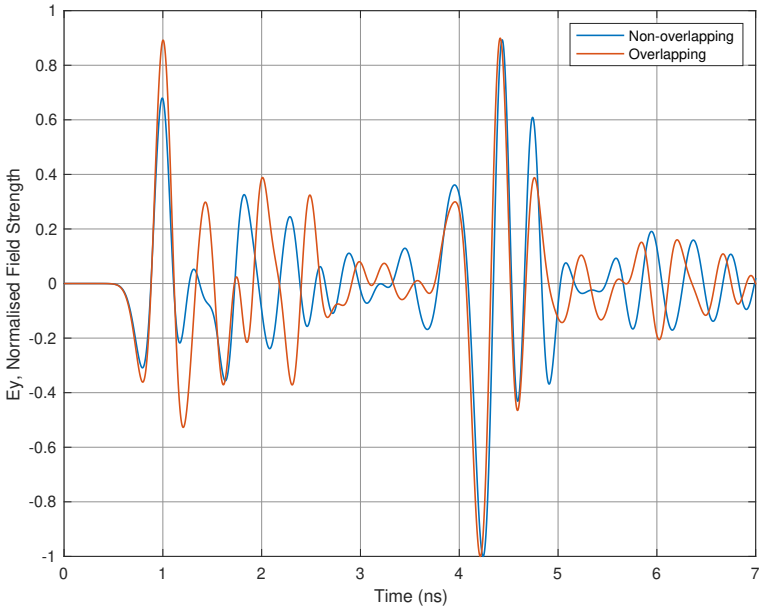

Figure 4.6: Normalised electric field E_y component output for a 2D model, simulating overlapping vs non-overlapping aggregates. The excitation for the model was done using a line source.

Modelling the same process in 3D resulted in Figure 4.7. Here a real GSSI 1.5 GHz antenna model was used that will be introduced later in this chapter. Moving from 2D to 3D changes the circle aggregates to sphere-shaped aggregates therefore the non-collision process becomes slightly more complex. Each sphere has a (x, y, z) position with a radius (r). Similarly to the circle's no-collision process, each sphere was checked

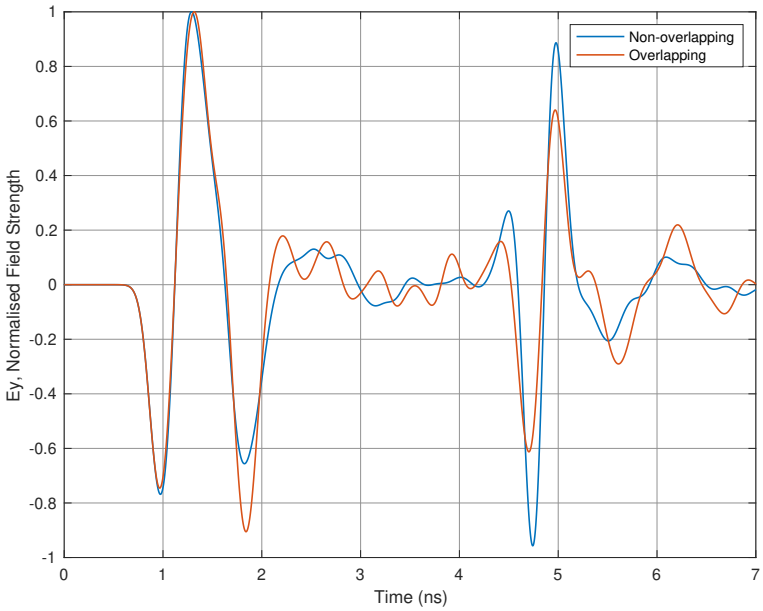

Figure 4.7: Normalised electric field E_y component output for a 3D model, simulating overlapping vs non-overlapping aggregates. The source used was a model of a GSSI antenna.

against other spheres and if there was no collision, the sphere was stored in a list of spheres. The process continues until the specified aggregate percentage has been met. The higher the percentage the higher the simulation run-time as the spheres need to find unoccupied positions. To accelerate the simulation process, after a given aggregate percentage, the size of the spheres were decreased in order to find a space more easily. Although the spheres were decreased in size, it was still a time-consuming process in comparison with the simulation run-time of the colliding spheres. The two models have the same amount of aggregates. The colliding spheres have less clutter but the main responses were in good agreement. Therefore, due to the less computational run-time required for the overlapping aggregates, the numerical modelling was continued using the faster and more efficient solution which is when the aggregate particles overlap. The process can be found in Appendix D.2.

4.3 ADDITIONAL DEVELOPMENT OF THE 2D MODEL

Further development on the 2D model was preformed to implement additional components that exist in a concrete mixture. As mentioned, concrete is a mixture of cement, aggregate, air-voids and moisture. To add to the complexity of the model, air-voids and moisture content were implemented in order to achieve a more realistic concrete model. As shown in Figures 4.8 and 4.9, air-void and moisture particles were randomly distributed. The model has a spatial discretisation of 1 mm

therefore each particle can be as small as 1 mm. By changing the moisture or air-void percentages we can achieve different medium permittivities. As the half-space's dielectric properties were not constant, the dielectric constant known as the bulk permittivity needed to be calculated. Once acceptable results were obtained from the 2D models, the next and final stage was to produce the same concept but in 3D modelling. As a consequence, we were able to use a real lookalike antenna design such as the GSSI antenna model rather than a theoretical source to excite the model which would add to the validity and reliability of the output results.

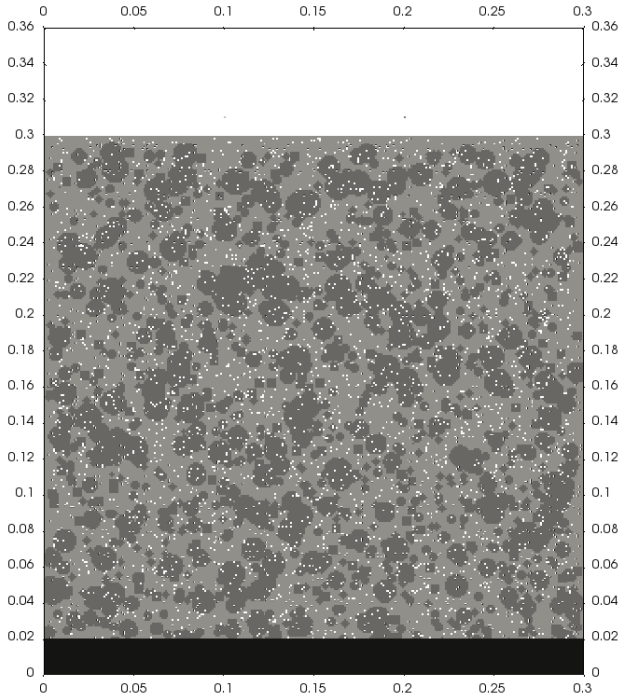

Figure 4.8: Heterogeneous two dimensional model with a mixture of aggregate and air-voids. The domain size (x, y) is 0.3 $m \times 0.36$ m.

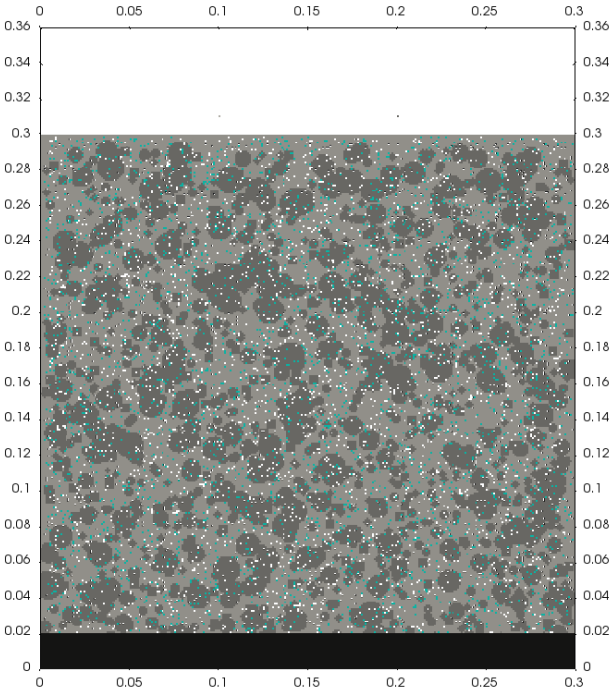

Figure 4.9: Heterogeneous two dimensional model with a mixture of aggregate, air-voids and moisture content.

4.3.1 *Development of a Rock Aggregate*

Aggregates come in different shapes and forms. Another challenge for designing a realistic concrete model was the aggregate shape. Random Polygon shapes were researched and programmed in which with each run, the output was a random shaped Polygon as shown in Figure 4.11. For each polygon a number of points were chosen at random. Each point has a random (x, y) position and radius for a polygon (r). Depending on the number of points, the angle about the centre of the polygon was calculated. For example, in Figure 4.10, their are six points which result in a 60° angle. To find the x and y coordinates of the points the Trigonometric functions were used. Finally, each point was added to a list of points which were then plotted in a window frame.

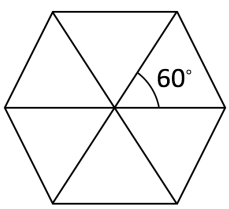

Figure 4.10: Interior angle of a polygon calculation. 2π divided by the number of points. Here there are 5 points resulting in the interior angle to be 60 degrees.

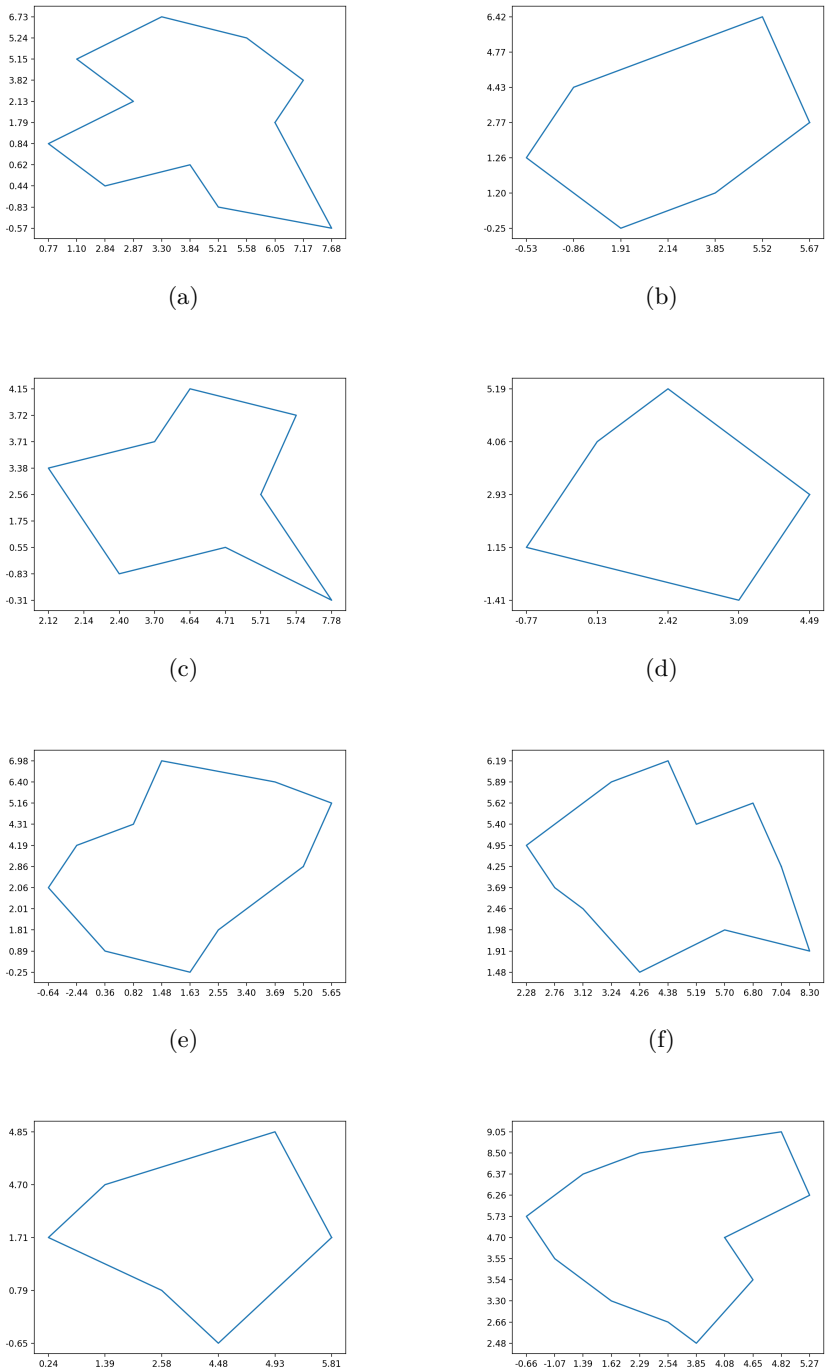

Figure 4.11: (a) to (h) shows different shaped polygons produced randomly. More information can be found in Appendix D.3.

The process for generating polygons in gprMax was done by generating a random sphere and picking random points on the sphere to produce a polygon. Figures 4.12 and 4.13 show a Polygon and sphere shaped aggregate produced in gprMax and viewed with Paraview (Ahrens, Geveci, & Law, 2005). To convert a sphere rock into a polygon rock, a polygon fill algorithm was used to fill the polygon based on the random points.

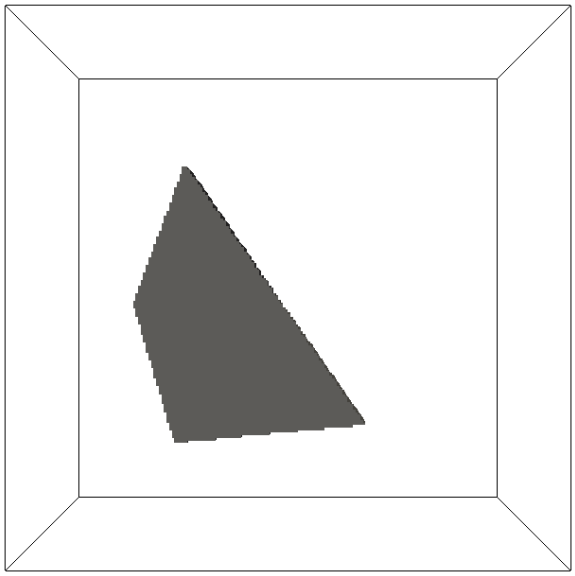

Figure 4.12: Polygon rock.

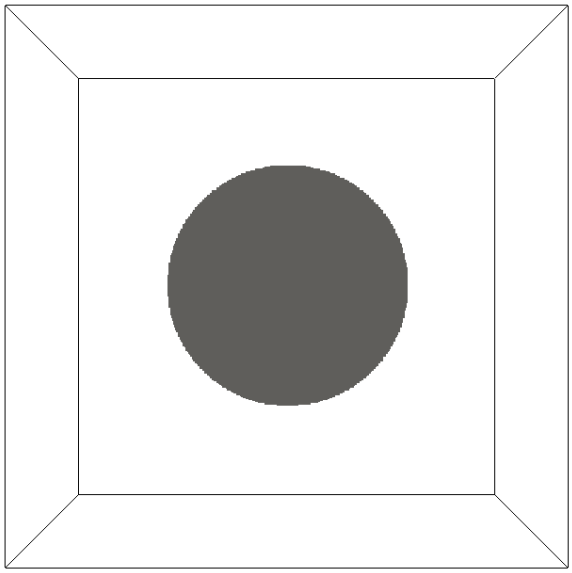

Figure 4.13: Sphere rock.

A 3D model with a domain size of 0.5 $m \times 0.2$ $m \times 0.36$ m and a spatial discretisation of 1 mm was simulated by employing random rocks in the input file using the polygon shape procedure discussed previously. Here, 5000 boxes were generated and the model does not have any losses.

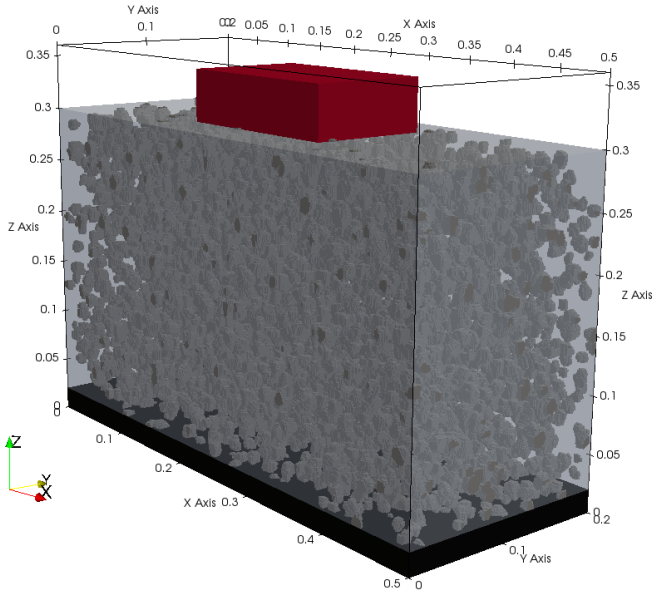

Figure 4.14: Random distributed rocks with relative permittivity of 7 and a background relative permittivity of 3. The model has a PEC target and the simulated GSSI antenna structure placed on the surface.

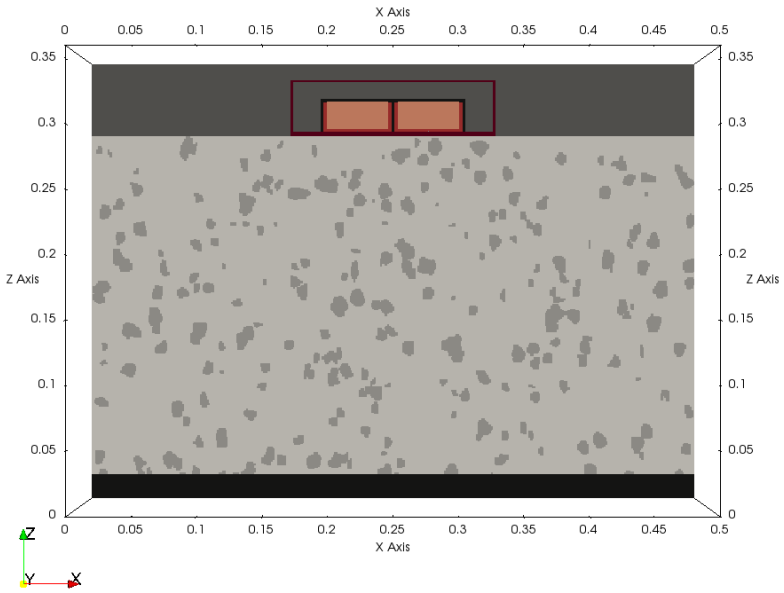

Figure 4.15: A slice of the 3D model shown in 4.14.

4.3.2 *Rock aggregates vs sphere aggregates*

Two 3D models containing polygon and sphere aggregates (Figures 4.15 and 4.18) were simulated and the results are shown in Figure 4.16. The results show a similar output despite the shape of the aggregate. Both models have the same amount of aggregate therefore in regards to the research topic of this study the type of aggregate used can be neglected. The rock aggregates come with some disadvantages. Firstly, it was difficult to calculate the volume of each aggregate hence not able to model a medium with a specific aggregate percentage. Secondly, a much higher computational run-time was needed to produce the rocks thus it was very time-consuming when dealing with a large number of aggregates. Consequently, although the rock aggregate model displays a more realistic concrete but taken into account the limitations and the fact that the results were similar to the sphere aggregates, in this study, the aggregate modelling were kept as spheres.

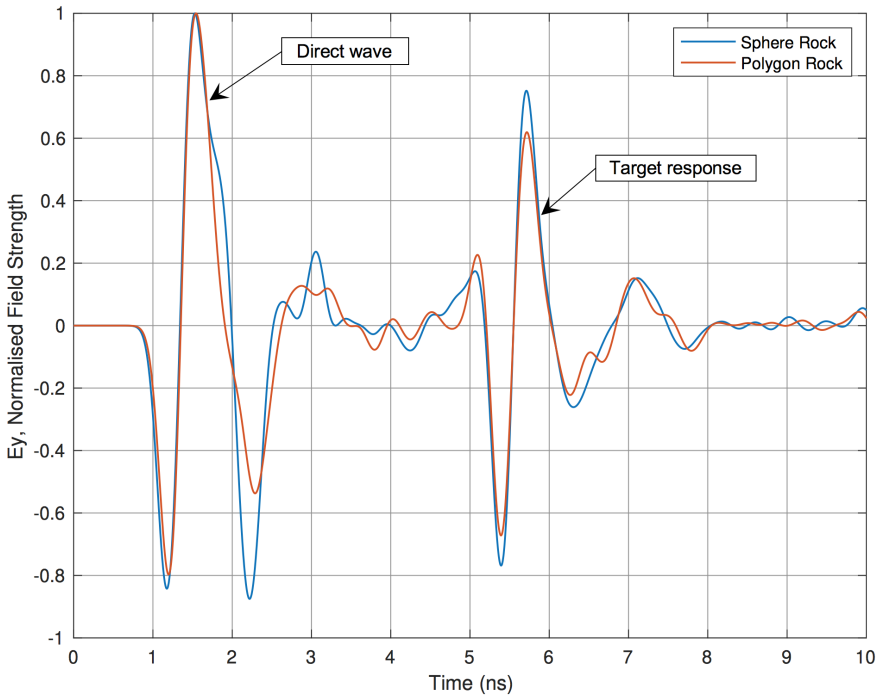

Figure 4.16: Electric field component showing the comparison between two concrete models. One designed with sphere rocks and one with polygon rocks. Both have a PEC target and are simulated using the GSSI centre frequency 1.5 GHz antenna structure as an excitation source.

4.3.3 *Permittivity calculation of complex model*

A complex Refractive Index Model (CRIM) is one of the most used models by GPR users for predicting the bulk permittivity of complex materials like concrete. The most common shape factor of CRIM model is usually $\alpha = 0.5$. By using the CRIM formula we can calculate the bulk permittivity.

$$\varepsilon_b = \left(V_{ag}\varepsilon_{ag}^{\alpha} + V_a\varepsilon_a^{\alpha} + V_c\varepsilon_c^{\alpha} + V_m\varepsilon_m^{\alpha}\right)^{1/\alpha} \tag{4.1}$$

where in (4.1):

ε_b = bulk permittivity of the concrete mixture
V_{ag} = volume of aggregate
ε_{ag} = relative permittivity of aggregate
V_a = volumetric fraction of air-voids
ε_a = relative permittivity of free_space
V_c = volumetric fraction of cement
ε_c = relative permittivity of cement
V_m = volumetric fraction of moisture content
ε_m = relative permittivity of the moisture content
α = shape factor

Material	Relative permittivity (ε_r)
Aggregate	7
Cement	3
Air-void	1
Bond Water	37.54 [1]

Table 4.1: Permittivity of concrete materials.

By using these permittivities and implementing a certain percentage of the material to produce a standard concrete mixture, on average the bulk permittivity output is usually around 8. Increasing the moisture content and air-voids can increase and decrease the permittivity, respectively. This process is used in the further chapters to optimise the shape factor of the CRIM model.

1 (Lachowicz & Rucka, 2017)

4.4 ADVANCED DEVELOPMENT OF THE CONCRETE MODEL

Once satisfactory results were obtained from the 2D heterogeneous modelling using a simple theoretical source, the process continued with 3D modelling and a look alike GSSI antenna (Warren & Giannopoulos, 2011) placed on the concrete surface. The 3D modelling simulation run-time was much higher due to the complexity in comparison with the previous 2D modelling. Therefore, advanced computational resources were needed in order to proceed. However, advantages of this kind of 3D modelling is that it is close to reality, mimics a real concrete slab, adds validity and reliability to the obtained results.

4.4.1 *Homogeneous three dimensional model*

Before adding the heterogeneous complexity to the 3D model, the model was kept simple and modelled as homogeneous allowing to get a better understanding of the antenna's mechanism and practice 3D modelling as shown in Figure 4.17. The model contains a homogeneous half-space with a PEC target at its bottom. The red bod on the surface is a GSSI 1.5 GHz antenna structure. This model is used in chapter 5 to simulate different dielectric constant half-spaces with various targets.

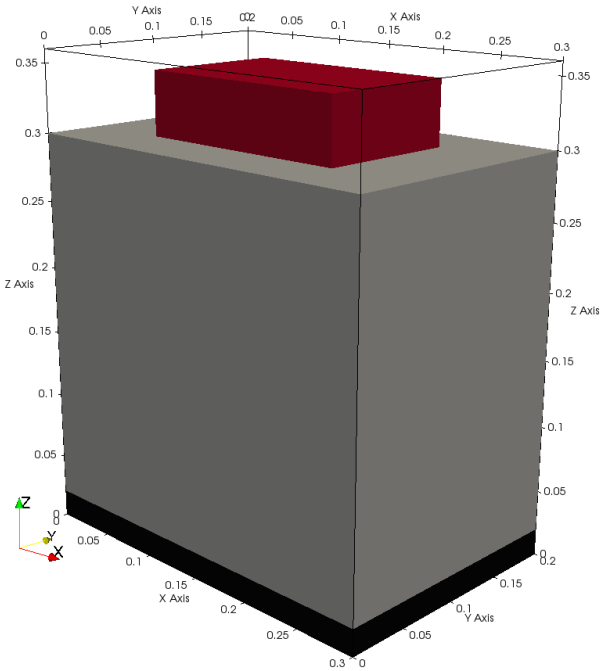

Figure 4.17: Homogeneous three dimensional model with PEC target at its bottom and a GSSI 1.5 GHz antenna on the surface of the half-space.

4.4.2 *Heterogeneous three dimensional model*

This section combines the heterogeneous 2D model with the homogeneous 3D model. As shown in Figure 4.18, the model contains aggregates, cement, air-void and moisture content which were randomly distributed making a heterogeneous concrete mixture. This model is used in chapters 5 and 7 in order to study the time-zero position more effectively and optimise the CRIM model's shape factor. By modifying the model's material percentages, different mixture content with different bulk permittivities were produced. In addition, by knowing the material percentages and permittivities, the bulk permittivity can be calculated and compared with a different bulk permittivity calculation obtained from the TWTT.

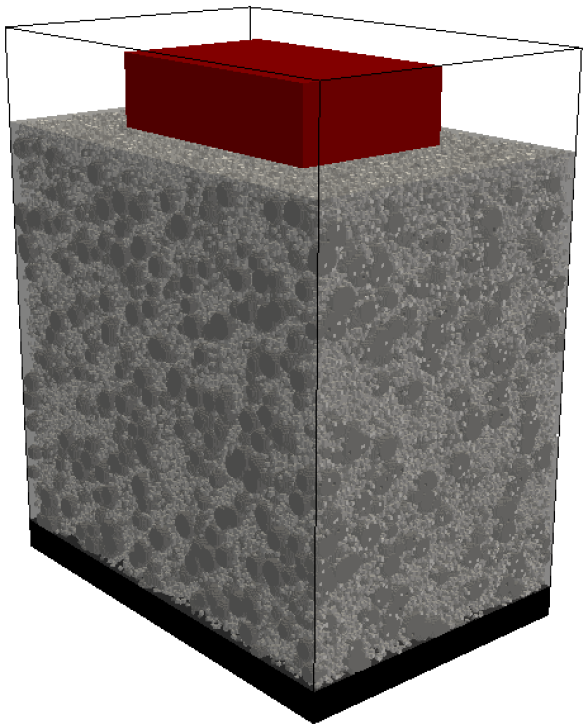

Figure 4.18: Heterogeneous three dimensional model with a domain size (x, y, z) of 0.3 $m \times 0.2$ $m \times 0.36$ m.

4.5 SUMMARY

This chapter focused on the development of a heterogeneous concrete model from a simple 2D homogeneous model to a complex 3D heterogeneous model. This was achieved through numerical modelling in gprMax, visualising the models in Paraview and plotting the output results in MATLAB. The main tasks in this chapter were, the aggregate modelling in which the shape and the way the aggregates are distributed were researched and compared, the air-void and moisture content addition and distribution and having the appropriate computational resources, the study was able to move into a 3D modelling scenario and make use of the GSSI 1.5 GHz antenna model.

5 GPR TRUE GROUND SURFACE (TIME-ZERO)

This chapter investigates the time-zero adjustment extensively. This correction can help predict the depth of targets more accurately with minimum amount of error. The investigation is accomplished by simulating a number of different target shapes, material, various half-space permittivities and the use of different antenna structures. Complex heterogeneous models such as the concrete model designed in chapter 4 are also taken into consideration.

5.1 INTRODUCTION

Time-zero or the true ground surface for GPR applications is a very important aspect and essential factor in order to carry out accurate shallow depth measurements. The transmitted and received signals from GPR antennas are affected by different materials with various dielectric constants and electromagnetic properties. This chapter uses numerical modelling of GPR using the FDTD method in order to study the best location for time-zero on a GPR trace. Time-zero can be placed at different positions on the direct wave. Some easy and obvious positions can be the positive peak, negative peak, mid-amplitude point, and the first break position. Using any of these positions gives a slight different result which may increase or decrease the accuracy of the thickness or depth of the target. With signal processing and different time-zero corrections, the precision of the results can be adjusted. This chapter investigates different approaches to propose a time-zero position that works for the majority of cases with consistent levels of error that are not strongly dependent on the target's response. The research starts with the simplest homogeneous model and moves to a more complex heterogeneous model in order to investigate the effect of time-zero adjustment in different environments. Finally, this chapter proposes a robust time-zero position which allows to get consistently accurate results. The results have been verified in practice by experimental work.

5.1.1 *Initial time-zero investigation*

Initially, to investigate the correct time-zero position a simple model was used. A PEC plate was placed at the base of the model and the distance between the GPR antenna and the PEC target was reduced by moving the GPR antenna closer to the PEC plate in regular intervals. The TWTT between the direct wave and reflected signal amplitudes for different distances were calculated. The time-zero was positioned at

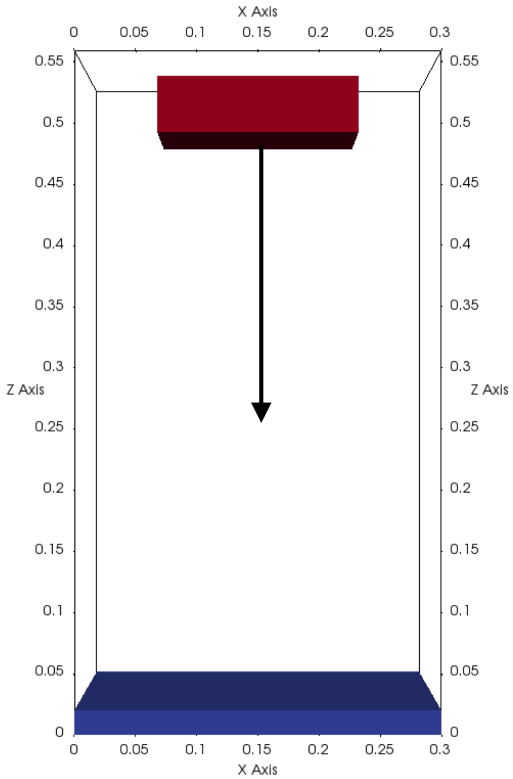

(a)

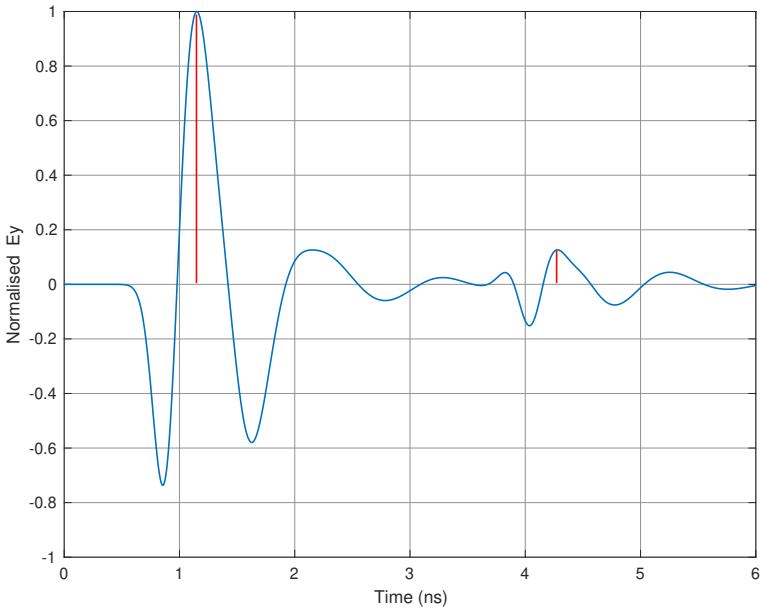

(b)

Figure 5.1: A simple technique to measure two way travel time is by placing an antenna above a PEC target in air at different heights (5.1a). This results in a direct wave wavelet and a single reflection from the target (5.1b). The positive peaks, as indicated by the red lines, are set as the measure points.

different easily to pick amplitude points such as the local maximum and minimum of the received wavelets and TWTT measurements from different positions were recorded. This allows to evaluate which time-zero position results in the best estimation with a minimum amount of error correction and most importantly consistency throughout the data collection.

This replicates what often other researchers such as Yelf (2004) used to establish the change of measurement of the two-way travel time when the antenna is above the ground. However, once such simple model has been used, the modelling can help us investigate more complex scenarios. As shown in Figure 5.1a, the antenna was placed in air above a PEC target and the TWTT was measured for different heights. This is the easiest way to measure the TWTT as there is only a single simple environment. The TWTT was taken from the positive peak of the direct wave to the positive peak of the reflected wavelet as suggested in (Yelf, 2004).

5.1.2 *Different antenna height comparison*

The results of the antenna moving towards the PEC plate is shown in three stages in Figure 5.2. As the antenna was moved towards the PEC target, a measurement from the two positive peaks, one of the direct wave and one of the target reflection were taken to calculate the TWTT. However, as the antenna moves closer to the target, the direct wave mixes with the target's response (distorted signal), which makes the TWTT hard to be measured.

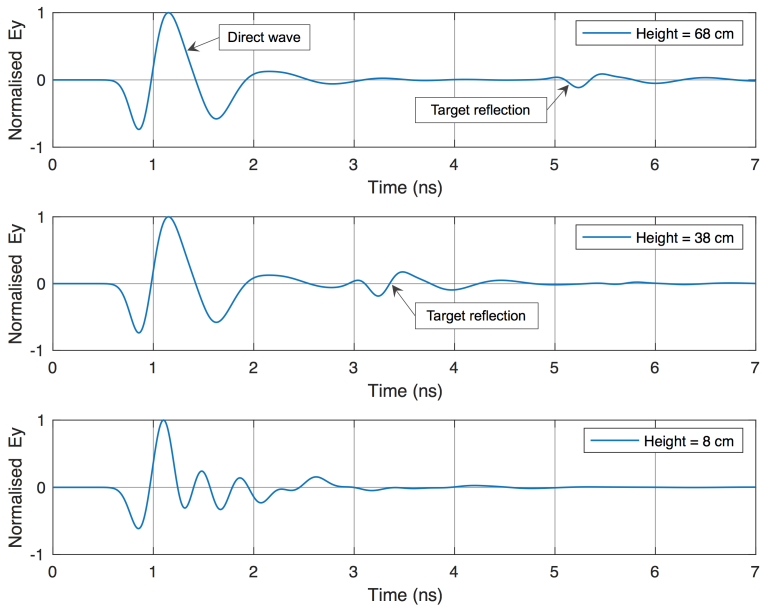

Figure 5.2: Electric field component amplitude when an antenna is moving towards a PEC target in steps of 2 *cm*. As the antenna gets close to the target the signal gets distorted (height=8 cm).

5.1.3 *Direct wave removal*

When the antenna reaches very close to the target, it is very hard to separate the direct and reflected waves, therefore, we cannot easily - in practice - follow the same procedure of obtaining the TWTT down to zero distance. However, in numerical modelling, we can subtract the background solution without the PEC target from the full model solution and obtain just the target reflected response. With this process in mind and assuming that the direct wave arrival is not changing a plot of the TWTT can be calculated even when the antenna is very close to the target as shown in Figure 5.3

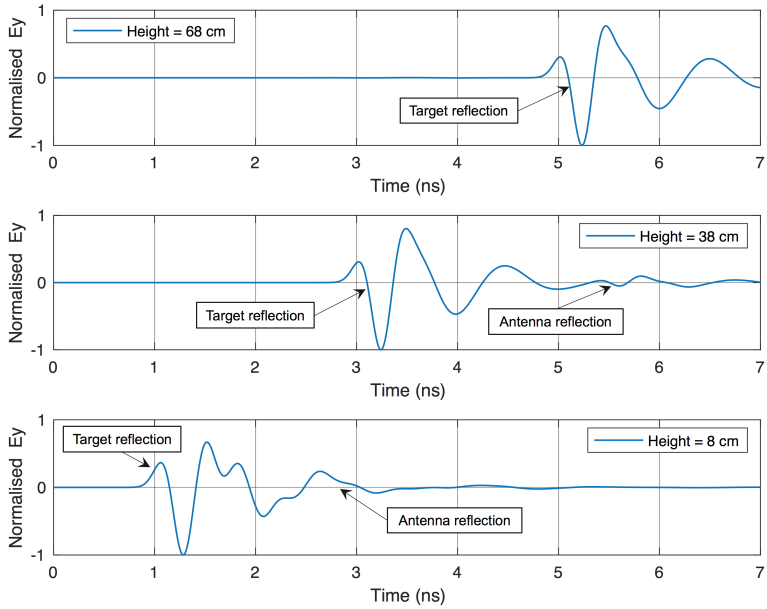

Figure 5.3: Figure 5.2 with the direct wave removed. The reflected wave travelling towards the antenna gets reflected back to the target due to the antenna structure, acting as a target. Here, is shown as the antenna reflection.

The numerical modelling results of the TWTT can be compared with the theoretical result obtained following the formula as shown in equation (5.1).

$$t = \frac{2\sqrt{h^2 + l^2/4}}{v} \tag{5.1}$$

Where t is the TWTT, h is the distance between the antenna and the target, l is the separation between the GPR transmitting and receiving antennas and v is the velocity of propagation.

5.1.4 *TWTT measurement comparison*

By removing the direct wave the target reflection can be easily identified and the TWTT measurement can be achieved. The results of the TWTT as obtained from the antenna movement and the theoretical result obtained from the formula 5.1 are presented in Figure 5.4. The theoretical result and the simulated results were in good agreement as expected from such a simple model.

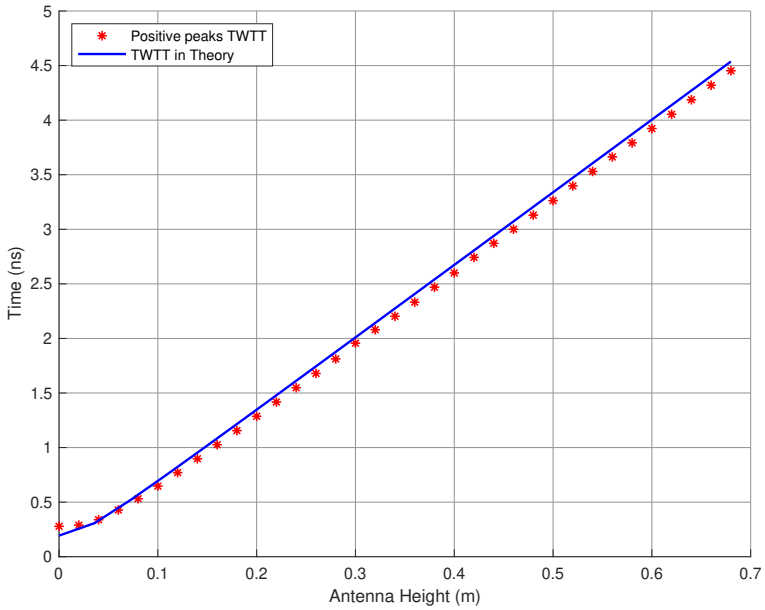

Figure 5.4: The two peaks used for the TWTT for the modelling results are the two positive peaks as suggested in Yelf's 2004 paper. The simulated results are compared with theoretical results obtained by formula 5.1.

5.1.5 *Antenna on and above surface*

However, using such a simple test to determine TWTT raises some concerns. Firstly, when placing the GPR antennas on the interface between two media as it is normal for GPR, the direct wave is expected to be affected by the ground surface as shown in Figure 5.5b. Secondly, selecting the two positive peaks for measuring the TWTT is arbitrarily decided in this case and might not be the best practice for different targets and antennas. So, in the following the GPR antenna was positioned on the surface of a half-space and the target was moved rather than the antenna as Figure 5.6 represents.

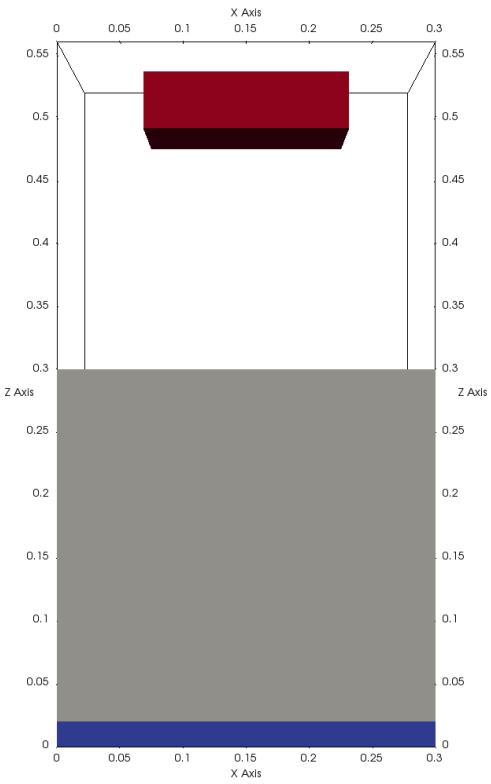

(a)

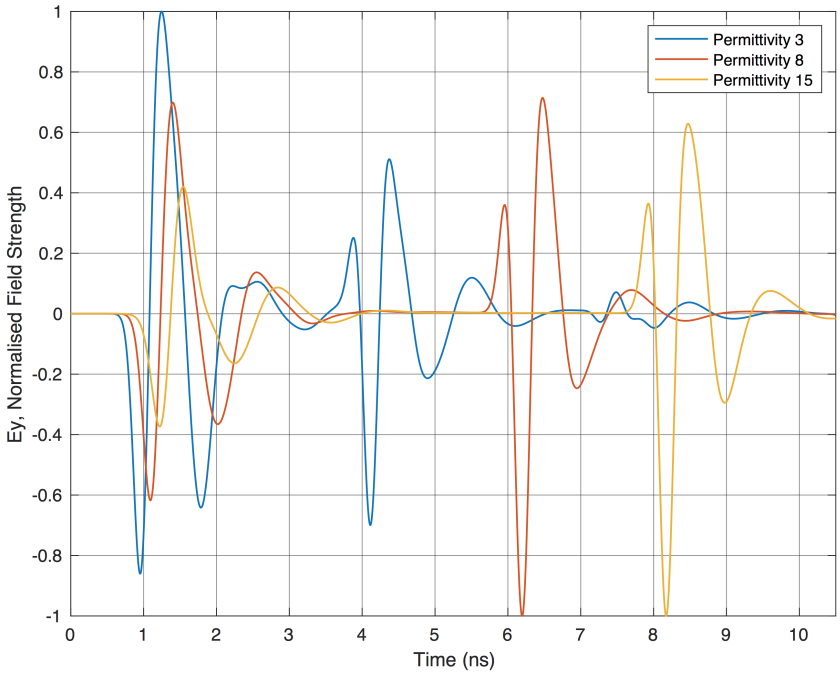

(b)

Figure 5.5: 5.5a represents the GSSI antenna above the ground surface (0.2 m) with a PEC target located at the bottom of the model. 5.5b shows the simulation results. Different relative permittivities were used to observe the impacts on the propagating wave.

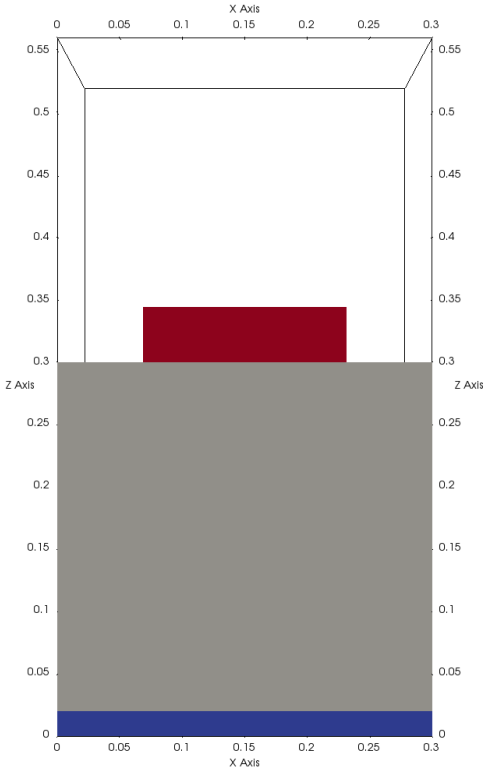

(a)

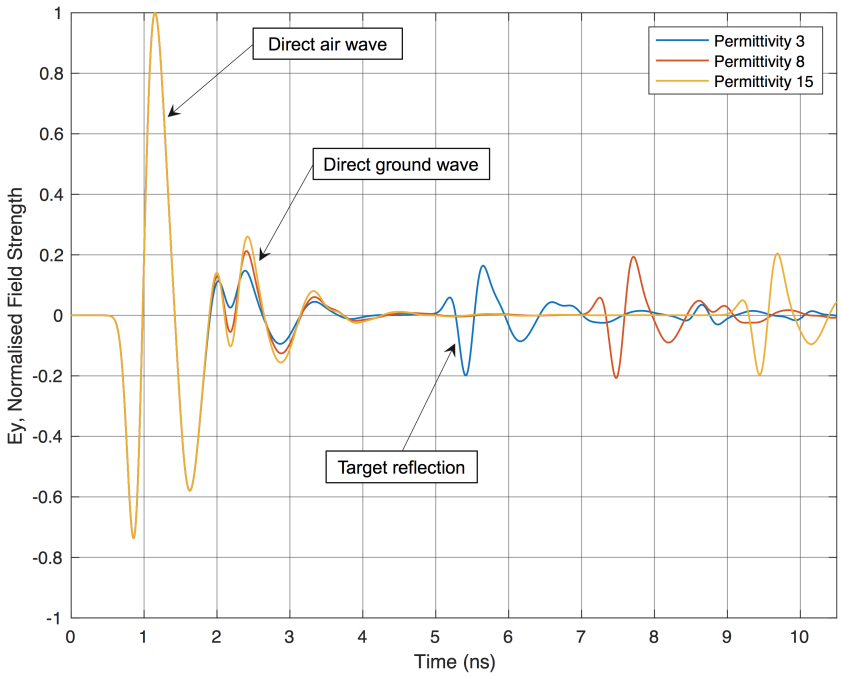

(b)

Figure 5.6: 5.6a shows the GSSI antenna on the ground surface with a PEC target. 5.6b shows the results of 5.6a simulation using different relative permittivities.

5.1.6 *PEC target TWTT*

GPR reflected signals have different wavelet shapes which mostly depend on the electrical properties and composition as well as the shape and extent of the target. They are also dependant on the dielectric contrast between the target and the background material. Variations in contrast often cause some of the wavelets to be inverted when compared to similarly shaped targets at similar depths. This is simply evident when responses from a PEC target and an air-void are compared. Changing the polarity of otherwise similarly shaped wavelets creates a problem in establishing the correct place for measuring the TWTT as most times it is not expected that the kind of received GPR wavelets are known *a priori* when collecting data in the field. In other words, the methodology that is based on picking TWTT using a positive to positive peaks will always be in error under certain conditions which are dependant on the unknown target characteristics. This method will be correct in some case and wrong in other therefore it lacks consistency.

In the following, using numerical modelling, numerical experiments was used to develop a process for measuring TWTT that it is reasonably accurate but most importantly robust and reliable regardless of the shape of the received GPR wavelet. To investigate all the possible TWTT peak combinations and determine the most reliable peaks to select, some simple models were used. As an alternative for having an antenna in air above a flat target, the antenna was positioned on the interface between air and a homogeneous environment with a moving target under control as shown in Figure 5.7.

The depth of the PEC target was decreased by moving the target closer to the antenna and monitor the changes and effects it has on the reflected wavelet. As the model (Figure 5.7a) was homogeneous and the electromagnetic properties were constant, the received wave will be visible and easy to process. The time-zero was positioned on the direct wave at four different positions. Positive peak, negative peak, the mid-amplitude point, and the first break position. Firstly, the time-zero was positioned on the positive peak and three measurements were taken with respect to the reflected wave. For example, different depth measurements were taken from the positive peak of the direct wave to the positive peak of the reflected wave (5.8). Next, the same process was repeated for the other time-zero positions. The results of this process are shown in Figure 5.9.

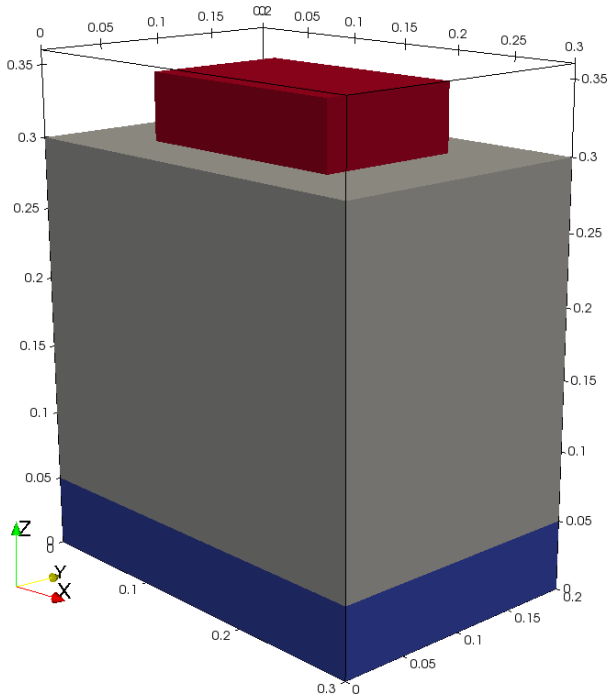

(a)

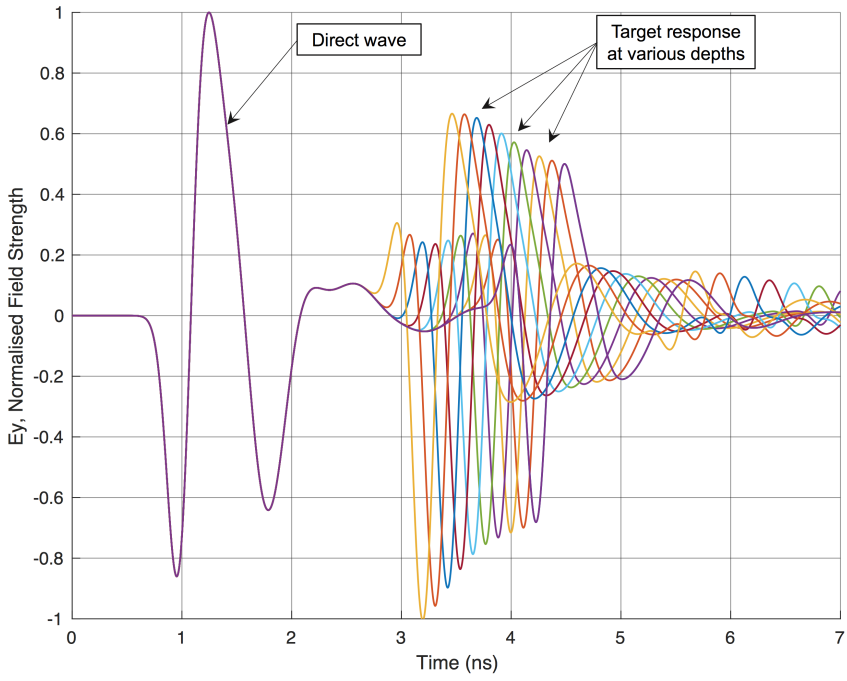

(b)

Figure 5.7: 5.7a homogeneous model with a PEC plate at the bottom and GSSI-like antenna on the surface. 5.7b simulation output showing the direct wave of the antenna and the target reflection at various depths. PEC reflections are an inverted version of the direct wave due to its reflection coefficient ($\Gamma = -1$) (Hussnain & Mughal, 2011).

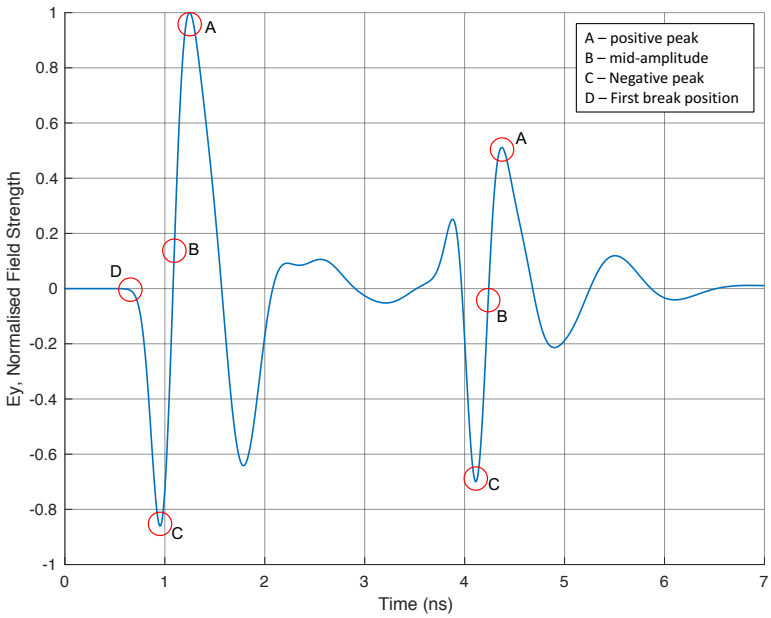

Figure 5.8: Locations of the time-zero position on the direct wave and the TWTT measurement points of the reflected wave.

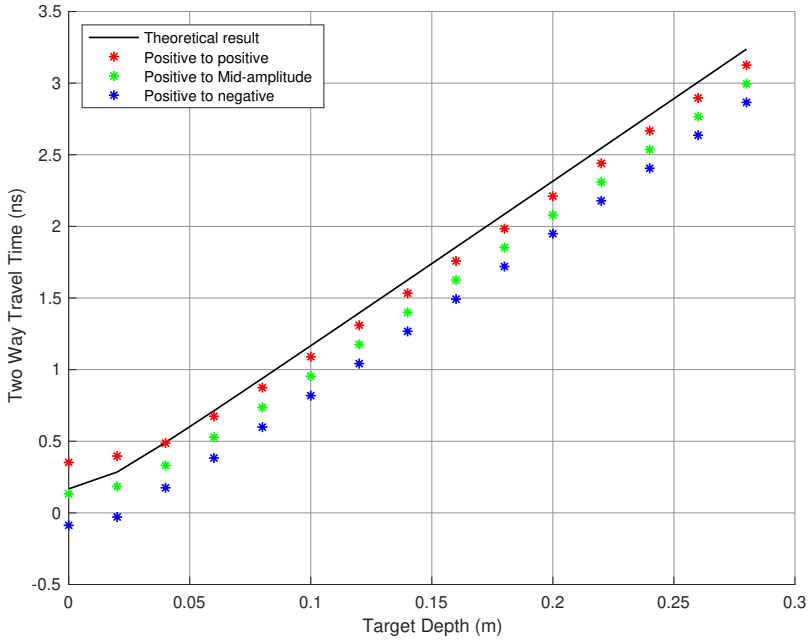

(a) Positive Peak

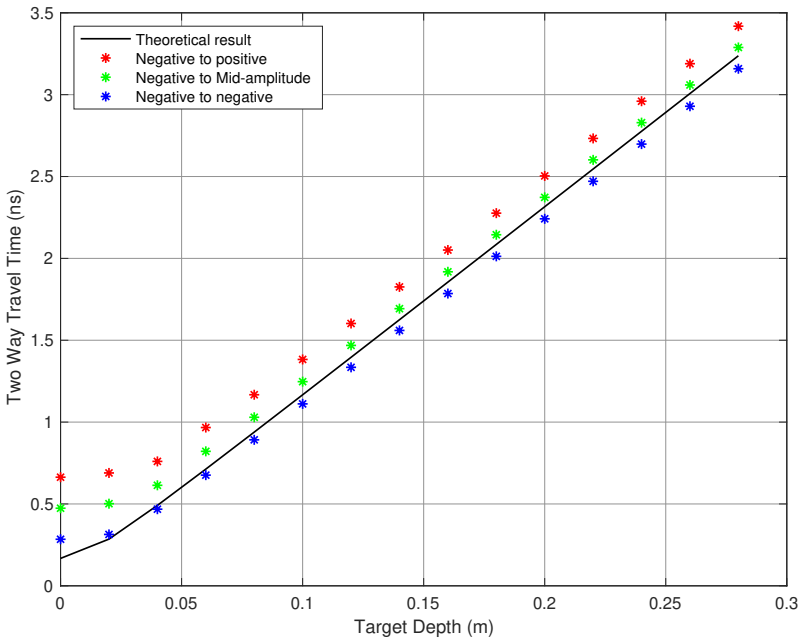

(b) Negative Peak

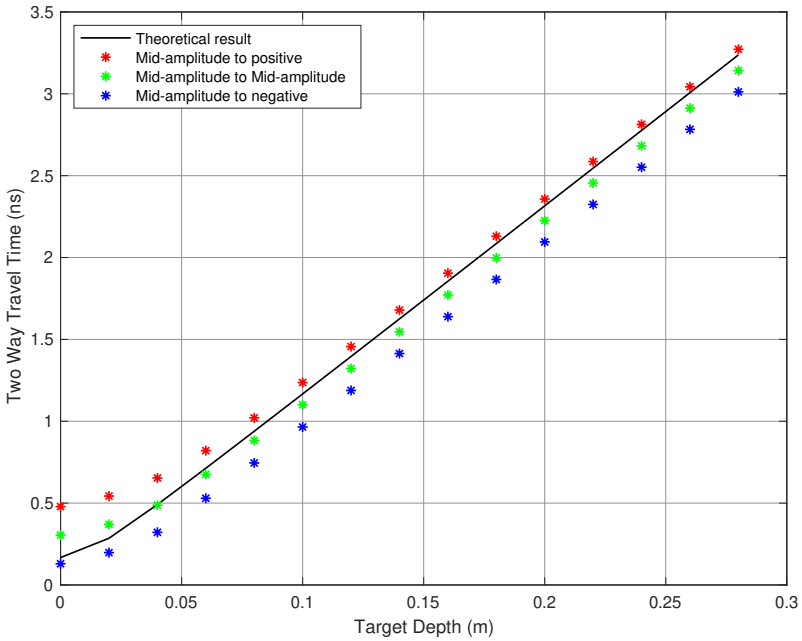

(c) Mid-amplitude Point

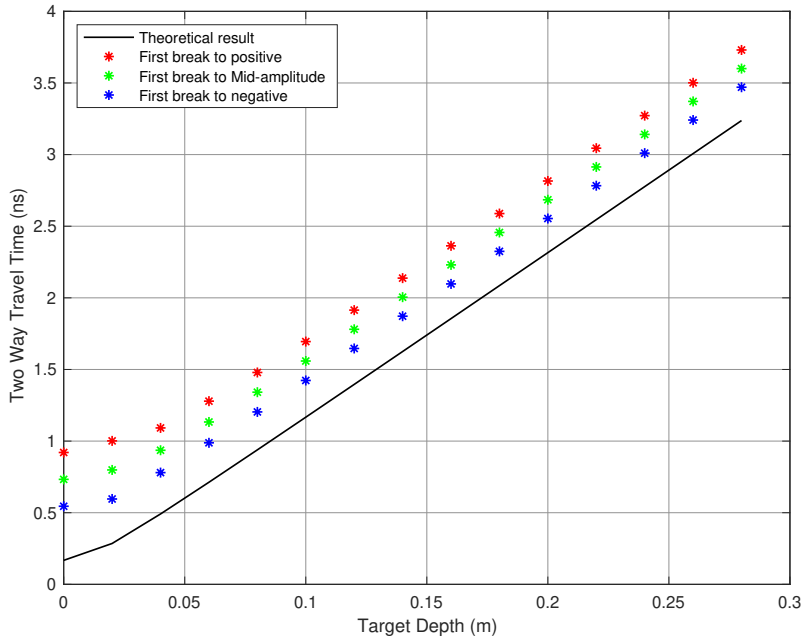

(d) Break Position

Figure 5.9: TWTT comparison for four time-zero positions of the direct wave with three different positions of the reflected wavelet. The results were compared with the theoretical result obtained from equation 5.1.

The results in Figure 5.9 indicate that when the time-zero is set to be the positive peak (Figure 5.9a), the positive peak of the reflected wave gives the best answer as its the closest to the simple theoretical result obtained using 5.1. The other positions introduce some time delay which results in inaccurate depth estimations. Alternatively, by setting the time-zero on the negative peak (Figure 5.9a) of the direct wave, the negative peak of the reflected wave gives another good answer. So far, for the PEC plate target response, the positive to positive peaks TWTT calculation was shown to be one of the most accurate methods. However, this needs to be verified when the target has different electrical properties (e.g. a low permittivity) such as an air-void. Therefore, the PEC target was replaced with air-void as shown in Figure 5.10.

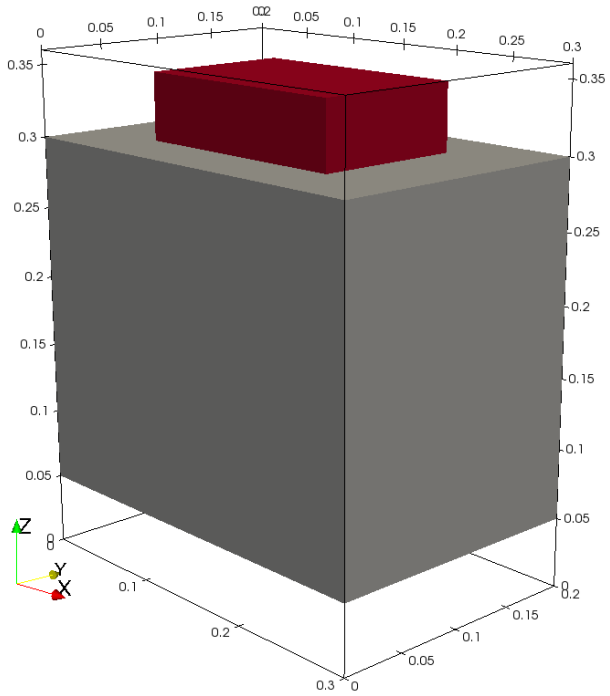

(a)

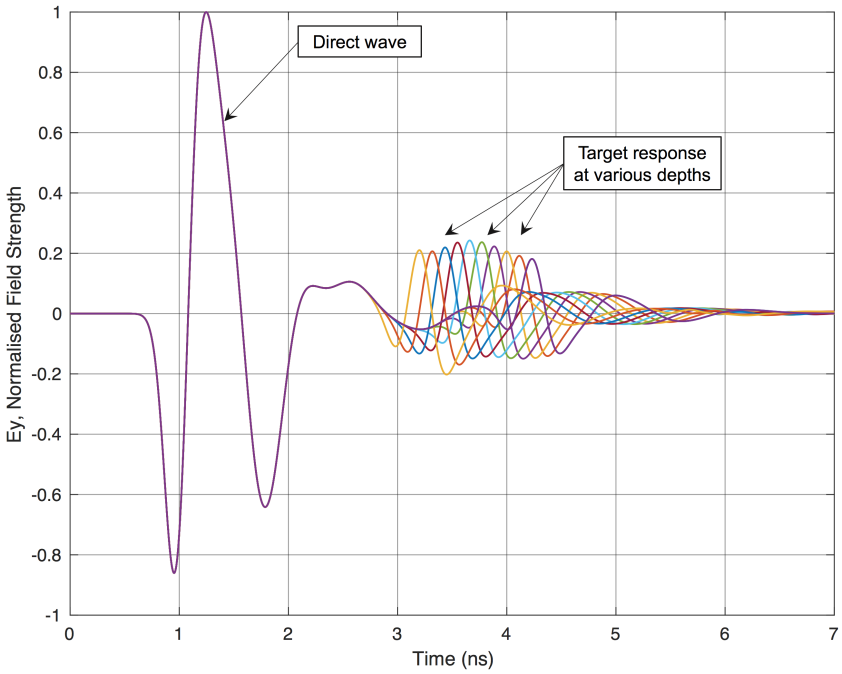

(b)

Figure 5.10: Figure 5.10a presents a homogeneous concrete model with an air-void target at the bottom and a GSSI-like antenna on the surface. Figure 5.10b shows the simulation output of the homogeneous model showing the direct wave of the antenna and the air-void reflection at various depths. Air-void reflections are a non-inverted version of the direct wave due to its reflection coefficient.

5.1.7 *Air-void target TWTT*

Carrying out the same measurement process as done previously, the simulation results presented in Figure 5.11 were achieved. The results show a major difference in comparison to the previous outputs. Closer inspection of the graph shows that the positive and negative outputs have been switched. This means that when the time-zero is positioned on the positive peak of the direct wave, the negative peak of the reflected wave gives the better answer for the depth measurements.

Setting the time-zero on the first break position is not ideal as it is very difficult to detect hence selecting the first break is not advisable in practice. Also, the first break position of the reflected wave in field data might be hard to find and pick the right peaks hence, it is not considered in this study. The results obtained from the two different targets we can state that the mid-amplitude point of the reflected wave can arguably be the safest position. However, in some circumstances, this position is hard to detect.

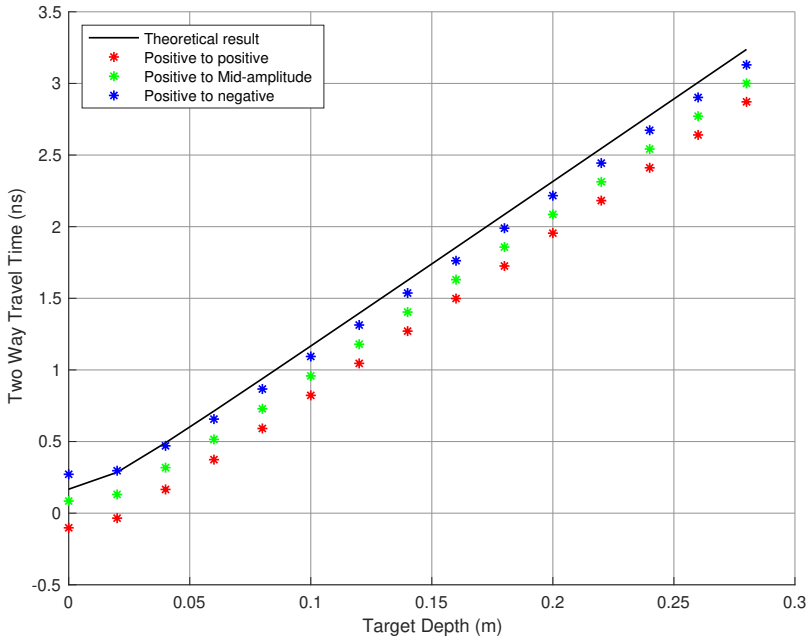

(a) Positive Peak

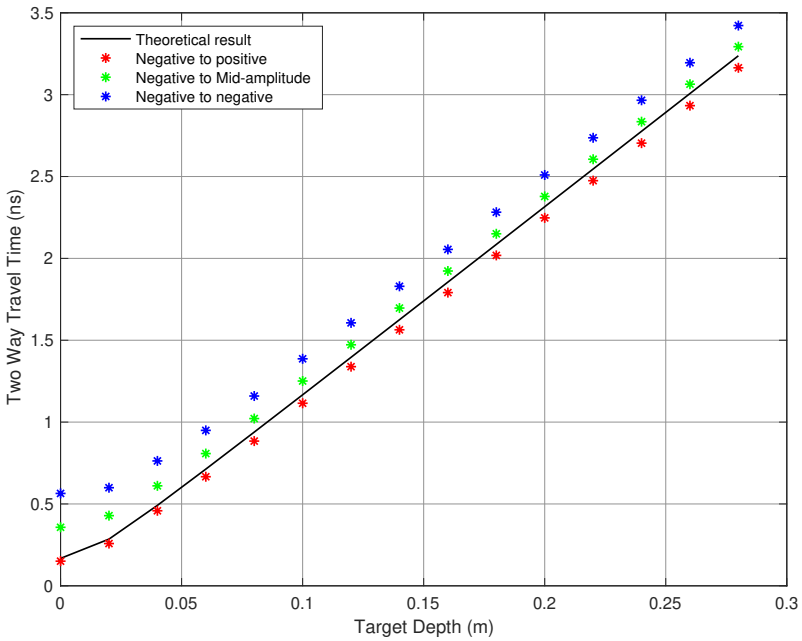

(b) Negative Peak

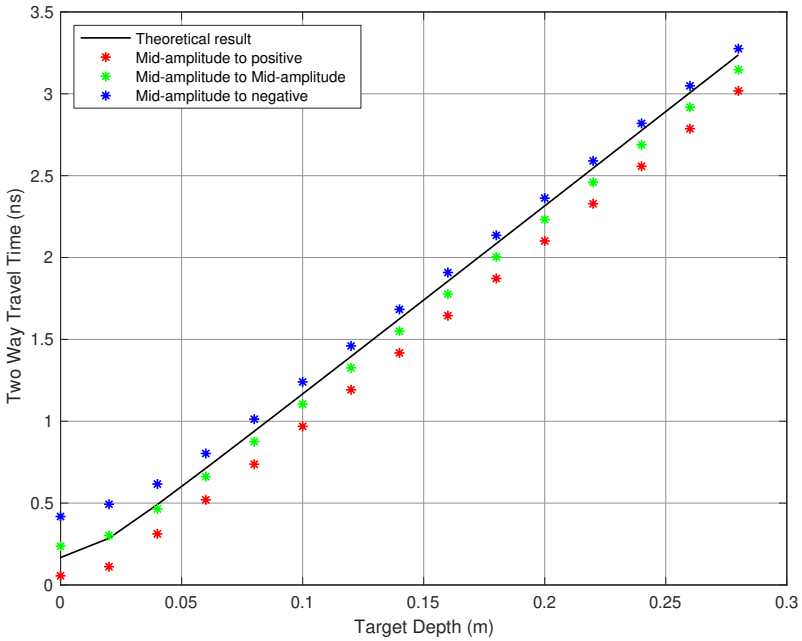

(c) Mid-amplitude Point

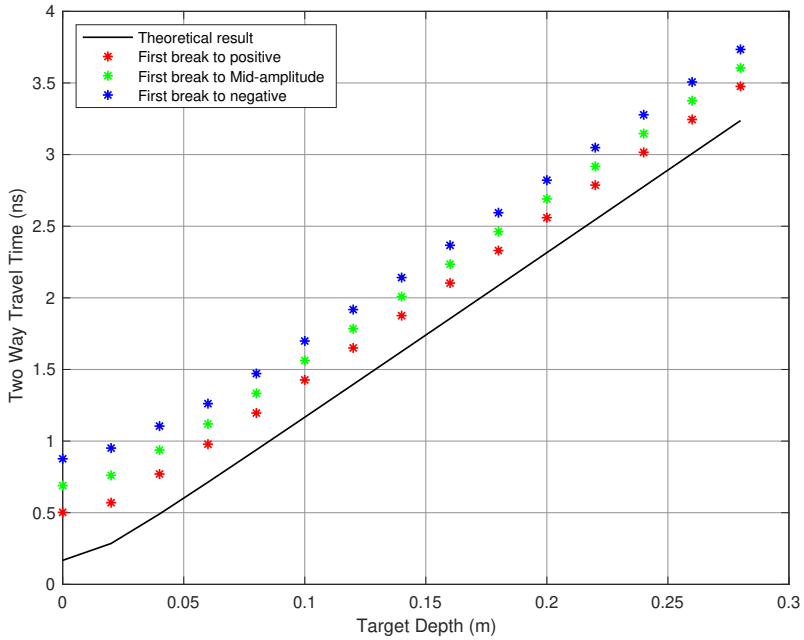

(d) Break Position

Figure 5.11: TWTT comparison for four time-zero positions on the direct wave with the positive peak, negative peak and mid-amplitude point of the air-void target response.

5.1.8 *Mid-amplitude picking*

In regards to a PEC target and the time-zero positioned on the positive peak of the direct wave and TWTT measurements taken from the positive peak of the reflected wave has a good result for the targets depth error. Nevertheless, changing the PEC to a low permittivity target such as air-voids, causes the results to be different. To be more precise, as the reflected wave from an air-void target was an upright version or same as transmitted of the direct wave, the measurements from the negative peak was more accurate. To overcome this issue, the mid-amplitude position can be used to eliminate the inverted or not inverted wave problem. desirably, all GPR users prefer a method that outputs the most accurate result constantly but this is not achievable in most cases. As a consequence, changing the point of TWTT measurement to the mid-amplitude point can arguably be the safest position when dealing with uncertain situations. unquestionably, the target depth error will increase but the increase in the consistency of the error can be the advantageous side. It is important for the depth error to be consistent as an adjustment can be processed and corrected at a later stage. Unfortunately, this position has a disadvantage. Depending on the targets surroundings, material and shape, the negative peaks

(not inverted reflection) and positive peaks (inverted reflection) can differ in amplitude. In some circumstance, the first negative peak was greater than the second peak and vice versa for another scenario. In an automated signal processing, this can cause the wrong peak to be detected. Hence, the wrong mid-amplitude point would be selected resulting in incorrect depth measurement.

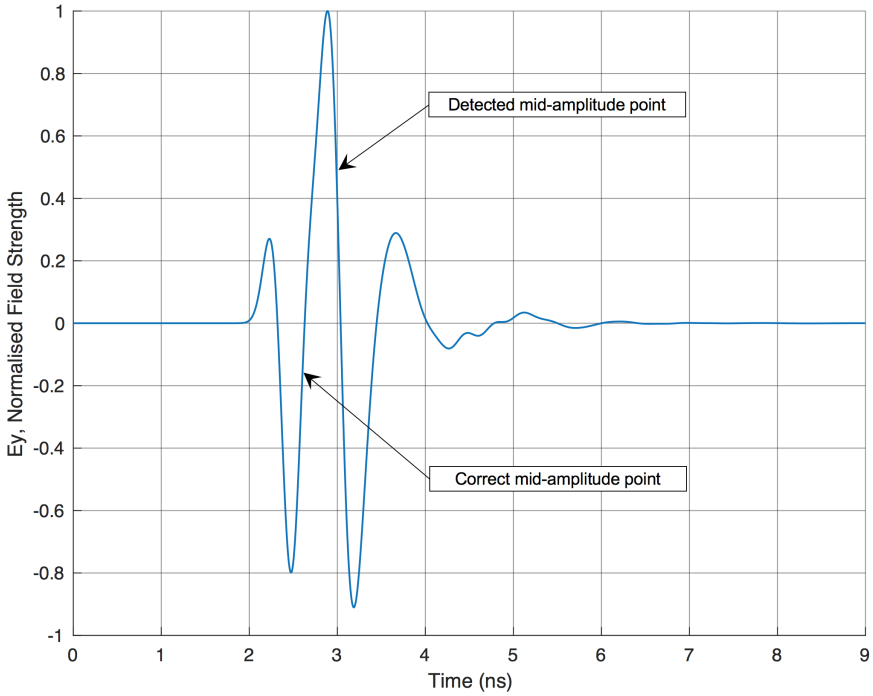

Figure 5.12: A reflected wave is presented that shows how the wrong mid-amplitude point can be detected. For demonstrating purposes the direct wave has been removed.

Figure 5.12 indicates a rare case that might occur during a GPR survey. For detecting the mid-amplitude point, the maximum and minimum amplitudes of the reflected wave were considered for locating the mid-amplitude of the wave. In this particular case, the minimum peak would not be detected because of an existing peak that was greater than the true minimum peak. In an automated processing technique, the wrong peak would be detected and therefore the target depth measurement would be inaccurate. Because of the presented issue, this optimisation process has a weak signature which makes the technique unreliable. In the next section, a methodology is proposed that eliminates this problem and limits the error range further.

5.1.9 *Proposed time-zero adjustment*

In this chapter, a powerful methodology that works for the majority of cases and most importantly it is consistent throughout has been introduced. This methodology proposes a minimum depth error correction

regardless of the target shape, size, material, surrounding environment (half-space) and the target's depth. The technique proposed is to compute the time window mean value for the first three detected peaks of the reflected wave. This method was tested with the time-zero positioned on the positive peak of the direct wave and great depth error consistency was observed. Moving the time-zero to the negative peak of the direct wave showed the same consistency but with a decrease in the calculated depth error. Therefore, the time-zero positioned on the negative peak resulted in the most accurate answer. In this chapter the time-zero position was positioned on the negative or the first detected peak to be more precise and it was kept at this position throughout this framework. The advantages were, it is easy to detect and according to the results, it is consistent and less error correction was needed. Also as stated in (Yelf, 2004), the negative peak position was more stable in comparison with the other positions. Therefore, the final proposal is that the time-zero should be placed on the first peak of the direct wave (in this case, the negative peak) and as mentioned, the TWTT measurements were taken from the mean value of the first three detected peaks of the reflected wave as shown in Figure 5.13.

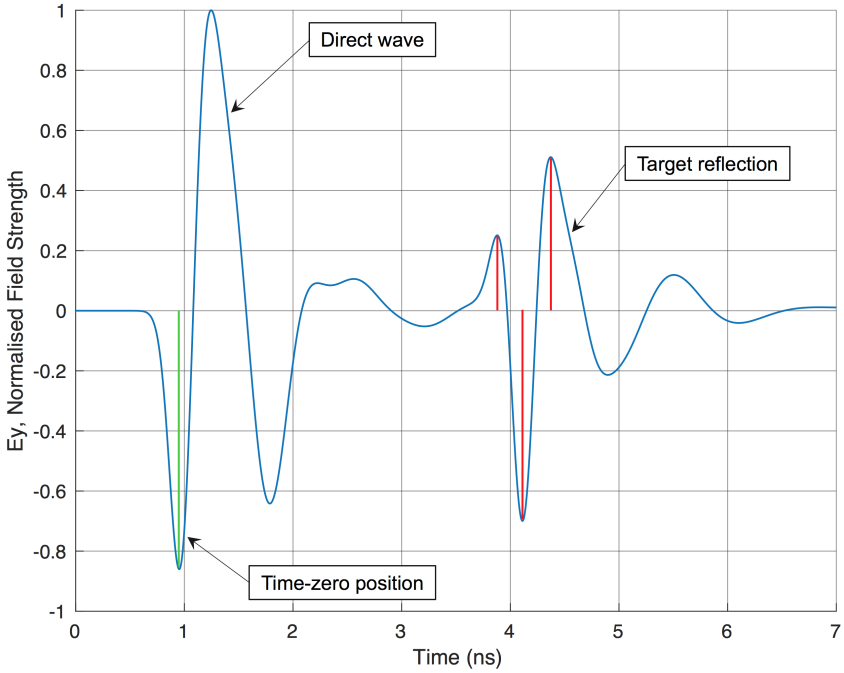

Figure 5.13: Time-zero is positioned on the negative peak of the direct wave (green line). Two way travel time is calculated from the time-zero position to the average time of the three peaks (PEC target response - red lines).

5.2 HOMOGENEOUS 2D MODELS WITH A LINE SOURCE

Initial work began on using a line source with a centre frequency of 1.5 GHz and a homogeneous concrete model with a PEC target. Although this model is not realistic, it is a good starting point. This helps to identify any possible problems before moving on to more complex models. The model has a size of 30 $cm \times 36$ cm with a spatial discretization of 1 mm. The transmitter and receiver were 4 cm apart. The concrete relative permittivity was 3 for the low dielectric case and was also set to 11 to simulate a higher dielectric half-space. This was done to check what would be the half-space effect on the antennas and whether it changes the level of consistency for the depth estimation. Two different targets were used in this scenario. One was a PEC target and one a free-space (air-void) target. These targets cause the reflected wave to be inverted or the same as transmitted (not inverted).

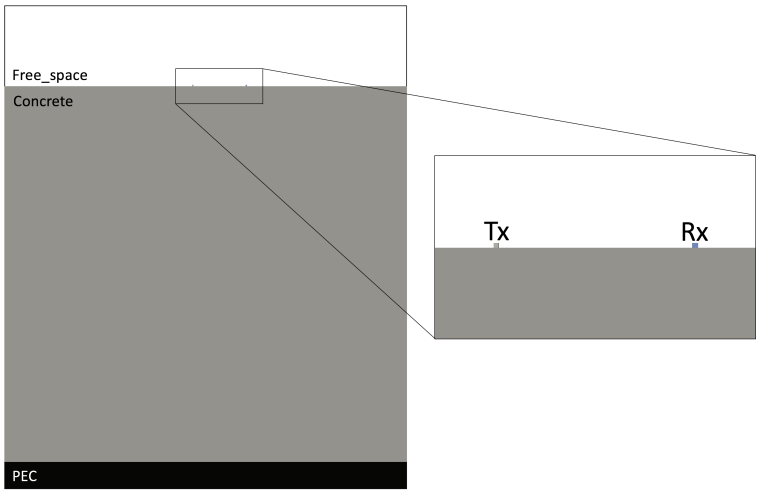

Figure 5.14: Homogeneous concrete model with a PEC plate at the bottom of the model and a line source on the surface. The transmitter and receiver are 4 cm apart and placed 28 cm away from the target.

The outcome result showed great consistency throughout all cases with a depth error of approximately 5 cm. This shows the case that the methodology is working and gives the confidence to move towards more complex models.

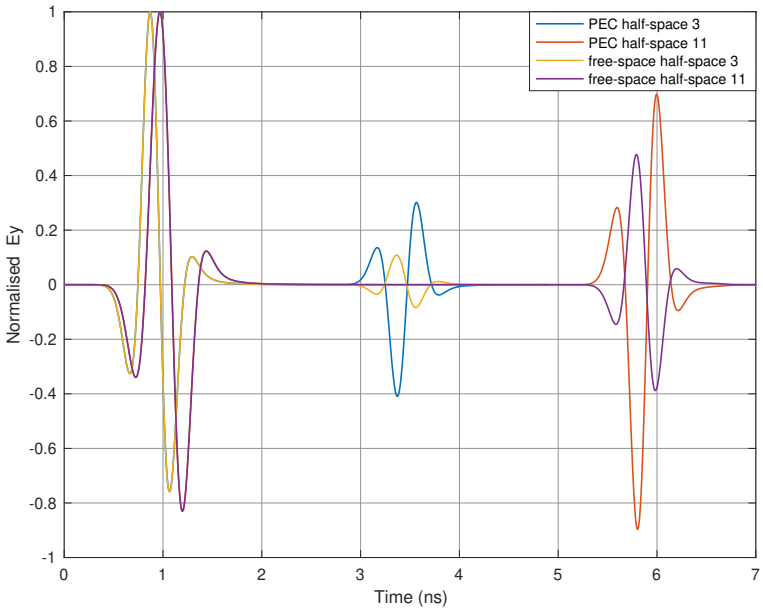

Figure 5.15: Electric field component when using PEC plate and air-void targets with different relative permittivity half-spaces of 3 and 11.

5.3 GSSI ANTENNA ON HOMOGENEOUS MODELS

5.3.1 *Homogeneous model development*

Once a working process was established, we moved on to investigate a number of different targets to see the effect they have on the received wavelet. The next step was to see how the moving target behaves when the environment becomes more complex. To take this technique further, four targets comprised by different materials, shapes, and background material were simulated.

Target shape	Target material	Half-space (ε_r)
Box	Free-space	3
Cylinder	PEC	8
Plate	Silicon	15
Sphere	Wood	23

Table 5.1: Homogeneous model combinations. Each model will consist of a specific shape, target material, and half space. After simulating all the models the outputs are processed to examine the robustness of the methodology proposed.

As shown in Table 5.1, a number of different targets comprised by different materials in various half-spaces at diverse depths were combined, simulated, processed and compared. The targets depth varies from 0.05 m to 0.28 m and the depth was incremented by 0.02 m steps. In this particular section, 64 combinations were simulated with 10 different depths resulting in 640 models. Regarding all the different targets, these cases can be implemented into the numerical framework in order to create a more complete and precise library of targets aimed to be used for evaluating the methodology proposed.

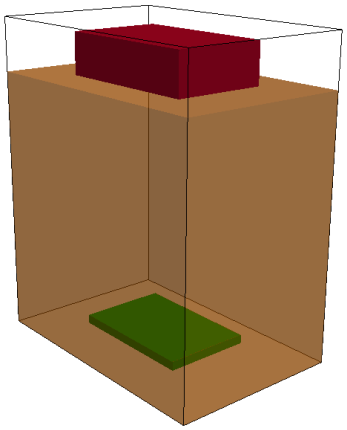

(a) Box target

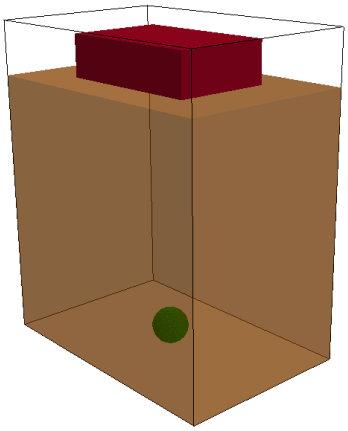

(b) Sphere target

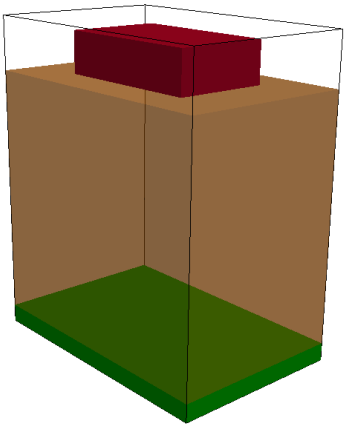

(c) Plate target

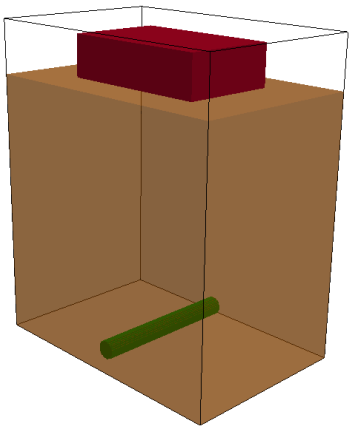

(d) Cylinder target

Figure 5.16: 3D homogeneous models with a half-space relative permittivity of 3 (sand) and various PEC target shapes.

5.3.2 *Simulation results for different target depths*

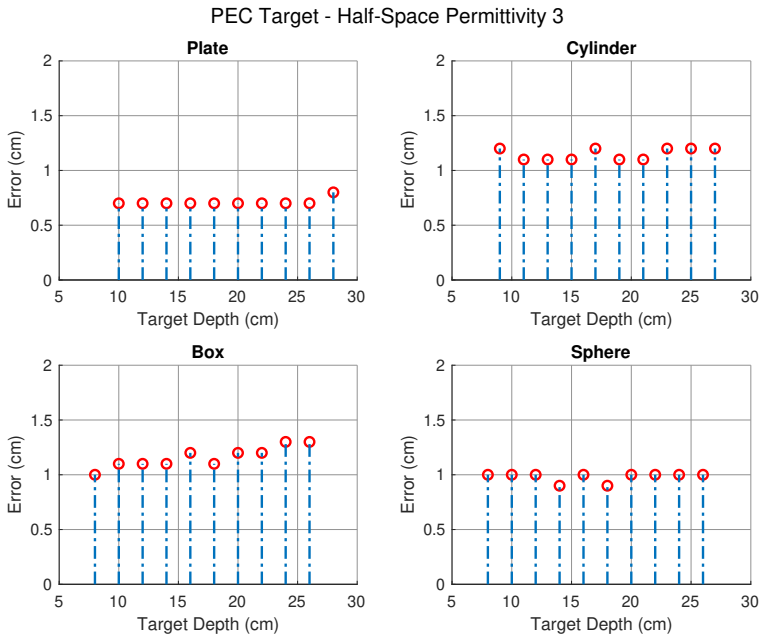

Figure 5.17: PEC targets of various shapes are buried in a half-space with a dielectric constant of 3. Simulations when targets are placed at various depths have been performed and the depth error has been shown for comparison.

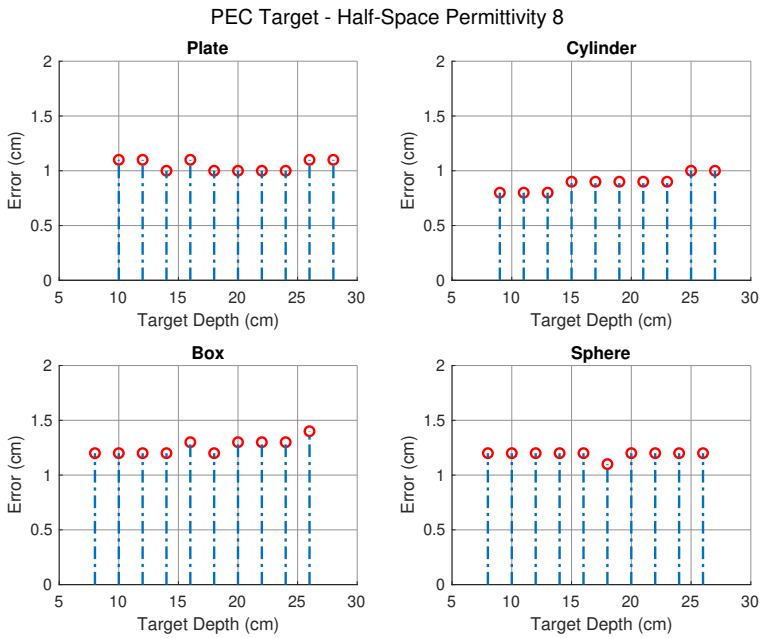

Figure 5.18: PEC targets of various shapes are buried in a half-space with a dielectric constant of 8.

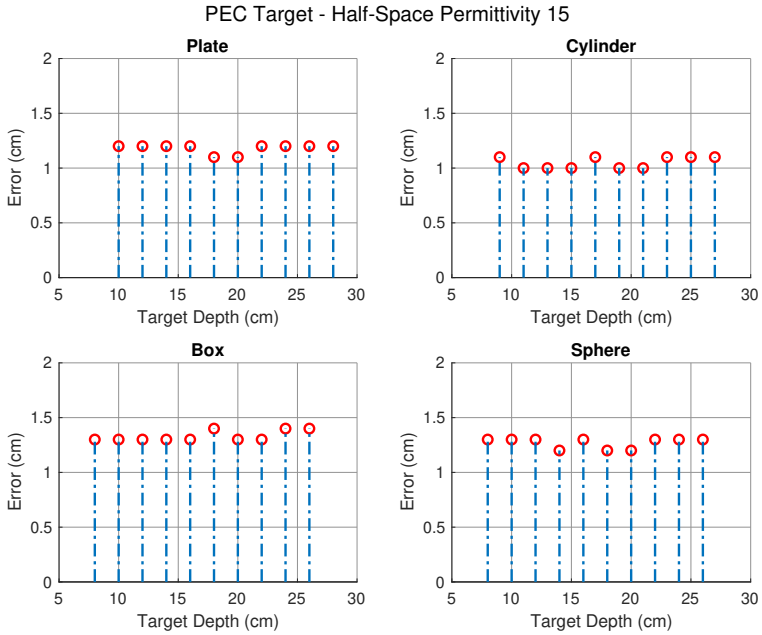

Figure 5.19: PEC targets of various shapes are buried in a half-space with a dielectric constant of 15.

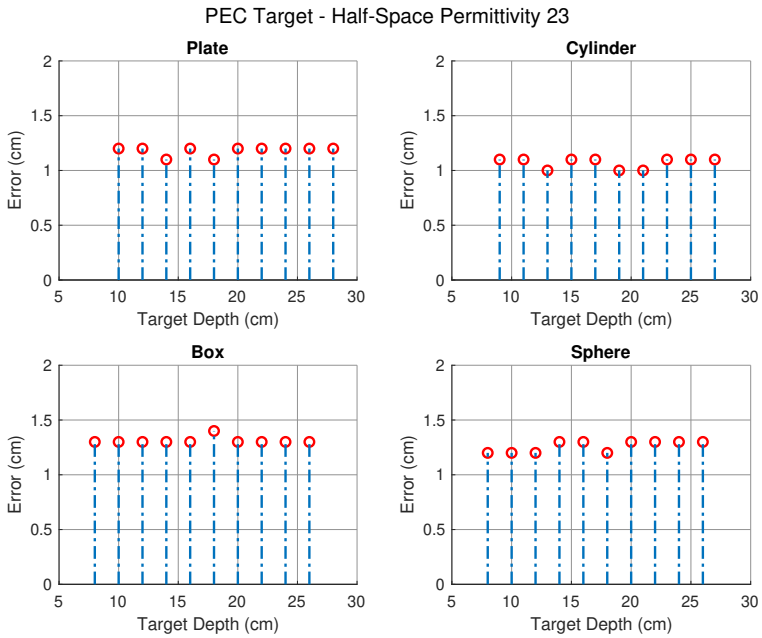

Figure 5.20: PEC targets of various shapes are buried in a half-space with a dielectric constant of 23.

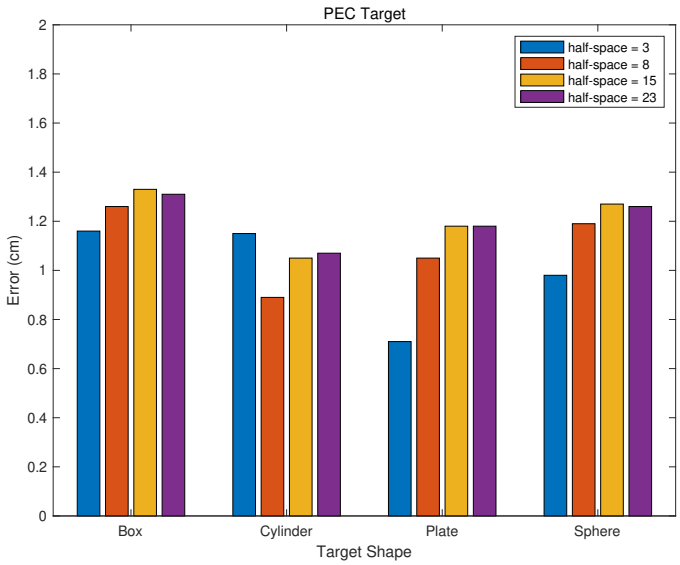

Figure 5.21: An average of all the depth errors for each target shape for all the different half-spaces has been displayed together for a better comparison and to show the consistency of the method. The results show an approximate 4% error range.

The calculated errors were almost consistent and very low throughout the process as shown in Figure 5.17 to 5.20. The remaining graphs are given in Appendix C. Previous methodology proposed by Yelf in (Yelf, 2004), showed that the errors varied due to the wavelet shape and lacked consistency. However, by proposing a better optimisation process, the consistency has increased and the depth errors were low thanks to the correct positioning of the time-zero and TWTT measurement points. Although error correction is still a requirement, the target depth is quite reliable and precise. In regards to the most used methodology by GPR users (positive to positive peak), the results are slightly different. In a particular case, using the positive to positive method, the depth error was better than the depth error resulted from the proposed methodology and in a different scenario, the depth error was inadequate in comparison with the proposed method. Therefore, the positive to positive peaks methodology lacks consistency hence not advisable when working in sensitive environments such as landmines.

Figure 5.22 presents all the different combinations that were simulated. Each column displays an average value of all the errors in a specific framework. Here it is shown that on average the error was around 1 *cm* which allows GPR users to perform error corrections when working with the GSSI antenna structure. The depth error for other types of antenna can be slightly different however with this method being consistent, the processing should be simple. According to the data collection circumstances, this eradicates multiple measurement adjustments hence a faster data processing approach.

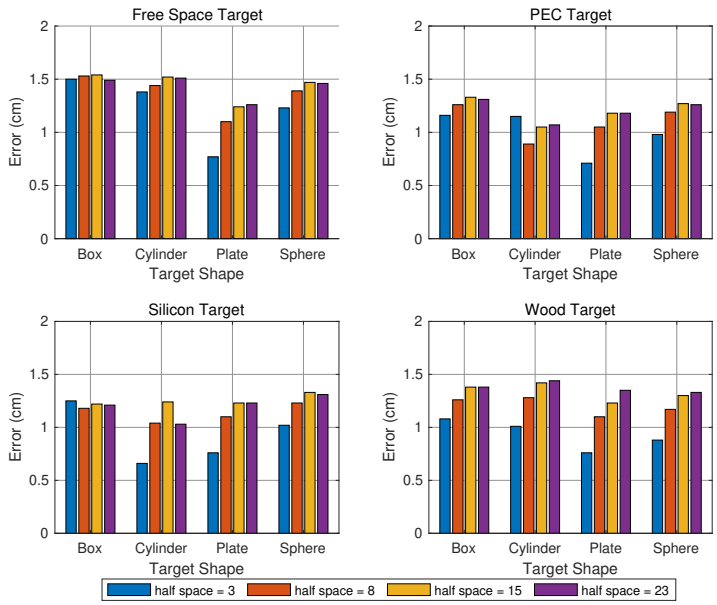

Figure 5.22: Target depth error comparison between all simulated models. The results show a low depth error and most importantly, it presents a good consistency throughout.

5.4 GSSI ANTENNA ON HETEROGENEOUS MODELS

Moving on to more complex models, two heterogeneous models were created in order to achieve a more realistic scenario. This allows to identify any problems that might affect the time-zero position and the output results.

5.4.1 *Concrete Model*

The concrete model is a mixture of aggregate ($\varepsilon_r = 7$), cement ($\varepsilon_r = 3$), air-void ($\varepsilon_r = 1$) and bound water ($\varepsilon_r = 37.54$ (Lachowicz & Rucka, 2017)). The simulated concrete properties were aggregate = 65%, cement = 14%, air-void = 5% and bound water = 16%.

5.4.2 *Peplinski Model*

The Peplinski model is a combination of soil, clay, and water fractions. The soil properties are $\rho_s = 2.66\ g/cm^3$, $\rho_b = 2\ g/cm^3$, $C = 0.5$, $S = 0.5$ and $f_w = 0.001 - 0.15$ where ρ_s, ρ_b, C, S and f_w are the soil density fraction, bulk density fraction, clay fraction, sand fraction and water volumetric fraction variation, respectively.

The models were three dimensional (3D) and have a size of 30 $cm \times$ 20 $cm \times 36$ cm with a spatial discretization of 1 mm. The processing here was more complex in comparison with the homogeneous environment as the bulk permittivity needed to be calculated. By calculating

the velocity of propagation of the signal through the medium, the average permittivity can be predicted and processed. This process was repeated for different material distributions until a more accurate bulk permittivity was reached. Once the bulk permittivity was calculated, the same measurement process that was performed on the homogeneous models, was also carried out for the more complex models. Obviously, as these model were closer to reality, data processing was slightly more challenging due to the clutter responses and variability in the subsurface casing the wavelets to be slightly distorted.

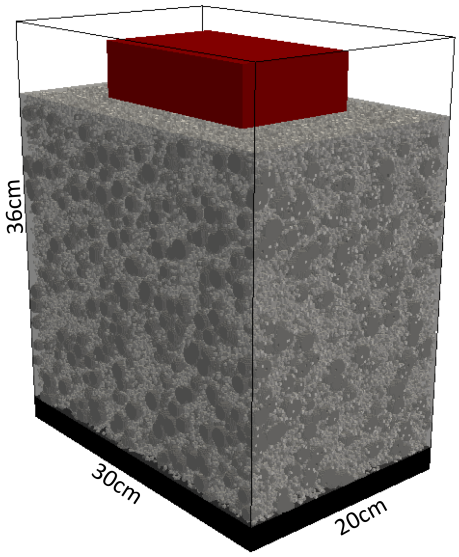

(a) Heterogeneous concrete model

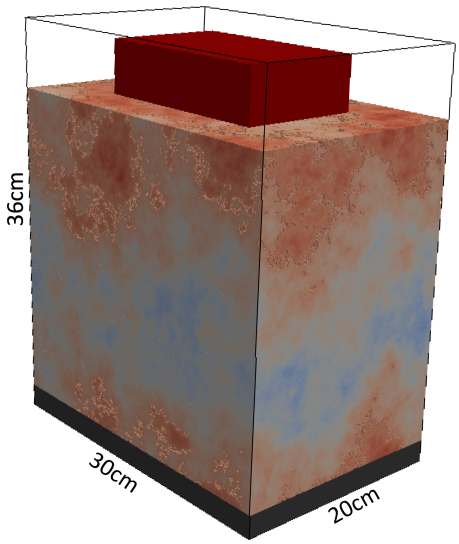

(b) Peplinski soil model ((Peplinski, Ulaby, & Dobson, 1995a, 1995b))

Figure 5.23: Two heterogeneous models viewed in Paraview (Ahrens, Geveci, & Law, 2005) with a GSSI antenna on the surface and a PEC plate placed at the bottom of the model.

5.5 SIMULATION RESULTS

5.5.1 *Concrete model*

Simulating the concrete model with no target resulted in Figure 5.24. As expected with heterogeneous models, there would be clutter responses. For homogeneous models, the velocity of propagation was constant, however, in more complex models the velocity varies depending on the amount of variability in the subsurface.

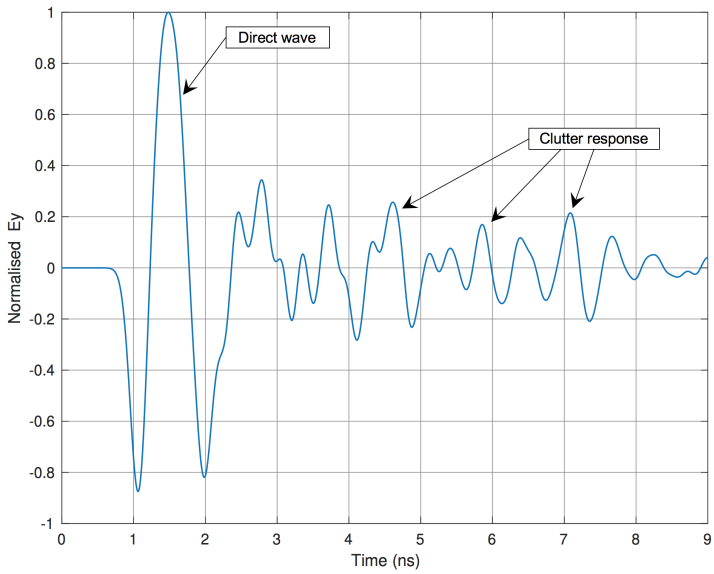

Figure 5.24: The direct wave and clutter response for a heterogeneous concrete model with no target.

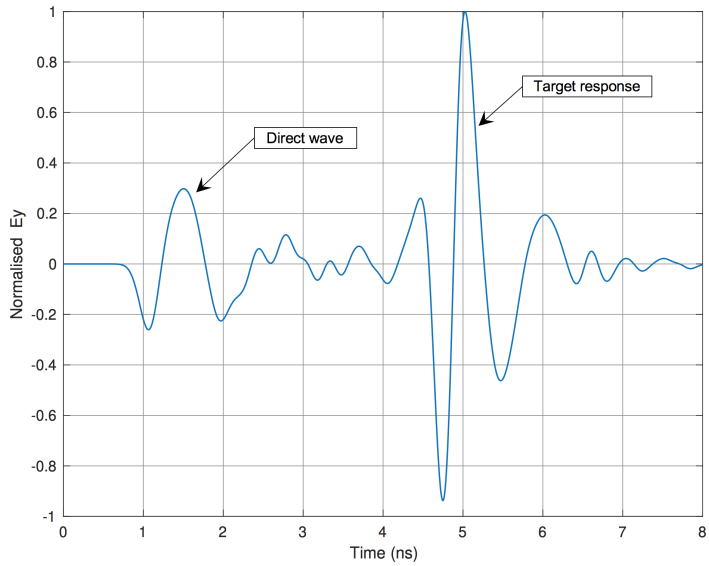

Figure 5.25: PEC target response buried in a heterogeneous concrete model.

In some cases, clutter and antenna ringing effects make it hard to clearly pick the correct wavelets for determining time-zero. Here, the velocity of propagation of the wave was not constant from the antenna to the target, therefore, an average bulk velocity was needed. From the velocity, an average value for the dielectric properties can be calculated along with target's depth estimation.

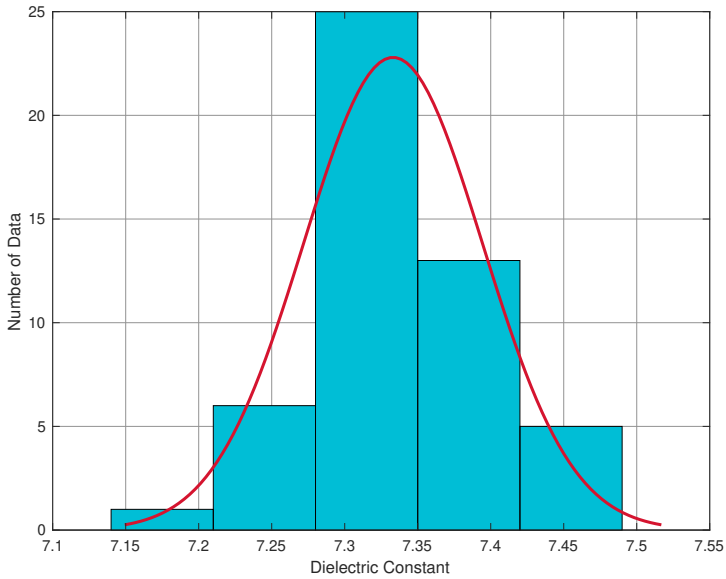

Figure 5.26: Average dielectric properties estimation for a dry concrete.

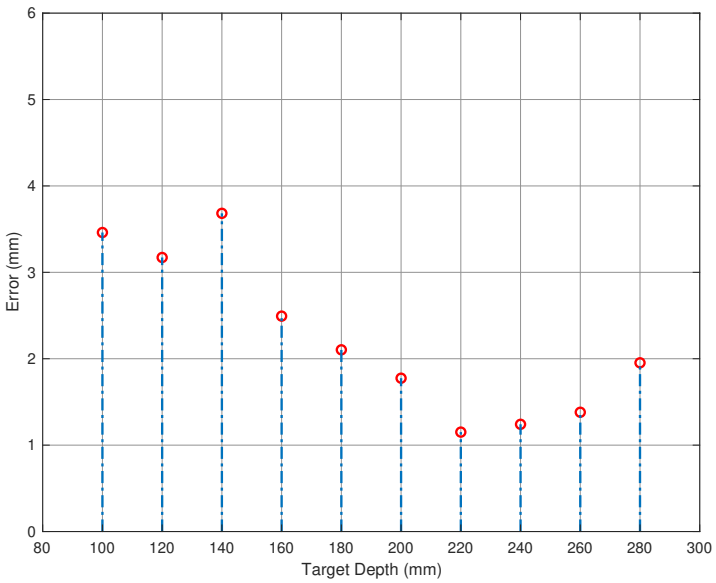

Figure 5.27: PEC target and a bulk permittivity of 7.3.

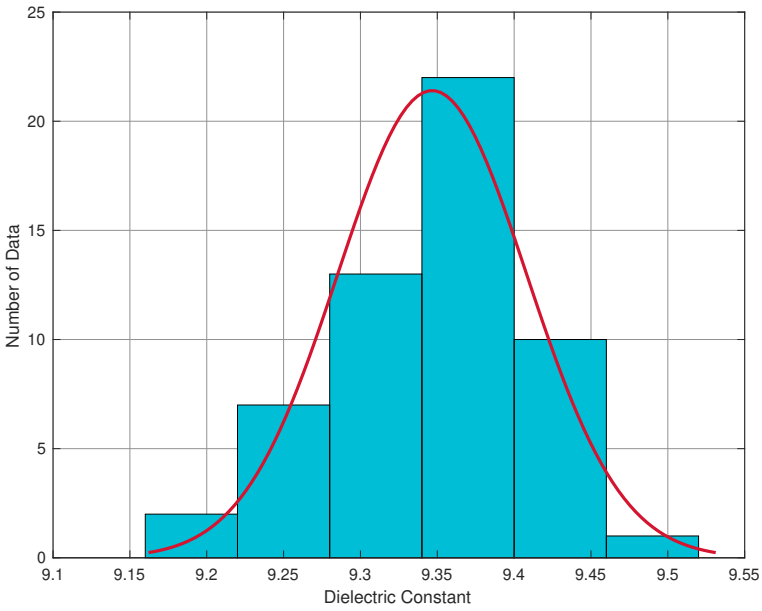

Figure 5.28: Average dielectric properties estimation for a wet concrete.

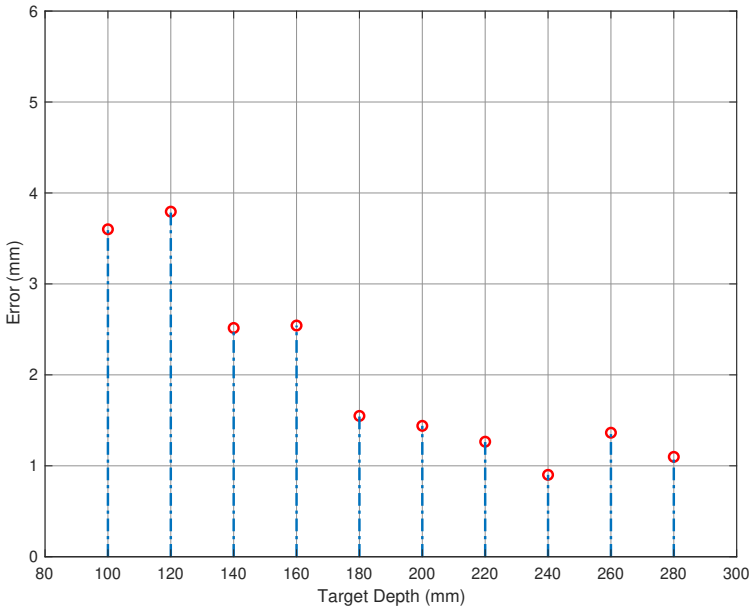

Figure 5.29: PEC target and a bulk permittivity of 9.3.

As shown in Figures 5.27 and 5.29, the depth errors were low and consistent. Figure 5.30, used the previous positive to positive peak method and as shown, the depth errors were still relatively low but higher than the proposed time-zero method. The depth error consistency was slightly poor in comparison with the proposed method hence has low efficiency. Therefore, even in complex situations, the proposed time-zero method has a better performance in estimating the targets depth in comparison to the the previous used methods. As stated previously, in the homogeneous modelling scenario, using different targets changes the depth error significantly. The following chapters will add to this framework.

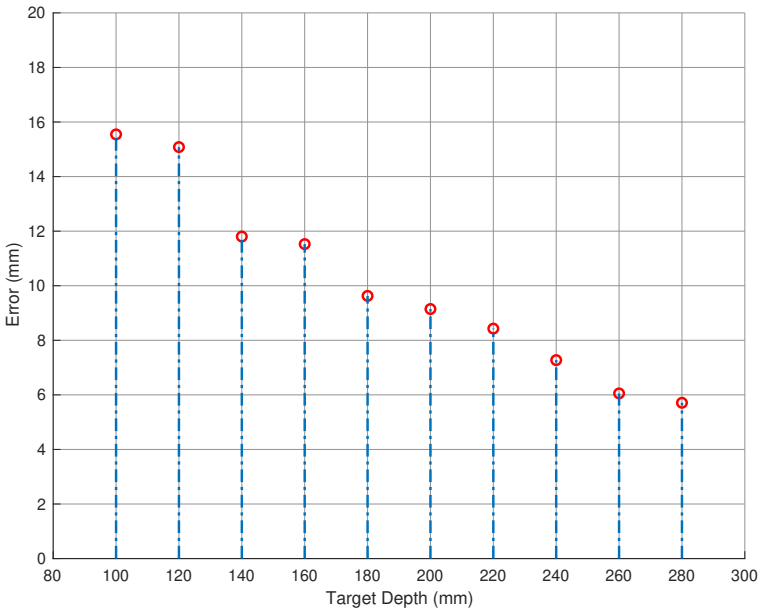

Figure 5.30: PEC target and a bulk permittivity of 9.3 showing a higher depth error. Here the positive to positive peak picking is used.

5.5.2 *Peplinski results*

For the Peplinski modelling, the same numerical modelling and depth estimation process achieved for the concrete model was repeated. Figures 5.31 and 5.32 show low and consistent (ranging in millimetres) depth errors were also achievable using the Peplinski model.

The reason for the slight decrease in consistency for heterogeneous models was that the errors for the depth estimation can be related to the velocity estimation. Meaning that in some parts of the model, a denser material such as moisture can be present. Therefore, the velocity can vary with the estimated bulk velocity hence a higher or lower depth error. Also for the shallow depth targets, the antenna can have an affect on the data collection.

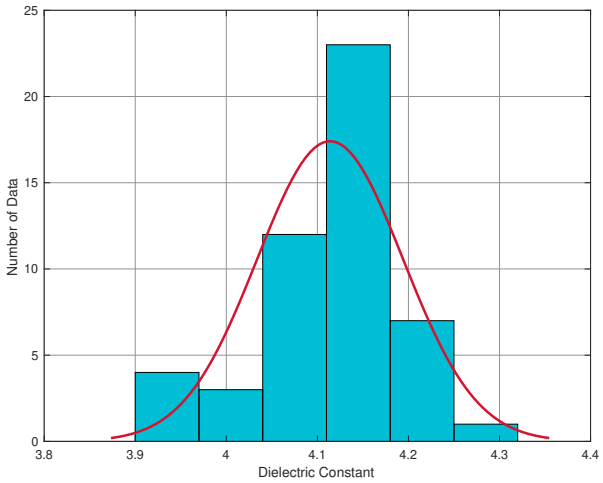

(a) Average bulk permittivity for dry soil

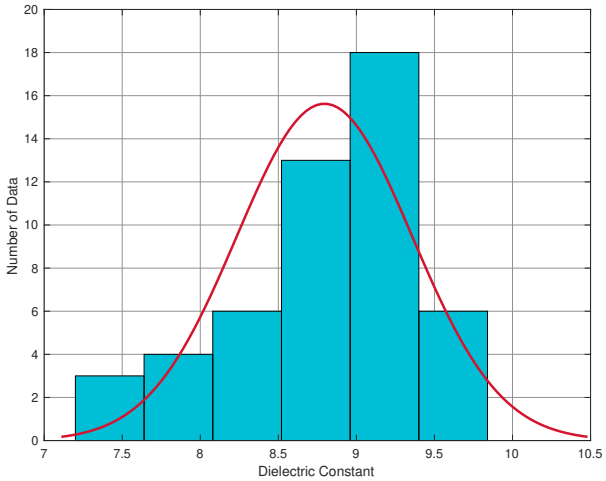

(b) Average bulk permittivity for moist soil

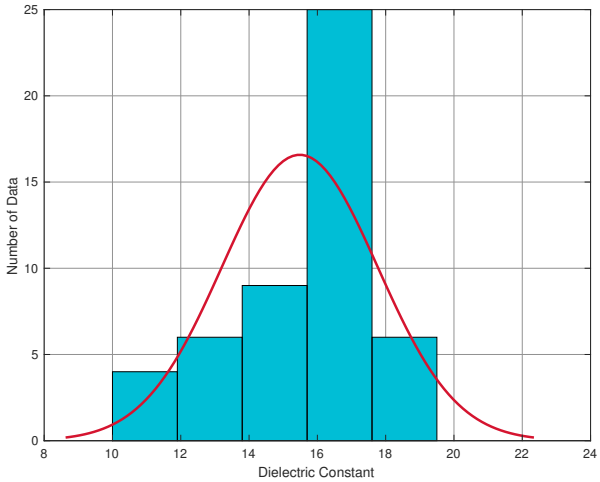

(c) Average bulk permittivity for wet soil

Figure 5.31: Each model is simulated 50 times with variable distribution to find a bulk permittivity.

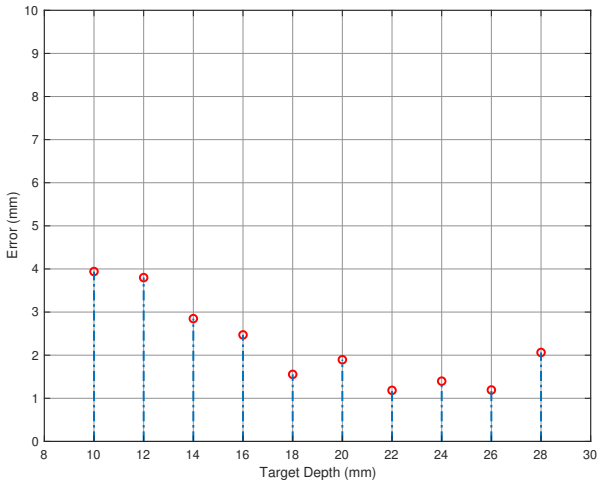

(a) Depth error (dry sand)

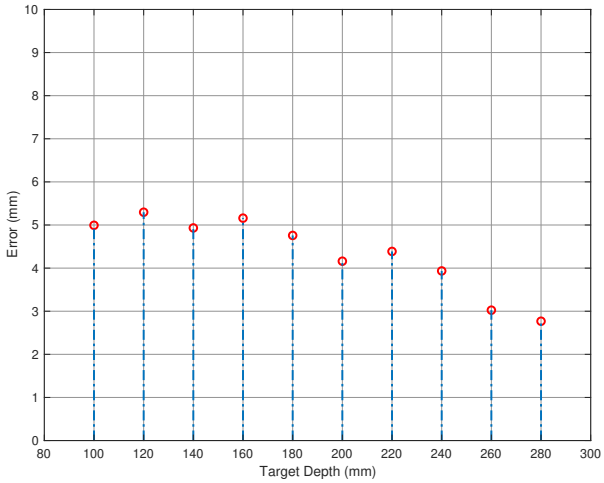

(b) Depth error (moist sand)

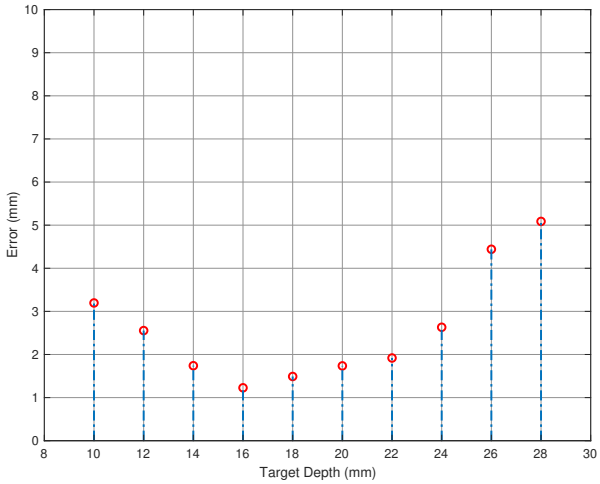

(c) Depth error (wet sand)

Figure 5.32: PEC target and a relative bulk permittivity of 4.1 for dry sand 5.31a, 9 for moist sand 5.31b and 16.5 for wet sand 5.31c.

5.6 SUMMARY

The main aim of this chapter was to achieve the best solution for the time-zero problem that many GPR researchers and users are dealing with. Most researchers tend to work in a 2D homogeneous model with a simple theoretical line source. In this chapter, a number of different 2D and 3D homogeneous and heterogeneous models that use either line sources or a realistic antenna were illustrated and the proposed time-zero methodology was implemented. This would lead GPR users to have a better understanding of real and modelled wavelet shape information from a typical GPR target and compare the amplitudes of the received signals and find a robust time-zero position. The time-zero method presented good results in which the consistency of the outputs was the priority. As presented, this chapter aims to discuss one of the main issues and challenging tasks (true ground surface) regarding GPR signal processing by examining the wavelet amplitudes of a large number of cases. GPR technology has been around for many years but the lack of a robust solution for the time-zero issue still remains. Research and literature conducted in the past and recently published papers are yet dealing with this problem. This chapter allows GPR users to become more familiar with the true time-zero positioning and resolve some of the issues in this particular field. Many time-zero methods have been processed and was illustrated that each one has advantages and disadvantages. Finally, the best and most consistent processing technique has been accomplished in this research. The proposed methodology has been applied to a number of different homogeneous cases. It has also been implemented in more complex heterogeneous models. Different types of antennas were also taken into consideration. Although a large number of scenarios have been considered, an odd case may still occur.

6 BOWTIE ANTENNA MODELLING

The purpose of this chapter is to create a model of a commercial GPR antenna that the transmitter and receiver can move independently. There are many antenna models that have been created by other authors but in those the Tx and Rx were unable to move separately. Methods such as the CMP and WARR as presented in chapter 2, require this type of antenna configuration. One of the most popular option available is a theoretical source such as line sources or Hertzian dipoles which are simple sources in which the Tx and Rx can move together or independently. There are many complex modelling studies but most authors prefer to use simplistic sources. Therefore, by modelling separate bowtie antennas can be beneficial to the obtained results from simulations and also, these models provide the option to compare the modelling results with real data.

6.1 INITIAL DEVELOPMENT OF ANTENNA MODEL

The main objective of this study was not antenna modelling therefore, only a brief overview is given. The antenna's structure is based on the GSSI 1.5 GHz antenna modelled by (Warren & Giannopoulos, 2011). Figure 6.1 presents the GSSI antenna design (Warren, 2009). As shown, it is comprised of a shield, absorber, case, Printed Circuit Board (PCB) and a bowtie pair for Tx/Rx.

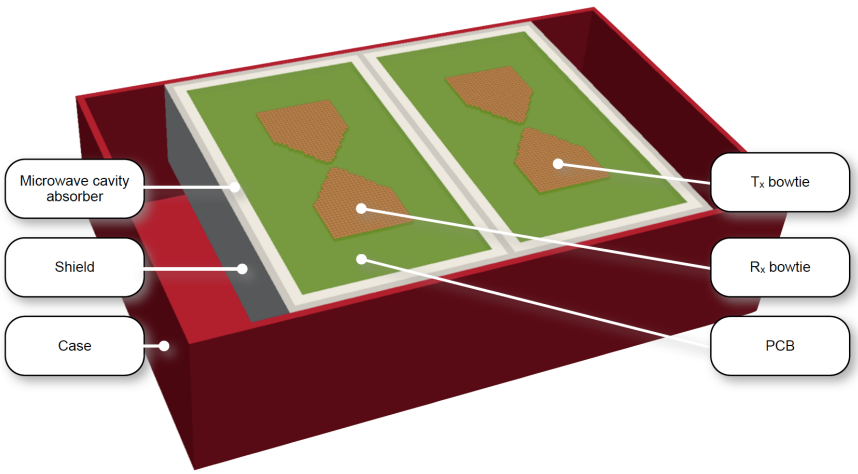

Figure 6.1: GSSI 1.5 GHz antenna model (Warren & Giannopoulos, 2011).

6.1.1 *Geometry of antenna*

The physical and electrical characteristics of the antenna pair has been modelled the same as the GSSI antenna (Warren, 2009). The geometry of the antenna was changed in order to separate the Tx and Rx with the ability to move them away or towards each other as shown in Figure 6.2. The antennas were made from a metal shield, a surrounding case, Tx and Rx bowtie engraved on to a PCB and electromagnetic absorber behind the PCB. This antenna structure was used for the further development of the time-zero adjustment. The scripts of the antenna model are given in Appendix D.5.

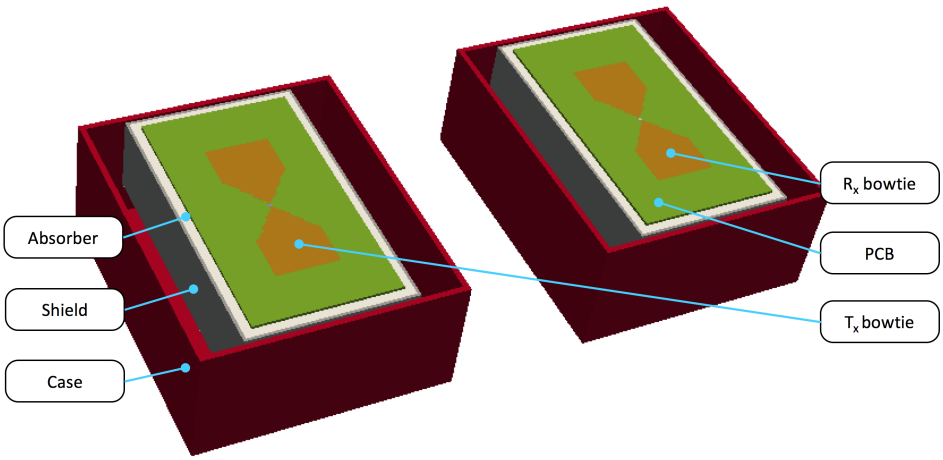

Figure 6.2: Separate bowtie 1.5 GHz antenna geometry.

6.2 PEC AND FREE-SPACE TARGET WITH VARYING HALF-SPACE PERMITTIVITY

The designed bowtie antenna was placed on a homogeneous concrete with relative permittivity of 4.5 and also, 11. A PEC plate and air-void targets were used as a high and low dielectric target respectively. As shown in Figure 6.3, the antenna was positioned directly on the concrete surface and the target was 0.28 m away from the antenna. The model has a size of 50 $cm \times 20$ $cm \times 36$ cm with a spatial discretization of 1 mm. The distance between the antennas was 20 cm.

6.2.1 *Effect of a larger Tx and Rx separation*

Simulating the model with a greater separation of the transmitter and receiver resulted in a small increase in the depth error to about 2 cm. However, the depth error remained consistent for the different targets and medium properties. The consistency is key here and as

long as it stays consistent (varying in a small range), the error can be eliminated resulting in a very low depth estimation error and can be used regardless of any environment the GPR is operating in.

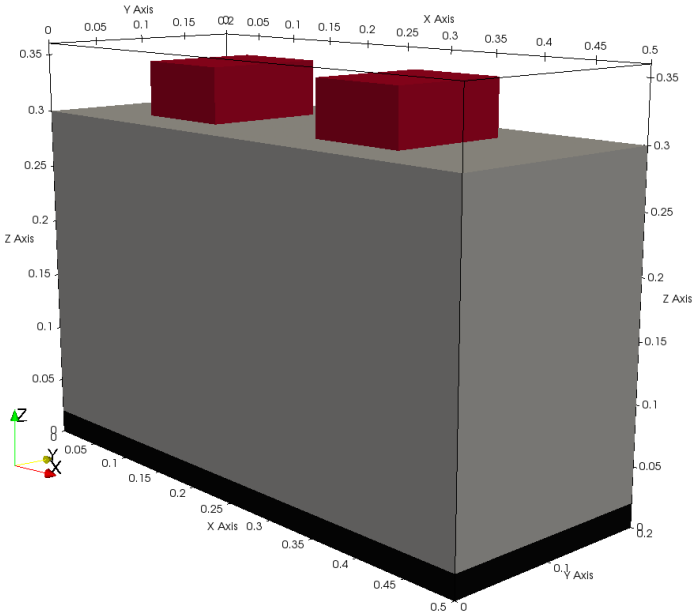

(a) Heterogeneous concrete model

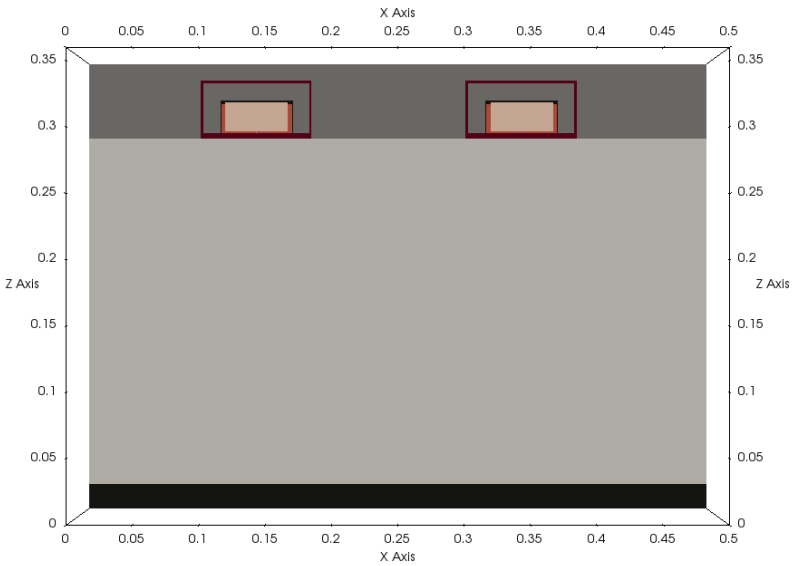

(b) 2D Slice

Figure 6.3: Homogeneous model with a Bowtie antenna pair on the surface and a PEC plate at the bottom of the model. 6.3a is the 3D view of the model and 6.3b is a 2D slice of the model.

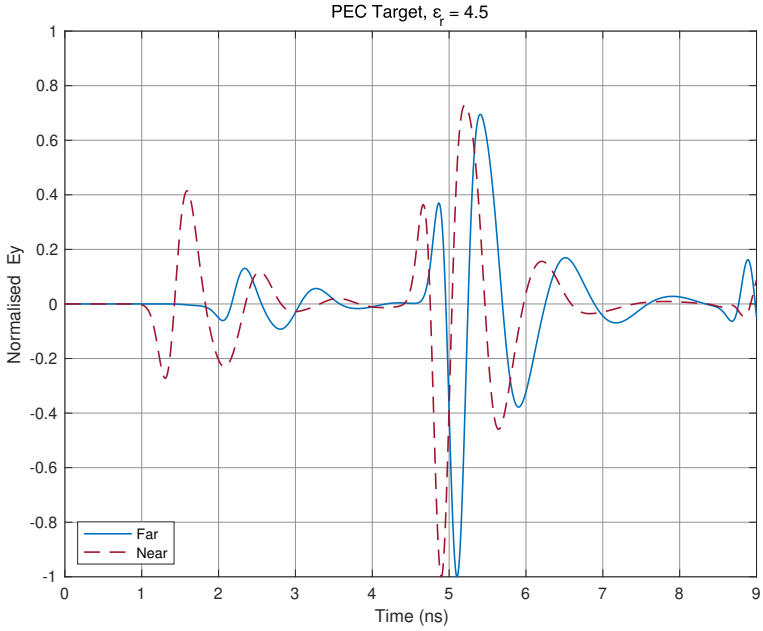
PEC Target, ε_r = 4.5
Normalised Ey
Time (ns)
Far
Near

(a)

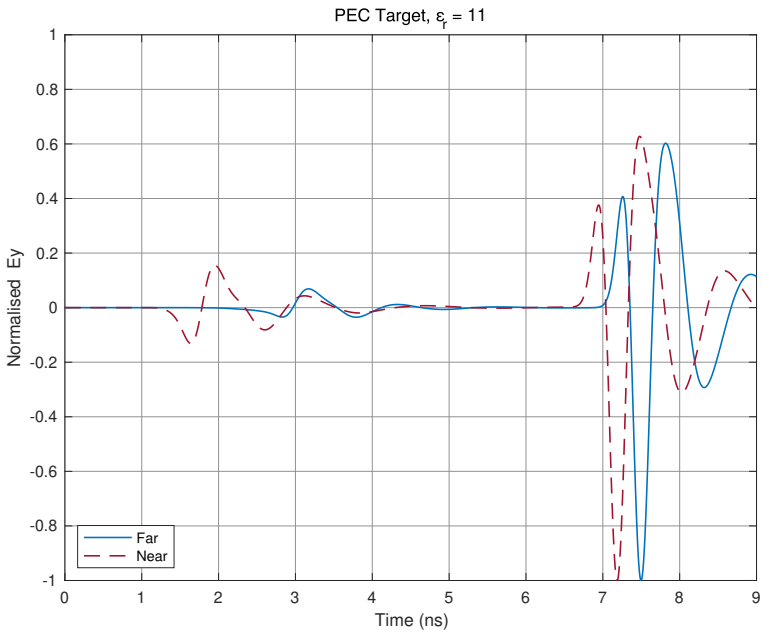
PEC Target, ε_r = 11
Normalised Ey
Time (ns)
Far
Near

(b)

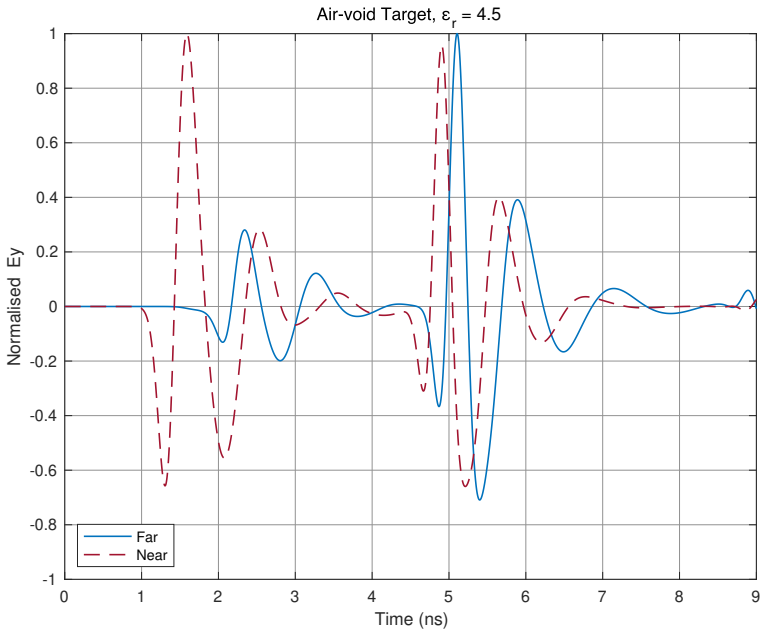

(c)

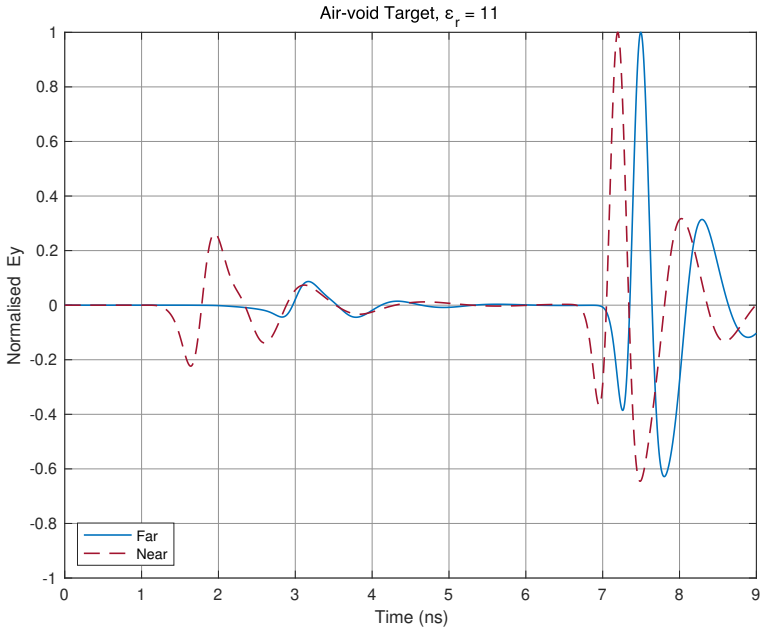

(d)

Figure 6.4: Bowtie antennas modelling results showing the direct wave and target response for different target and medium permittivities. The antenna separation for "Far" was 30 *cm* and for "Near" was 15 *cm*.

6.2.2 *Time-zero*

The model with the bowtie antennas was simulated for different target depths and the TWTT were calculated and compared to the real or known depth. The results for this antenna showed great error consistency for all the test cases despite all the changes for the half-space, target material and antenna separation which is presented in following section.

6.3 TIME-ZERO COMPARISON

Following the different antenna separations, a number of different scenarios were tested for estimating the depth and analysing the depth error. The simulations involved two types of target, high (11) and low (4.5) relative permittivity environments and different separations of the antennas (Far = 30 *cm*, Near = 15 *cm*). The first section (6.3.1) employs the proposed time-zero method and the second section (6.3.2) employs the proposed method by Yelf (2004).

6.3.1 *Proposed time-zero method*

A combination of all the different simulation scenarios and their depth errors have been presented in Table 6.1. As shown, the depth error was not affected as the permittivity of the target and medium was changed. However, the same target and medium for a greater Tx and Rx distance, the depth error had a slight increase. Further investigation of this is presented in section 6.4.

Target material	Medium relative permittivity	Antenna separation	Depth error (*cm*)
Air-void	4.5	Far	5.17
Air-void	11	Far	5.50
PEC	11	Far	5.47
PEC	4.5	Far	5.17
Air-void	4.5	Near	3.39
Air-void	11	Near	3.67
PEC	11	Near	3.71
PEC	4.5	Near	3.43

Table 6.1: The proposed time-zero method using the average of the three peaks of the reflected wavelet. High and low permittivities for the target materials and half-spaces were used. The antenna separation for "Far" was 30 *cm* and for "Near" was 15 *cm*.

6.3.2 *Yelf (2004) time-zero picking method*

Table 6.2 shows the outcome of using the time-zero picking method proposed by Yelf (2004). Here the same process as the previous section was repeated. As Table 6.2 presents, there were two disadvantages for using the positive to positive peak method (Yelf, 2004). Firstly, the depth error was higher in comparison with the proposed methodology and secondly, there was no consistency for the depth error as the target and half-space varied. For example, there was approximately 2 *cm* difference in the depth error when the target changed from a high to a low permittivity or vice versa. Therefore, the efficiency of the proposed time-zero method is proved again to be better with the use of separated antennas.

Target material	Medium relative permittivity	Antenna separation	Depth error (cm)
Air-void	4.5	Far	7.90
Air-void	11	Far	7.54
PEC	11	Far	5.78
PEC	4.5	Far	5.33
Air-void	4.5	Near	5.78
Air-void	11	Near	5.41
PEC	11	Near	4.06
PEC	4.5	Near	3.56

Table 6.2: The positive peak of the direct wave to the positive peak of the reflected wavelet time-zero method proposed by Yelf (2004). The antenna separation for "Far" was 30 *cm* and for "Near" was 15 *cm*. Different permittivities was used for the target and half-space.

In previous chapters, it has been shown that the proposed time-zero method in comparison to the most used method (positive to positive peak) has shown to work better and produce more accurate results. Homogeneous and heterogeneous environments have also been tested along with different sources such as the GSSI antenna and a theoretical line source. In this chapter, a bowtie antenna has been designed with a separate transmitter and receiver feature. The proposed time-zero method has been also tested against the bowtie antennas. As shown in Table 6.1, the proposed method has shown satisfactory results. Comparing the outcomes with the previous time-zero method results (Table 6.2), the proposed method presented more efficiency and consistency in terms of depth estimation.

6.4 FURTHER INVESTIGATION OF THE ANTENNA SEPARATION

This section looks into some potential reasons behind the increase of the depth error.

6.4.1 *Initial Tx/Rx distance*

The initial step before carrying out a field data collection is to have the transmitter and receiver close to one another and set the time-zero position. As the receiver moves away from the transmitter, the time-zero position remains the same despite the change in the direct wave position (Figure 6.6). The GSSI antenna is apart of one unit therefore, the time-zero will always be positioned on the direct wave as the Tx and Rx can not be separated. It has been shown that the closer the Tx/Rx, the less the signal was affected. Due to the structure of the antennas, the distance between the Tx and Rx of the GSSI antenna is approximately 6 *cm* and for the separated bowtie antenna is about 15 *cm* as shown in Figure 6.5. The distance causes the direct wave to be detected at different times. Therefore, as the Tx/Rx distance of the bowtie antenna (Figure 6.5b) in a "Near" position was greater than the GSSI antenna (Figure 6.5a), the time-zero position was slightly different. This maybe one of the reasons there was a small increase in the depth error.

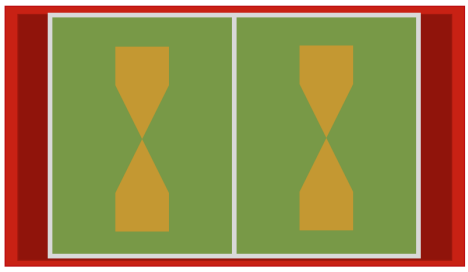

(a) GSSI antenna.

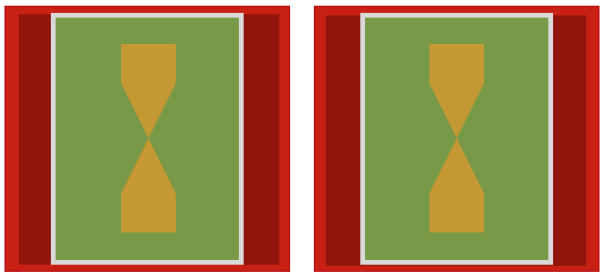

(b) Separated bowtie antenna.

Figure 6.5: The GSSI antenna and a separated bowtie antenna have been shown here to illustrate the distance between the transmitter and receiver. Due to the structure of the antenna, the GSSI antenna has a closer Tx and Rx.

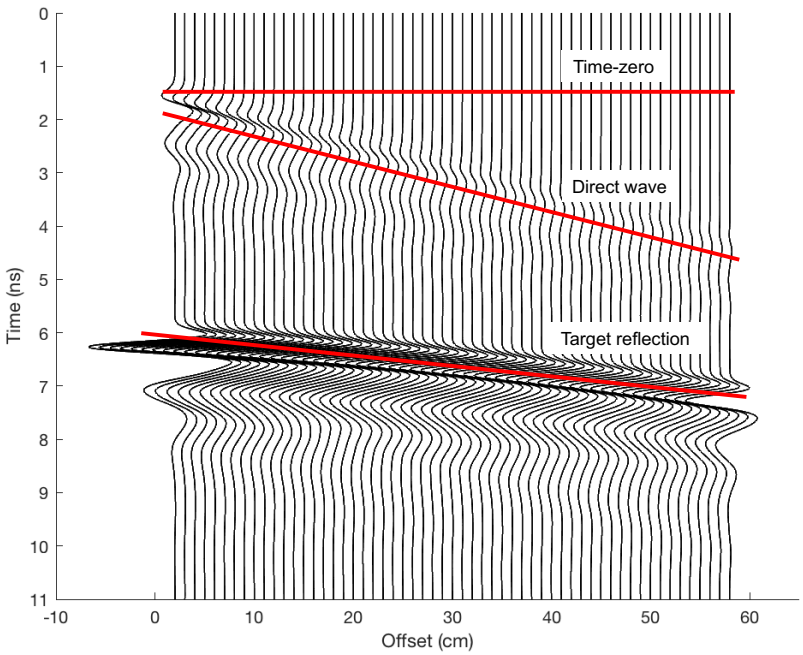

Figure 6.6: The time-zero position is set when the Tx and Rx are close to one another. As the receiver moves away from the transmitter, the direct wave arrives at a later time but the time-zero position remains the same.

6.4.2 *Multiple propagation paths from Tx to Rx*

When the transmitter transmits a signal, the signal propagates in various paths. These paths have been presented in Figure 6.7. As shown, these paths can affect the arrival time of the signal as each path has a different time delay. The further the Tx and Rx are from one another the more complexity is added. This can also be another reason for the slight increase in the depth error.

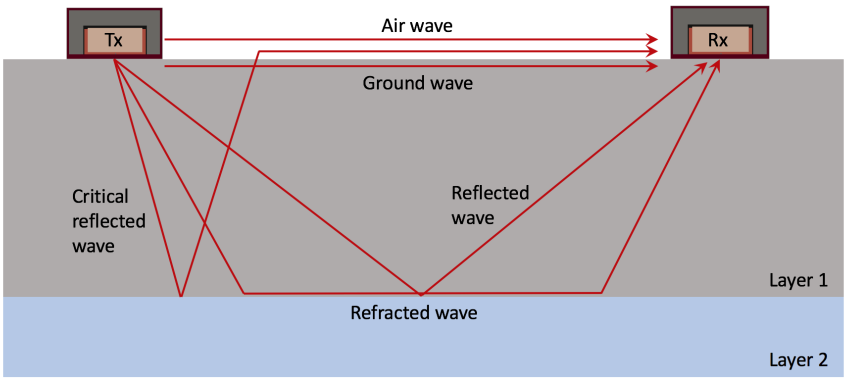

Figure 6.7: For separated antennas, the transmitted signal from the transmitter propagate in many paths. Here, these paths are shown.

6.4.3 *Wider separation of Tx & Rx*

To investigate this matter further, a wider separation of the antenna has been simulated. This was achieved by using a 2D model with a theoretical line source above the surface with various antenna separations. The results showed that as the separation was increased, the direct wave was affected by the separation causing it to split in to two separate wavelets. Additionally, when a pulse is radiated from a transmitter, a wave propagates towards a receiver (direct wave) in two paths. One path is in the air (air wave) and the second path is the tangent to the surface (ground wave). These scenarios can be seen in Figure 6.7. The Tx and Rx of a non-separable antenna are very close hence the direct waves of both paths (air and ground) are merged in one wave. Increasing the separation causes the waves to be separated as the wave that travels to the tangent of the surface has a slower velocity. Therefore, it arrives to the receiver at a later time. This maybe another reason of the increase of the depth error. Figures 6.8 to 6.14 illustrate how the direct wave was affected as the separation of the Tx and Rx was increased.

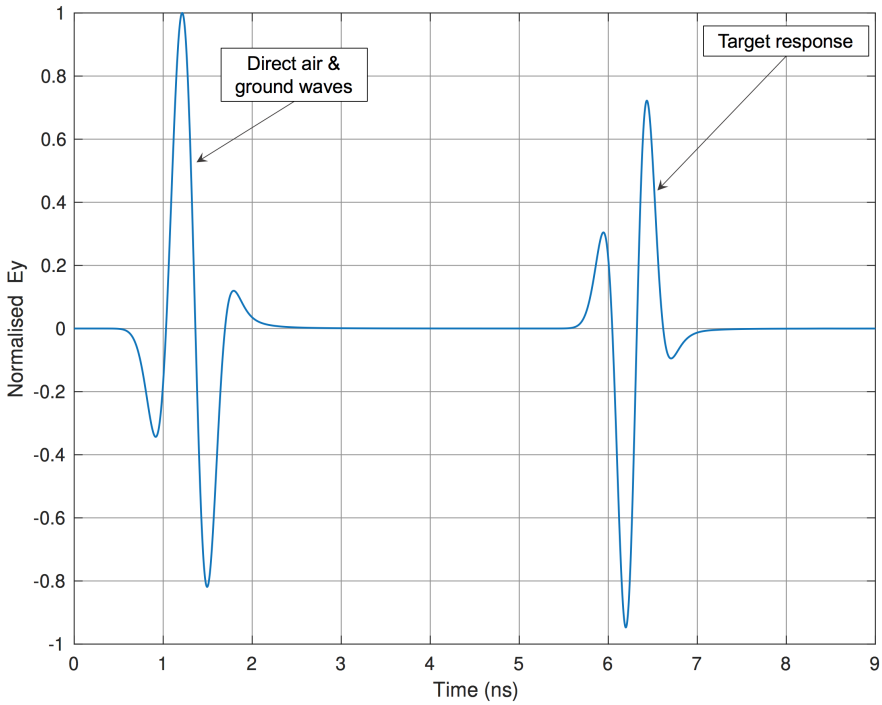

Figure 6.8: line source with Tx and Rx separation of 5 *cm* with a PEC target.

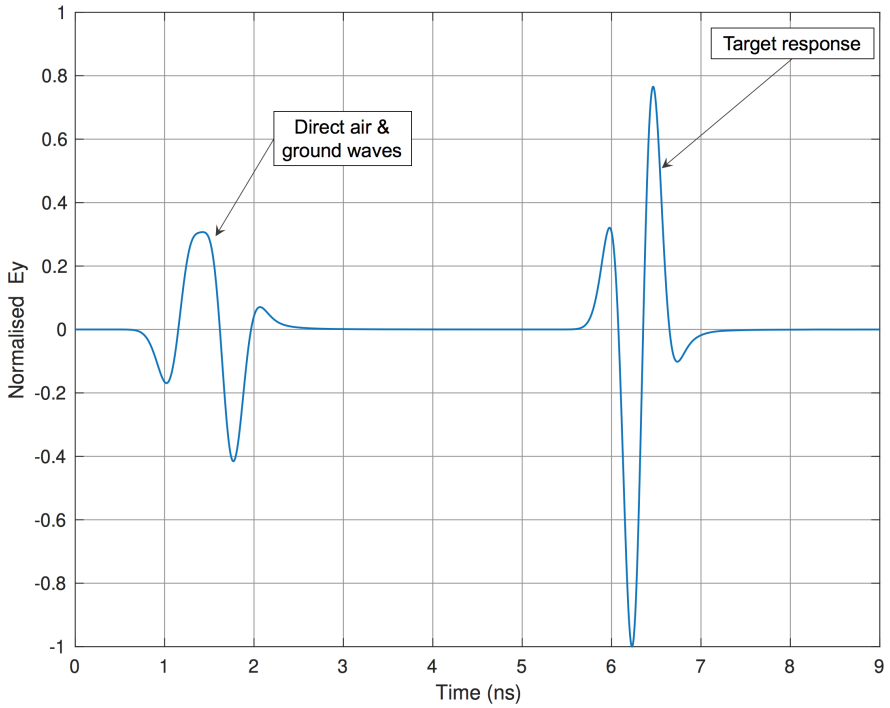

Figure 6.9: line source with Tx and Rx separation of 8 *cm* with a PEC target.

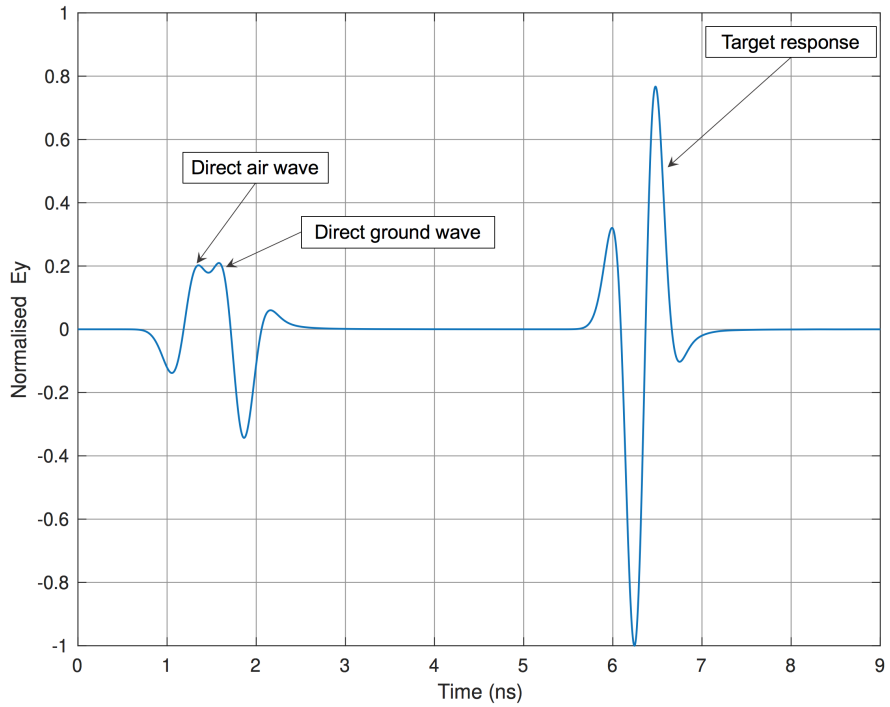

Figure 6.10: line source with Tx and Rx separation of 9 *cm* with a PEC target.

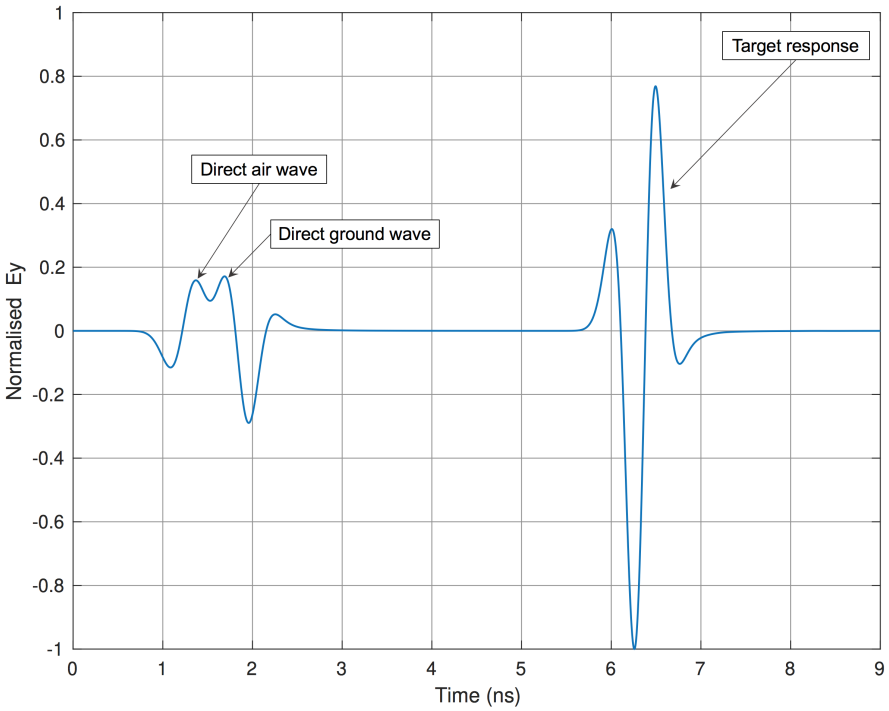

Figure 6.11: line source with Tx and Rx separation of 10 *cm* with a PEC target.

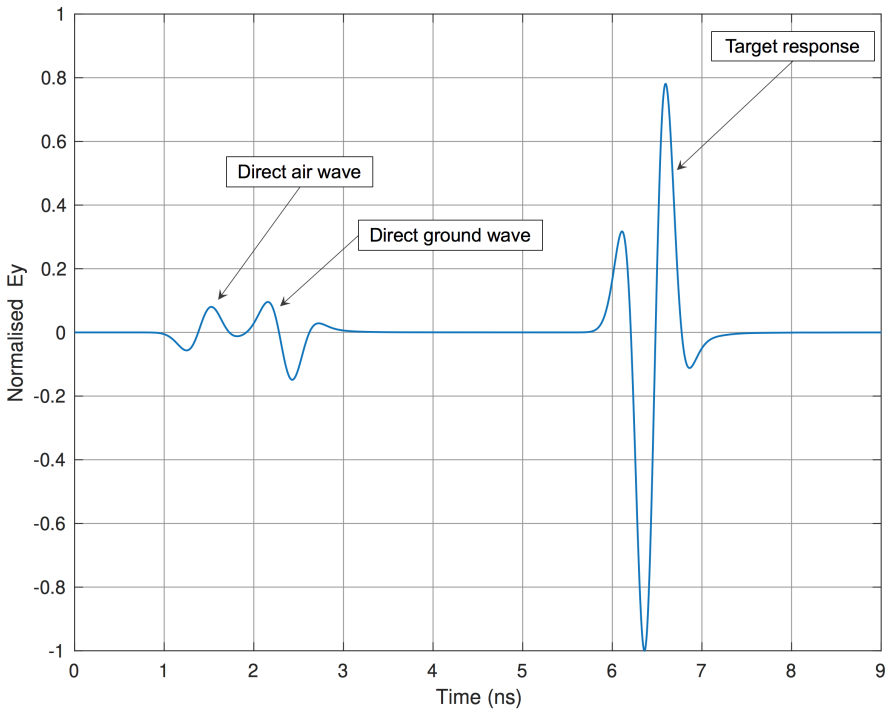

Figure 6.12: line source with Tx and Rx separation of 15 *cm* with a PEC target.

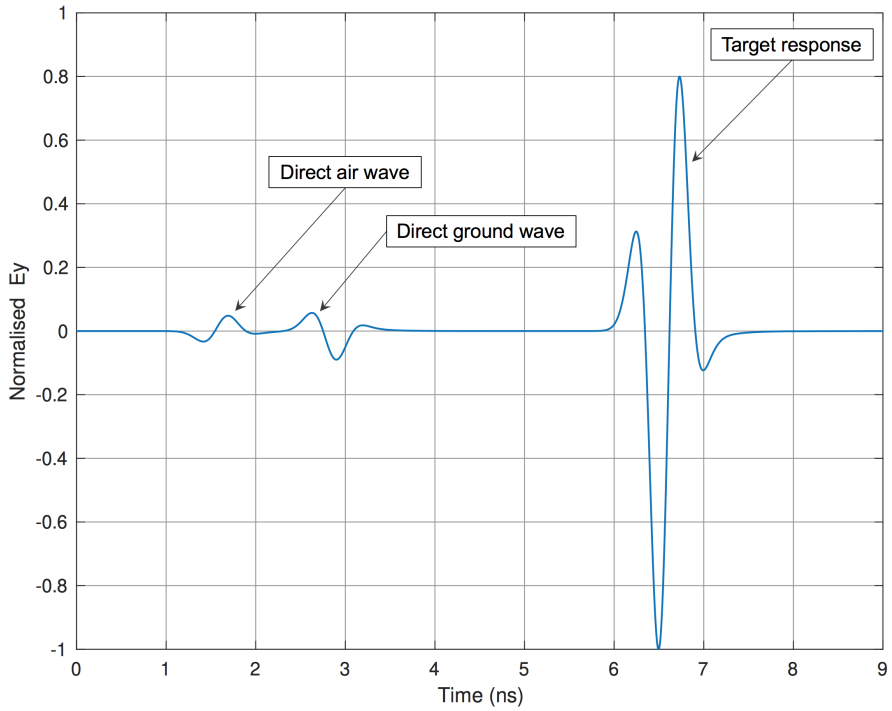

Figure 6.13: line source with Tx and Rx separation of 20 *cm* with a PEC target.

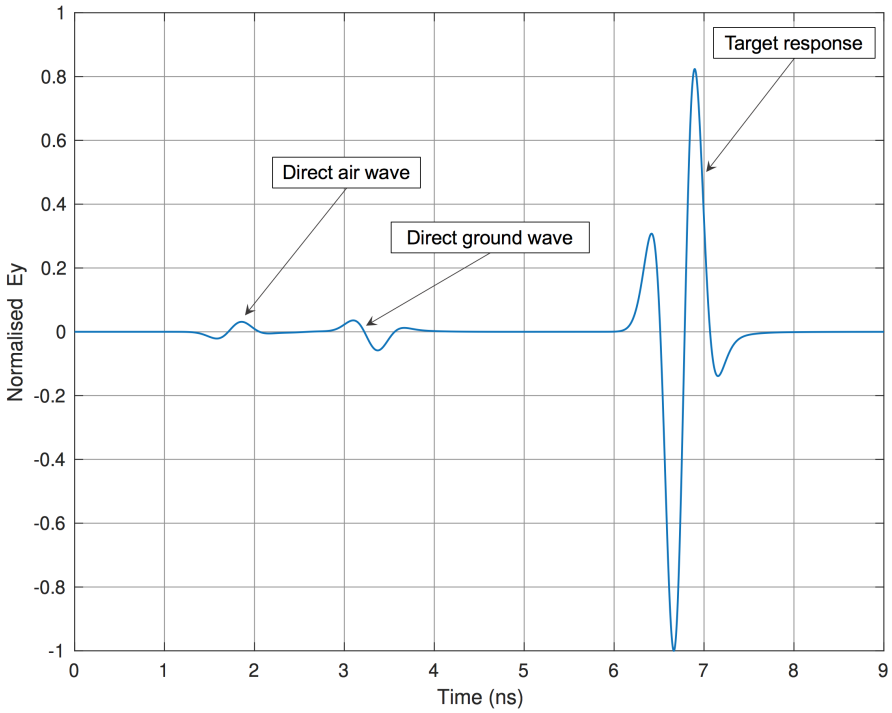

Figure 6.14: line source with Tx and Rx separation of 25 *cm* with a PEC target.

6.5 SUMMARY

This chapter illustrated the modelling of a separated bowtie antenna pair in order to have the ability of the transmitter and receiver to move independently. The model characteristics and materials were based on a previous GSSI antenna model but the antenna was produced from scratch as the Tx and Rx geometry needed to be modelled separately with a slightly different size case and shield. The main purpose of this antenna was to develop a realistic 3D antenna rather than use a simple line source that the Tx and Rx were able to move independently. The motivation came from chapter 4, as an effort was made to model a realistic environment. Therefore, a realistic separated source that was not modelled before was obtained. The antenna model was used for the time-zero adjustment for different Tx and Rx separations. The results showed consistency throughout various target materials but an increase in the depth error for larger antenna separations was shown.

7

GEOMETRIC PARAMETER INVESTIGATION OF THE CRIM MODEL

In this chapter, the Complex Refractive Index Model's shape factor is investigated in order to determine a high accuracy shape factor for the bulk permittivity estimation. Many mixtures with different content percentages are simulated and the bulk permittivities are calculated. These permittivities are also calculated in theory and compared with the simulation results. In addition, the results are compared with other mixing models such as the Böttcher model and Rayleigh model. Hence from this investigation, a better shape factor is accomplished.

7.1 INTRODUCTION

Estimating the permittivity of heterogeneous mixtures based on the permittivity of their individual components is of high importance with many applications using ground penetrating radar (GPR) and electrodynamics-based sensing in general. Complex Refractive Index Model (CRIM) is the most mainstream approach for estimating the bulk permittivity of heterogeneous materials and has been widely used in many GPR applications. The popularity of CRIM is primarily based on its simplicity while its accuracy has never been rigorously tested. In the current study, an optimised shape factor is derived that is fine-tuned for modelling the dielectric properties of concrete. The bulk permittivity of concrete is expressed with respect to its components i.e. aggregate particles, cement particles, air-voids and volumetric water fraction. Different combinations of the above materials are accurately modelled using the Finite-Difference Time-Domain (FDTD) method. The numerically estimated bulk permittivity is then used to fine-tune the shape factor of the CRIM model. Then, using laboratory measurements it is shown that the revised CRIM model over-performs the default shape factor and provides with more accurate estimations of the bulk permittivity of concrete.

7.2 METHODOLOGY

Complex Refractive Index Model (CRIM) formula (7.1) describes one of the most used models by GPR practitioners for predicting the bulk permittivity of complex materials like concrete.

$$\varepsilon_b = \left(V_{ag}\varepsilon_{ag}^{\alpha} + V_a\varepsilon_a^{\alpha} + V_c\varepsilon_c^{\alpha} + V_w\varepsilon_w^{\alpha}\right)^{1/\alpha} \tag{7.1}$$

where ε_b is the bulk permittivity of the concrete mixture, V_{ag} and ε_{ag} are the volume and relative permittivity of aggregate, V_a and ε_a are the volumetric fraction of air-voids and relative permittivity of free space, V_c and ε_c are the volumetric fraction and relative permittivity of cement, V_m and ε_m are the volumetric fraction and relative permittivity of the moisture content and α is the shape factor.

The most common shape factor of CRIM model is usually $\alpha = 0.5$. This study investigates the CRIM formula in order to find an optimise shape factor. To be able to take this matter further, a training set needs to be built and to have control over this, numerical modelling is used.

Numerical modelling is a great tool when it comes to optimisation. In order to find the optimum shape factor, we used synthetic data. These data were collected from a number of modelling experiments in gprMax (Warren, Giannopoulos, & Giannakis, 2016; Warren et al., 2019). After creating heterogeneous concrete models, a reflection from a PEC target was used to predict the velocity and calculate the bulk permittivity. In order to achieve this, an accurate time-zero should be defined.

7.3 TIME-ZERO

GPR applications require great accuracy and precision. Such cases are when trying to locate gas pipes (Terrasse et al., 2016), landmine detection (Daniels, 2006) or concrete inspection (Brown, 1990) where it is necessary to position the time-zero accurately. Defining the exact location of time-zero on a GPR trace is still an open issue with no specific conclusive solution and usually addressed by taking into account the GPR manufacturers recommendations (Yelf, 2004).

In chapter 5, it was proposed that the time-zero should be positioned on the first peak of the direct wave and a two-way travel time was calculated from the time arrival average of the three reflected peaks of the target (Zadhoush & Giannopoulos, 2021). Figure 5.13 presents a GPR trace with a reflection from a PEC target. The proposed time-zero picking methodology has been successfully evaluated using numerous numerical scenarios indicating the validity of the current approach hence it was used in this chapter for the shape factor investigation.

7.4 CONCRETE MODELLING

The initial investigation of the CRIM model was performed based on a homogeneous two dimensional (2D) model with a simple theoretical source for simplicity. The simulation showed promising results for the permittivity estimation of the concrete. In other words, the real and the estimated permittivities using CRIM were close. This provided confidence to upgrade the framework and design models which are much closer to reality. To increase the complexity of the model and be more realistic, a three dimensional (3D) concrete model was created including

a realistic GSSI-like antenna. For more information on the development of the concrete model visit chapter 4.

7.4.1 *Computational resources*

There is a limited number of studies where realistic models are employed due to the complexity and lack of computational resources. Simulating a 3D model, especially employing 3D realistic sources, can be very time-consuming in comparison with a 2D model. Therefore, the demand for High-Performance Computing (HPC) has risen significantly over the past decade. This allows for the simulation times to be reduced and enables us to investigate more complex GPR problems. The open-source Graphics Processing Unit (GPU) engine for gprMax (Warren et al., 2019) has greatly accelerated simulations. The simulations that are conducted using the GPU based gprMax solver are up to 30 times faster in comparison with the traditional CPU based ones (Warren et al., 2019). CPU uses a few cores and is generally used for simple tasks whereas GPU works with thousands of efficient cores with a parallel architecture (Warren et al., 2019).

7.4.2 *Model geometry & material percentage*

Figure 7.1 illustrates a heterogeneous concrete model with a size of 30 $cm \times 20$ $cm \times 36$ cm and a spatial discretization of 1 mm. Aggregate, cement, air-voids and moisture content with different percentages were randomly distributed in order to achieve different concrete mixtures. A PEC was placed at the bottom of the model has a thickness of 2 cm and results in a strong reflection which will be used later on to derive the bulk permittivity of the investigated medium. Each mixture was simulated and the reflected signals were processed to find the GPR wave propagation of velocity and therefore, calculate the bulk permittivity. The GSSI-like antenna was coupled to the concrete surface. The GSSI-like 1.5 GHz centre frequency transducer consist of a transmitter/receiver (Tx/Rx) bowtie (copper) pair, printed circuit boards - PCB (glass fiber), electromagnetic absorber (carbon-loaded foam), shield (PEC) and a red case (polypropylene) (Warren & Giannopoulos, 2012).

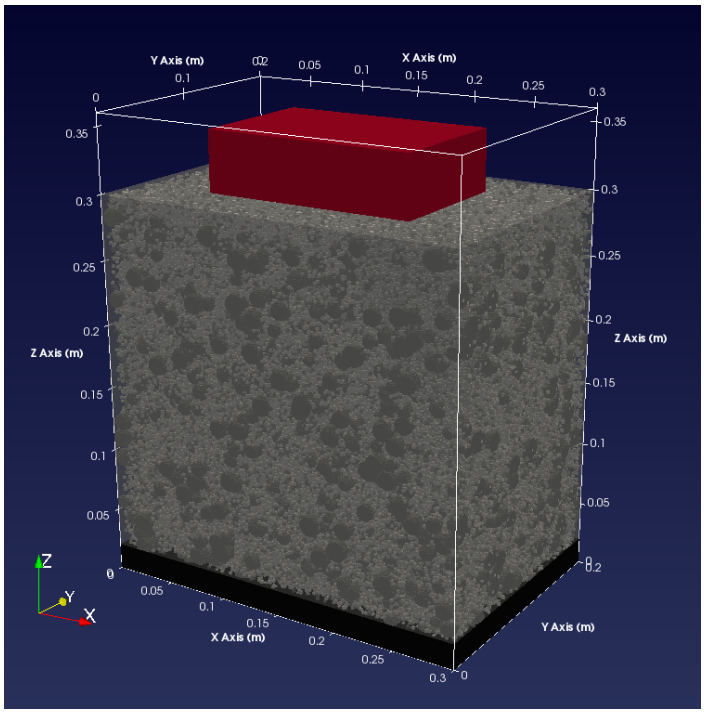

(a) Heterogeneous 3D concrete model

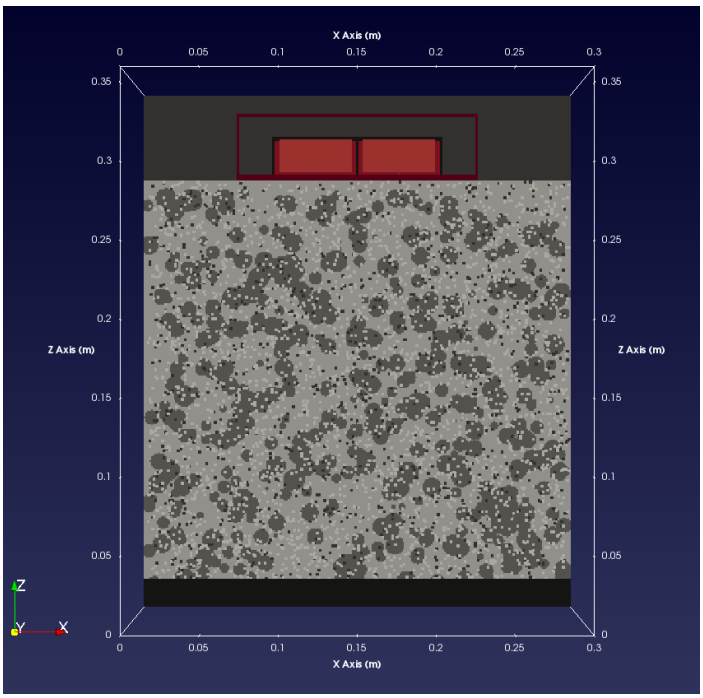

(b) Slice of heterogeneous concrete model

Figure 7.1: Heterogeneous concrete model was plotted using Paraview (Ahrens, Geveci, & Law, 2005). The model employs a 1.5 GHz GSSI antenna pair placed on top of the concrete. A PEC plate was placed below the concrete model in order to obtain a perfect reflection. (a) 3D view of the concrete model. (b) 2D slice of the 3D model which allows for a better understanding of the material distribution.

7.4.3 *Permittivity calculation*

Producing a realistic concrete model requires the material mixture to follow a rational percentage range. The permittivity of the materials used in the concrete mixture with their corresponding percentage ranges are shown in Table 7.1.

Material	Mixture Percentage	Relative permittivity (ε_r)
Aggregate	60% - 75%	7
Cement	7% - 15%	3
Air-void	1% - 8%	1
Bond Water	14% - 21%	37.54 [1]

Table 7.1: The range of components used to generate the training data. The percentages of the components were for on service concrete.

Notice that the water was assumed to be bound and therefore its relaxation frequency was shifted to lower frequencies which results to a lower permittivity value for the frequency range of interest Lachowicz and Rucka, 2017. Also note that the imaginary part was omitted from the simulations since in the current study we try to infer the permittivity from the bulk velocity which is not affected by electromagnetic losses. Numerous concrete mixtures were synthetically generated based on these percentages. Various concretes with different aggregate, cement, air and water fraction percentage were investigated numerically in order to calculate their resulting bulk permittivity. Keeping the same material percentages, each concrete mixture was simulated multiple times with different distribution to find the average permittivity as presented in Figure 7.2. The estimated bulk permittivity from the numerical modelling will be used in section 7.5 to calibrate the shape factor of the CRIM model and generate a better formula with a more accurate shape factor that can accurately predict the bulk permittivity of concrete mixtures based on its aggregate, cement, water and air fraction.

The GPR signals propagating through the medium does not transmit through the PEC and all of the energy from the impinging signals on the plate is reflected hence its thickness is not important. The size of the aggregates distributed in the mixture have a radius range from 4 *mm* to 8 *mm* (Grassl, Wong, & Buenfeld, 2010) for coarse aggregates. As the aggregate percentage reaches 60%, the radius was automatically decreased to a range from 1 *mm* to 2 *mm* (Kemper & Rosenau, 1986) in order to simulate smaller or fine aggregates into the model and reach the specified percentage. This makes the resulting shape factor tuned for an average size of particles and not for a specific one. Moisture and air-void particles were randomly distributed around the aggregates

1 (Lachowicz & Rucka, 2017)

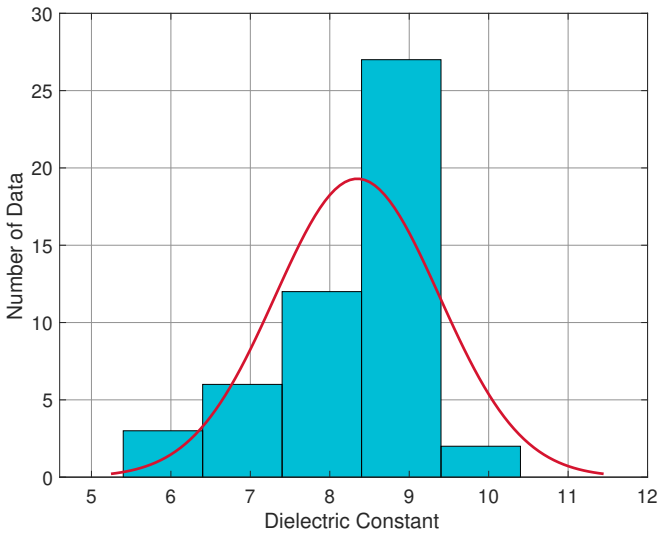

Figure 7.2: A random concrete model was simulated a number of times (x50) with different particle distributions in order to find its average bulk permittivity based on the reflection from the PEC reflector. This process neglects abnormal permittivity and allows the output to be more precise.

according to the selected percentage. The cement material was used as background material. In other words, it fills the remaining spaces of the concrete mixture. In regards to the water permittivity, there are two types of water. Bound and unbound (free) water. Bound water is a thin layer of water or moisture which surrounds mineral surfaces such as soil and concrete. Water has a strong electrical polarity hence it bounds very easily with other surfaces (Jury & Robert, 2004). This has a high impact on the permittivity of the material which the water molecules bound with. The dielectric constant of bound water in comparison with free water ($\varepsilon_r = 81$) is much smaller. In a recent study, the permittivity of the liquid phase was fitted in a non-linear CRIM and permittivity of $\varepsilon_r = 37.54$ was calculated (Lachowicz & Rucka, 2017). Figure 7.3 illustrates a set of concrete mixtures generated using the aforementioned procedure.

Model	Aggregate	Cement	air-voids	Moisture content
a	65%	15%	5%	15%
b	45%	27%	11%	17%
c	60%	14%	5%	21%
d	65%	10%	15%	10%

Table 7.2: The volumetric fractions of the concrete's components of the models shown in Figure 7.3. Some of these percentages are not within the ranges shown in Table 1 in order to illustrate the modelling capabilities of the current framework for extreme cases.

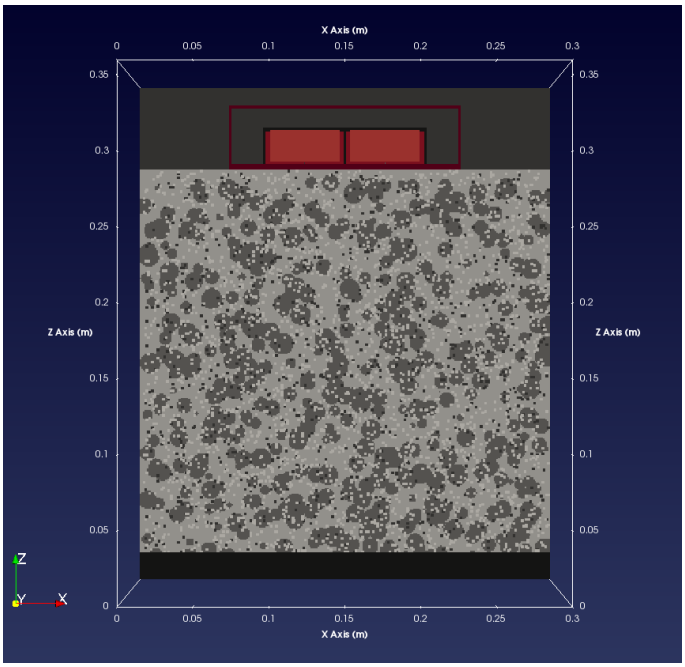

(a) Different content distribution of 7.1b

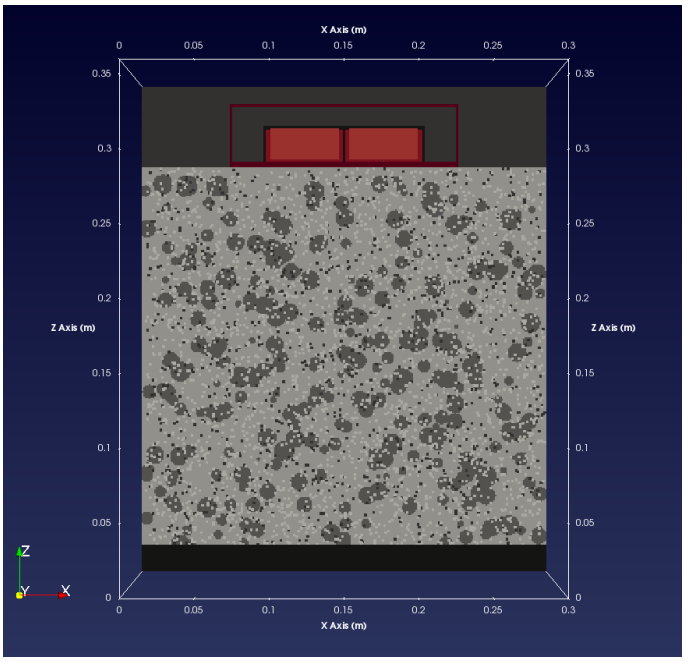

(b) Low aggregate content mix

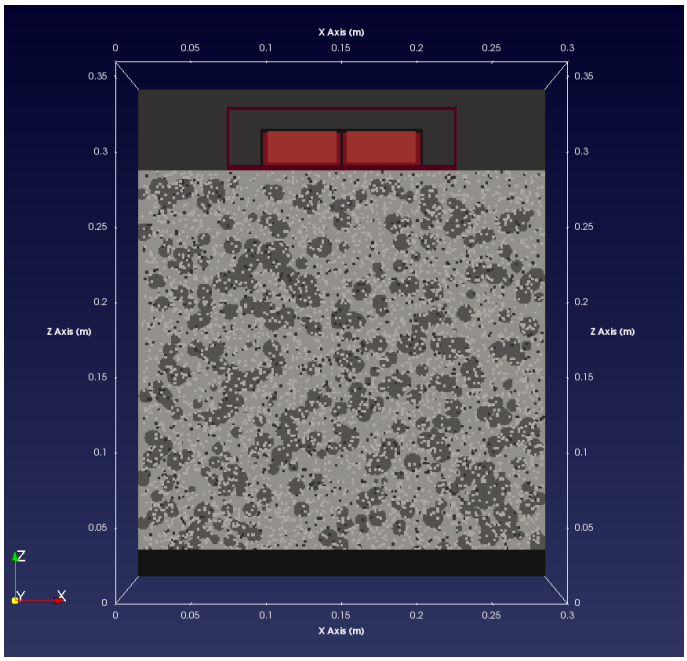

(c) High moisture content mix

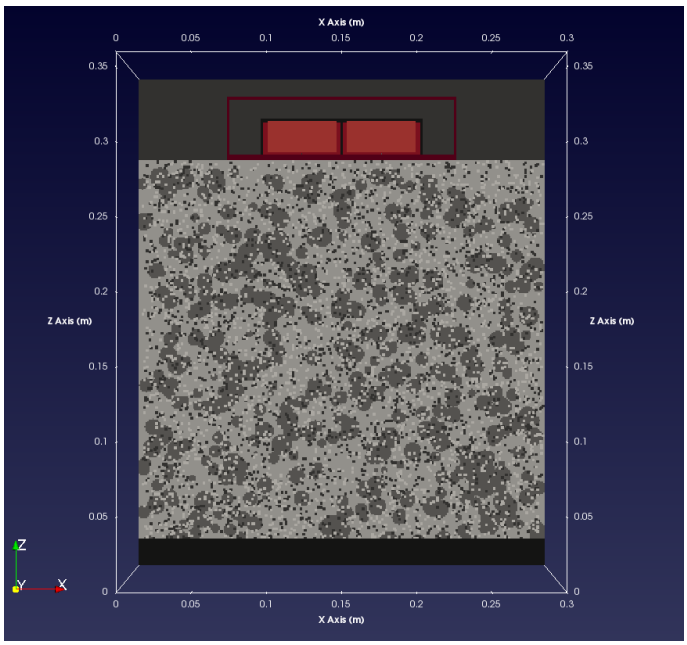

(d) High air-void content mix

Figure 7.3: Heterogeneous concrete mix with different aggregates, air-voids and moisture content. (7.3a) presents the same mixture content as (7.1b) but using a different distribution. (7.3b) shows a mixture with low aggregate content. (7.4c) illustrates high moisture content concrete resulting in a high permittivity. Finally, (7.4d) indicates high air-void content allowing the GPR signal to travel with a higher velocity. 64 representative concrete mixtures were selected from the training pool and each one was simulated 50 times resulting in 3200 simulations. The red box corresponds to the numerical equivalent of the GSSI-like 1.5 GHz centre frequency antenna structure. The volumetric percentages of the components for each model are shown in Table 7.2.

7.5 BULK PERMITTIVITY CALCULATION

7.5.1 *CRIM model*

A simple method that was used to estimate the bulk relative effective permittivity for complex mixtures such as heterogeneous concrete models was the CRIM model as presented in (7.2).

$$\varepsilon_{mix} = \left(\sum_{i=1}^{N} f_i \varepsilon_i^{\alpha} \right)^{1/\alpha} \tag{7.2}$$

where ε_{mix} is the bulk permittivity of a mixture, f_i is the volume fraction of ith material, ε_i is the permittivity of the ith material, N is the number of phases and α is a constant that is usually set up to $\alpha = 1/2$. For concrete, equation (7.2) becomes:

$$\varepsilon_r^{\alpha} = V_{ag}\varepsilon_{ag}^{\alpha} + V_c\varepsilon_c^{\alpha} + V_a\varepsilon_a^{\alpha} + V_w\varepsilon_w^{\alpha} \tag{7.3}$$

where in (7.3):

α	=	geometric parameter
ε_r	=	relative bulk permittivity
V_{ag}	=	aggregate volume
V_c	=	cement volume
V_a	=	air-void volume
V_w	=	water volume
ε_{ag}	=	relative permittivity of aggregate (solid phase - matrix)
ε_c	=	relative permittivity of cement (solid phase - matrix)
ε_a	=	relative permittivity of air-void (gaseous phase - air)
ε_w	=	relative permittivity of moisture content (liquid phase - water)

It has been reported that the most common value used was $\alpha = 0.5$ (Roth et al., 1990; Ukaegbu, Gamage, & Aspinall, 2019). In some studies, the value of $\alpha = 0.46$ was substituted and other studies have shown that $\alpha = 0.66$ was more satisfactory for the research conducted (Gardner, Dean, & Cooper, 1998). Other work presented the shape factor to be $\alpha = 0.65$ (Dobson et al., 1985; Peplinski, Ulaby, & Dobson, 1995b).

7.5.2 *Calculated shape factor*

This work is focused on finding the optimum α for modelling concrete mixtures (Zadhoush, Giannopoulos, & Giannakis, 2021). In order for the

shape factor investigation to take place, all the material permittivities and volumetric properties were implemented in the CRIM formula. In comparison with the simulated results (derived in section 7.5.1), the error difference is plotted in Figure 7.4a with respect to α. The error with respect to the shape factor was calculated using 64 representative and realistic mixing models from the available training pool. As shown in Figure 7.4a, the error was minimised for $\alpha = 0.13$. When using an simplistic time-zero approach, like the positive to positive peaks, will result in the shape factor to be $\alpha = 0.25$. Using an explicit time-zero method, like the one proposed in this thesis, will result in a better accurate shape factor hence a more accurate bulk permittivity.

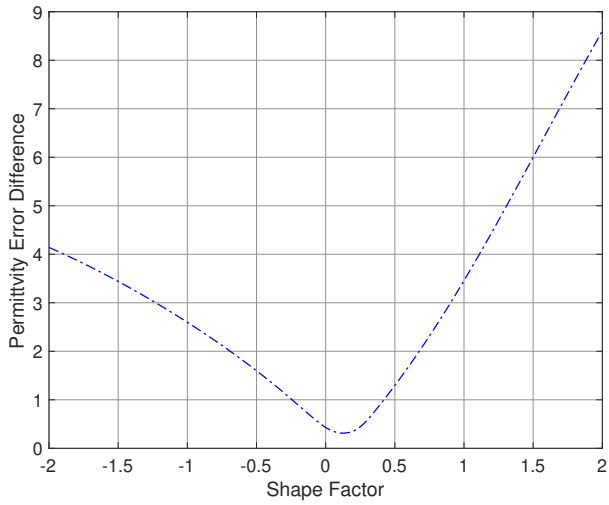

(a)

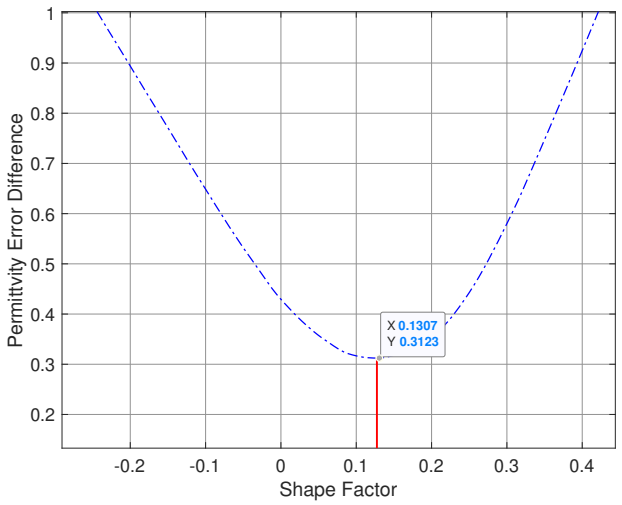

(b)

Figure 7.4: The error between the estimated permittivity using FDTD and the CRIM model is shown in Figure (7.4a). Sub-figure (7.4b), zooms in to better visualise the resulting shape factor.

To compare the results of this research with other mixing models such as the Rayleigh (Rayleigh, 1892) and the Böttcher (Böttcher & Bordewijk, 1978) models, the same calculation process was executed.

7.5.3 *Rayleigh model & Bötcher model*

Rayleigh mixing model is presented as:

$$\frac{\varepsilon_{bulk}-\varepsilon_b}{\varepsilon_{bulk}+2\varepsilon_b}=V_{sb}\frac{\varepsilon_s-\varepsilon_b}{\varepsilon_s+2\varepsilon_b}+V_a\frac{\varepsilon_a-\varepsilon_b}{\varepsilon_a+2\varepsilon_b}+V_{sw}\frac{\varepsilon_{sw}-\varepsilon_b}{\varepsilon_{sw}+2\varepsilon_b} \tag{7.4}$$

And Böttcher mixing model is presented as:

$$\frac{\varepsilon_{bulk}-\varepsilon_b}{3\varepsilon_{bulk}}=V_{sb}\frac{\varepsilon_s-\varepsilon_b}{\varepsilon_s+2\varepsilon_{bulk}}+V_a\frac{\varepsilon_a-\varepsilon_b}{\varepsilon_a+2\varepsilon_{bulk}}+V_{sw}\frac{\varepsilon_{sw}-\varepsilon_b}{\varepsilon_{sw}+2\varepsilon_{bulk}} \tag{7.5}$$

where in (7.4) and (7.5):

ε_{bulk}	=	bulk permittivity
ε_b	=	dielectric constant of binder
ε_s	=	dielectric constant of the solid phase (matrix)
ε_a	=	dielectric constant of the gaseous phase (air)
ε_{sw}	=	dielectric constant of the liquid phase (water)
V_{sb}	=	bulk volume of aggregate
V_a	=	volume of air
V_{sw}	=	volume of water

Equations (7.4) and (7.5) were used to calculate the bulk permittivity of Rayleigh model and Böttcher model respectively. By inserting the dielectric constant and the volume of each material, the formula calculates a specific bulk permittivity according to the given parameters. The Rayleigh mixing model has one output hence the permittivity calculation was simple. On the other hand, Böttcher mixing models output was mathematically more complex. To overcome this time-consuming calculation, an automated procedure was programmed in MATLAB. A symbolic variable was created followed by a Variable Precision Arithmetic (VPA) operation in order to derive four potential solutions. The positive solution was chosen as the bulk electric permittivity while the negative solutions were omitted.

7.6 COMPARISON

Figure 7.5 illustrates the estimated permittivty using FDTD and the predicted permittivity using the aforementioned mixing models. It is apparent that the revised shape factor (geometric factor) performs better in comparison with the traditional CRIM model ($\alpha = 0.5$) and the other mixing models. This supports the premise that the revised CRIM using $\alpha = 0.13$ is a reliable mixing formula for predicting the bulk permittivity of concrete based on its aggregate, cement, water and air fraction content.

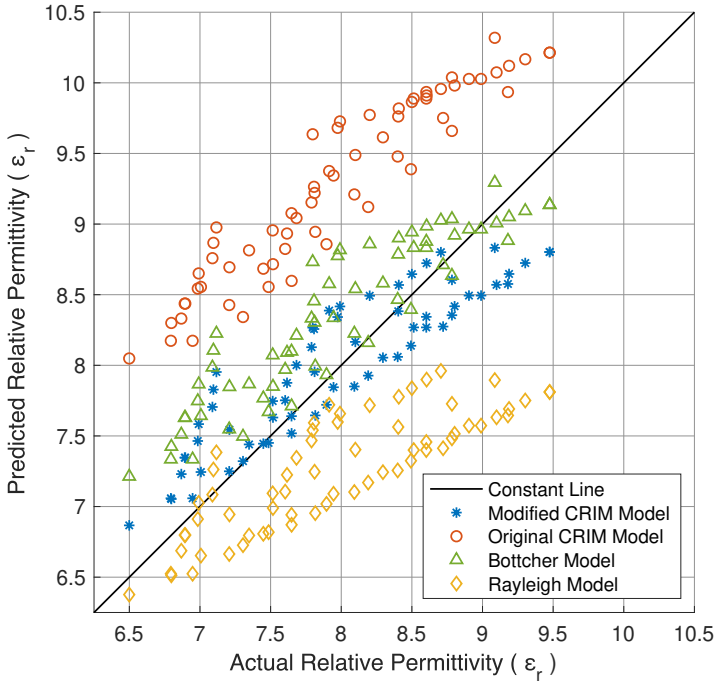

Figure 7.5: Comparison between different mixing models and the modified CRIM model. The model closest to the single constant line gives the most accurate answer for the relative bulk permittivity.

7.7 SUMMARY

This chapter presented a new and more accurate shape factor for the CRIM model in order to estimate the bulk permittivity more accurately. Many concrete mixtures with various material components were simulated and tested. The bulk permittivities were calculated through the mixing model formula and numerical modelling. The bulk permittivities of the mixtures were compared and analysed. This resulted in a better shape factor for the CRIM model. With the new shape factor, the modified CRIM model out preformed the traditional CRIM model. Other models such as the Rayleigh and Böttcher were also tested and compared with the new CRIM model. Overall the modified model in this study preformed the best in predicting the bulk permittivity.

8

VALIDATION STUDY THROUGH LABORATORY EXPERIMENTS

In Chapters 5 and 7 the true ground surface for GPR applications and the geometric parameter investigation of the CRIM model has been presented. In this chapter, the work carried out in previous chapters were validated through experimental work. A series of laboratory experiments were carried out that mimic the work done through numerical modelling. The results from the laboratory and modelled experiments were compared in order to access the validity and accuracy of the framework. The antenna used for both laboratory and modelling work was the GSSI 1.5 GHz.

8.1 EXPERIMENTAL SETUP

8.1.1 *GPR*

The GPR system used for the experimental work was the SIR3000 GSSI system which consists of the digital control unit, display screen, battery, charger, the antenna and a survey cart or buggy. The cart was not needed for this experiment. The antenna has a centre frequency of 1.5 GHz which was ideal for low penetration depth with high resolution as needed for this study.

8.1.2 *Sand box and buried targets*

The experiment took place over a large sandbox that was used to bury targets at a specific depth. In this study a PEC or metal sheet and a foam or air-void were buried at various depths and the TWTT were recorded and compared with simulated data.

8.2 LABORATORY EXPERIMENTS FOR TIME-ZERO

8.2.1 *Experimental method*

During the experiment, a PEC plate was positioned at the bottom of a sandbox. The sand thickness above the PEC varied between 0.1 to 0.28 meters. The received signals are affected by the depth of the target hence different thicknesses were examined as in reality the depth is unknown. The antenna was positioned directly on top of the sand. The slope of the sand and wood structure surrounding the experiment had zero effect on the GPR signals. The GPR time window was set

at 6 *ns*. To keep the experiment simple, the surface of the sand was made relatively smooth as rough surfaces can substantially affect the directivity pattern of the signal. Figure 8.1 shows this experimental setup.

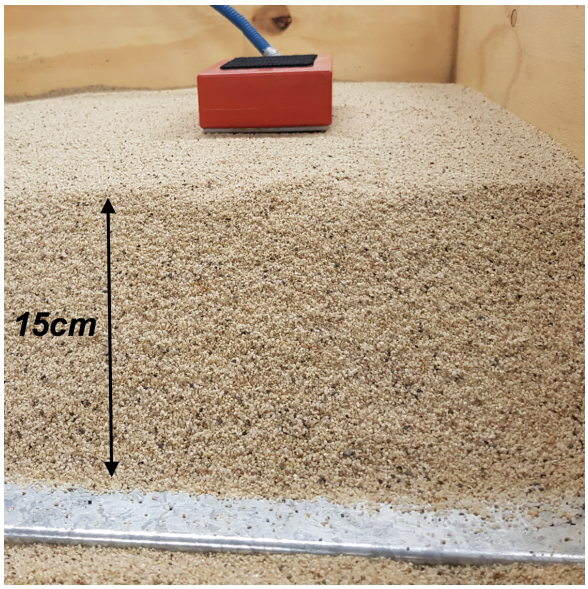

Figure 8.1: Experimental setup for verification of the proposed time-zero methodology. Here the real GSSI 1.5 GHz centre frequency antenna was placed in a sandbox directly above the sand, with a metal (PEC) sheet buried at the bottom.

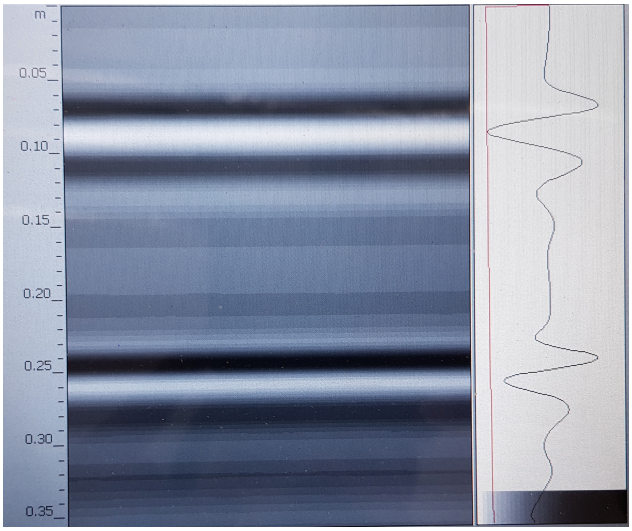

Figure 8.2: Trace (A-scan) representation and cross section (B-scan) shown on the GPR display unit.

8.2.2 *Permittivity calculation of sand*

In order to process the collected data, the permittivity of the sand needed to be calculated and verified. The known parameters were the travels distance of the signal and the two-way travel time (TWTT). Therefore, the velocity of the signal that travels through the medium was calculated. Using the calculated velocity and dielectric properties of free-space the relative permittivity of the sand was predicted. The value in this particular case was determined to be $\varepsilon_r = 2.25$ (very dry sand). By using this value, the target depth was back calculated and compared with the real or known depth.

8.2.3 *Depth measurement method*

The Distance Measurement Instrument (DMI) for measuring the depth from the antenna to the target was carried out using a ruler as shown in Figure 8.3.

Figure 8.3: A ruler was used to measure the depth of the target.

8.2.4 *Real and simulated data comparison*

Figure 8.4 presents a comparison of the real and modelled data in terms of the field strength, phase, and shape of individual wavelets. The real wavelet was produced by the real GSSI 1.5 GHz antenna and the model uses a look-alike GSSI model. The target for both cases was a PEC plate with a low permittivity half-space such as dry sand. As shown in Figure 8.4, both signals were in great agreement.

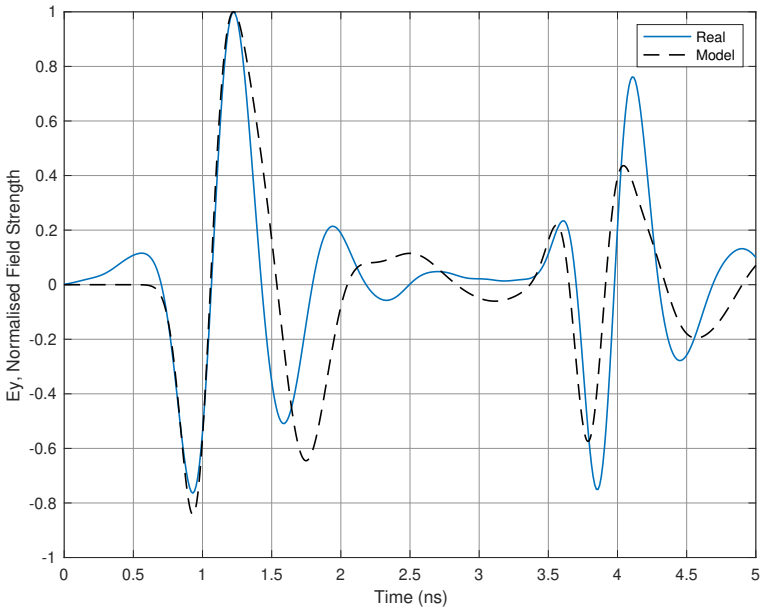

Figure 8.4: Numerical and real normalised traces (A-scans) for the experiment presented in Figure 8.1. The traces presents a PEC reflection through a half-space of sand. Both real and numerical outputs were in great agreement.

8.2.5 *Air-void target experiment*

To verify the procedure using a low permittivity target such as air-void, we replace the PEC target with a foam sheet which mimics free-space or an air-void target. The foam was 5.5 *cm* thick and it was buried 23 *cm* away from the antenna in dry sand as shown in Figure 8.5.

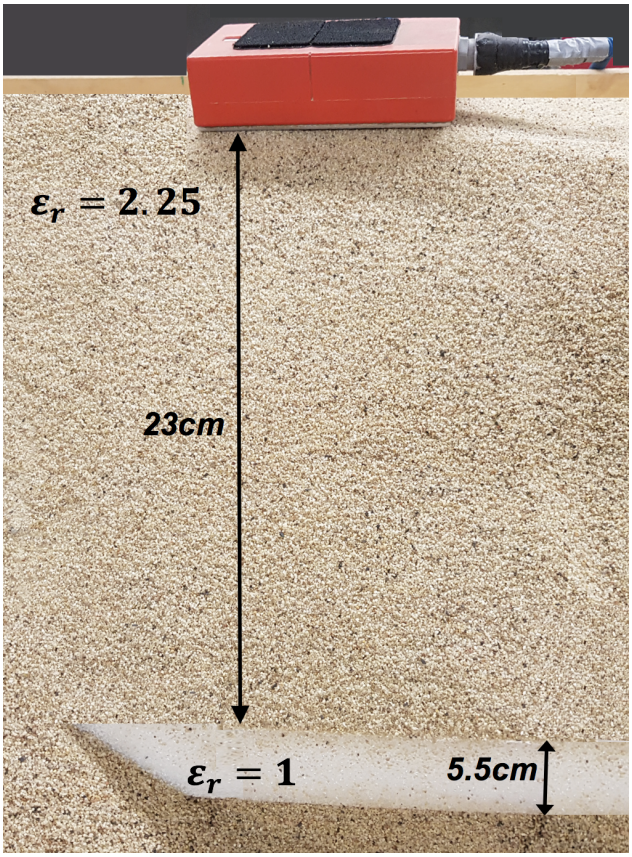

Figure 8.5: Air-void target experiment setup.

Figure 8.6: Foam sheet were used as an air-void target as they have an equivalent permittivity to air $\varepsilon_r = 1$.

The results for this experiment and the numerical modelling for a air-void target can be seen in Figure 8.7. Both the wavelets were in great agreement. Calculating the depth from the TWTT of the real signal results in around 1 *cm* depth error. This process was repeated for different depths and consistency can be seen during the calculations.

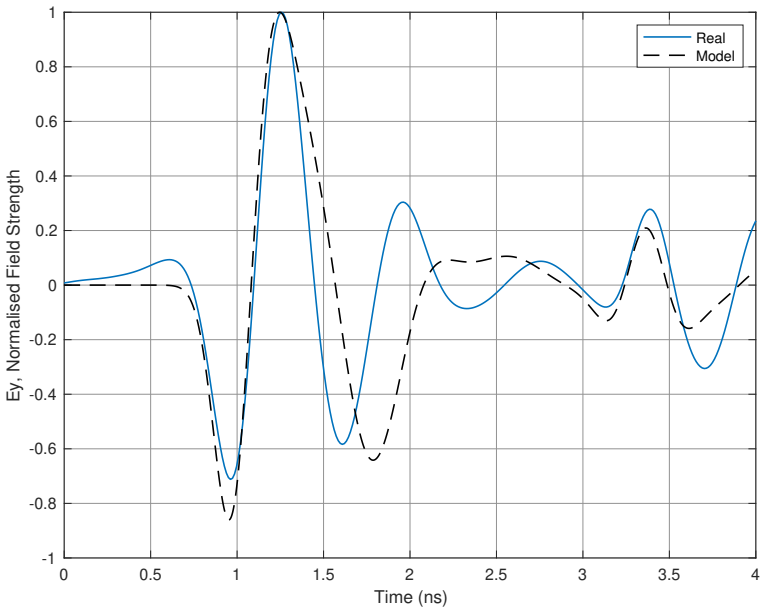

Figure 8.7: Numerical and real normalised traces (A-scans) for the experiment presented in Figure 8.5. The traces presents the air-void reflection through a sand medium. Both real and numerical outputs were in great agreement.

8.2.6 *Silicon target*

A silicon pipe target was also examined but due to the closeness of the permittivity of sand and the pipe, the received reflection was hard to observe on the trace displayed. Therefore, no further work was done in terms of the silicon target.

Figure 8.8: Silicon pipe target.

The proposed time-zero methodology has shown great potential. Overall the depth error was low and showed great consistency. Following the success of validating the proposed methodology through numerical modelling, the same error calculation procedure was performed for the real data collected for the laboratory experiments. As shown in Figure 8.9, the output results have great consistency with average depth error of 1 *cm*. In comparison with all the time-zero picking methods such as positive to positive, positive to negative, etc, the new method has shown to be the most reliable and precise method. The accuracy of the method has been carefully analysed at a detailed level and it has shown great success both in numerical modelling and experimental work.

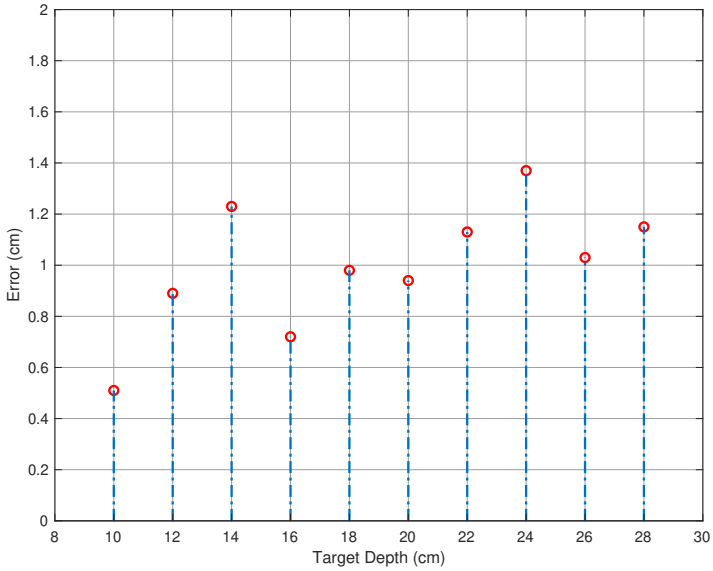

Figure 8.9: The outcome of the laboratory experiment for different PEC target depths and error correction needed. The results have great consistency with low depth error. It is also in good agreement with the simulation results.

Table 8.1 shows the depth error with the proposed time-zero and the previously used method (Yelf, 2004). As shown in this table, in some cases the positive to positive method (Yelf, 2004) works well but once the target is changed the depth error changes significantly. However, the proposed time-zero method shows consistency throughout the numerical and laboratory work performed during this thesis.

Time-zero method	Air-void target	PEC target
Positive to positive peaks (Yelf, 2004)	2 *cm* error	0.7 *cm* error
Negative to three peaks (proposed methodology)	1.1 *cm* error	1.2 *cm* error

Table 8.1: Proposed time-zero method comparison.

8.3 LABORATORY EXPERIMENTS FOR CRIM MODEL

In this section, the revised shape factor was tested in a laboratory experiment using a commercial horn antenna with 1 GHz central frequency. The experimental configuration is shown in Figure 8.10. The horn antenna was placed at ≈ 40 *cm* above a surface consisted of 18 homogeneous and well matured concrete blocks tightly packed. The dimensions of the concrete blocks were $40\ cm \times 20\ cm \times 10\ cm$. The bulk permittivity of the concrete surface was evaluated based on equation (8.1) (Saarenketo & Scullion, 2000b).

$$\varepsilon = \left(\frac{1 + A_1/A_m}{1 - A_1/A_m}\right)^2 \tag{8.1}$$

where A_1 is the amplitude of the reflection from the concrete surface and A_m is the amplitude of the reflection when the concrete surface was replaced with a PEC (Saarenketo & Scullion, 2000b). A zero-offset correction was applied to each scan in an effort to remove static components that might compromise the accuracy of the measurements. The bulk permittivity of the concrete blocks was estimated using (8.1) $\varepsilon_c \approx 7.8$. Subsequently, the gaps between the concrete blocks were gradually widen from $0 - 2$ *cm* with 5 *mm* steps in an effort to artificially increase the air-voids in a controlled manner and see the overall effects to the bulk permittivity. Doing this, the bulk permittivity of the mixture concrete/air-voids can be evaluated with respect to the artificially created air-voids.

Since the permittivity of the concrete blocks is known ($\varepsilon_c \approx 7.8$), the bulk permittivity of the concrete/air-voids mixture can also be estimated using the CRIM model

$$\varepsilon_b = ((1 - V_a)\varepsilon_c^{\alpha} + V_a\varepsilon_a^{\alpha})^{1/\alpha} \tag{8.2}$$

where ε_b is the CRIM-based bulk permittivity of the mixture concrete/air-voids, V_a is volumetric fraction of the artificially created air-voids, $\varepsilon_c \approx 7.8$ is the relative bulk permittivity of the concrete blocks, $\varepsilon_a = 1$ is the relative permittivity of free-space and α is the shape factor. The revised shape factor $\alpha = 0.13$ and the default-one $\alpha = 0.5$ were used for the current example. The results are shown in Figure 8.11. The measured relative permittivity using (8.1) with respect to the artificially created air-gaps is illustrated with dots. The relative bulk permittivity estimated using CRIM (8.2) with $\alpha = 0.5$ and $\alpha = 0.13$ are illustrated with dotted and solid lines respectively. It is apparent that the CRIM model using the optimised shape factor $\alpha = 0.13$ matches the measured bulk permittivity and clearly over-performs the default $\alpha = 0.5$.

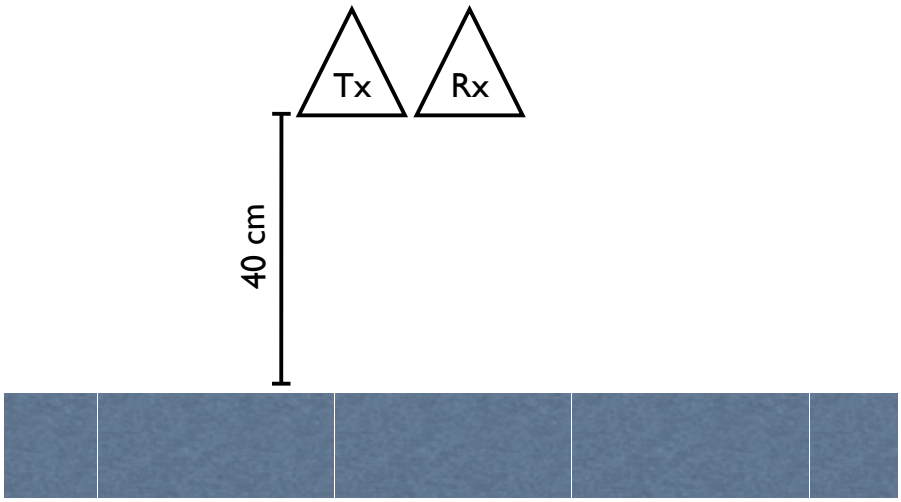

Figure 8.10: The experimental framework used to validate the revised shape factor. A horn antenna with 1 GHz central frequency was placed on top of a surface consisted of concrete blocks. The gaps between the concrete blocks were gradually increased in an effort to increase the overall volumetric fraction of air.

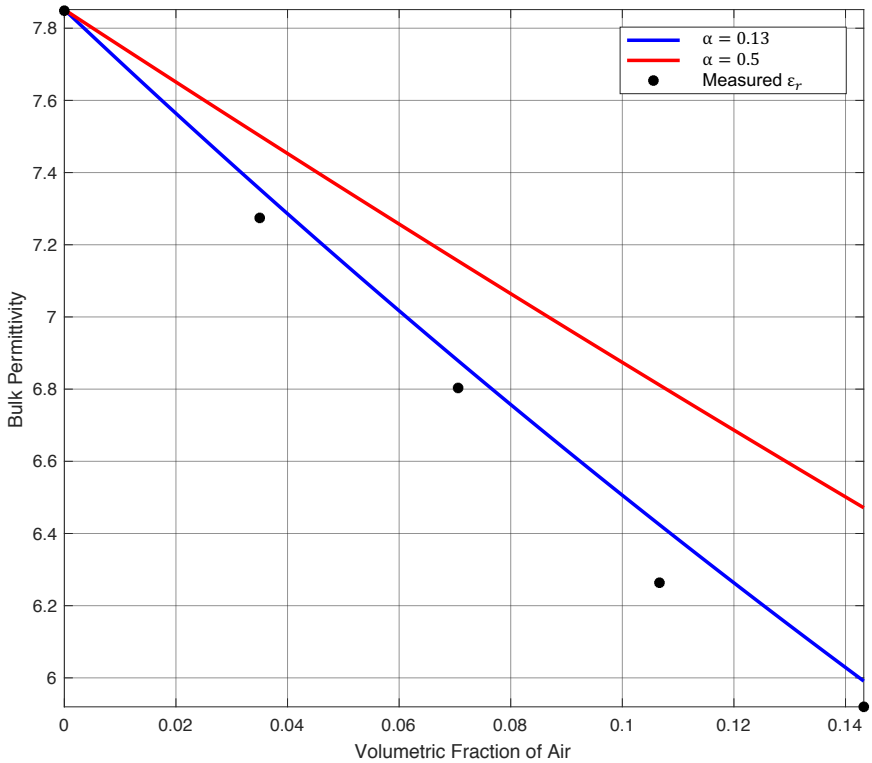

Figure 8.11: The measured and the calculated bulk permittivity using $\alpha = 0.5$ and $\alpha = 0.13$. It is apparent that the revised shape factor $\alpha = 0.13$ out performs the default $\alpha = 0.5$.

8.4 SUMMARY

In this chapter, laboratory experiments were conducted in order to validate the simulation results. A series of experiments with different target materials and depths were carried out. The comparison of the real and modelled data showed great agreement. This complements the numerical modelling work and shows the accuracy of the half-space and antenna models providing confidence for future more complex studies.

9 CONCLUSION AND RECOMMENDATIONS

The aim of this chapter is to summarise the outputs of each chapter and to provide the overall conclusions for the thesis. Further to this research, some recommendations are given for further research and development.

9.1 CONCLUSIONS

The main two aims of this thesis were to investigate the time-zero problem that many GPR users are dealing with and to define a certain position that works for most scenarios and that target depths can be estimated with the least amount of error and high consistency. Secondly, research was conducted in regards to the shape factor of the CRIM model formula in order to find a better geometric parameter to accurately calculate the bulk permittivity of different mixtures.

To investigate the time-zero issue, a large number of environments were tested. These environments involve different target depths, various target shapes, sizes and targets material compositions, half-space permittivity, use of different antennas, and so forth. Homogeneous and heterogeneous media were also taken into consideration to test how the signal behaves in the simplest environments with realistic features. The process was accomplished by using gprMax, MATLAB and ParaView to build and evaluate the models.

9.1.1 *Development of heterogeneous model*

This study needed a realistic and accurate numerical framework. The dielectric properties of the model, the geometry of the material, how the electrical properties are distributed and the use of realistic mixture percentages were researched and modelled. The benefit of such model allows GPR users to investigate the time-zero position problem by employing a model that is realistic and that it allows to compare its results with real tests done on actual concrete.

- Aggregates were designed as spheres and were randomly distributed within the model. The aggregate comes in different random sizes. The reason for the sphere shape was discussed in depth in Chapter 4.
- Concrete construction contains some air-voids (free-space) within the mixture. The air-voids have also been randomly distributed as small particles.

- Another key component to the concrete mixture is the moisture content. The moisture is bond water which has a lower permittivity in comparison to free water. As the permittivity is high, a small change in the moisture percentage can vary the concrete permittivity significantly. Here, it was distributed in the same way as the air-voids.
- The final component is cement, programmed as the background material which fills in all the gaps in the model.
- Features such as the random distribution of the concrete components, overlapping of the materials, how the overlapping affects the material percentage or volume and the different shaped aggregates effect have been taken into consideration and can be found in Chapter 4.

9.1.2 *Development of a bowtie separated antenna model*

At the time of the research, a realistic antenna that the transmitter and receiver are able to move independently was not available. The benefits of such an antenna model allows for a realistic simulation. The GSSI 1.5 GHz centre frequency antenna designed by Warren (2009) was used as a reference point for the modelling of the antenna. The main new features of the separated antenna are:

- Separated transmitter and receiver bowties that can move independently. These antenna features are used for GPR data acquisition methods such as the WARR and CMP methods.
- The transmitter and receiver each have a separated electromagnetic absorber, PCB, shielding and case.
- Different case and shield geometries were used in comparison with the existing GSSI antenna model structure.

9.1.3 *Optimising the time-zero method*

The main aim of this study was to achieve the best solution for the time-zero position that works for the majority of cases (Chapter 5). This would lead GPR users to become more familiar to the real and modelled wavelet shape information from a typical GPR target. As the target shape, material, depth etc are unknown, a time-zero method was needed to not be dependant on such features. The benefit of the proposed time-zero method allows GPR users to be consistent throughout a survey or data collection without the need of adjusting the time-zero position. On the other hand, this method on average results in a low depth error in comparison with other time-zero picking methods. The numerical modelling to find the optimum position experimented with:

- Different target depths to examine shallow and deep target responses.
- Various target shapes such as cylinder, sphere, box, etc were modelled. Obviously there many other target shapes but it is impossible to model everything plus it would not benefit this study to a great extent.
- The target materials were unknown so each target shape was simulated using different dielectric properties.
- The subsurface can vary in many patterns or structural appearances therefore, embedding targets in different environments (different half-space permittivities) were taken into consideration.
- The antennas used for the numerical simulations was an existing model of a GSSI 1.5 GHz centre frequency antenna, however, other excitation sources such as a theoretical line source and the new separated bowtie antenna structure were also tested.
- To be realistic, heterogeneous modelling was also considered. This involvement was discussed in depth in Chapter 4.
- The time-zero was validated using experimental work in the laboratory as discussed in Chapter 8.

9.1.4 *Optimising the CRIM model*

Another aspect of this research was to optimise the shape factor for the CRIM mixing model by using realistic GPR models. Having obtained a realistic heterogeneous model and antenna plus having an accurate time-zero method gave the confidence to investigate the shape factor further. The proposed shape factor or modified CRIM model resulted in higher reliability and more accurate bulk permittivity prediction. Having such accuracy in the permittivity estimation of complex mixture allows GPR measurements to be more precise. This can have a positive impact on GPR research and overall benefit GPR studies in many ways. The numerical modelling for the CRIM model investigation involved the following:

- Based on concretes components (aggregate, cement, air-void and moisture content), different mixture percentages were simulated and the bulk permittivity of each model was calculated based on the TWTT of the received wavelet.
- Using the original CRIM model, the bulk permittivity for the given material percentages were also calculated.
- The same percentages were inserted in other mixing models such as the Rayleigh and Böttcher models in order to compare with

the original and proposed CRIM models. Other mixing models can also be implemented for comparing purposes but in this study two mixing models were used.

- The simulated models were designed in 3D with a GSSI 1.5 GHz centre frequency antenna pair on the surface. At first, the modelling was kept as 2D using a line source for a higher time efficiency until a working framework was accomplished. This gave the confidence to move on to complex modelling with higher time-consuming simulations. This made the results have higher reliability.
- Through numerical and laboratory measurements, the proposed modified CRIM is a more reliable method for predicting the dielectric properties of concrete based on its components.

9.2 RECOMMENDATIONS

This study has led to a more accurate and consistent time-zero methodology, a better shape factor for the CRIM model and a new 3D separated bowtie antenna design. Although all of the above have been tested in every aspect, further research maybe needed to increase the reliability and investigate further improvements for a higher accuracy of the models and apply them to other research topics. Here are some opportunities for further research:

- Depending on computational resources, increasing the realistic geometry of the models can be beneficial to the result reliability.
- Include losses into the concrete model. This can make picking a more challenging issue as signal amplitudes will reduce with increasing sigma.
- Surface roughness can be added to the concrete model especially at high frequencies. This can be important as it can affect the received signals.
- Take advantage of the designed separated bowtie antenna for further research that requires this kind of antenna geometry.
- Employ the bowtie antenna pair in a user-friendly package to be used by a wider range of researchers and solve any related problems.
- Other commercial antennas structures such as the $MALÅ$ 1.2 GHz can be modelled and used as another source to simulate mixing models for further investigation of the time-zero.
- Employ the proposed time-zero method to other research topics which involve target distance or depth estimations for better consistency and higher accuracy results.

- Further research on the CRIM shape factor can use Particle Swarm Optimisation (PSO) method to investigate a more precise shape factor. This method will have different shape factor values for each material rather than having one shape factor for all the materials. This may benefit the accuracy of the shape factor and predict better bulk permittivities.

A

UPDATE EQUATIONS FOR THE FDTD METHOD

$$
\begin{aligned}
E_x\Big|_{i,j+\frac{1}{2},k+\frac{1}{2}}^{n+\frac{1}{2}} = & \left(\frac{1-\frac{\sigma_{i,j+\frac{1}{2},k+\frac{1}{2}}\Delta t}{2\epsilon_{i,j+\frac{1}{2},k+\frac{1}{2}}}}{1+\frac{\sigma_{i,j+\frac{1}{2},k+\frac{1}{2}}\Delta t}{2\epsilon_{i,j+\frac{1}{2},k+\frac{1}{2}}}} \right) E_x\Big|_{i,j+\frac{1}{2},k+\frac{1}{2}}^{n-\frac{1}{2}} \\
& + \left(\frac{\frac{\Delta t}{\epsilon_{i,j+\frac{1}{2},k+\frac{1}{2}}}}{1+\frac{\sigma_{i,j+\frac{1}{2},k+\frac{1}{2}}\Delta t}{2\epsilon_{i,j+\frac{1}{2},k+\frac{1}{2}}}} \right) \frac{H_x\Big|_{i,j+1,k+\frac{1}{2}}^{n} - H_z\Big|_{i,j,k+\frac{1}{2}}^{n}}{\Delta y} \\
& - \left(\frac{\frac{\Delta t}{\epsilon_{i,j+\frac{1}{2},k+\frac{1}{2}}}}{1+\frac{\sigma_{i,j+\frac{1}{2},k+\frac{1}{2}}\Delta t}{2\epsilon_{i,j+\frac{1}{2},k+\frac{1}{2}}}} \right) \frac{H_y\Big|_{i,j+\frac{1}{2},k+1}^{n} - H_y\Big|_{i,j+\frac{1}{2},k}^{n}}{\Delta z} \\
& - \left(\frac{\frac{\Delta t}{\epsilon_{i,j+\frac{1}{2},k+\frac{1}{2}}}}{1+\frac{\sigma_{i,j+\frac{1}{2},k+\frac{1}{2}}\Delta t}{2\epsilon_{i,j+\frac{1}{2},k+\frac{1}{2}}}} \right) J_{S_x}\Big|_{i,j+\frac{1}{2},k+\frac{1}{2}}^{n}
\end{aligned}
\tag{A.1}
$$

$$
\begin{aligned}
E_y\Big|_{i-\frac{1}{2},j+1,k+\frac{1}{2}}^{n+\frac{1}{2}} = & \left(\frac{1-\frac{\sigma_{i-\frac{1}{2},j+1,k+\frac{1}{2}}\Delta t}{2\epsilon_{i-\frac{1}{2},j+1,k+\frac{1}{2}}}}{1+\frac{\sigma_{i-\frac{1}{2},j+1,k+\frac{1}{2}}\Delta t}{2\epsilon_{i-\frac{1}{2},j+1,k+\frac{1}{2}}}} \right) E_y\Big|_{i-\frac{1}{2},j+1,k+\frac{1}{2}}^{n-\frac{1}{2}} \\
& + \left(\frac{\frac{\Delta t}{\epsilon_{i-\frac{1}{2},j+1,k+\frac{1}{2}}}}{1+\frac{\sigma_{i-\frac{1}{2},j+1,k+\frac{1}{2}}\Delta t}{2\epsilon_{i-\frac{1}{2},j+1,k+\frac{1}{2}}}} \right) \frac{H_x\Big|_{i-\frac{1}{2},j+1,k+1}^{n} - H_z\Big|_{i-\frac{1}{2},j+1,k}^{n}}{\Delta z} \\
& - \left(\frac{\frac{\Delta t}{\epsilon_{i-\frac{1}{2},j+1,k+\frac{1}{2}}}}{1+\frac{\sigma_{i-\frac{1}{2},j+1,k+\frac{1}{2}}\Delta t}{2\epsilon_{i-\frac{1}{2},j+1,k+\frac{1}{2}}}} \right) \frac{H_z\Big|_{i,j+1,k+\frac{1}{2}}^{n} - H_z\Big|_{i-1,j+1,k+\frac{1}{2}}^{n}}{\Delta x} \\
& - \left(\frac{\frac{\Delta t}{\epsilon_{i-\frac{1}{2},j+1,k+\frac{1}{2}}}}{1+\frac{\sigma_{i-\frac{1}{2},j+1,k+\frac{1}{2}}\Delta t}{2\epsilon_{i-\frac{1}{2},j+1,k+\frac{1}{2}}}} \right) J_{S_y}\Big|_{i-\frac{1}{2},j+1,k+\frac{1}{2}}^{n}
\end{aligned}
\tag{A.2}
$$

$$
\begin{aligned}
E_z\Big|_{i-\frac{1}{2},j+\frac{1}{2},k+1}^{n+\frac{1}{2}} = {} & \left(\frac{1-\frac{\sigma_{i-\frac{1}{2},j+\frac{1}{2},k+1}\Delta t}{2\epsilon_{i-\frac{1}{2},j+\frac{1}{2},k+1}}}{1+\frac{\sigma_{i-\frac{1}{2},j+\frac{1}{2},k+1}\Delta t}{2\epsilon_{i-\frac{1}{2},j+\frac{1}{2},k+1}}} \right) E_z\Big|_{i-\frac{1}{2},j+\frac{1}{2},k+1}^{n-\frac{1}{2}} \\
& + \left(\frac{\frac{\Delta t}{\epsilon_{i-\frac{1}{2},j+\frac{1}{2},k+1}}}{1+\frac{\sigma_{i-\frac{1}{2},j+\frac{1}{2},k+1}\Delta t}{2\epsilon_{i-\frac{1}{2},j+\frac{1}{2},k+1}}} \right) \frac{H_y\Big|_{i,j+\frac{1}{2},k+1}^{n} - H_y\Big|_{i-1,j+\frac{1}{2},k+1}^{n}}{\Delta x} \\
& + \left(\frac{\frac{\Delta t}{\epsilon_{i-\frac{1}{2},j+\frac{1}{2},k+1}}}{1+\frac{\sigma_{i-\frac{1}{2},j+\frac{1}{2},k+1}\Delta t}{2\epsilon_{i-\frac{1}{2},j+\frac{1}{2},k+1}}} \right) \frac{H_x\Big|_{i-\frac{1}{2},j+1,k+1}^{n} - H_x\Big|_{i-\frac{1}{2},j,k+1}^{n}}{\Delta y} \\
& + \left(\frac{\frac{\Delta t}{\epsilon_{i-\frac{1}{2},j+\frac{1}{2},k+1}}}{1+\frac{\sigma_{i-\frac{1}{2},j+\frac{1}{2},k+1}\Delta t}{2\epsilon_{i-\frac{1}{2},j+\frac{1}{2},k+1}}} \right) J_{S_z}\Big|_{i-\frac{1}{2},j+\frac{1}{2},k+1}^{n}
\end{aligned}
\tag{A.3}
$$

$$
\begin{aligned}
H_x\Big|_{i-\frac{1}{2},j+1,k+1}^{n+1} = {} & \left(\frac{1-\frac{\sigma^*_{i-\frac{1}{2},j+1,k+1}\Delta t}{2\mu_{i-\frac{1}{2},j+1,k+1}}}{1+\frac{\sigma^*_{i-\frac{1}{2},j+\frac{1}{2},k+1}\Delta t}{2\mu_{i-\frac{1}{2},j+1,k+1}}} \right) H_x\Big|_{i-\frac{1}{2},j+1,k+1}^{n} \\
& + \left(\frac{\frac{\Delta t}{\mu_{i-\frac{1}{2},j+1,k+1}}}{1+\frac{\sigma^*_{i-\frac{1}{2},j+1,k+1}\Delta t}{2\mu_{i-\frac{1}{2},j+1,k+1}}} \right) \frac{E_y\Big|_{i-\frac{1}{2},j+1,k+\frac{3}{2}}^{n+\frac{1}{2}} - E_y\Big|_{i-\frac{1}{2},j+1,k+\frac{1}{2}}^{n+\frac{1}{2}}}{\Delta z} \\
& + \left(\frac{\frac{\Delta t}{\mu_{i-\frac{1}{2},j+1,k+1}}}{1+\frac{\sigma^*_{i-\frac{1}{2},j+1,k+1}\Delta t}{2\mu_{i-\frac{1}{2},j+1,k+1}}} \right) \frac{E_z\Big|_{i-\frac{1}{2},j+\frac{3}{2},k+1}^{n+\frac{1}{2}} - E_z\Big|_{i-\frac{1}{2},j+\frac{1}{2},k+1}^{n+\frac{1}{2}}}{\Delta y} \\
& + \left(\frac{\frac{\Delta t}{\mu_{i-\frac{1}{2},j+1,k+1}}}{1+\frac{\sigma^*_{i-\frac{1}{2},j+1,k+1}\Delta t}{2\mu_{i-\frac{1}{2},j+1,k+1}}} \right) M_{S_x}\Big|_{i-\frac{1}{2},j+1,k+1}^{n+\frac{1}{2}}
\end{aligned}
\tag{A.4}
$$

$$
\begin{aligned}
H_y\Big|_{i,j+\frac{1}{2},k+1}^{n+1} = & \left(\frac{1-\frac{\sigma^*_{i,j+\frac{1}{2},k+1}\Delta t}{2\mu_{i,j+\frac{1}{2},k+1}}}{1+\frac{\sigma^*_{i,j+\frac{1}{2},k+1}\Delta t}{2\mu_{i,j+\frac{1}{2},k+1}}} \right) H_y\Big|_{i,j+\frac{1}{2},k+1}^{n} \\
& + \left(\frac{\frac{\Delta t}{\mu_{i,j+\frac{1}{2},k+1}}}{1+\frac{\sigma^*_{i,j+\frac{1}{2},k+1}\Delta t}{2\mu_{i,j+\frac{1}{2},k+1}}} \right) \frac{E_z\Big|_{i+\frac{1}{2},j+\frac{1}{2},k+1}^{n+\frac{1}{2}} - E_z\Big|_{i-\frac{1}{2},j+\frac{1}{2},k+1}^{n+\frac{1}{2}}}{\Delta x} \\
& + \left(\frac{\frac{\Delta t}{\mu_{i,j+\frac{1}{2},k+1}}}{1+\frac{\sigma^*_{i,j+\frac{1}{2},k+1}\Delta t}{2\mu_{i,j+\frac{1}{2},k+1}}} \right) \frac{E_x\Big|_{i,j+\frac{1}{2},k+\frac{3}{2}}^{n+\frac{1}{2}} - E_x\Big|_{i,j+\frac{1}{2},k+\frac{1}{2}}^{n+\frac{1}{2}}}{\Delta z} \\
& + \left(\frac{\frac{\Delta t}{\mu_{i,j+\frac{1}{2},k+1}}}{1+\frac{\sigma^*_{i,j+\frac{1}{2},k+1}\Delta t}{2\mu_{i,j+\frac{1}{2},k+1}}} \right) M_{S_y}\Big|_{i,j+\frac{1}{2},k+1}^{n+\frac{1}{2}}
\end{aligned}
\tag{A.5}
$$

$$
\begin{aligned}
H_z\Big|_{i,j+1,k+\frac{1}{2}}^{n+1} = & \left(\frac{1-\frac{\sigma^*_{i,j+1,k+\frac{1}{2}}\Delta t}{2\mu_{i,j+1,k+\frac{1}{2}}}}{1+\frac{\sigma^*_{i,j+1,k+\frac{1}{2}}\Delta t}{2\mu_{i,j+1,k+\frac{1}{2}}}} \right) H_z\Big|_{i,j+1,k+\frac{1}{2}}^{n} \\
& + \left(\frac{\frac{\Delta t}{\mu_{i,j+1,k+\frac{1}{2}}}}{1+\frac{\sigma^*_{i,j+1,k+\frac{1}{2}}\Delta t}{2\mu_{i,j+1,k+\frac{1}{2}}}} \right) \frac{E_x\Big|_{i,j+\frac{3}{2},k+\frac{1}{2}}^{n+\frac{1}{2}} - E_x\Big|_{i,j+\frac{1}{2},k+\frac{1}{2}}^{n+\frac{1}{2}}}{\Delta y} \\
& + \left(\frac{\frac{\Delta t}{\mu_{i,j+1,k+\frac{1}{2}}}}{1+\frac{\sigma^*_{i,j+1,k+\frac{1}{2}}\Delta t}{2\mu_{i,j+1,k+\frac{1}{2}}}} \right) \frac{E_y\Big|_{i+\frac{1}{2},j+1,k+\frac{1}{2}}^{n+\frac{1}{2}} - E_y\Big|_{i-\frac{1}{2},j+1,k+\frac{1}{2}}^{n+\frac{1}{2}}}{\Delta x} \\
& + \left(\frac{\frac{\Delta t}{\mu_{i,j+1,k+\frac{1}{2}}}}{1+\frac{\sigma^*_{i,j+1,k+\frac{1}{2}}\Delta t}{2\mu_{i,j+1,k+\frac{1}{2}}}} \right) M_{S_z}\Big|_{i,j+1,k+\frac{1}{2}}^{n+\frac{1}{2}}
\end{aligned}
\tag{A.6}
$$

B

DERIVING EQUATIONS

B.1 DERIVING FARADAY'S LAW

$$V = -\frac{d}{dt}\iint_S \vec{B} \cdot ds \qquad (Faraday's\ Law) \tag{B.1}$$

$$V = -\iint_S \frac{\partial \vec{B}}{\partial t} \cdot ds \tag{B.2}$$

$$V = \oint \vec{E} \cdot d\vec{L} \tag{B.3}$$

$$\oint \vec{E} \cdot d\vec{L} = -\iint_S \frac{\partial \vec{B}}{\partial t} \cdot ds \tag{B.4}$$

$$\oint \vec{E} \cdot d\vec{L} = \iint_S \nabla \times \vec{E} \cdot ds \qquad (Stoke's\ \ Theorem) \tag{B.5}$$

$$\iint_S \nabla \times \vec{E} \cdot ds = -\iint_S \frac{\partial \vec{B}}{\partial t} \cdot ds \tag{B.6}$$

$$\nabla \times \vec{E} = -\frac{\partial \vec{B}}{\partial t} \tag{B.7}$$

B.2 DERIVING AMPERE'S LAW

$$I = \oint \vec{H} \cdot d\vec{L} \qquad (Ampere's\ Law) \tag{B.8}$$

$$I = \iint_S \vec{J} \cdot \vec{ds} \tag{B.9}$$

$$\oint \vec{H} \cdot d\vec{L} = \iint_S (\nabla \times \vec{H}) \cdot \vec{ds} \quad (Stoke's\ \ Theorem) \tag{B.10}$$

$$\iint_S (\nabla \times \vec{H}) \cdot \vec{ds} = \iint_S \vec{J} \cdot \vec{ds} \tag{B.11}$$

$$\nabla \times \vec{H} = \vec{J} \tag{B.12}$$

$$\vec{J}_d = \frac{\partial \vec{D}}{\partial t} \qquad (Displacement\ Current\ Density) \tag{B.13}$$

$$\vec{J}_c = \sigma \vec{E} \qquad (Conduction\ Current\ Density) \tag{B.14}$$

$$\vec{J} = \vec{J}_s + \vec{J}_c + \vec{J}_d \tag{B.15}$$

$$\iint_S (\nabla \times \vec{H}) \cdot \vec{ds} = \iint_S \left(\vec{J}_s + \vec{J}_c + \vec{J}_d\right) \cdot \vec{ds} \tag{B.16}$$

$$\iint_S (\nabla \times \vec{H}) \cdot \vec{ds} = \iint_S \left(\vec{J}_s + \sigma \vec{E} + \frac{\partial \vec{D}}{\partial t}\right) \cdot \vec{ds} \tag{B.17}$$

$$\nabla \times \vec{H} = \vec{J}_s + \sigma \vec{E} + \frac{\partial \vec{D}}{\partial t} \tag{B.18}$$

$$\vec{J} = \vec{J}_s + \sigma\vec{E} \tag{B.19}$$

$$\vec{M} = \vec{M}_s + \sigma^*\vec{H} \tag{B.20}$$

C

PLOTS

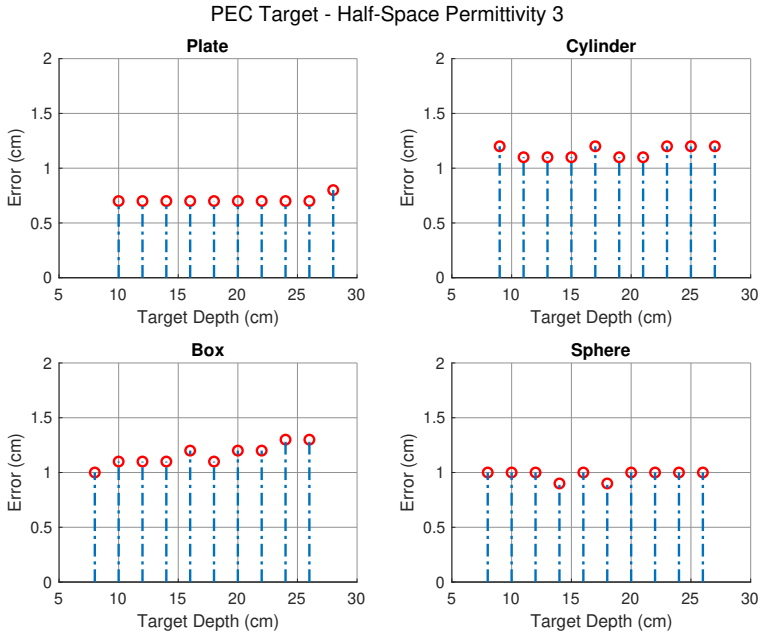

Figure C.1: PEC targets of various shapes were buried in a half-space with a dielectric constant of 3. Simulations with different shape targets at various depths have been simulated and the depth error has been shown for comparison.

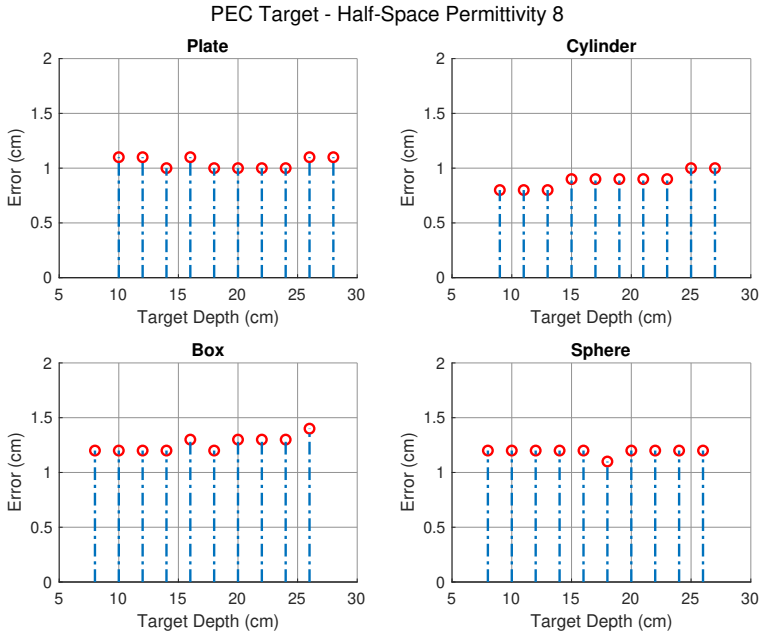

Figure C.2: PEC targets of various shapes were buried in a half-space with a dielectric constant of 8. Simulations with different shape targets at various depths have been simulated and the depth error has been shown for comparison.

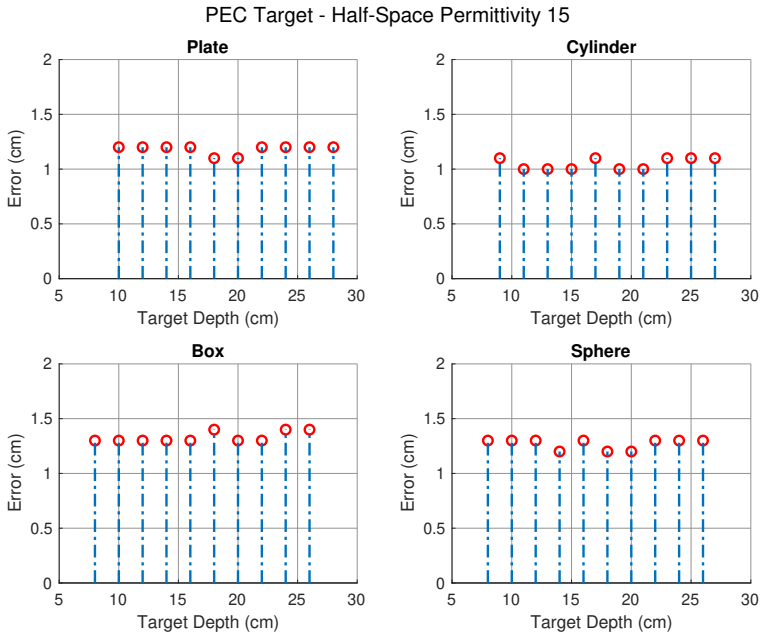

Figure C.3: PEC targets of various shapes were buried in a half-space with a dielectric constant of 15. Simulations with different shape targets at various depths have been simulated and the depth error has been shown for comparison.

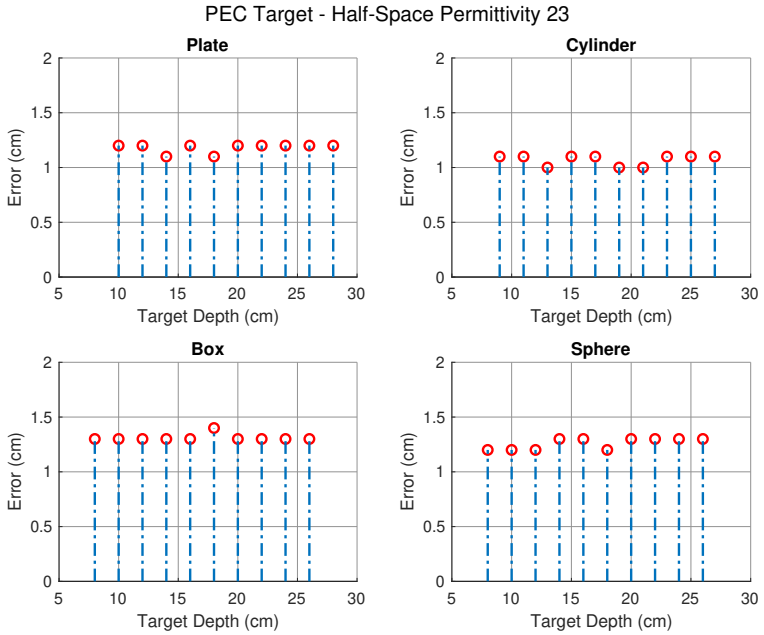

Figure C.4: PEC targets of various shapes were buried in a half-space with a dielectric constant of 23. Simulations with different shape targets at various depths have been simulated and the depth error has been shown for comparison.

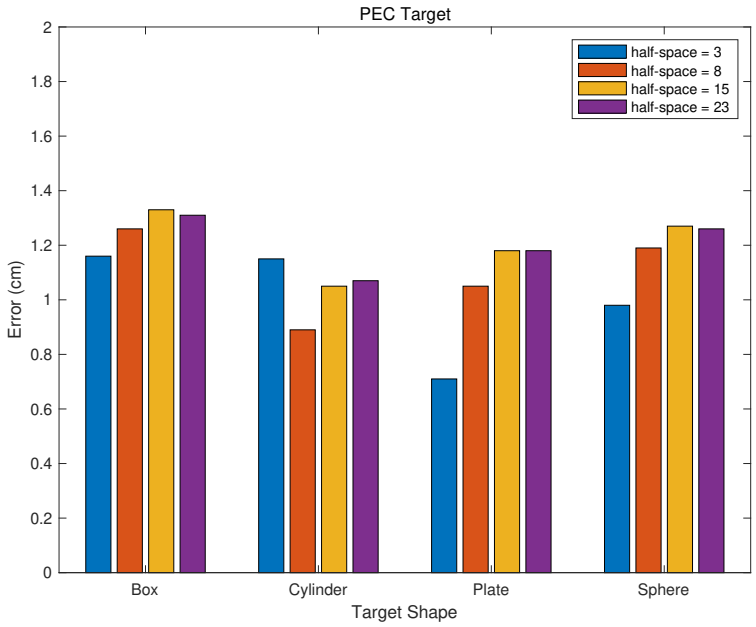

Figure C.5: An average of all the depth errors for each target shape for all the different half-spaces have been displayed together for a better comparison and to show the consistency of the method.

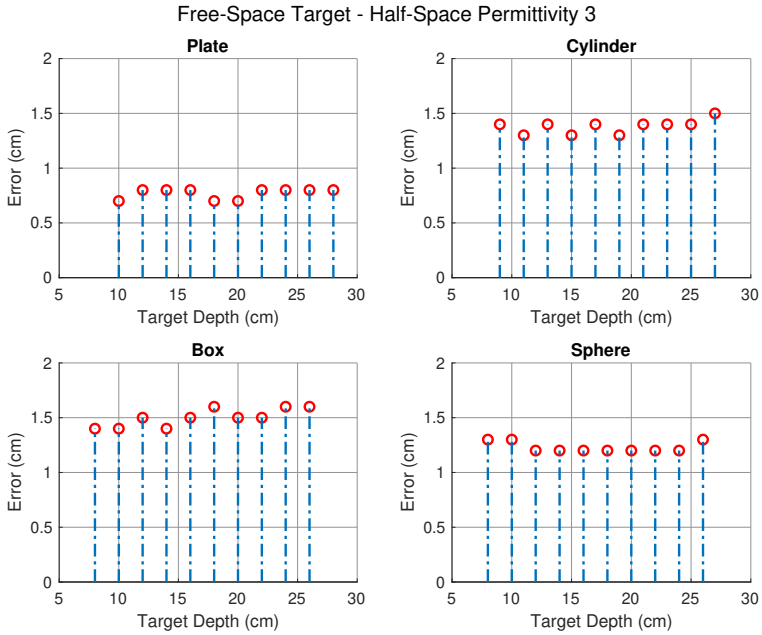

Figure C.6: Free-space targets of various shapes with relative permittivity of 1 were buried in a half-space with a dielectric constant of 3. Simulations with different shape targets at various depths have been simulated and the depth error has been shown for comparison.

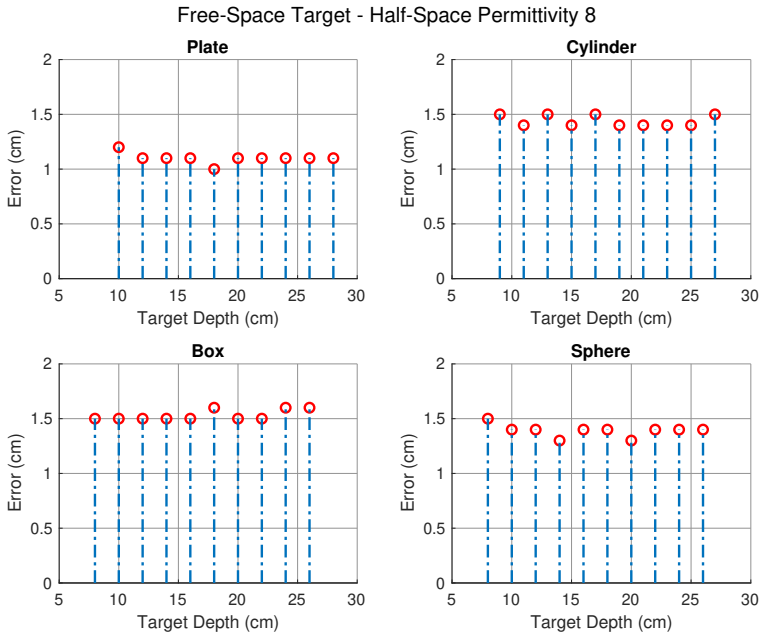

Figure C.7: Free-space targets of various shapes with relative permittivity of 1 were buried in a half-space with a dielectric constant of 8. Simulations with different shape targets at various depths have been simulated and the depth error has been shown for comparison.

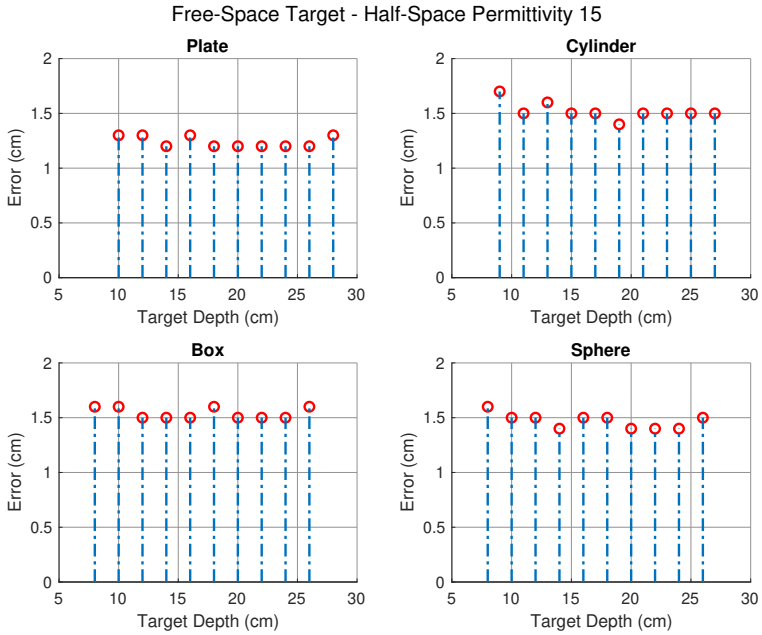

Figure C.8: Free-space targets of various shapes with relative permittivity of 1 were buried in a half-space with a dielectric constant of 15. Simulations with different shape targets at various depths have been simulated and the depth error has been shown for comparison.

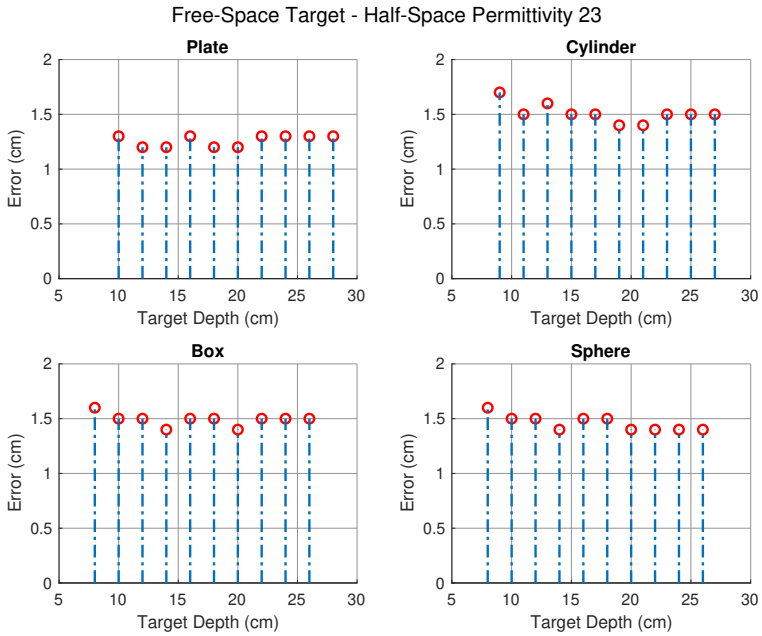

Figure C.9: Free-space targets of various shapes with relative permittivity of 1 were buried in a half-space with a dielectric constant of 23. Simulations with different shape targets at various depths have been simulated and the depth error has been shown for comparison.

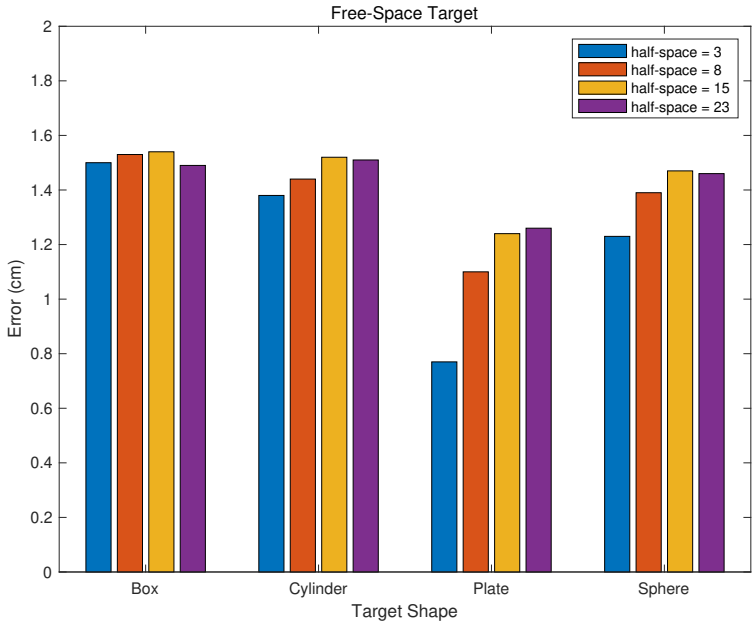

Figure C.10: An average of all the depth errors for each target shape for all the different half-spaces have been displayed together for a better comparison and to show the consistency of the method.

Figure C.11: Silicon targets of various shapes with relative permittivity of 11 were buried in a half-space with a dielectric constant of 3. Simulations with different shape targets at various depths have been simulated and the depth error has been shown for comparison.

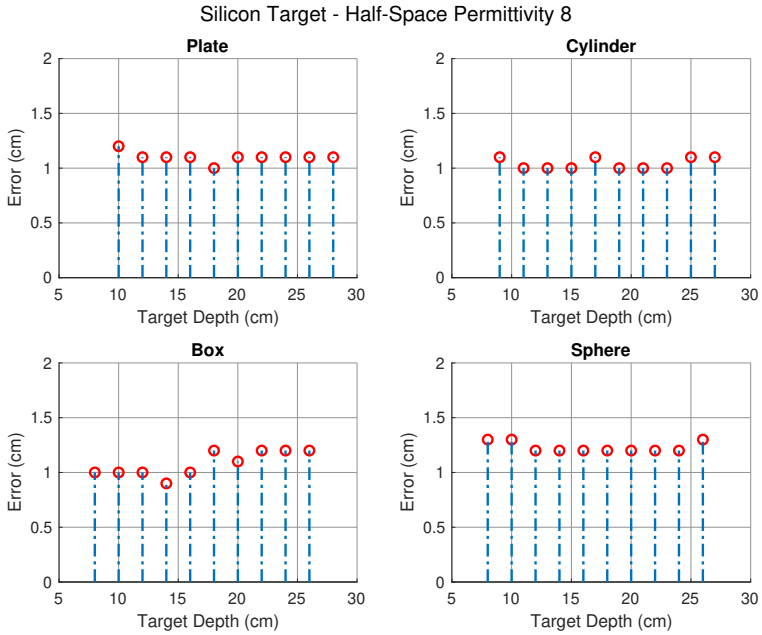

Figure C.12: Silicon targets of various shapes with relative permittivity of 11 were buried in a half-space with a dielectric constant of 8. Simulations with different shape targets at various depths have been simulated and the depth error has been shown for comparison.

Figure C.13: Silicon targets of various shapes with relative permittivity of 11 were buried in a half-space with a dielectric constant of 15. Simulations with different shape targets at various depths have been simulated and the depth error has been shown for comparison.

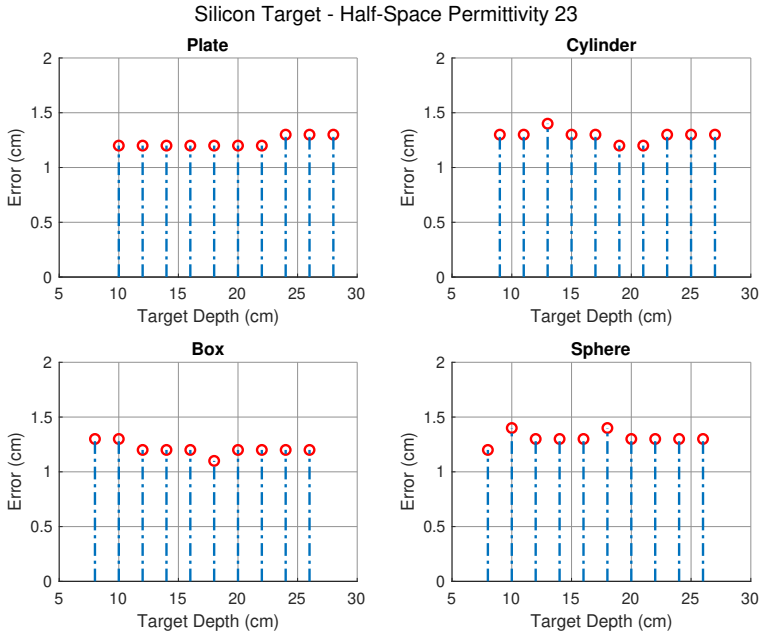

Figure C.14: Silicon targets of various shapes with relative permittivity of 11 were buried in a half-space with a dielectric constant of 23. Simulations with different shape targets at various depths have been simulated and the depth error has been shown for comparison.

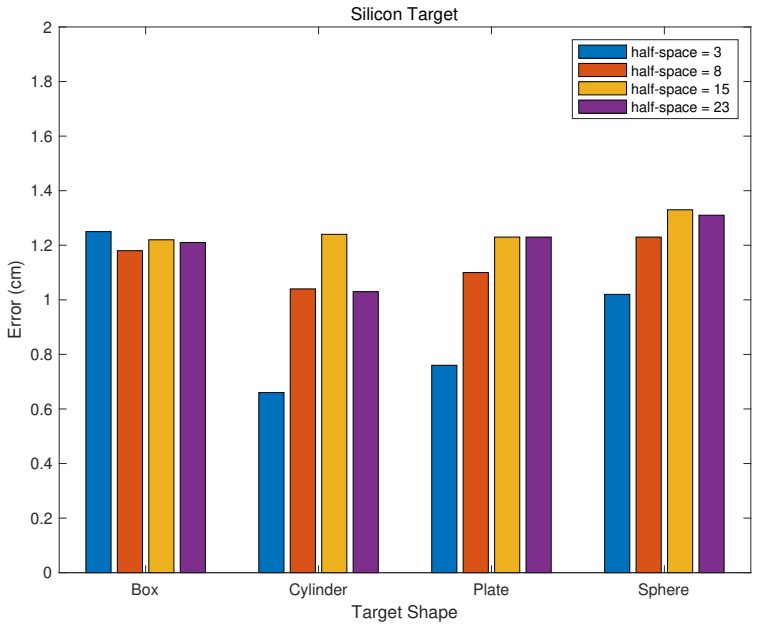

Figure C.15: An average of all the depth errors for each target shape for all the different half-spaces have been displayed together for a better comparison and to show the consistency of the method.

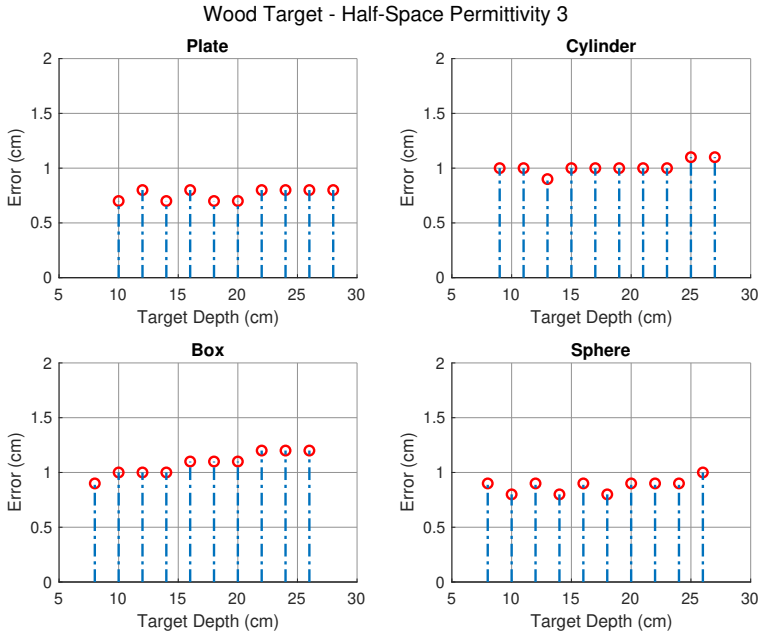

Figure C.16: Wood targets of various shapes with relative permittivity of 5 were buried in a half-space with a dielectric constant of 3. Simulations with different shape targets at various depths have been simulated and the depth error has been shown for comparison.

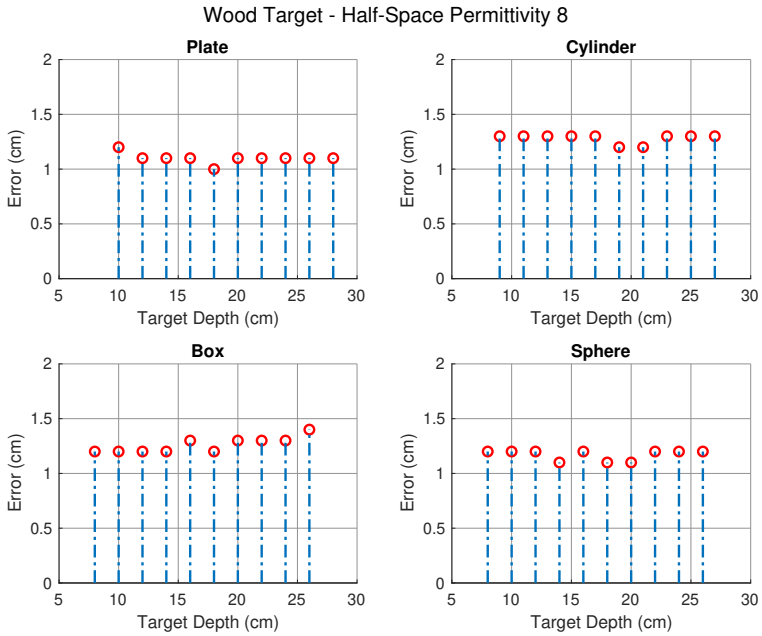

Figure C.17: Wood targets of various shapes with relative permittivity of 5 were buried in a half-space with a dielectric constant of 8. Simulations with different shape targets at various depths have been simulated and the depth error has been shown for comparison.

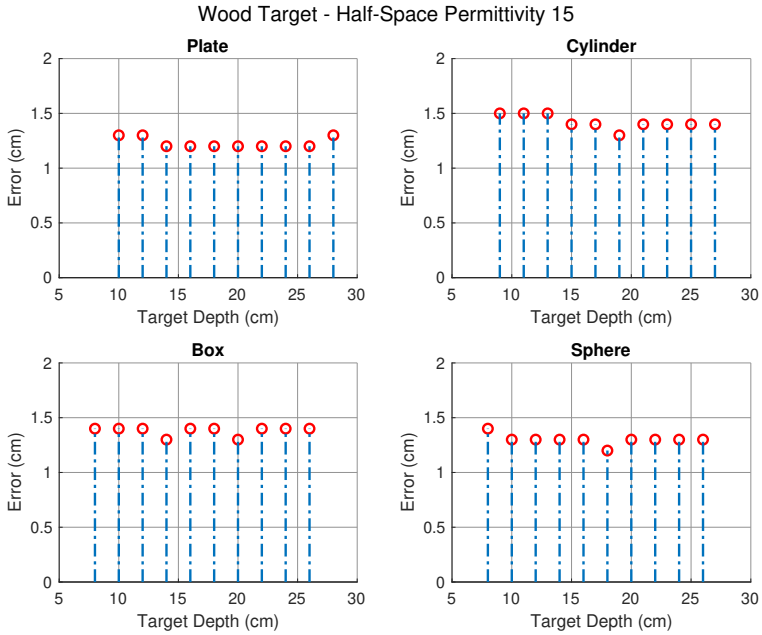

Figure C.18: Wood targets of various shapes with relative permittivity of 5 were buried in a half-space with a dielectric constant of 15. Simulations with different shape targets at various depths have been simulated and the depth error has been shown for comparison.

Figure C.19: Wood targets of various shapes with relative permittivity of 5 were buried in a half-space with a dielectric constant of 23. Simulations with different shape targets at various depths have been simulated and the depth error has been shown for comparison.

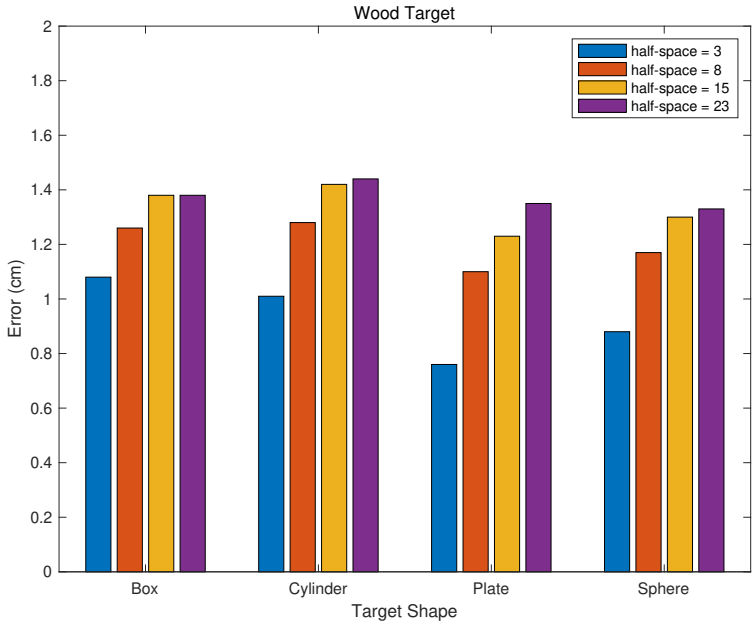

Figure C.20: An average of all the depth errors for each target shape for all the different half-spaces have been displayed together for a better comparison and to show the consistency of the method.

D

CODE

D.1 CIRCLE PACKING

```
#title: concrete 2D

#domain: 0.3 0.001 0.36
#dx_dy_dz: 0.001 0.001 0.001
#time_window: 12e-9

#material: 7 0 1 0 aggregate
#material: 3 0 1 0 cement
#material: 37.54 0 1 0 water

#box: 0 0 0.05 0.3 0.001 0.3 cement n

#python:


import random
import math
from gprMax.input_cmd_funcs import sphere
from gprMax.input_cmd_funcs import box

class Aggregate():
    def __init__(self, p_aggregate):
        self.x = random.uniform(0.01,0.29)
        self.z = random.uniform(0.05,0.29)

        if p_aggregate > 0.60:
            lower = 0.001
            upper = 0.002
        if p_aggregate > 0.80:
            lower = 0.0005
            upper = 0.001
        else:
            lower = 0.004
            upper = 0.008

        radius = random.uniform(lower,upper)
        self.r = radius

    def check_collision(*args): #*args = (aggregate =
        [], agg = Aggregate())
        j = 0
        no_coll = False
        while j < len(aggregate) and no_coll is False
            :
```

```
            other = aggregate[j]
            point_dist = math.sqrt((agg.x - other.x)
                **2 + (agg.z - other.z)**2)
            j += 1
            if point_dist <= agg.r + other.r:
                no_coll = True
        return no_coll

area_sum = 0

p_aggregate = 0

area_box = 0.28 * 0.24

aggregate = []

while p_aggregate < 0.6:
    agg = Aggregate(p_aggregate)
    if agg.check_collision(aggregate, agg) is False:
    aggregate.append(agg)
    area_sum += math.pi*agg.r**2
    p_aggregate = area_sum / area_box

for i in range(0, len(aggregate)):
    agg = aggregate[i]
    sphere(agg.x, 0.001, agg.z, agg.r, 'aggregate', '
        n')

class Water():
    def __init__(self):
        self.x = random.uniform(0.01,0.29)
        self.z = random.uniform(0.052,0.298)

k = 0.001

area_sum = 0

p_water = 0

area_box = 0.28 * 0.246

water = []

while p_water < 0.14:
    w = Water()
    water.append(w)
    area_sum += k**2
    p_water = area_sum / area_box

for i in range(0, len(water)):
    w = water[i]
```

```
    box(w.x, 0, w.z, w.x + k, 0.001, w.z + k, 'water'
        , 'n')


class Air():
    def __init__(self):
        self.x = random.uniform(0.01,0.29)
        self.z = random.uniform(0.052,0.298)

k = 0.001

area_sum = 0

p_air = 0

area_box = 0.28 * 0.246

air = []

while p_air < 0.05:
    a = Air()
    air.append(a)
    area_sum += k**2
    p_air = area_sum / area_box

for i in range(0, len(air)):
    a = air[i]
    box(a.x, 0, a.z, a.x + k, 0.001, a.z + k, '
        free_space', 'n')

#end_python:

#waveform: gaussian 1 1.5e9 my_gaussian
#hertzian_dipole: y 0.15 0 0.34 my_gaussian
#rx: 0.155 0 0.34

#box: 0 0 0 0.3 0.001 0.05 pec n

#geometry_view: 0 0 0 0.3 0.001 0.36 0.001 0.001
    0.001 concrete_model n
```

D.2 SPHERE PACKING

```
#title: 3D Concrete model

#domain: 0.3 0.2 0.36
#dx_dy_dz: 0.001 0.001 0.001
#time_window: 9e-9

#material: 7 0 1 0 aggregate
#material: 3 0 1 0 cement
#material: 37.54 0 1 0 water

#box: 0 0 0 0.3 0.2 0.3 cement n

#python:

import random
import math
from gprMax.input_cmd_funcs import cylinder
from gprMax.input_cmd_funcs import box
from gprMax.input_cmd_funcs import sphere
from user_libs.antennas.GSSI import
   antenna_like_GSSI_1500
import os
from gprMax.input_cmd_funcs import *

class Aggregate():
    def __init__(self, p_aggregate):
        self.x = random.uniform(0.002,0.298)
        self.y = random.uniform(0.002,0.198)
        self.z = random.uniform(0.005,0.29)

        if p_aggregate > 0.60:
            lower = 0.001
            upper = 0.002
        if p_aggregate > 0.80:
            lower = 0.0005
            upper = 0.001
        else:
            lower = 0.004
            upper = 0.008

        radius = random.uniform(lower,upper)
        self.r = radius

    def check_collision(*args): #*args = (aggregate =
        [], agg = Aggregate())
        j = 0
        no_coll = False
        while j < len(aggregate) and no_coll is False
           :
            other = aggregate[j]
```

```
            point_dist = math.sqrt((agg.x - other.x)
                **2 + (agg.y - other.y)**2 + (agg.z -
                other.z)**2)
            j += 1
            if point_dist <= agg.r + other.r:
                no_coll = True
        return no_coll


random.seed(1)

volume_sum = 0

p_aggregate = 0

volume_box = 0.296 * 0.196 * 0.24

aggregate = []

while p_aggregate < 0.6:
    agg = Aggregate(p_aggregate)
    if agg.check_collision(aggregate, agg) is False:
    aggregate.append(agg)
    volume_sum += (4/3)*math.pi*agg.r**3
    p_aggregate = volume_sum / volume_box

for i in range(0, len(aggregate)):
    agg = aggregate[i]
    sphere(agg.x, agg.y, agg.z, agg.r, 'aggregate', '
        n')

class Air():
    def __init__(self):
        self.x = random.uniform(0.002,0.298)
        self.y = random.uniform(0.002,0.198)
        self.z = random.uniform(0.002,0.298)

k = 0.002

volume_sum = 0

p_air = 0

volume_box = 0.296 * 0.196 * 0.296

air = []

while p_air < 0.08:
    a = Air()
    air.append(a)
    volume_sum += k**3
    p_air = volume_sum / volume_box
```

```
for i in range(0, len(air)):
    a = air[i]
    box(a.x, a.y, a.z, a.x + k, a.y + k, a.z + k, '
        free_space', 'n')

class Water():
    def __init__(self):
        self.x = random.uniform(0.002,0.298)
        self.y = random.uniform(0.002,0.198)
        self.z = random.uniform(0.002,0.298)

k = 0.002

volume_sum = 0

p_water = 0

volume_box = 0.296 * 0.196 * 0.296

water = []

while p_water < 0.1:
    w = Water()
    water.append(w)
    volume_sum += k**3
    p_water = volume_sum / volume_box

for i in range(0, len(water)):
    w = water[i]
    box(w.x, w.y, w.z, w.x + k, w.y + k, w.z + k, '
        water', 'n')

antenna_like_GSSI_1500(0.15, 0.1, 0.3, 0.001)

#end_python:

#box: 0 0 0 0.3 0.2 0.05 pec n

#geometry_view: 0 0 0 0.3 0.2 0.36 0.001 0.001 0.001
    concrete_model n
```

D.3 POLYGON CREATION

```
import random
import math

import matplotlib.pyplot as plt # only used for
    python printing

class Aggregate():
```

```
        def __init__(self):
                self.numberOfVertices = random.
                    randint(5,15) # get a random
                    number of points for polygon
                self.angle = (2*math.pi)/self.
                    numberOfVertices # get angle of
                    points about centre
                self.xcoord = random.uniform(1, 5) #
                    x-coordinate of centre of
                    aggregate
                self.ycoord = random.uniform(1, 5) #
                    y-coordinate of centre of
                    aggregate
                self.vertices = [] # list to hold
                    coordinate points

                for i in range(0, self.
                    numberOfVertices): # for
                    determining point coordinates
                        self.radius = random.uniform
                            (1, 5) # set radius to
                            value between 1 and 5
                        self.x = self.xcoord + self.
                            radius*math.cos(i*self.
                            angle) # determine x-
                            coordinate of point
                        self.y = self.ycoord + self.
                            radius*math.sin(i*self.
                            angle) # determine y-
                            coordinate of point
                        self.vertexX = format(self.x,
                             '.2f') # limit x-
                            coordinate to 2 decimal
                            places
                        self.vertexY = format(self.y,
                             '.2f') # limit y-
                            coordinate to 2 decimal
                            places
                        self.vertices.append([self.
                            vertexX, self.vertexY]) #
                            add coordinates to list


        def get_points(self): # method for obtaining
            list of coordinates
                return self.vertices

# the following code just plots the grain in python
    and lists the points

alg = Aggregate()       # create instance of class
    Aggregate
```

```
alg = alg.get_points() # call method to obtain list
    of vertices
alg.append(alg[0])     # close the list of vertices
    by adding the first point to end
xs, ys = zip(*alg)     # create lists of x-coords and
     y-coords in appropriate format

plt.figure()           # create window to hold grain
plt.plot(xs, ys)       # plot polygon via points

plt.show()             # show image
print(alg)             # print out list of points
```

D.4 ROCK

```
#domain: 0.5 0.2 0.36
#dx_dy_dz: 0.001 0.001 0.001
#time_window: 9e-9

#material: 7 0 1 0 rock
#material: 8 0 1 0 concrete
#material: 2.8 0 1 0 bitumen

#box: 0 0 0 0.5 0.2 0.3 concrete n

#python:

from user_libs.antennas.GSSI import antenna_like_GSSI
    _1500
#from user_libs.antennas import antenna_like_GSSI
    _1500

antenna_like_GSSI_1500(0.25, 0.1, 0.3, 0.001)


#end_python:

#box: 0 0 0 0.5 0.2 0.02 pec n


#geometry_view: 0 0 0 0.5 0.2 0.36 0.001 0.001 0.001
    rock n


#box: 0.1953102085144741 0.09103209972543466
    0.26169316207209004 0.1973102085144741
    0.09303209972543466 0.26708013312761925 rock n
#box: 0.1953102085144741 0.09214536428780108
    0.2627899048359723 0.1973102085144741
    0.09414536428780108 0.2659833903637369 rock n
```

```
#box: 0.19651530834552686 0.08991883516306823
   0.26169316207209004 0.19851530834552686
   0.09191883516306823 0.2703703614192661 rock n
#box: 0.19651530834552686 0.09103209972543466
   0.2605964193082077 0.19851530834552686
   0.09303209972543466 0.26927361865538385 rock n
#box: 0.19651530834552686 0.09214536428780108
   0.2605964193082077 0.19851530834552686
   0.09414536428780108 0.2681768758915015 rock n
#box: 0.19651530834552686 0.0932586288501675
   0.26388664759985464 0.19851530834552686
   0.0952586288501675 0.26708013312761925 rock n
#box: 0.19772040817657963 0.08880557060070181
   0.2605964193082077 0.19972040817657963
   0.09080557060070181 0.26927361865538385 rock n
#box: 0.19772040817657963 0.08991883516306823
   0.2605964193082077 0.19972040817657963
   0.09191883516306823 0.2703703614192661 rock n
#box: 0.19772040817657963 0.09103209972543466
   0.25949967654432543 0.19972040817657963
   0.09303209972543466 0.27146710418314846 rock n
#box: 0.19772040817657963 0.09214536428780108
   0.25949967654432543 0.19972040817657963
   0.09414536428780108 0.2703703614192661 rock n
#box: 0.19772040817657963 0.0932586288501675
   0.26169316207209004 0.19972040817657963
   0.0952586288501675 0.2703703614192661 rock n
#box: 0.19772040817657963 0.09437189341253392
   0.2649833903637369 0.19972040817657963
   0.09637189341253392 0.26927361865538385 rock n
#box: 0.1989255080076324 0.08769230603833539
   0.2605964193082077 0.2009255080076324
   0.08969230603833539 0.2681768758915015 rock n
#box: 0.1989255080076324 0.08880557060070181
   0.2605964193082077 0.2009255080076324
   0.09080557060070181 0.2681768758915015 rock n
#box: 0.1989255080076324 0.08991883516306823
   0.25949967654432543 0.2009255080076324
   0.09191883516306823 0.26927361865538385 rock n
#box: 0.1989255080076324 0.09103209972543466
   0.25949967654432543 0.2009255080076324
   0.09303209972543466 0.2703703614192661 rock n
#box: 0.1989255080076324 0.09214536428780108
   0.25949967654432543 0.2009255080076324
   0.09414536428780108 0.27146710418314846 rock n
#box: 0.1989255080076324 0.0932586288501675
   0.25949967654432543 0.2009255080076324
   0.0952586288501675 0.27146710418314846 rock n
#box: 0.1989255080076324 0.09437189341253392
   0.2627899048359723 0.2009255080076324
   0.09637189341253392 0.2703703614192661 rock n
```

```
#box: 0.1989255080076324 0.09548515797490036
    0.26608013312761924 0.2009255080076324
    0.09748515797490036 0.2703703614192661 rock n
#box: 0.20013060783868514 0.08657904147596895
    0.26169316207209004 0.20213060783868514
    0.08857904147596896 0.2659833903637369 rock n
#box: 0.20013060783868514 0.08769230603833539
    0.2605964193082077 0.20213060783868514
    0.08969230603833539 0.26708013312761925 rock n
#box: 0.20013060783868514 0.08880557060070181
    0.2605964193082077 0.20213060783868514
    0.09080557060070181 0.2681768758915015 rock n
#box: 0.20013060783868514 0.08991883516306823
    0.25949967654432543 0.20213060783868514
    0.09191883516306823 0.26927361865538385 rock n
#box: 0.20013060783868514 0.09103209972543466
    0.25949967654432543 0.20213060783868514
    0.09303209972543466 0.2703703614192661 rock n
#box: 0.20013060783868514 0.09214536428780108
    0.25949967654432543 0.20213060783868514
    0.09414536428780108 0.2703703614192661 rock n
#box: 0.20013060783868514 0.0932586288501675
    0.25949967654432543 0.20213060783868514
    0.0952586288501675 0.27146710418314846 rock n
#box: 0.20013060783868514 0.09437189341253392
    0.2605964193082077 0.20213060783868514
    0.09637189341253392 0.27146710418314846 rock n
#box: 0.20013060783868514 0.09548515797490036
    0.2649833903637369 0.20213060783868514
    0.09748515797490036 0.2703703614192661 rock n
#box: 0.2013357076697379 0.08657904147596895
    0.26169316207209004 0.2033357076697379
    0.08857904147596896 0.2659833903637369 rock n
#box: 0.2013357076697379 0.08769230603833539
    0.2605964193082077 0.2033357076697379
    0.08969230603833539 0.2659833903637369 rock n
#box: 0.2013357076697379 0.08880557060070181
    0.2605964193082077 0.2033357076697379
    0.09080557060070181 0.26708013312761925 rock n
#box: 0.2013357076697379 0.08991883516306823
    0.25949967654432543 0.2033357076697379
    0.09191883516306823 0.2681768758915015 rock n
#box: 0.2013357076697379 0.09103209972543466
    0.25949967654432543 0.2033357076697379
    0.09303209972543466 0.26927361865538385 rock n
#box: 0.2013357076697379 0.09214536428780108
    0.25949967654432543 0.2033357076697379
    0.09414536428780108 0.26927361865538385 rock n
#box: 0.2013357076697379 0.0932586288501675
    0.25949967654432543 0.2033357076697379
    0.0952586288501675 0.2703703614192661 rock n
```

```
#box: 0.2013357076697379 0.09437189341253392
   0.2605964193082077 0.2033357076697379
   0.09637189341253392 0.27146710418314846 rock n
#box: 0.2013357076697379 0.09548515797490036
   0.2671768758915015 0.2033357076697379
   0.09748515797490036 0.2703703614192661 rock n
#box: 0.20254080750079068 0.08657904147596895
   0.2627899048359723 0.20454080750079068
   0.08857904147596896 0.26488664759985464 rock n
#box: 0.20254080750079068 0.08769230603833539
   0.26169316207209004 0.20454080750079068
   0.08969230603833539 0.2659833903637369 rock n
#box: 0.20254080750079068 0.08880557060070181
   0.2605964193082077 0.20454080750079068
   0.09080557060070181 0.2659833903637369 rock n
#box: 0.20254080750079068 0.08991883516306823
   0.2605964193082077 0.20454080750079068
   0.09191883516306823 0.26708013312761925 rock n
#box: 0.20254080750079068 0.09103209972543466
   0.2605964193082077 0.20454080750079068
   0.09303209972543466 0.2681768758915015 rock n
#box: 0.20254080750079068 0.09214536428780108
   0.25949967654432543 0.20454080750079068
   0.09414536428780108 0.2681768758915015 rock n
#box: 0.20254080750079068 0.0932586288501675
   0.25949967654432543 0.20454080750079068
   0.0952586288501675 0.26927361865538385 rock n
#box: 0.20254080750079068 0.09437189341253392
   0.26388664759985464 0.20454080750079068
   0.09637189341253392 0.2703703614192661 rock n
#box: 0.20374590733184345 0.08991883516306823
   0.26169316207209004 0.20574590733184345
   0.09191883516306823 0.2637899048359723 rock n
#box: 0.20374590733184345 0.09103209972543466
   0.2605964193082077 0.20574590733184345
   0.09303209972543466 0.26488664759985464 rock n
#box: 0.20374590733184345 0.09214536428780108
   0.2605964193082077 0.20574590733184345
   0.09414536428780108 0.2659833903637369 rock n
#box: 0.20374590733184345 0.0932586288501675
   0.26169316207209004 0.20574590733184345
   0.0952586288501675 0.26708013312761925 rock n
#box: 0.013067125902035287 0.1311705707644719
   0.24453389310552254 0.015067125902035287
   0.1331705707644719 0.24947332639425332 rock n
#box: 0.013067125902035287 0.13251957532415476
   0.24453389310552254 0.015067125902035287
   0.13451957532415476 0.24947332639425332 rock n
#box: 0.014469314008533117 0.13251957532415476
   0.24453389310552254 0.016469314008533117
   0.13451957532415476 0.24947332639425332 rock n
```

```
#box: 0.1021735806581349 0.1856195172294866
   0.21817780608065285 0.1041735806581349
   0.1876195172294866 0.22247303401833365 rock n
#box: 0.1021735806581349 0.18675179829753435
   0.21927621539321313 0.1041735806581349
   0.18875179829753436 0.22247303401833365 rock n
#box: 0.1021735806581349 0.1878840793655821
   0.2203746247057734 0.1041735806581349
   0.1898840793655821 0.22247303401833365 rock n
#box: 0.1032886624076458 0.18448723616143886
   0.214882578142972 0.1052886624076458
   0.18648723616143886 0.22027621539321313 rock n
#box: 0.1032886624076458 0.1856195172294866
   0.2159809874555323 0.1052886624076458
   0.1876195172294866 0.22357144333089393 rock n
#box: 0.1032886624076458 0.18675179829753435
   0.21707939676809257 0.1052886624076458
   0.18875179829753436 0.22357144333089393 rock n
#box: 0.1032886624076458 0.1878840793655821
   0.21817780608065285 0.1052886624076458
   0.1898840793655821 0.22357144333089393 rock n
#box: 0.1032886624076458 0.18901636043362982
   0.21927621539321313 0.1052886624076458
   0.19101636043362982 0.22357144333089393 rock n
#box: 0.1032886624076458 0.19014864150167757
   0.2203746247057734 0.1052886624076458
   0.19214864150167757 0.22247303401833365 rock n
#box: 0.1044037441571567 0.18448723616143886
   0.214882578142972 0.1064037441571567
   0.18648723616143886 0.22357144333089393 rock n
#box: 0.1044037441571567 0.1856195172294866
   0.21378416883041176 0.1064037441571567
   0.1876195172294866 0.22357144333089393 rock n
#box: 0.1044037441571567 0.18675179829753435
   0.214882578142972 0.1064037441571567
   0.18875179829753436 0.2246698526434542 rock n
#box: 0.1044037441571567 0.1878840793655821
   0.2159809874555323 0.1064037441571567
   0.1898840793655821 0.2246698526434542 rock n
#box: 0.1044037441571567 0.18901636043362982
   0.21707939676809257 0.1064037441571567
   0.19101636043362982 0.2246698526434542 rock n
#box: 0.1044037441571567 0.19014864150167757
   0.21817780608065285 0.1064037441571567
   0.19214864150167757 0.2246698526434542 rock n
#box: 0.1044037441571567 0.19128092256972531
   0.2203746247057734 0.1064037441571567
   0.19328092256972532 0.22247303401833365 rock n
#box: 0.10551882590666758 0.18448723616143886
   0.21707939676809257 0.10751882590666759
   0.18648723616143886 0.2246698526434542 rock n
```

```
#box: 0.10551882590666758 0.1856195172294866
   0.21378416883041176 0.10751882590666759
   0.1876195172294866 0.2246698526434542 rock n
#box: 0.10551882590666758 0.18675179829753435
   0.21378416883041176 0.10751882590666759
   0.18875179829753436 0.2246698526434542 rock n
#box: 0.10551882590666758 0.1878840793655821
   0.21378416883041176 0.10751882590666759
   0.1898840793655821 0.2246698526434542 rock n
#box: 0.10551882590666758 0.18901636043362982
   0.2148825781429720 0.10751882590666759
   0.19101636043362982 0.2246698526434542 rock n
#box: 0.10551882590666758 0.19014864150167757
   0.2159809874555323 0.10751882590666759
   0.19214864150167757 0.2246698526434542 rock n
#box: 0.10551882590666758 0.19128092256972531
   0.21817780608065285 0.10751882590666759
   0.19328092256972532 0.22357144333089393 rock n
#box: 0.10663390765617847 0.18448723616143886
   0.21817780608065285 0.10863390765617847
   0.18648723616143886 0.2246698526434542 rock n
#box: 0.10663390765617847 0.1856195172294866
   0.21378416883041176 0.10863390765617847
   0.1876195172294866 0.2246698526434542 rock n
#box: 0.10663390765617847 0.18675179829753435
   0.21268575951785149 0.10863390765617847
   0.18875179829753436 0.2246698526434542 rock n
#box: 0.10663390765617847 0.1878840793655821
   0.21268575951785149 0.10863390765617847
   0.1898840793655821 0.2246698526434542 rock n
#box: 0.10663390765617847 0.18901636043362982
   0.21378416883041176 0.10863390765617847
   0.19101636043362982 0.2246698526434542 rock n
#box: 0.10663390765617847 0.19014864150167757
   0.21378416883041176 0.10863390765617847
   0.19214864150167757 0.2246698526434542 rock n
#box: 0.10663390765617847 0.19128092256972531
   0.21707939676809257 0.10863390765617847
   0.19328092256972532 0.22357144333089393 rock n
#box: 0.10774898940568937 0.1856195172294866
   0.21378416883041176 0.10974898940568938
   0.1876195172294866 0.2246698526434542 rock n
#box: 0.10774898940568937 0.18675179829753435
   0.21268575951785149 0.10974898940568938
   0.18875179829753436 0.2246698526434542 rock n
#box: 0.10774898940568937 0.1878840793655821
   0.21268575951785149 0.10974898940568938
   0.1898840793655821 0.2246698526434542 rock n
#box: 0.10774898940568937 0.18901636043362982
   0.21268575951785149 0.10974898940568938
   0.19101636043362982 0.2246698526434542 rock n
```

```
#box: 0.10774898940568937 0.19014864150167757
    0.21268575951785149 0.10974898940568938
    0.19214864150167757 0.22357144333089393 rock n
#box: 0.10774898940568937 0.19128092256972531
    0.2159809874555323 0.10974898940568938
    0.19328092256972532 0.22357144333089393 rock n
#box: 0.10886407115520028 0.1856195172294866
    0.21927621539321313 0.11086407115520028
    0.1876195172294866 0.22247303401833365 rock n
#box: 0.10886407115520028 0.18675179829753435
    0.21268575951785149 0.11086407115520028
    0.18875179829753436 0.2246698526434542 rock n
#box: 0.10886407115520028 0.1878840793655821
    0.21268575951785149 0.11086407115520028
    0.1898840793655821 0.2246698526434542 rock n
#box: 0.10886407115520028 0.18901636043362982
    0.21378416883041176 0.11086407115520028
    0.19101636043362982 0.22357144333089393 rock n
#box: 0.10886407115520028 0.19014864150167757
    0.21378416883041176 0.11086407115520028
    0.19214864150167757 0.22357144333089393 rock n
#box: 0.10886407115520028 0.19128092256972531
    0.21817780608065285 0.11086407115520028
    0.19328092256972532 0.22357144333089393 rock n
#box: 0.10997915290471116 0.18675179829753435
    0.214882578142972 0.11197915290471117
    0.18875179829753436 0.2213746247057734 rock n
#box: 0.10997915290471116 0.1878840793655821
    0.21378416883041176 0.11197915290471117
    0.1898840793655821 0.22247303401833365 rock n
#box: 0.10997915290471116 0.18901636043362982
    0.21378416883041176 0.11197915290471117
    0.19101636043362982 0.22357144333089393 rock n
#box: 0.10997915290471116 0.19014864150167757
    0.2159809874555323 0.11197915290471117
    0.19214864150167757 0.22357144333089393 rock n
#box: 0.11109423465422205 0.1878840793655821
    0.214882578142972 0.11309423465422205
    0.1898840793655821 0.21917780608065285 rock n
#box: 0.11109423465422205 0.18901636043362982
    0.214882578142972 0.11309423465422205
    0.19101636043362982 0.2213746247057734 rock n
#box: 0.09207253129080199 0.14295257190806634
    0.23966347246461242 0.094072531290802
    0.14495257190806635 0.24672237290451818 rock n
#box: 0.09207253129080199 0.1443576770051298
    0.23966347246461242 0.094072531290802
    0.14635767700512 98 0.2442988127285559 rock n
#box: 0.09336617411723624 0.14295257190806634
    0.24087525255259357 0.09536617411723625
    0.14495257190806635 0.24672237290451818 rock n
```

```
#box: 0.09336617411723624 0.1443576770051298
   0.23966347246461242 0.09536617411723625
   0.1463576770051298 0.24672237290451818 rock n
#box: 0.09336617411723624 0.14576278210219326
   0.23966347246461242 0.09536617411723625
   0.14776278210219326 0.2442988127285559 rock n
#box: 0.0946598169436705 0.14295257190806634
   0.24208703264057474 0.0966598169436705
   0.14495257190806635 0.24672237290451818 rock n
#box: 0.0946598169436705 0.1443576770051298
   0.23966347246461242 0.0966598169436705
   0.1463576770051298 0.24551059281653703 rock n
#box: 0.0946598169436705 0.14576278210219326
   0.23966347246461242 0.0966598169436705
   0.14776278210219326 0.2442988127285559 rock n
#box: 0.3292576629043837 0.1943612765124076
   0.22939960977113705 0.3312576629043837
   0.1963612765124076 0.23267755832915105 rock n
#box: 0.3292576629043837 0.19557418434160506
   0.22598268693411602 0.3312576629043837
   0.19757418434160506 0.23153858405014405 rock n
#box: 0.3292576629043837 0.19678709217080254
   0.22598268693411602 0.3312576629043837
   0.19878709217080254 0.23153858405014405 rock n
#box: 0.3292576629043837 0.198 0.22712166121312302
   0.3312576629043837 0.2 0.23039960977113705 rock n
#box: 0.3304022149494174 0.1931483686832101
   0.22484371265510902 0.3324022149494174
   0.1951483686832101 0.23495550688716507 rock n
#box: 0.3304022149494174 0.1943612765124076
   0.22484371265510902 0.3324022149494174
   0.1963612765124076 0.23495550688716507 rock n
#box: 0.3304022149494174 0.19557418434160506
   0.22370473837610202 0.3324022149494174
   0.19757418434160506 0.23381653260815807 rock n
#box: 0.3304022149494174 0.19678709217080254
   0.22370473837610202 0.3324022149494174
   0.19878709217080254 0.23381653260815807 rock n
#box: 0.3304022149494174 0.198 0.22598268693411602
   0.3324022149494174 0.2 0.23267755832915105 rock n
#box: 0.3315467669944511 0.1919354608540126
   0.22370473837610202 0.3335467669944511
   0.19393546085401261 0.23381653260815807 rock n
#box: 0.3315467669944511 0.1931483686832101
   0.222565764097095 0.3335467669944511
   0.1951483686832101 0.23495550688716507 rock n
#box: 0.3315467669944511 0.1943612765124076
   0.222565764097095 0.3335467669944511
   0.1963612765124076 0.23495550688716507 rock n
#box: 0.3315467669944511 0.19557418434160506
   0.222565764097095 0.3335467669944511
   0.19757418434160506 0.23495550688716507 rock n
```

```
#box: 0.3315467669944511 0.19678709217080254
   0.22370473837610202 0.3335467669944511
   0.19878709217080254 0.23495550688716507 rock n
#box: 0.3315467669944511 0.198 0.22598268693411602
   0.3335467669944511 0.2 0.23381653260815807 rock n
#box: 0.33269131903948485 0.19072255302481514
   0.22370473837610202 0.33469131903948485
   0.19272255302481514 0.23039960977113705 rock n
#box: 0.33269131903948485 0.1919354608540126
   0.222565764097095 0.33469131903948485
   0.19393546085401261 0.23495550688716507 rock n
#box: 0.33269131903948485 0.1931483686832101
   0.222565764097095 0.33469131903948485
   0.1951483686832101 0.23495550688716507 rock n
#box: 0.33269131903948485 0.1943612765124076
   0.222565764097095 0.33469131903948485
   0.1963612765124076 0.23495550688716507 rock n
#box: 0.33269131903948485 0.19557418434160506
   0.222565764097095 0.33469131903948485
   0.19757418434160506 0.23495550688716507 rock n
#box: 0.33269131903948485 0.19678709217080254
   0.22484371265510902 0.33469131903948485
   0.19878709217080254 0.23495550688716507 rock n
#box: 0.33269131903948485 0.198 0.22712166121312302
   0.33469131903948485 0.2 0.23381653260815807 rock n
#box: 0.3338358710845186 0.19072255302481514
   0.22370473837610202 0.3358358710845186
   0.19272255302481514 0.23381653260815807 rock n
#box: 0.3338358710845186 0.1919354608540126
   0.222565764097095 0.3358358710845186
   0.19393546085401261 0.23495550688716507 rock n
#box: 0.3338358710845186 0.1931483686832101
   0.222565764097095 0.3358358710845186
   0.1951483686832101 0.23495550688716507 rock n
#box: 0.3338358710845186 0.1943612765124076
   0.222565764097095 0.3358358710845186
   0.1963612765124076 0.23495550688716507 rock n
#box: 0.3338358710845186 0.19557418434160506
   0.22484371265510902 0.3358358710845186
   0.19757418434160506 0.23495550688716507 rock n
#box: 0.3338358710845186 0.19678709217080254
   0.22712166121312302 0.3358358710845186
   0.19878709217080254 0.23495550688716507 rock n
#box: 0.3338358710845186 0.198 0.22939960977113705
   0.3358358710845186 0.2 0.23381653260815807 rock n
#box: 0.33498042312955234 0.19072255302481514
   0.22370473837610202 0.33698042312955234
   0.19272255302481514 0.23381653260815807 rock n
#box: 0.33498042312955234 0.1919354608540126
   0.22370473837610202 0.33698042312955234
   0.19393546085401261 0.23495550688716507 rock n
```

```
#box: 0.33498042312955234 0.1931483686832101
   0.22370473837610202 0.33698042312955234
   0.1951483686832101 0.23495550688716507 rock n
#box: 0.33498042312955234 0.1943612765124076
   0.22370473837610202 0.33698042312955234
   0.1963612765124076 0.23495550688716507 rock n
#box: 0.33498042312955234 0.19557418434160506
   0.22712166121312302 0.33698042312955234
   0.19757418434160506 0.23495550688716507 rock n
#box: 0.33498042312955234 0.19678709217080254
   0.22939960977113705 0.33698042312955234
   0.19878709217080254 0.23495550688716507 rock n
#box: 0.33612497517458606 0.19072255302481514
   0.22484371265510902 0.33812497517458606
   0.19272255302481514 0.23267755832915105 rock n
#box: 0.33612497517458606 0.1919354608540126
   0.22484371265510902 0.33812497517458606
   0.19393546085401261 0.23495550688716507 rock n
#box: 0.33612497517458606 0.1931483686832101
   0.22484371265510902 0.33812497517458606
   0.1951483686832101 0.23495550688716507 rock n
#box: 0.33612497517458606 0.1943612765124076
   0.22598268693411602 0.33812497517458606
   0.1963612765124076 0.23495550688716507 rock n
#box: 0.33612497517458606 0.19557418434160506
   0.22939960977113705 0.33812497517458606
   0.19757418434160506 0.23495550688716507 rock n
#box: 0.3372695272196198 0.19072255302481514
   0.22598268693411602 0.3392695272196198
   0.19272255302481514 0.22926063549213005 rock n
#box: 0.3372695272196198 0.1919354608540126
   0.22598268693411602 0.3392695272196198
   0.19393546085401261 0.23381653260815807 rock n
#box: 0.3372695272196198 0.1931483686832101
   0.22598268693411602 0.3392695272196198
   0.1951483686832101 0.23381653260815807 rock n
#box: 0.3372695272196198 0.1943612765124076
   0.22826063549213005 0.3392695272196198
   0.1963612765124076 0.23381653260815807 rock n
#box: 0.3384140792646535 0.1919354608540126
   0.22712166121312302 0.3404140792646535
   0.19393546085401261 0.23153858405014405 rock n
#box: 0.3384140792646535 0.1931483686832101
   0.22826063549213005 0.3404140792646535
   0.1951483686832101 0.23153858405014405 rock n
#box: 0.0599530511830957 0.17157024436864357
   0.24599852510771233 0.06195305118309574
   0.17357024436864357 0.2518257598035319 rock n
#box: 0.0599530511830957 0.17291118522251503
   0.24479171643375744 0.06195305118309574
   0.17491118522251503 0.2494121424556221 rock n
```

```
#box: 0.06131316155407418 0.17157024436864357
    0.24599852510771233 0.06331316155407418
    0.17357024436864357 0.250618951129577 rock n
#box: 0.06131316155407418 0.17291118522251503
    0.24479171643375744 0.06331316155407418
    0.17491118522251503 0.2518257598035319 rock n
#box: 0.06267327192505262 0.17291118522251503
    0.24479171643375744 0.06467327192505262
    0.17491118522251503 0.250618951129577 rock n
#box: 0.07091955300029497 0.13827709236416197
    0.27053317194291615 0.07291955300029497
    0.14027709236416197 0.27405219322914703 rock n
#box: 0.07091955300029497 0.1396931945970415
    0.2692736612998007 0.07291955300029497
    0.1416931945970415 0.27405219322914703 rock n
#box: 0.019037209052666336 0.10657337154016128
    0.20731082351175786 0.021037209052666338
    0.10857337154016128 0.20947397114314464 rock n
#box: 0.019037209052666336 0.10781469177594519
    0.20614767588037108 0.021037209052666338
    0.10981469177594519 0.21063711877453142 rock n
#box: 0.019037209052666336 0.1090560120117291
    0.2049845282489843 0.021037209052666338
    0.1110560120117291 0.2118002664059182 rock n
#box: 0.019037209052666336 0.11029733224751301
    0.2049845282489843 0.021037209052666338
    0.11229733224751301 0.21063711877453142 rock n
#box: 0.019037209052666336 0.11153865248329692
    0.20382138061759753 0.021037209052666338
    0.11353865248329692 0.20831082351175786 rock n
#box: 0.02041284674120089 0.10533205130437737
    0.2049845282489843 0.022412846741200892
    0.10733205130437737 0.20714767588037108 rock n
#box: 0.02041284674120089 0.10657337154016128
    0.2049845282489843 0.022412846741200892
    0.10857337154016128 0.21063711877453142 rock n
#box: 0.02041284674120089 0.10781469177594519
    0.20382138061759753 0.022412846741200892
    0.10981469177594519 0.2118002664059182 rock n
#box: 0.02041284674120089 0.1090560120117291
    0.20265823298621075 0.022412846741200892
    0.1110560120117291 0.2118002664059182 rock n
#box: 0.02041284674120089 0.11029733224751301
    0.20265823298621075 0.022412846741200892
    0.11229733224751301 0.2118002664059182 rock n
#box: 0.02041284674120089 0.11153865248329692
    0.20265823298621075 0.022412846741200892
    0.11353865248329692 0.21063711877453142 rock n
#box: 0.02041284674120089 0.11277997271908083
    0.20382138061759753 0.022412846741200892
    0.11477997271908083 0.20831082351175786 rock n
```

```
#box: 0.02178848442973545 0.10533205130437737
   0.20265823298621075 0.023788484429735447
   0.10733205130437737 0.21063711877453142 rock n
#box: 0.02178848442973545 0.10657337154016128
   0.20265823298621075 0.023788484429735447
   0.10857337154016128 0.2118002664059182 rock n
#box: 0.02178848442973545 0.10781469177594519
   0.20149508535482397 0.023788484429735447
   0.10981469177594519 0.2118002664059182 rock n
#box: 0.02178848442973545 0.1090560120117291
   0.20149508535482397 0.023788484429735447
   0.1110560120117291 0.2118002664059182 rock n
#box: 0.02178848442973545 0.11029733224751301
   0.20149508535482397 0.023788484429735447
   0.11229733224751301 0.2118002664059182 rock n
#box: 0.02178848442973545 0.11153865248329692
   0.20265823298621075 0.023788484429735447
   0.11353865248329692 0.21063711877453142 rock n
#box: 0.02178848442973545 0.11277997271908083
   0.20382138061759753 0.023788484429735447
   0.11477997271908083 0.20947397114314464 rock n
#box: 0.023164122118270007 0.10781469177594519
   0.20614767588037108 0.02516412211827001
   0.10981469177594519 0.2118002664059182 rock n
#box: 0.023164122118270007 0.1090560120117291
   0.2049845282489843 0.02516412211827001
   0.1110560120117291 0.2118002664059182 rock n
#box: 0.023164122118270007 0.11029733224751301
   0.20382138061759753 0.02516412211827001
   0.11229733224751301 0.2118002664059182 rock n
#box: 0.023164122118270007 0.11153865248329692
   0.20382138061759753 0.02516412211827001
   0.11353865248329692 0.21063711877453142 rock n
#box: 0.023164122118270007 0.11277997271908083
   0.20382138061759753 0.02516412211827001
   0.11477997271908083 0.20947397114314464 rock n
#box: 0.04989795282683717 0.13326799294180255
   0.2897950243895647 0.05189795282683717
   0.13526799294180256 0.294211329099369 rock n
#box: 0.04989795282683717 0.1343943544534045
   0.2886562561529633 0.05189795282683717
   0.1363943544534045 0.294211329099369 rock n
#box: 0.04989795282683717 0.13552071596500645
   0.2863787196797604 0.05189795282683717
   0.13752071596500645 0.2953500973359704 rock n
#box: 0.04989795282683717 0.13664707747660843
   0.285239951443159 0.05189795282683717
   0.13864707747660843 0.2953500973359704 rock n
#box: 0.04989795282683717 0.13777343898821037
   0.28296241496995617 0.05189795282683717
   0.13977343898821037 0.2953500973359704 rock n
```

```
#box: 0.04989795282683717 0.13889980049981232
    0.28182364673335475 0.05189795282683717
    0.14089980049981232 0.2953500973359704 rock n
#box: 0.04989795282683717 0.14002616201141427
    0.285239951443159 0.05189795282683717
    0.14202616201141427 0.294211329099369 rock n
#box: 0.05098848191959113 0.1321416314302006
    0.29093379262616614 0.05298848191959113
    0.1341416314302006 0.294211329099369 rock n
#box: 0.05098848191959113 0.13326799294180255
    0.2886562561529633 0.05298848191959113
    0.13526799294180256 0.294211329099369 rock n
#box: 0.05098848191959113 0.1343943544534045
    0.2875174879163619 0.05298848191959113
    0.1363943544534045 0.2953500973359704 rock n
#box: 0.05098848191959113 0.13552071596500645
    0.285239951443159 0.05298848191959113
    0.13752071596500645 0.2953500973359704 rock n
#box: 0.05098848191959113 0.13664707747660843
    0.2841011832065576 0.05298848191959113
    0.13864707747660843 0.2964888655725718 rock n
#box: 0.05098848191959113 0.13777343898821037
    0.28182364673335475 0.05298848191959113
    0.13977343898821037 0.2953500973359704 rock n
#box: 0.05098848191959113 0.13889980049981232
    0.28182364673335475 0.05298848191959113
    0.14089980049981232 0.2953500973359704 rock n
#box: 0.05098848191959113 0.14002616201141427
    0.285239951443159 0.05298848191959113
    0.14202616201141427 0.2953500973359704 rock n
#box: 0.05098848191959113 0.14115252352301622
    0.2897950243895647 0.05298848191959113
    0.14315252352301622 0.294211329099369 rock n
#box: 0.05207901101234509 0.1321416314302006
    0.2897950243895647 0.05407901101234509
    0.1341416314302006 0.294211329099369 rock n
#box: 0.05207901101234509 0.13326799294180255
    0.2886562561529633 0.05407901101234509
    0.13526799294180256 0.294211329099369 rock n
#box: 0.05207901101234509 0.1343943544534045
    0.2863787196797604 0.05407901101234509
    0.1363943544534045 0.2953500973359704 rock n
#box: 0.05207901101234509 0.13552071596500645
    0.2841011832065576 0.05407901101234509
    0.13752071596500645 0.2964888655725718 rock n
#box: 0.05207901101234509 0.13664707747660843
    0.28296241496995617 0.05407901101234509
    0.13864707747660843 0.2964888655725718 rock n
#box: 0.05207901101234509 0.13777343898821037
    0.28068487849675333 0.05407901101234509
    0.13977343898821037 0.2964888655725718 rock n
```

```
#box: 0.05207901101234509 0.13889980049981232
   0.28182364673335475 0.05407901101234509
   0.14089980049981232 0.2953500973359704 rock n
#box: 0.05207901101234509 0.14002616201141427
   0.285239951443159 0.05407901101234509
   0.14202616201141427 0.2953500973359704 rock n
#box: 0.05207901101234509 0.14115252352301622
   0.2897950243895647 0.05407901101234509
   0.14315252352301622 0.294211329099369 rock n
#box: 0.05316954010509905 0.13101526991859866
   0.29093379262616614 0.05516954010509905
   0.13301526991859866 0.29307256086276756 rock n
#box: 0.05316954010509905 0.1321416314302006
   0.2886562561529633 0.05516954010509905
   0.1341416314302006 0.294211329099369 rock n
#box: 0.05316954010509905 0.13326799294180255
   0.2875174879163619 0.05516954010509905
   0.13526799294180256 0.2953500973359704 rock n
#box: 0.05316954010509905 0.1343943544534045
   0.285239951443159 0.05516954010509905
   0.1363943544534045 0.2953500973359704 rock n
#box: 0.05316954010509905 0.13552071596500645
   0.28296241496995617 0.05516954010509905
   0.13752071596500645 0.2964888655725718 rock n
#box: 0.05316954010509905 0.13664707747660843
   0.28182364673335475 0.05516954010509905
   0.13864707747660843 0.2964888655725718 rock n
#box: 0.05316954010509905 0.13777343898821037
   0.28068487849675333 0.05516954010509905
   0.13977343898821037 0.2964888655725718 rock n
#box: 0.05316954010509905 0.13889980049981232
   0.28182364673335475 0.05516954010509905
   0.14089980049981232 0.2964888655725718 rock n
#box: 0.05316954010509905 0.14002616201141427
   0.285239951443159 0.05516954010509905
   0.14202616201141427 0.2953500973359704 rock n
#box: 0.05426006919785301 0.13101526991859866
   0.2897950243895647 0.056260069197853015
   0.13301526991859866 0.294211329099369 rock n
#box: 0.05426006919785301 0.1321416314302006
   0.2886562561529633 0.056260069197853015
   0.1341416314302006 0.294211329099369 rock n
#box: 0.05426006919785301 0.13326799294180255
   0.2863787196797604 0.056260069197853015
   0.13526799294180256 0.2953500973359704 rock n
#box: 0.05426006919785301 0.1343943544534045
   0.2841011832065576 0.056260069197853015
   0.1363943544534045 0.2964888655725718 rock n
#box: 0.05426006919785301 0.13552071596500645
   0.28296241496995617 0.056260069197853015
   0.13752071596500645 0.2964888655725718 rock n
```

```
#box: 0.05426006919785301 0.13664707747660843
    0.28068487849675333 0.056260069197853015
    0.13864707747660843 0.2964888655725718 rock n
#box: 0.05426006919785301 0.13777343898821037
    0.28068487849675333 0.056260069197853015
    0.13977343898821037 0.2964888655725718 rock n
#box: 0.05426006919785301 0.13889980049981232
    0.28182364673335475 0.056260069197853015
    0.14089980049981232 0.2964888655725718 rock n
#box: 0.05426006919785301 0.14002616201141427
    0.2897950243895647 0.056260069197853015
    0.14202616201141427 0.29193379262616614 rock n
#box: 0.05535059829060697 0.13101526991859866
    0.2897950243895647 0.05735059829060697
    0.13301526991859866 0.29307256086276756 rock n
#box: 0.05535059829060697 0.1321416314302006
    0.2886562561529633 0.05735059829060697
    0.1341416314302006 0.2953500973359704 rock n
#box: 0.05535059829060697 0.13326799294180255
    0.2863787196797604 0.05735059829060697
    0.13526799294180256 0.2953500973359704 rock n
#box: 0.05535059829060697 0.1343943544534045
    0.2841011832065576 0.05735059829060697
    0.1363943544534045 0.2964888655725718 rock n
#box: 0.05535059829060697 0.13552071596500645
    0.28296241496995617 0.05735059829060697
    0.13752071596500645 0.2964888655725718 rock n
#box: 0.05535059829060697 0.13664707747660843
    0.28182364673335475 0.05735059829060697
    0.13864707747660843 0.2964888655725718 rock n
#box: 0.05535059829060697 0.13777343898821037
    0.28068487849675333 0.05735059829060697
    0.13977343898821037 0.2964888655725718 rock n
#box: 0.05535059829060697 0.13889980049981232
    0.285239951443159 0.05735059829060697
    0.14089980049981232 0.2964888655725718 rock n
#box: 0.056441127383360934 0.13101526991859866
    0.2897950243895647 0.058441127383360936
    0.13301526991859866 0.29307256086276756 rock n
#box: 0.056441127383360934 0.1321416314302006
    0.2886562561529633 0.058441127383360936
    0.1341416314302006 0.294211329099369 rock n
#box: 0.056441127383360934 0.13326799294180255
    0.2863787196797604 0.058441127383360936
    0.13526799294180256 0.2953500973359704 rock n
#box: 0.056441127383360934 0.1343943544534045
    0.2841011832065576 0.058441127383360936
    0.1363943544534045 0.2953500973359704 rock n
#box: 0.056441127383360934 0.13552071596500645
    0.28296241496995617 0.058441127383360936
    0.13752071596500645 0.2953500973359704 rock n
```

```
#box: 0.056441127383360934 0.13664707747660843
   0.28182364673335475 0.058441127383360936
   0.13864707747660843 0.2953500973359704 rock n
#box: 0.056441127383360934 0.13777343898821037
   0.28182364673335475 0.058441127383360936
   0.13977343898821037 0.2953500973359704 rock n
#box: 0.0575316564761149 0.1321416314302006
   0.2886562561529633 0.0595316564761149
   0.1341416314302006 0.29307256086276756 rock n
#box: 0.0575316564761149 0.13326799294180255
   0.2863787196797604 0.0595316564761149
   0.13526799294180256 0.294211329099369 rock n
#box: 0.0575316564761149 0.1343943544534045
   0.285239951443159 0.0595316564761149
   0.1363943544534045 0.294211329099369 rock n
#box: 0.0575316564761149 0.13552071596500645
   0.2841011832065576 0.0595316564761149
   0.13752071596500645 0.294211329099369 rock n
#box: 0.0575316564761149 0.13664707747660843
   0.28296241496995617 0.0595316564761149
   0.13864707747660843 0.294211329099369 rock n
#box: 0.0575316564761149 0.13777343898821037
   0.285239951443159 0.0595316564761149
   0.13977343898821037 0.29307256086276756 rock n
#box: 0.058622185568868855 0.1321416314302006
   0.2886562561529633 0.06062218556886886
   0.1341416314302006 0.29307256086276756 rock n
#box: 0.058622185568868855 0.13326799294180255
   0.2875174879163619 0.06062218556886886
   0.13526799294180256 0.29307256086276756 rock n
#box: 0.058622185568868855 0.1343943544534045
   0.2863787196797604 0.06062218556886886
   0.1363943544534045 0.29307256086276756 rock n
#box: 0.058622185568868855 0.13552071596500645
   0.2841011832065576 0.06062218556886886
   0.13752071596500645 0.29307256086276756 rock n
#box: 0.058622185568868855 0.13664707747660843
   0.2841011832065576 0.06062218556886886
   0.13864707747660843 0.29307256086276756 rock n
#box: 0.05971271466162282 0.1321416314302006
   0.2897950243895647 0.06171271466162282
   0.1341416314302006 0.29193379262616614 rock n
#box: 0.05971271466162282 0.13326799294180255
   0.2875174879163619 0.06171271466162282
   0.13526799294180256 0.29193379262616614 rock n
#box: 0.05971271466162282 0.1343943544534045
   0.2863787196797604 0.06171271466162282
   0.1363943544534045 0.29193379262616614 rock n
#box: 0.05971271466162282 0.13552071596500645
   0.285239951443159 0.06171271466162282
   0.13752071596500645 0.29193379262616614 rock n
```

```
#box: 0.05971271466162282 0.13664707747660843
    0.285239951443159 0.06171271466162282
    0.13864707747660843 0.2907950243895647 rock n
#box: 0.060803243754376776 0.13326799294180255
    0.2886562561529633 0.06280324375437678
    0.13526799294180256 0.2907950243895647 rock n
#box: 0.060803243754376776 0.1343943544534045
    0.2875174879163619 0.06280324375437678
    0.1363943544534045 0.2907950243895647 rock n
#box: 0.060803243754376776 0.13552071596500645
    0.2863787196797604 0.06280324375437678
    0.13752071596500645 0.2896562561529633 rock n
#box: 0.019737944002385484 0.10235997540672222
    0.2774415421004959 0.021737944002385483
    0.10435997540672222 0.2807019281496156 rock n
#box: 0.019737944002385484 0.1034532402277137
    0.2740509630268163 0.021737944002385483
    0.1054532402277137 0.2807019281496156 rock n
#box: 0.019737944002385484 0.10454650504870518
    0.27292077000225645 0.021737944002385483
    0.10654650504870518 0.27957173512505573 rock n
#box: 0.019737944002385484 0.10563976986969664
    0.27179057697769654 0.021737944002385483
    0.10763976986969664 0.2784415421004959 rock n
#box: 0.019737944002385484 0.10673303469068812
    0.27292077000225645 0.021737944002385483
    0.10873303469068812 0.27618115605137616 rock n
#box: 0.020849654015823782 0.10235997540672222
    0.276311349075936 0.022849654015823784
    0.10435997540672222 0.2807019281496156 rock n
#box: 0.020849654015823782 0.1034532402277137
    0.27292077000225645 0.022849654015823784
    0.1054532402277137 0.2818321211741755 rock n
#box: 0.020849654015823782 0.10454650504870518
    0.2706603839531367 0.022849654015823784
    0.10654650504870518 0.2818321211741755 rock n
#box: 0.020849654015823782 0.10563976986969664
    0.2706603839531367 0.022849654015823784
    0.10763976986969664 0.2818321211741755 rock n
#box: 0.020849654015823782 0.10673303469068812
    0.27179057697769654 0.022849654015823784
    0.10873303469068812 0.2807019281496156 rock n
#box: 0.020849654015823782 0.1078262995116796
    0.27179057697769654 0.022849654015823784
    0.1098262995116796 0.2784415421004959 rock n
#box: 0.020849654015823782 0.10891956433267108
    0.27292077000225645 0.022849654015823784
    0.11091956433267108 0.27618115605137616 rock n
#box: 0.021961364029262083 0.10126671058573074
    0.27857173512505573 0.023961364029262085
    0.10326671058573074 0.2807019281496156 rock n
```

```
#box: 0.021961364029262083 0.10235997540672222
   0.27518115605137616 0.023961364029262085
   0.10435997540672222 0.2818321211741755 rock n
#box: 0.021961364029262083 0.10345324022771 37
   0.27179057697769654 0.023961364029262085
   0.10545324022771 37 0.28296231419873535 rock n
#box: 0.021961364029262083 0.10454650504870518
   0.2706603839531367 0.023961364029262085
   0.10654650504870518 0.28296231419873535 rock n
#box: 0.021961364029262083 0.10563976986969664
   0.2706603839531367 0.023961364029262085
   0.10763976986969664 0.2840925072232952 rock n
#box: 0.021961364029262083 0.10673303469068812
   0.2706603839531367 0.023961364029262085
   0.10873303469068812 0.2840925072232952 rock n
#box: 0.021961364029262083 0.1078262995116796
   0.2706603839531367 0.023961364029262085
   0.1098262995116796 0.2818321211741755 rock n
#box: 0.021961364029262083 0.10891956433267108
   0.27179057697769654 0.023961364029262085
   0.11091956433267108 0.2807019281496156 rock n
#box: 0.021961364029262083 0.11001282915366256
   0.27292077000225645 0.023961364029262085
   0.11201282915366256 0.2784415421004959 rock n
#box: 0.021961364029262083 0.11110609397465404
   0.27292077000225645 0.023961364029262085
   0.11310609397465404 0.27618115605137616 rock n
#box: 0.02307307404270038 0.10126671058573074
   0.2774415421004959 0.02507307404270038
   0.10326671058573074 0.2818321211741755 rock n
#box: 0.02307307404270038 0.10235997540672222
   0.2740509630268163 0.02507307404270038
   0.10435997540672222 0.28296231419873535 rock n
#box: 0.02307307404270038 0.10345324022771 37
   0.27179057697769654 0.02507307404270038
   0.10545324022771 37 0.28296231419873535 rock n
#box: 0.02307307404270038 0.10454650504870518
   0.2706603839531367 0.02507307404270038
   0.10654650504870518 0.2840925072232952 rock n
#box: 0.02307307404270038 0.10563976986969664
   0.26953019092857683 0.02507307404270038
   0.10763976986969664 0.2840925072232952 rock n
#box: 0.02307307404270038 0.10673303469068812
   0.26953019092857683 0.02507307404270038
   0.10873303469068812 0.28522270024785507 rock n
#box: 0.02307307404270038 0.1078262995116796
   0.26953019092857683 0.02507307404270038
   0.1098262995116796 0.28522270024785507 rock n
#box: 0.02307307404270038 0.10891956433267108
   0.2706603839531367 0.02507307404270038
   0.11091956433267108 0.28296231419873535 rock n
```

```
#box: 0.02307307404270038 0.11001282915366256
    0.27179057697769654 0.02507307404270038
    0.11201282915366256 0.2807019281496156 rock n
#box: 0.02307307404270038 0.11110609397465404
    0.27179057697769654 0.02507307404270038
    0.11310609397465404 0.27957173512505573 rock n
#box: 0.02307307404270038 0.11219935879564552
    0.27292077000225645 0.02507307404270038
    0.11419935879564552 0.277311349075936 rock n
#box: 0.024184784056138678 0.10126671058573074
    0.276311349075936 0.02618478405613868
    0.10326671058573074 0.28296231419873535 rock n
#box: 0.024184784056138678 0.10235997540672222
    0.2740509630268163 0.02618478405613868
    0.10435997540672222 0.2840925072232952 rock n
#box: 0.024184784056138678 0.1034532402277137
    0.27179057697769654 0.02618478405613868
    0.1054532402277137 0.2840925072232952 rock n
#box: 0.024184784056138678 0.10454650504870518
    0.26953019092857683 0.02618478405613868
    0.10654650504870518 0.28522270024785507 rock n
#box: 0.024184784056138678 0.10563976986969664
    0.26953019092857683 0.02618478405613868
    0.10763976986969664 0.28522270024785507 rock n
#box: 0.024184784056138678 0.10673303469068812
    0.26953019092857683 0.02618478405613868
    0.10873303469068812 0.28522270024785507 rock n
#box: 0.024184784056138678 0.1078262995116796
    0.26953019092857683 0.02618478405613868
    0.1098262995116796 0.28522270024785507 rock n
#box: 0.024184784056138678 0.10891956433267108
    0.26953019092857683 0.02618478405613868
    0.11091956433267108 0.28296231419873535 rock n
#box: 0.024184784056138678 0.11001282915366256
    0.2706603839531367 0.02618478405613868
    0.11201282915366256 0.2807019281496156 rock n
#box: 0.024184784056138678 0.11110609397465404
    0.27179057697769654 0.02618478405613868
    0.11310609397465404 0.27957173512505573 rock n
#box: 0.024184784056138678 0.11219935879564552
    0.27292077000225645 0.02618478405613868
    0.11419935879564552 0.277311349075936 rock n
#box: 0.02529649406957698 0.10017344576473926
    0.27857173512505573 0.02729649406957698
    0.10217344576473926 0.2818321211741755 rock n
#box: 0.02529649406957698 0.10126671058573074
    0.27518115605137616 0.02729649406957698
    0.10326671058573074 0.2840925072232952 rock n
#box: 0.02529649406957698 0.10235997540672222
    0.27292077000225645 0.02729649406957698
    0.10435997540672222 0.2840925072232952 rock n
```

```
#box: 0.02529649406957698 0.1034532402277137
   0.2706603839531367 0.02729649406957698
   0.1054532402277137 0.28522270024785507 rock n
#box: 0.02529649406957698 0.10454650504870518
   0.26953019092857683 0.02729649406957698
   0.10654650504870518 0.28522270024785507 rock n
#box: 0.02529649406957698 0.10563976986969664
   0.26953019092857683 0.02729649406957698
   0.10763976986969664 0.28522270024785507 rock n
#box: 0.02529649406957698 0.10673303469068812
   0.26953019092857683 0.02729649406957698
   0.10873303469068812 0.28522270024785507 rock n
#box: 0.02529649406957698 0.1078262995116796
   0.26953019092857683 0.02729649406957698
   0.1098262995116796 0.2840925072232952 rock n
#box: 0.02529649406957698 0.10891956433267108
   0.2706603839531367 0.02729649406957698
   0.11091956433267108 0.28296231419873535 rock n
#box: 0.02529649406957698 0.11001282915366256
   0.2706603839531367 0.02729649406957698
   0.11201282915366256 0.2807019281496156 rock n
#box: 0.02529649406957698 0.11110609397465404
   0.27179057697769654 0.02729649406957698
   0.11310609397465404 0.2784415421004959 rock n
#box: 0.02529649406957698 0.11219935879564552
   0.27292077000225645 0.02729649406957698
   0.11419935879564552 0.277311349075936 rock n
#box: 0.026408204083015276 0.10017344576473926
   0.2774415421004959 0.028408204083015275
   0.10217344576473926 0.2818321211741755 rock n
#box: 0.026408204083015276 0.10126671058573074
   0.27518115605137616 0.028408204083015275
   0.10326671058573074 0.28296231419873535 rock n
#box: 0.026408204083015276 0.10235997540672222
   0.27292077000225645 0.028408204083015275
   0.10435997540672222 0.2840925072232952 rock n
#box: 0.026408204083015276 0.1034532402277137
   0.2706603839531367 0.028408204083015275
   0.1054532402277137 0.28522270024785507 rock n
#box: 0.026408204083015276 0.10454650504870518
   0.26953019092857683 0.028408204083015275
   0.10654650504870518 0.28522270024785507 rock n
#box: 0.026408204083015276 0.10563976986969664
   0.26953019092857683 0.028408204083015275
   0.10763976986969664 0.28522270024785507 rock n
#box: 0.026408204083015276 0.10673303469068812
   0.26953019092857683 0.028408204083015275
   0.10873303469068812 0.28522270024785507 rock n
#box: 0.026408204083015276 0.1078262995116796
   0.2706603839531367 0.028408204083015275
   0.1098262995116796 0.2840925072232952 rock n
```

```
#box: 0.026408204083015276 0.10891956433267108
    0.2706603839531367 0.028408204083015275
    0.11091956433267108 0.28296231419873535 rock n
#box: 0.026408204083015276 0.11001282915366256
    0.27179057697769654 0.028408204083015275
    0.11201282915366256 0.2807019281496156 rock n
#box: 0.026408204083015276 0.11110609397465404
    0.27179057697769654 0.028408204083015275
    0.11310609397465404 0.2784415421004959 rock n
#box: 0.026408204083015276 0.11219935879564552
    0.27292077000225645 0.028408204083015275
    0.11419935879564552 0.277311349075936 rock n
#box: 0.027519914096453574 0.10017344576473926
    0.2774415421004959 0.029519914096453576
    0.10217344576473926 0.2807019281496156 rock n
#box: 0.027519914096453574 0.10126671058573074
    0.27518115605137616 0.029519914096453576
    0.10326671058573074 0.2818321211741755 rock n
#box: 0.027519914096453574 0.10235997540672222
    0.27292077000225645 0.029519914096453576
    0.10435997540672222 0.28296231419873535 rock n
#box: 0.027519914096453574 0.1034532402277137
    0.2706603839531367 0.029519914096453576
    0.1054532402277137 0.2840925072232952 rock n
#box: 0.027519914096453574 0.10454650504870518
    0.26953019092857683 0.029519914096453576
    0.10654650504870518 0.28522270024785507 rock n
#box: 0.027519914096453574 0.10563976986969664
    0.26953019092857683 0.029519914096453576
    0.10763976986969664 0.28522270024785507 rock n
#box: 0.027519914096453574 0.10673303469068812
    0.2706603839531367 0.029519914096453576
    0.10873303469068812 0.2840925072232952 rock n
#box: 0.027519914096453574 0.10782629995116796
    0.2706603839531367 0.029519914096453576
    0.1098262995116796 0.28296231419873535 rock n
#box: 0.027519914096453574 0.10891956433267108
    0.27179057697769654 0.029519914096453576
    0.11091956433267108 0.2818321211741755 rock n
#box: 0.027519914096453574 0.11001282915366256
    0.27179057697769654 0.029519914096453576
    0.11201282915366256 0.2807019281496156 rock n
#box: 0.027519914096453574 0.11110609397465404
    0.27292077000225645 0.029519914096453576
    0.11310609397465404 0.2784415421004959 rock n
#box: 0.027519914096453574 0.11219935879564552
    0.2740509630268163 0.029519914096453576
    0.11419935879564552 0.277311349075936 rock n
#box: 0.02863162410989187 0.10126671058573074
    0.276311349075936 0.03063162410989187
    0.10326671058573074 0.2807019281496156 rock n
```

```
#box: 0.02863162410989187 0.10235997540672222
   0.2740509630268163 0.03063162410989187
   0.10435997540672222 0.2818321211741755 rock n
#box: 0.02863162410989187 0.1034532402277137
   0.27179057697769654 0.03063162410989187
   0.1054532402277137 0.28296231419873535 rock n
#box: 0.02863162410989187 0.10454650504870518
   0.2706603839531367 0.03063162410989187
   0.10654650504870518 0.2840925072232952 rock n
#box: 0.02863162410989187 0.10563976986969664
   0.2706603839531367 0.03063162410989187
   0.10763976986969664 0.2840925072232952 rock n
#box: 0.02863162410989187 0.10673303469068812
   0.2706603839531367 0.03063162410989187
   0.10873303469068812 0.28296231419873535 rock n
#box: 0.02863162410989187 0.1078262995116796
   0.27179057697769654 0.03063162410989187
   0.1098262995116796 0.2818321211741755 rock n
#box: 0.02863162410989187 0.10891956433267108
   0.27179057697769654 0.03063162410989187
   0.11091956433267108 0.2807019281496156 rock n
#box: 0.02863162410989187 0.11001282915366256
   0.27292077000225645 0.03063162410989187
   0.11201282915366256 0.27957173512505573 rock n
#box: 0.02863162410989187 0.11110609397465404
   0.27292077000225645 0.03063162410989187
   0.11310609397465404 0.2784415421004959 rock n
#box: 0.02863162410989187 0.11219935879564552
   0.2740509630268163 0.03063162410989187
   0.11419935879564552 0.277311349075936 rock n
#box: 0.02974333412333017 0.10235997540672222
   0.276311349075936 0.03174333412333017
   0.10435997540672222 0.2807019281496156 rock n
#box: 0.02974333412333017 0.1034532402277137
   0.27292077000225645 0.03174333412333017
   0.1054532402277137 0.2818321211741755 rock n
#box: 0.02974333412333017 0.10454650504870518
   0.2706603839531367 0.03174333412333017
   0.10654650504870518 0.28296231419873535 rock n
#box: 0.02974333412333017 0.10563976986969664
   0.27179057697769654 0.03174333412333017
   0.10763976986969664 0.28296231419873535 rock n
#box: 0.02974333412333017 0.10673303469068812
   0.27179057697769654 0.03174333412333017
   0.10873303469068812 0.2818321211741755 rock n
#box: 0.02974333412333017 0.1078262995116796
   0.27292077000225645 0.03174333412333017
   0.1098262995116796 0.2807019281496156 rock n
#box: 0.02974333412333017 0.10891956433267108
   0.27292077000225645 0.03174333412333017
   0.11091956433267108 0.27957173512505573 rock n
```

```
#box: 0.02974333412333017 0.11001282915366256
    0.27292077000225645 0.03174333412333017
    0.11201282915366256 0.2784415421004959 rock n
#box: 0.02974333412333017 0.11110609397465404
    0.2740509630268163 0.03174333412333017
    0.11310609397465404 0.277311349075936 rock n
#box: 0.03085504413676847 0.1034532402277137
    0.276311349075936 0.03285504413676847
    0.1054532402277137 0.2807019281496156 rock n
#box: 0.03085504413676847 0.10454650504870518
    0.27179057697769654 0.03285504413676847
    0.10654650504870518 0.2818321211741755 rock n
#box: 0.03085504413676847 0.10563976986969664
    0.27179057697769654 0.03285504413676847
    0.10763976986969664 0.2818321211741755 rock n
#box: 0.03085504413676847 0.10673303469068812
    0.27292077000225645 0.03285504413676847
    0.10873303469068812 0.2807019281496156 rock n
#box: 0.03085504413676847 0.1078262995116796
    0.2740509630268163 0.03285504413676847
    0.1098262995116796 0.27957173512505573 rock n
#box: 0.03085504413676847 0.10891956433267108
    0.27518115605137616 0.03285504413676847
    0.11091956433267108 0.2784415421004959 rock n
#box: 0.031966754150206764 0.10454650504870518
    0.276311349075936 0.033966754150206765
    0.10654650504870518 0.2807019281496156 rock n
#box: 0.031966754150206764 0.10563976986969664
    0.27518115605137616 0.033966754150206765
    0.10763976986969664 0.2807019281496156 rock n
#box: 0.031966754150206764 0.10673303469068812
    0.276311349075936 0.033966754150206765
    0.10873303469068812 0.27957173512505573 rock n
#box: 0.24767609573216193 0.05711775102217344
    0.20660425846449315 0.24967609573216193
    0.05911775102217344 0.21108447718257625 rock n
#box: 0.24767609573216193 0.05839179202357376
    0.20660425846449315 0.24967609573216193
    0.06039179202357376 0.21224455008860393 rock n
```

D.5 BOWTIE ANTENNA

```
#title: Bowtie antenna

#domain: 0.5 0.2 0.36
#dx_dy_dz: 0.001 0.001 0.001
#time_window: 9e-9

#python:
```

```
from gprMax.exceptions import CmdInputError
from gprMax.input_cmd_funcs import *
from gprMax.input_cmd_funcs import material
from gprMax.input_cmd_funcs import box
from gprMax.input_cmd_funcs import triangle
from gprMax.input_cmd_funcs import waveform
from gprMax.input_cmd_funcs import transmission_line
from gprMax.input_cmd_funcs import voltage_source
from gprMax.input_cmd_funcs import rx
from gprMax.input_cmd_funcs import geometry_view
from gprMax.input_cmd_funcs import edge
from gprMax.input_cmd_funcs import plate
from gprMax.input_cmd_funcs import sphere

#material(1.58, 0.428, 1, 0, 'absorber')
material(1, 0, 1, 0, 'absorber')
print('#add_dispersion_debye: 3 3.7733 1.00723e-11
    3.14418 1.55686e-10 20.2441 3.44129e-10 absorber')

material(3, 0, 1, 0, 'pcb')
material(2.35, 0, 1, 0, 'hdpe')
material(3, 1.0810810810810811, 1, 0, 'rxres')

def my_transmitter(x, y, z, rotate90 = False):

        if rotate90:
                rotate90origin = (x, y)
                output = 'Ex'
        else:
                rotate90origin = ()
                output = 'Ey'

        box(0.020 + x, 0.02 + y, 0.104 + z, 0.110 + x
            , 0.128 + y, 0.147 + z, 'hdpe',
            rotate90origin=rotate90origin)

        box(0.022 + x, 0.022 + y, 0.104 + z, 0.108 +
            x, 0.126 + y, 0.145 + z, 'free_space',
            rotate90origin=rotate90origin)

        box(0.036 + x, 0.023 + y, 0.104 + z, 0.095 +
            x, 0.125 + y, 0.131 + z, 'pec',
            rotate90origin=rotate90origin)

        box(0.037 + x, 0.024 + y, 0.104 + z, 0.094 +
            x, 0.124 + y, 0.128 + z, 'pcb',
            rotate90origin=rotate90origin)

        box(0.04 + x, 0.027 + y, 0.104 + z, 0.091 + x
            , 0.121 + y, 0.129 + z, 'absorber',
            rotate90origin=rotate90origin)
```

```
        box(0.04 + x, 0.027 + y, 0.104 + z, 0.091 + x
            , 0.121 + y, 0.106 + z, 'pcb',
            rotate90origin=rotate90origin)

        triangle(0.054 + x, 0.059 + y, 0.104 + z,
            0.076 + x, 0.059 + y, 0.104 + z, 0.065 + x
            , 0.073 + y, 0.104 + z, 0, 'pec',
            rotate90origin=rotate90origin)

        triangle(0.054 + x, 0.088 + y, 0.104 + z,
            0.076 + x, 0.088 + y, 0.104 + z, 0.065 + x
            , 0.074 + y, 0.104 + z, 0, 'pec',
            rotate90origin=rotate90origin)

        plate(0.054 + x, 0.088 + y, 0.104 + z, 0.076
            + x, 0.103 + y, 0.104 + z, 'pec',
            rotate90origin=rotate90origin)
        plate(0.054 + x, 0.044 + y, 0.104 + z, 0.076
            + x, 0.059 + y, 0.104 + z, 'pec',
            rotate90origin=rotate90origin)

        plate(0.065 + x, 0.072 + y, 0.104 + z, 0.066
            + x, 0.073 + y, 0.104 + z, 'pec',
            rotate90origin=rotate90origin)
        plate(0.065 + x, 0.074 + y, 0.104 + z, 0.066
            + x, 0.075 + y, 0.104 + z, 'pec',
            rotate90origin=rotate90origin)

        box(0.020 + x, 0.020 + y, 0.1 + z, 0.110 + x,
             0.128 + y, 0.104 + z, 'hdpe',
            rotate90origin=rotate90origin)


        waveform('gaussian', 1, 1710000000.0, '
            myGaussian')
        voltage_source('y', 0.065 + x, 0.073 + y,
            0.104 + z, 230, 'myGaussian',
            rotate90origin=rotate90origin)

def my_receiver(x, y, z, rotate90 = False):

        if rotate90:
                rotate90origin = (x, y)
                output = 'Ex'
        else:
                rotate90origin = ()
                output = 'Ey'


        box(0.125 + x, 0.020 + y, 0.104 + z, 0.215 +
            x, 0.128 + y, 0.147 + z, 'hdpe',
            rotate90origin=rotate90origin)
```

```
box(0.127 + x, 0.022 + y, 0.104 + z, 0.213 +
    x, 0.126 + y, 0.145 + z, 'free_space',
    rotate90origin=rotate90origin)

box(0.141 + x, 0.023 + y, 0.104 + z, 0.200 +
    x, 0.125 + y, 0.131 + z, 'pec',
    rotate90origin=rotate90origin)

box(0.142 + x, 0.024 + y, 0.104 + z, 0.199 +
    x, 0.124 + y, 0.128 + z, 'pcb',
    rotate90origin=rotate90origin)

box(0.145 + x, 0.027 + y, 0.104 + z, 0.196 +
    x, 0.121 + y, 0.129 + z, 'absorber',
    rotate90origin=rotate90origin)

box(0.145 + x, 0.027 + y, 0.104 + z, 0.196 +
    x, 0.121 + y, 0.106 + z, 'pcb',
    rotate90origin=rotate90origin)

triangle(0.159 + x, 0.059 + y, 0.104 + z,
    0.181 + x, 0.059 + y, 0.104 + z, 0.170 + x
    , 0.073 + y, 0.104 + z, 0, 'pec',
    rotate90origin=rotate90origin)

triangle(0.159 + x, 0.088 + y, 0.104 + z,
    0.181 + x, 0.088 + y, 0.104 + z, 0.170 + x
    , 0.074 + y, 0.104 + z, 0, 'pec',
    rotate90origin=rotate90origin)

plate(0.159 + x, 0.088 + y, 0.104 + z, 0.181
    + x, 0.103 + y, 0.104 + z, 'pec',
    rotate90origin=rotate90origin)
plate(0.159 + x, 0.044 + y, 0.104 + z, 0.181
    + x, 0.059 + y, 0.104 + z, 'pec',
    rotate90origin=rotate90origin)

plate(0.170 + x, 0.072 + y, 0.104 + z, 0.171
    + x, 0.073 + y, 0.104 + z, 'pec',
    rotate90origin=rotate90origin)
plate(0.170 + x, 0.074 + y, 0.104 + z, 0.171
    + x, 0.075 + y, 0.104 + z, 'pec',
    rotate90origin=rotate90origin)

box(0.125 + x, 0.02 + y, 0.1 + z, 0.215 + x,
    0.128 + y, 0.104 + z, 'hdpe',
    rotate90origin=rotate90origin)
```

```
        edge(0.170 + x, 0.073 + y, 0.104 + z, 0.170 +
            x, 0.074 + y, 0.104 + z, 'rxres',
           rotate90origin=rotate90origin)
        output = 'Ey'
        rx(0.170 + x, 0.073 + y, 0.104 + z,
           identifier='rxbowtie', to_save=[output],
           polarisation='y', rotate90origin=
           rotate90origin)

my_transmitter(0, 0.025, 0.2)
my_receiver(0 + current_model_run * 0.005, 0.025,
   0.2)

geometry_view(0, 0, 0, 0.5, 0.2, 0.36, 0.001, 0.001,
   0.001, 'antenna_model', 'n')

#end_python:
```

BIBLIOGRAPHY

Ahrens, J., Geveci, B., & Law, C. (2005). Paraview: An end-user tool for large data visualization. *The visualization handbook*, *717* (Cited on pages 56, 88, 114).

Al-Qadi, I. L., Leng, Z., Lahouar, S., & Baek, J. (2010). In-place hot-mix asphalt density estimation using ground-penetrating radar. *Transportation research record*, *2152*(1), 19–27 (Cited on page 5).

Al-Qadi, I. L., Xie, W., Roberts, R., & Leng, Z. (2010). Data analysis techniques for GPR used for assessing railroad ballast in high radio-frequency environment. *Journal of transportation engineering*, *136*(4), 392–399 (Cited on page 2).

Al-Saleh, S. A. (2015). Analysis of total chloride content in concrete. *Case Studies in Construction Materials*, *3*, 78–82 (Cited on page 6).

Angelis, D., Warren, C., & Diamanti, N. (2019). Preliminary development of a workflow for processing multi-concurrent receiver GPR data. *10th International Workshop on Advanced Ground Penetrating Radar*, *2019*(1), 1–7 (Cited on page 3).

Annan, A. P. (2002). GPR—History, trends, and future developments. *Subsurface sensing technologies and applications*, *3*(4), 253–270 (Cited on page 9).

Annan, A. P., Diamanti, N., Redman, J. D., & Jackson, S. R. (2016). Ground-penetrating radar for assessing winter roadsGPR for assessing winter roads. *Geophysics*, *81*(1), WA101–WA109 (Cited on page 1).

Annan, A. (2005). Ground-penetrating radar. *Near-surface geophysics* (pp. 357–438). Society of Exploration Geophysicists, Tulsa, Oklahoma. (Cited on page 1).

Anthony. (2017). *Python Pygame Circle Packing*. https://www.youtube.com/watch?v=HLUqDIOng80&t=1047s&ab_channel=code.Pylet. (Cited on page 49)

Balanis, C. A. (1989). Advanced Engineering Electromagnetics, John Willey & Sons. *Inc., New York* (Cited on pages 13, 26, 27).

Benedetto, A., Tosti, F., Ciampoli, L. B., & D'Amico, F. (2017). An overview of ground-penetrating radar signal processing techniques for road inspections. *Signal processing*, *132*, 201–209 (Cited on page 3).

Berenger, J. P. et al. (1994). A perfectly matched layer for the absorption of electromagnetic waves. *Journal of computational physics*, *114*(2), 185–200 (Cited on page 43).

Bérenger, J. P. (2007). Perfectly matched layer (PML) for computational electromagnetics. *Synthesis Lectures on Computational Electromagnetics*, *2*(1), 1–117 (Cited on page 43).

Bergmann, T., Blanch, J. O., Robertsson, J. O., & Holliger, K. (1999). A simplified Lax-Wendroff correction for staggered-grid FDTD modeling of electromagnetic wave propagation in frequency dependent media. *Geophysics*, *64*(5), 1369–1377 (Cited on page 9).

Betz, V., & Mittra, R. (1992). Comparison and evaluation of boundary conditions for the absorption of guided waves in an FDTD simulation. *IEEE Microwave and Guided wave letters*, *2*(12), 499–501 (Cited on page 43).

Birchak, J. R., Gardner, C. G., Hipp, J. E., & Victor, J. M. (1974). High dielectric constant microwave probes for sensing soil moisture. *Proceedings of the IEEE*, *62*(1), 93–98 (Cited on page 5).

Böttcher, C. J. F. (1952). *Theory of Electric Polarisation*. Elsevier Publishing Company, Amsterdam, Netherlands. (Cited on page 5).

Böttcher, C. J. F., & Bordewijk, P. (1978). *Theory of electric polarization* (Vol. 2). Elsevier Science Limited, Amsterdam, The Netherlands. (Cited on pages 5, 121).

Bourdi, T., Rhazi, J. E., Boone, F., & Ballivy, G. (2008). Application of Jonscher model for the characterization of the dielectric permittivity of concrete. *Journal of Physics D: Applied Physics*, *41*(20), 205410 (Cited on page 4).

Bourdi, T., Rhazi, J. E., Boone, F., & Ballivy, G. (2012). Modelling dielectric-constant values of concrete: An aid to shielding effectiveness prediction and ground-penetrating radar wave technique interpretation. *Journal of Physics D: Applied Physics*, *45*(40), 405401 (Cited on page 5).

Bourgeois, J. M., & Smith, G. S. (1996). A fully three-dimensional simulation of a ground-penetrating radar: FDTD theory compared with experiment. *IEEE Transactions on geoscience and remote sensing*, *34*(1), 36–44 (Cited on pages 5, 9).

Bourgeois, J. M., & Smith, G. S. (1997). A complete electromagnetic simulation of a ground penetrating radar for mine detection: Theory and experiment. *IEEE Antennas and Propagation Society International Symposium 1997. Digest*, *2*, 986–989 (Cited on page 5).

Brown, E. (1990). Density of asphalt concrete-how much is needed? *69th Annual Meeting of the Transportation Research Board* (Cited on page 112).

Brown, W. F., Franz, W., & Forsbergh, P. W. (1956). Dielectrics/Dielektrika. *Handbuch der Physik, Springer: Heidelberg, Germany*, *17* (Cited on page 5).

Bruggeman, V. D. (1935). Berechnung verschiedener physikalischer Konstanten von heterogenen Substanzen. I. Dielektrizitätskonstanten und Leitfähigkeiten der Mischkörper aus isotropen Substanzen. *Annalen der physik*, *416*(7), 636–664 (Cited on page 5).

Caratelli, D., Yarovoy, A., & Ligthart, L. P. (2009). Accurate FDTD modelling of resistively-loaded bow-tie antennas for GPR applications. *2009 3rd European Conference on Antennas and Propagation*, 2115–2118 (Cited on page 5).

Cardarelli, E., Marrone, C., & Orlando, L. (2003). Evaluation of tunnel stability using integrated geophysical methods. *Journal of Applied Geophysics*, *52*(2-3), 93–102 (Cited on page 1).

Cassidy, N. J. (2007). A review of practical numerical modelling methods for the advanced interpretation of ground-penetrating radar in near-surface environments. *Near Surface Geophysics*, *5*(1), 5–21 (Cited on page 5).

Cassidy, N. J., & Jol, H. M. (2009). *Electrical and magnetic properties of rocks, soils and fluids* (Vol. 2). chapter. (Cited on page 15).

Cassidy, N. J., & Millington, T. M. (2009). The application of finite-difference time-domain modelling for the assessment of GPR in magnetically lossy materials. *Journal of Applied Geophysics*, *67*(4), 296–308 (Cited on page 5).

Chang, C. W., Lin, C. H., & Lien, H. S. (2009). Measurement radius of reinforcing steel bar in concrete using digital image GPR. *Construction and Building Materials*, *23*(2), 1057–1063 (Cited on page 1).

Chen, H. W., & Huang, T. M. (1998). Finite-difference time-domain simulation of GPR data. *Journal of Applied Geophysics*, *40*(1-3), 139–163 (Cited on page 5).

Chew, W. C., & Weedon, W. H. (1994). A 3D perfectly matched medium from modified Maxwell's equations with stretched coordinates. *Microwave and optical technology letters*, *7*(13), 599–604 (Cited on page 43).

Cook, J. C. (1973). Radar exploration through rock in advance of mining. *Trans. Soc. Min. Eng. AIME*, *254*, 140–146 (Cited on page 9).

Crank, J., & Nicolson, P. (1947). A practical method for numerical evaluation of solutions of partial differential equations of the heat-conduction type. *Mathematical Proceedings of the Cambridge Philosophical Society*, *43*(1), 50–67 (Cited on page 38).

Daniels, D. J. (2004). *Ground Penetrating Radar, 2nd edition*. The Institution of Electrical Engineers. (Cited on pages 1, 9).

Daniels, D. J. (2006). A review of GPR for landmine detection. *Sensing and Imaging: An international journal*, *7*(3), 90–123 (Cited on page 112).

De Pue, J., Van Meirvenne, M., & Cornelis, W. M. (2016). Accounting for surface refraction in velocity semblance analysis with air-coupled GPR. *IEEE Journal of Selected Topics in Applied Earth Observations and Remote Sensing*, *9*(1), 60–73 (Cited on page 3).

Devaux, V., Gardner, G. H. F., & Rampersad, T. (1996). 3-D prestack depth migration by Kirchhoff operator splitting. *SEG Technical Program Expanded Abstracts 1996* (pp. 455–458). Society of Exploration Geophysicists. (Cited on page 23).

Diamanti, N., & Annan, A. P. (2013). Characterizing the energy distribution around GPR antennas. *Journal of Applied Geophysics*, *99*, 83–90 (Cited on page 5).

Diamanti, N., Annan, A. P., & Redman, J. D. (2017). Concrete bridge deck deterioration assessment using ground penetrating radar (GPR). *Journal of Environmental and Engineering Geophysics*, *22*(2), 121–132 (Cited on page 1).

Diamanti, N., Elliott, E. J., Jackson, S. R., & Annan, A. P. (2018). The WARR machine: System design, implementation and data. *Journal of Environmental and Engineering Geophysics*, *23*(4), 469–487 (Cited on page 3).

Diamanti, N., & Giannopoulos, A. (2011). Employing ADI-FDTD subgrids for GPR numerical modelling and their application to study ring separation in brick masonry arch bridges. *Near surface geophysics*, *9*(3), 245–256 (Cited on page 38).

Diamanti, N., & Redman, D. (2012). Field observations and numerical models of GPR response from vertical pavement cracks. *Journal of Applied Geophysics*, *81*, 106–116 (Cited on page 1).

Dinh, K., Gucunski, N., & Duong, T. H. (2018a). An algorithm for automatic localization and detection of rebars from GPR data of concrete bridge decks. *Automation in Construction*, *89*, 292–298 (Cited on page 3).

Dinh, K., Gucunski, N., & Duong, T. H. (2018b). Migration-based automated rebar picking for condition assessment of concrete bridge

decks with ground penetrating radar. *NDT & E International*, *98*, 45–54 (Cited on page 3).

Dinh, K., Gucunski, N., & Zayed, T. (2019). Automated visualization of concrete bridge deck condition from GPR data. *NDT & E International*, *102*, 120–128 (Cited on page 3).

Dobson, M. C., Ulaby, F. T., Hallikainen, M. T., & El-Rayes, M. A. (1985). Microwave dielectric behavior of wet soil-Part II: Dielectric mixing models. *IEEE Transactions on Geoscience and Remote Sensing*, (1), 35–46 (Cited on page 119).

Drossaert, F. H., & Giannopoulos, A. (2007). A nonsplit complex frequency-shifted PML based on recursive integration for FDTD modeling of elastic waves. *Geophysics*, *72*(2), T9–T17 (Cited on page 43).

El-Mahallawy, M. S., & Hashim, M. (2013). Material classification of underground utilities from GPR images using DCT-based SVM approach. *IEEE Geoscience and Remote Sensing Letters*, *10*(6), 1542–1546 (Cited on page 1).

El-Said, M. A. H. (1956). Geophysical prospection of underground water in the desert by means of electromagnetic interference fringes. *Proceedings of the IRE*, *44*(1), 24–30 (Cited on page 9).

Engquist, B., & Majda, A. (1977). Absorbing boundary conditions for numerical simulation of waves. *Proceedings of the National Academy of Sciences*, *74*(5), 1765–1766 (Cited on page 43).

Ernenwein, E. G. (2006). Imaging in the ground-penetrating radar near-field zone: a case study from New Mexico, USA. *Archaeological Prospection*, *13*(2), 154–156 (Cited on page 3).

Everett, M. E. (2013). *Ground-penetrating radar, In Near-Surface Applied Geophysics*. Cambridge University Press. (Cited on pages 13, 14).

Garcia, D., Le Tarnec, L., Muth, S., Montagnon, E., Porée, J., & Cloutier, G. (2013). Stolt's fk migration for plane wave ultrasound imaging. *IEEE transactions on ultrasonics, ferroelectrics, and frequency control*, *60*(9), 1853–1867 (Cited on page 23).

Gardner, C. M. K., Dean, T. J., & Cooper, J. D. (1998). Soil water content measurement with a high-frequency capacitance sensor. *Journal of Agricultural Engineering Research*, *71*(4), 395–403 (Cited on page 119).

Gazdag, J. (1978). Wave equation migration with the phase-shift method. *Geophysics*, *43*(7), 1342–1351 (Cited on page 23).

Gazdag, J., & Sguazzero, P. (1984). Migration of seismic data. *Proceedings of the IEEE*, *72*(10), 1302–1315 (Cited on page 23).

Gedney, S. D. (1996a). An anisotropic perfectly matched layer-absorbing medium for the truncation of FDTD lattices. *IEEE transactions on Antennas and Propagation*, *44*(12), 1630–1639 (Cited on page 43).

Gedney, S. D. (1996b). An anisotropic PML absorbing media for the FDTD simulation of fields in lossy and dispersive media. *Electromagnetics*, *16*(4), 399–415 (Cited on page 43).

Gedney, S. D. (2011). Introduction to the finite-difference time-domain (FDTD) method for electromagnetics. *Synthesis Lectures on Computational Electromagnetics*, *6*(1), 1–250 (Cited on pages 38, 42, 43).

Giannakis, I. (2016). *Realistic numerical modelling of ground penetrating radar for landmine detection*. Department of Infrastructure; Environment, The University of Edinburgh. (Cited on page 10).

Giannakis, I., Giannopoulos, A., & Davidson, N. (2014). Realistic modelling of ground penetrating radar for landmine detection using FDTD. *Proceedings of the 15th International Conference on Ground Penetrating Radar*, 954–959 (Cited on page 1).

Giannakis, I., Giannopoulos, A., & Warren, C. (2016). A realistic FDTD numerical modeling framework of ground penetrating radar for landmine detection. *IEEE journal of selected topics in applied earth observations and remote sensing*, *9*(1), 37–51 (Cited on page 5).

Giannakis, I., Giannopoulos, A., & Warren, C. (2019). Realistic FDTD GPR antenna models optimized using a novel linear/nonlinear Full-Waveform Inversion. *IEEE Transactions on Geoscience and Remote Sensing*, *57*(3), 1768–1778 (Cited on page 5).

Giannopoulos, A. (1998). *The investigation of transmission-line matrix and finite-difference time-domain methods for the forward problem of ground probing radar.* (Doctoral dissertation). University of York. (Cited on pages 9, 38, 39).

Giannopoulos, A. (2005). Modelling ground penetrating radar by GprMax. *Construction and building materials*, *19*(10), 755–762 (Cited on pages 5, 38).

Giannopoulos, A. (2008). An improved new implementation of complex frequency shifted PML for the FDTD method. *IEEE Transactions on antennas and propagation*, *56*(9), 2995–3000 (Cited on page 44).

Giannopoulos, A. (2011). Unsplit implementation of higher order PMLs. *IEEE transactions on antennas and propagation*, *60*(3), 1479–1485 (Cited on page 44).

Giannopoulos, A. (2018). Multipole perfectly matched layer for finite-difference time-domain electromagnetic modeling. *IEEE Transactions on Antennas and Propagation*, *66*(6), 2987–2995 (Cited on page 44).

González-Huici, M. A., Catapano, I., & Soldovieri, F. (2014). A comparative study of GPR reconstruction approaches for landmine detection. *IEEE Journal of Selected Topics in Applied Earth Observations and Remote Sensing*, *7*(12), 4869–4878 (Cited on page 23).

Goodman, D. (1994). Ground-penetrating radar simulation in engineering and archaeology. *Geophysics*, *59*(2), 224–232 (Cited on page 9).

Grassl, P., Wong, H. S., & Buenfeld, N. R. (2010). Influence of aggregate size and volume fraction on shrinkage induced micro-cracking of concrete and mortar. *Cement and concrete research*, *40*(1), 85–93 (Cited on page 115).

Hartley, J., Giannopoulos, A., & Warren, C. (2018). A Huygens subgridding approach for efficient modelling of Ground Penetrating Radar using the Finite-Difference Time-Domain method. *2018 17th International Conference on Ground Penetrating Radar (GPR)*, 1–6 (Cited on page 38).

Higdon, R. L. (1986). Absorbing boundary conditions for difference approximations to the multidimensional wave equation. *Mathematics of computation*, *47*(176), 437–459 (Cited on page 43).

Higdon, R. L. (1987). Numerical absorbing boundary conditions for the wave equation. *Mathematics of computation*, *49*(179), 65–90 (Cited on page 43).

Hoegh, K., Khazanovich, L., Dai, S., & Yu, T. (2015). Evaluating asphalt concrete air void variation via GPR antenna array data. *Case Studies in Nondestructive Testing and Evaluation*, *3*, 27–33 (Cited on page 1).

Holser, W., Brown, R. J. S., Roberts, F. A., Fredriksson, O. A., & Unterberger, R. R. (1972). Radar logging of a salt dome. *Geophysics*, *37*(5), 889–906 (Cited on page 9).

Hugenschmidt, J. (2002). Concrete bridge inspection with a mobile GPR system. *Construction and building materials*, *16*(3), 147–154 (Cited on page 1).

Hugenschmidt, J., & Mastrangelo, R. (2006). GPR inspection of concrete bridges. *Cement and Concrete Composites*, *28*(4), 384–392 (Cited on page 1).

Hussnain, M. M., & Mughal, M. J. (2011). Uniform Plane Wave Reflection from PEC Plane Embedded in a Nonlinear Medium. *Progress In Electromagnetics Research*, *18*, 31–42 (Cited on page 71).

Jin, J. M. (2002). *The finite element method in electromagnetics*. John Wiley & Sons. (Cited on page 38).

Jol, H. M. (2008). *Ground penetrating radar theory and applications*. elsevier, Amsterdam, The Netherlands. (Cited on page 1).

Jol, H. M., Smith, D. G., & Meyers, R. A. (1996). Digital ground penetrating radar (GPR): A new geophysical tool for coastal barrier research (examples from the Atlantic, Gulf and Pacific coasts, USA). *Journal of Coastal Research*, 960–968 (Cited on page 9).

Jury, W. A., & Robert, H. (2004). *Soil physics*. John Wiley & Sons, Hoboken, New Jersey, USA. (Cited on page 116).

Kaufmann, M. S., Klotzsche, A., Vereecken, H., & van der Kruk, J. (2018). Simultaneous multi-channel GPR measurements for soil characterization. *17th International Conference on Ground Penetrating Radar(GPR)*, 1–4 (Cited on page 3).

Kemper, W., & Rosenau, R. (1986). Aggregate stability and size distribution. *Methods of soil analysis: Part 1 Physical and mineralogical methods*, *5*, 425–442 (Cited on page 115).

Klysz, G., & Balayssac, J. P. (2007). Determination of volumetric water content of concrete using ground-penetrating radar. *Cement and concrete research*, *37*(8), 1164–1171 (Cited on page 1).

Klysz, G., Balayssac, J. P., & Ferrières, X. (2008). Evaluation of dielectric properties of concrete by a numerical FDTD model of a GPR coupled antenna—parametric study. *NDT & e International*, *41*(8), 621–631 (Cited on page 4).

Klysz, G., Balayssac, J. P., Laurens, S., & Ferrieres, X. (2004). Numerical FDTD simulation of the direct wave propagation of a GPR coupled antenna. *Proceedings of the Tenth International Conference on Grounds Penetrating Radar, 2004. GPR 2004.*, *1*, 45–48 (Cited on page 5).

Lachowicz, J., & Rucka, M. (2017). A concept of heterogeneous numerical model of concrete for GPR simulations. *2017 9th International Workshop on Advanced Ground Penetrating Radar (IWAGPR)*, 1–4 (Cited on pages 59, 87, 115, 116).

Lampe, B., & Holliger, K. (2000). Finite-difference modeling of ground penetrating radar antenna radiation. *Eighth International Con-*

ference on Ground Penetrating Radar, *4084*, 556–560 (Cited on page 9).

Lampe, B., & Holliger, K. (2005). Resistively loaded antennas for ground-penetrating radar: A modeling approach. *Geophysics*, *70*(3), K23–K32 (Cited on page 5).

Laurens, S., Balayssac, J. P., Rhazi, J., Klysz, G., & Arliguie, G. (2005). Non-destructive evaluation of concrete moisture by GPR: experimental study and direct modeling. *Materials and structures*, *38*(9), 827–832 (Cited on page 6).

Lauro, S. E., Mattei, E., Barone, P. M., Pettinelli, E., Vannaroni, G., Valerio, G., Comite, D., & Galli, A. (2013). Estimation of subsurface dielectric target depth for GPR planetary exploration: Laboratory measurements and modeling. *Journal of Applied Geophysics*, *93*, 93–100 (Cited on page 1).

Lee, J. F., Lee, R., & Cangellaris, A. (1997). Time-domain finite-element methods. *IEEE transactions on antennas and propagation*, *45*(3), 430–442 (Cited on page 38).

Lee, K. H., Chen, C. C., Teixeira, F. L., & Lee, R. (2004). Modeling and investigation of a geometrically complex UWB GPR antenna using FDTD. *IEEE Transactions on Antennas and Propagation*, *52*(8), 1983–1991 (Cited on page 5).

Liao, Z. F., Huang, K. l., Yang, B. P., & Yuan, Y. F. (1984). A transmitting boundary for transient wave analyses. *Science in China Series A-Mathematics, Physics, Astronomy & Technological Science*, *27*(10), 1063–1076 (Cited on page 43).

Mai, T. C., Razafindratsima, S., Sbartai, Z. M., Demontoux, F., & Bos, F. (2015). Non-destructive evaluation of moisture content of wood material at GPR frequency. *Construction and Building Materials*, *77*, 213–217 (Cited on page 1).

Maierhofer, C. (2003). Nondestructive evaluation of concrete infrastructure with ground penetrating radar. *Journal of Materials in Civil Engineering*, *15*(3), 287–297 (Cited on page 1).

Maijala, P. et al. (1992). Application of some seismic data processing methods to ground penetrating radar data. *Fourth International Conference on Ground Penetrating Radar* (Cited on page 9).

Mezgeen, R., Vega, P. G., & Assunção, S. S. (2018). Analysis and Calibration of Ground Penetrating Radar Shielded Antennas, 605–609 (Cited on page 3).

Moghaddam, M., Yannakakis, E., Chew, W. C., & Randall, C. (1991). Modeling of the subsurface interface radar. *Journal of Elec-*

tromagnetic Waves and Applications, *5*(1), 17–39 (Cited on page 9).

Mur, G. (1981). Absorbing boundary conditions for the finite-difference approximation of the time-domain electromagnetic-field equations. *IEEE transactions on Electromagnetic Compatibility*, (4), 377–382 (Cited on page 43).

Olhoeft, G. R. (1998). Electrical, magnetic and geometric properties that determine ground penetrating radar performance. *Proceedings of GPR*, *98*, 27–30 (Cited on page 15).

Olsson, O., Falk, L., Sandberg, E., Forslund, O., & Lundmark, L. (1987). *Crosshole investigations-Results from borehole radar investigations* (tech. rep.). Swedish Nuclear Fuel and Waste Management Co. (Cited on page 9).

Oristaglio, M. L., & Hohmann, G. W. (1984). Diffusion of electromagnetic fields into a two-dimensional earth: A finite-difference approach. *Geophysics*, *49*(7), 870–894 (Cited on page 9).

Owen, T. R. (1981). Cavity detection using VHF hole-to-hole electromagnetic techniques. *Proceedings of the Second Tunnel Detection Symposium, Colorado School of Mines, Golden CO*, 126–141 (Cited on page 9).

Peplinski, N. R., Ulaby, F. T., & Dobson, M. C. (1995a). Corrections to" Dielectric Properties of Soils in the 0.3-1.3-GHz Range". *IEEE Transactions on Geoscience and Remote Sensing*, *33*(6), 1340 (Cited on page 88).

Peplinski, N. R., Ulaby, F. T., & Dobson, M. C. (1995b). Dielectric properties of soils in the 0.3-1.3-GHz range. *IEEE transactions on Geoscience and Remote sensing*, *33*(3), 803–807 (Cited on pages 22, 88, 119).

Pérez-Gracia, V., Garcia, F. G., & Abad, I. R. (2008). GPR evaluation of the damage found in the reinforced concrete base of a block of flats: A case study. *NDT & e International*, *41*(5), 341–353 (Cited on page 4).

Peterson, A. F., Ray, S. L., & Mittra, R. (1998). *Computational methods for electromagnetics* (Vol. 1). IEEE press New York. (Cited on page 38).

Philipp, K., Jens, T., Niklas, A., Andreas, K., & Michael, W. (2018). Estimating moisture changes in concrete using GPR velocity analysis: potential and limitations, 664–669 (Cited on page 3).

Radzevicius, S. J., Chen, C. C., Peters Jr, L., & Daniels, J. J. (2003). Near-field dipole radiation dynamics through FDTD modeling. *Journal of applied geophysics*, *52*(2-3), 75–91 (Cited on page 5).

Rayleigh, L. (1892). LVI. On the influence of obstacles arranged in rectangular order upon the properties of a medium. *The London, Edinburgh, and Dublin Philosophical Magazine and Journal of Science*, *34*(211), 481–502 (Cited on pages 5, 121).

Robert, A. (1998). Dielectric permittivity of concrete between 50 MHz and 1 GHz and GPR measurements for building materials evaluation. *Journal of applied geophysics*, *40*(1-3), 89–94 (Cited on page 6).

Roberts, R. L., & Daniels, J. J. (1997). Modeling near-field GPR in three dimensions using the FDTD method. *Geophysics*, *62*(4), 1114–1126 (Cited on page 9).

Roden, J. A., & Gedney, S. D. (2000). Convolution PML (CPML): An efficient FDTD implementation of the CFS–PML for arbitrary media. *Microwave and optical technology letters*, *27*(5), 334–339 (Cited on page 43).

Roth, K., Schulin, R., Flühler, H., & Attinger, W. (1990). Calibration of time domain reflectometry for water content measurement using a composite dielectric approach. *Water Resources Research*, *26*(10), 2267–2273 (Cited on page 119).

Saarenketo, T., & Scullion, T. (2000a). Road evaluation with ground penetrating radar. *Journal of applied geophysics*, *43*(2-4), 119–138 (Cited on page 1).

Saarenketo, T., & Scullion, T. (2000b). Road evaluation with ground penetrating radar. *Journal of Applied Geophysics*, *43* (Cited on page 132).

Sacks, Z. S., Kingsland, D. M., Lee, R., & Lee, J. F. (1995). A perfectly matched anisotropic absorber for use as an absorbing boundary condition. *IEEE transactions on Antennas and Propagation*, *43*(12), 1460–1463 (Cited on page 43).

Sadiku, M. N. (2000). *Numerical techniques in electromagnetics*. CRC press. (Cited on page 5).

Schneider, W. A. (1978). Integral formulation for migration in two and three dimensions. *Geophysics*, *43*(1), 49–76 (Cited on page 23).

Schofield, J., Daniels, D., & Hammerton, P. (2014). A multiple migration and stacking algorithm designed for land mine detection. *IEEE transactions on geoscience and remote sensing*, *52*(11), 6983–6988 (Cited on page 23).

Shang, J. Q. (2002). Effects of asphalt pavement properties on complex permittivity. *International Journal of Pavement Engineering*, *3*(4), 217–226 (Cited on page 1).

Shangguan, P., & Al-Qadi, I. L. (2014). Calibration of FDTD simulation of GPR signal for asphalt pavement compaction monitoring. *IEEE Transactions on Geoscience and Remote Sensing*, *53*(3), 1538–1548 (Cited on page 1).

Shaw, M. R. (1998). The permittivity and conductivity of concretes at ground-penetrating radar frequencies. *Advances in cement Research*, *10*(4), 187–194 (Cited on page 6).

Sihvola, A. H. (1999). *Electromagnetic mixing formulas and applications*. Iet, padstow, cornwall. (Cited on page 5).

Smitha, N., Bharadwaj, D. U., Abilash, S., Sridhara, S. N., & Singh, V. (2016). Kirchhoff and FK migration to focus ground penetrating radar images. *International Journal of Geo-Engineering*, *7*(1), 4 (Cited on page 23).

Soutsos, M. N., Bungey, J. H., Millard, S. G., Shaw, M. R., & Patterson, A. (2001). Dielectric properties of concrete and their influence on radar testing. *NDT & e International*, *34*(6), 419–425 (Cited on page 6).

Stolt, R. H. (1978). Migration by Fourier transform. *Geophysics*, *43*(1), 23–48 (Cited on page 23).

Taflove, A., & Hagness, S. C. (2005). Computational electromagnetics: the finite-difference time-domain method. *Artech House, Norwood, MA, 3rd edition.* (Cited on pages 5, 42, 43).

Terrasse, G., Nicolas, J. M., Trouvé, E., & Drouet, É. (2016). Automatic localization of gas pipes from GPR imagery. *2016 24th European Signal Processing Conference (EUSIPCO)*, 2395–2399 (Cited on page 112).

Topp, G. C., Davis, J. L., & Annan, A. P. (1980). Electromagnetic determination of soil water content: Measurements in coaxial transmission lines. *Water resources research*, *16*(3), 574–582 (Cited on page 5).

Tsui, F., & Matthews, S. L. (1997). Analytical modelling of the dielectric properties of concrete for subsurface radar applications. *Construction and Building Materials*, *11*(3), 149–161 (Cited on page 4).

Turk, A. S., Sahinkaya, D. A., Sezgin, M., & Nazli, H. (2007). Investigation of convenient antenna designs for ultra-wide band GPR systems. *2007 4th International Workshop on, Advanced Ground Penetrating Radar*, 192–196 (Cited on page 5).

Uduwawala, D. (2006). Modeling and investigation of planar parabolic dipoles for GPR applications: A comparison with bow-tie using

FDTD. *Journal of Electromagnetic Waves and Applications*, *20*(2), 227–236 (Cited on page 5).

Ukaegbu, I. K., Gamage, K. A., & Aspinall, M. D. (2019). Nonintrusive Depth Estimation of Buried Radioactive Wastes Using Ground Penetrating Radar and a Gamma Ray Detector. *Remote Sensing*, *11*(2), 141 (Cited on page 119).

Venkatarayalu, N. V., Chen, C. C., Teixeira, F. L., & Lee, R. (2004). Numerical modeling of ultrawide-band dielectric horn antennas using FDTD. *IEEE Transactions on Antennas and Propagation*, *52*(5), 1318–1323 (Cited on page 5).

Viriyametanont, K., Laurens, S., Klysz, G., Balayssac, J. P., & Arliguie, G. (2008). Radar survey of concrete elements: Effect of concrete properties on propagation velocity and time-zero. *NDT & E International*, *41*(3), 198–207 (Cited on page 3).

Wagner, A. (1914). Physik, 40, 817 (1913). *Arch. Elektroteeh*, *3*, 83 (Cited on page 5).

Warren, C. (2009). *Numerical modelling of high-frequency Ground-Penetrating Radar antennas* (Doctoral dissertation PhD thesis). Department of Infrastructure; Environment, The University of Edinburgh. (Cited on pages 17, 97, 98, 136).

Warren, C., & Giannopoulos, A. (2011). Creating finite-difference time-domain models of commercial ground-penetrating radar antennas using Taguchi's optimization method. *Geophysics*, *76*(2), G37–G47 (Cited on pages 5, 6, 60, 97).

Warren, C., & Giannopoulos, A. (2012). Investigation of the directivity of a commercial ground-penetrating radar antenna using a finite-difference time-domain antenna model. *2012 14th International Conference on Ground Penetrating Radar (GPR)*, 226–231 (Cited on page 113).

Warren, C., Giannopoulos, A., & Giannakis, I. (2016). gprMax: Open source software to simulate electromagnetic wave propagation for Ground Penetrating Radar. *Computer Physics Communications*, *209*, 163–170 (Cited on pages 5, 38, 112).

Warren, C., Giannopoulos, A., Gray, A., Giannakis, I., Patterson, A., Wetter, L., & Hamrah, A. (2019). A CUDA-based GPU engine for gprMax: open source FDTD electromagnetic simulation software. *Computer Physics Communications*, *237*, 208–218 (Cited on pages 38, 112, 113).

Wei, X.-K., Zhang, X., Diamanti, N., Shao, W., & Sarris, C. D. (2017). Subgridded FDTD modeling of ground penetrating radar scenarios beyond the courant stability limit. *IEEE Transactions*

on Geoscience and Remote Sensing, *55*(12), 7189–7198 (Cited on page 38).

Wu, Z., Wong, H., & Buenfeld, N. (2017). Transport properties of concrete after drying-wetting regimes to elucidate the effects of moisture content, hysteresis and microcracking. *Cement and concrete research*, *98*, 136–154 (Cited on page 6).

Yee, K. (1966). Numerical solution of initial boundary value problems involving Maxwell's equations in isotropic media. *IEEE Transactions on antennas and propagation*, *14*(3), 302–307 (Cited on pages 5, 38).

Yelf, R. (2004). Where is true time zero? *Ground Penetrating Radar, 2004. GPR 2004. Proceedings of the Tenth International Conference on*, *1*, 279–282 (Cited on pages 2, 3, 65, 67, 80, 86, 102, 103, 112, 131).

Yilmaz, Ö. (2001). *Seismic data analysis: Processing, inversion, and interpretation of seismic data*. Society of exploration geophysicists. (Cited on page 23).

Zadhoush, H., & Giannopoulos, A. (2021). Optimising GPR time-zero adjustment and two-way travel time wavelet measurement using a realistic 3D numerical model. *Near Surface Geophysics* (Cited on page 112).

Zadhoush, H., Giannopoulos, A., & Giannakis, I. (2021). Optimising the Complex Refractive Index Model for estimating the permittivity of heterogeneous concrete models. *Remote Sensing*, *13*(4), 723 (Cited on page 119).

Zeng, X., McMechan, G. A., Cai, J., & Chen, H. W. (1995). Comparison of ray and Fourier methods for modeling monostatic ground-penetrating radar profiles. *Geophysics*, *60*(6), 1727–1734 (Cited on page 9).